

AD-A052 633

HONEYWELL INC MINNEAPOLIS MINN SYSTEMS AND RESEARCH --ETC F/6 22/2
NTS-2 INDEPENDENT STABILITY AND CONTROL ANALYSIS. VOLUME I. TEC--ETC(U)
MAR 77 R E POPE, M D WARD, S M SCHWANTES
77SRC17-VOL-1

UNCLASSIFIED

NL

4
1 OF
AD A052633



**SYSTEMS AND RESEARCH CENTER
2800 RIDGWAY PARKWAY
MINNEAPOLIS, MINNESOTA 55413**

30 March 1977

FINAL REPORT

VOLUME I TECHNICAL REPORT

Prepared for

SAMSO (YEES)

P.O. BOX 92000

WORLDWAY POSTAL CENTER

LOS ANGELES CALIFORNIA 90009

**D. D.
FOR
APR 1
RECEIVED**

DISTRIBUTION STATEMENT

Approved for public release

Unclassified

SECURITY CLASSIFICATION OF THIS PAGE (WHEN DATA ENTERED)

REPORT DOCUMENTATION PAGE		READ INSTRUCTIONS BEFORE COMPLETING FORM								
1. REPORT NUMBER <u>ADG Report F0360-24</u>	2. GOV'T ACCESSION NUMBER	3. RECIPIENT'S CATALOG NUMBER								
4. TITLE (AND SUBTITLE) <u>NTS-2 Independent Stability and Control Analysis • Volume I • Technical Report</u>		5. TYPE OF REPORT PERIOD COVERED <u>Final Report</u> <u>Feb 76-Mar 77</u>								
7. AUTHOR(S) <u>R. E. Pope, M. D. Ward, S. M. Schwantes</u> <u>J. G. Rupert</u>		6. CONTRACT OR GRANT NUMBER(S) <u>77SRC17-Vol-1, F0360-24-Vol-1</u>								
9. PERFORMING ORGANIZATIONS NAME/ADDRESS <u>Honeywell Systems & Research Center</u> <u>2600 Ridgway Parkway</u> <u>Minneapolis, Minnesota 55413</u>		10. PROGRAM ELEMENT, PROJECT, TASK AREA & WORK UNIT NUMBERS								
11. CONTROLLING OFFICE NAME/ADDRESS <u>SAMSO (YEES)</u> <u>P. O. Box 92960, Worldway Postal Center</u> <u>Los Angeles, California 90009</u>		12. REPORT DATE <u>30 Mar 77</u>								
14. MONITORING AGENCY NAME/ADDRESS (IF DIFFERENT FROM CONT. OFF.)		13. NUMBER OF PAGES <u>288</u>								
		15. SECURITY CLASSIFICATION (OF THIS REPORT) <u>Unclassified</u>								
16. DISTRIBUTION STATEMENT (OF THIS REPORT) <u>Approved for public release; distribution unlimited</u>		15a. DECLASSIFICATION DOWNGRADING SCHEDULE								
17. DISTRIBUTION STATEMENT (OF THE ABSTRACT ENTERED IN BLOCK 20, IF DIFFERENT FROM REPORT)										
18. SUPPLEMENTARY NOTES <u>This is Volume I of two volumes. Volume II contains Appendices A through M (243 pages).</u>										
19. KEY WORDS (CONTINUE ON REVERSE SIDE IF NECESSARY AND IDENTIFY BY BLOCK NUMBER) <table border="0"><tr><td><u>NTS-2</u></td><td><u>Reaction wheels</u></td></tr><tr><td><u>Stability analysis</u></td><td><u>GPS</u></td></tr><tr><td><u>Satellite simulation</u></td><td><u>NAVSTAR</u></td></tr><tr><td><u>Gravity gradient</u></td><td></td></tr></table>			<u>NTS-2</u>	<u>Reaction wheels</u>	<u>Stability analysis</u>	<u>GPS</u>	<u>Satellite simulation</u>	<u>NAVSTAR</u>	<u>Gravity gradient</u>	
<u>NTS-2</u>	<u>Reaction wheels</u>									
<u>Stability analysis</u>	<u>GPS</u>									
<u>Satellite simulation</u>	<u>NAVSTAR</u>									
<u>Gravity gradient</u>										
20. ABSTRACT (CONTINUE ON REVERSE SIDE IF NECESSARY AND IDENTIFY BY BLOCK NUMBER) <u>Volume I presents the results of the NTS-2 Independent Stability and Control Analysis. Critical mission items investigated were nutation damper performance, gravity gradient rod deployment and acquisition, on-orbit performance, and rod and solar array flexibility effects. Detailed descriptions of vehicle/orbital dynamics, disturbances and control components are also presented.</u>										

HD-168 REV 11/74

DD FORM
1 JAN 73

1473

EDITION OF 1 NOV 55 IS OBSOLETE

Unclassified

SECURITY CLASSIFICATION OF THIS PAGE (WHEN DATA ENTERED)

402349

SECURITY CLASSIFICATION OF THIS PAGE (WHEN DATA ENTERED)

SECURITY CLASSIFICATION OF THIS PAGE (WHEN DATA ENTERED)

TABLE OF CONTENTS

<u>Section</u>	<u>Page</u>
I	INTRODUCTION 1
II	SUMMARY OF RESULTS AND RECOMMENDATIONS 2
III	MODEL DEVELOPMENT 5
IV	PRESENTATION OF RESULTS 79
V	CONCLUSIONS 288

ADDRESS <input type="checkbox"/> IN	
RTG <input type="checkbox"/> 10	UNIT SECTION <input checked="" type="checkbox"/>
DOB <input type="checkbox"/>	UNIT CODE <input type="checkbox"/>
1. SIGNATURE <input type="checkbox"/>	
INITIALS <input type="checkbox"/>	
BY	
SIGNATURE/AVAILABILITY CODES	
SIL	AVAIL. NO. IN SPECIAL
A	

LIST OF FIGURES

<u>Figure</u>		<u>Page</u>
1	Inertial and Local Vertical Coordinate System	6
2	Body and Panel Coordinate System	7
3	NRL/NTS-2 Coordinate System	9
4	NDS and NTS-2 Nutation Damper Characteristics	11
5	ACE Control System--Spacetac Print	13
6	ACE System--Spacetac Print	14
7	Roll Angle to Wheel 1 Relationship	15
8	Modified Wheel Control System	17
9	Modified Wheel Dynamics	18
10	NTS-2 Satellite Tip Mass Acceleration vs. Time	24
11	NTS-2 Satellite Rotation vs. Time About Solar Array Drive Axis	25
12	Straight Beam Model	26
13	Curved Beam Model	29
14	Solar Array Drive Motor	35
15	Solar Array Bending Flexure Model	36
16	STARDYNE Math Model for Flexible Solar Arrays	40
17	Gravity Gradient Rod and Spacecraft Definition	41
18	STARDYNE Model Node 2 θ_Y Response Versus Time	44

LIST OF FIGURES (continued)

<u>Figure</u>		<u>Page</u>
19	Solar Array Torsion Model 4 Pulse Input Forcing Function (Normalized) (Amplitude of 1.0 = .04 ft-lb)	45
20	Solar Array Torsion Model, Node 2 = Outer Panel Display, Velocity, Acceleration and Response (in Radian Units) to Four Pulse Excitation	46
21	Solar Array Torsion Model Response at Drive Motor to 4 Pulses Applied at Drive Motor	47
22	Solar Array Torsion Model Response of Rigid Spacecraft to 4 Pulses	48
23	Response of -Z Gravity Rod Tip Mass (Node 48) X Direction Response (Inch Units) Relative* to Spacecraft Attach Point, 4 Pulses on Solar Array Drive Motor	49
24	Spring Location	57
25	Spring Location--No Misalignment	58
26	Spring Location--Misalignment as Shown	59
27	Spring Force Displacement Calculation	60
28	Solar Array Drive Functional Block Diagram	65
29	Torsional Spring Mass Damper System	66
30	Solar Array Response	69
31	Coulomb Friction Effect	71
32	Bendix Test Data	73
33	Yaw Sun Sensor Characteristics	75

LIST OF FIGURES (continued)

<u>Figure</u>		<u>Page</u>
34	Damper Position	80
35	Nutation Damper Run Launch 90 RPM, 3 Deg Nutation Angle Inelastic	82
36	Damper Performance, Post Separation	84
37	Damper Performance, Post AKM Burn	85
38	Damper Performance, Post AKM Jettison	86
39	Nutation Damper Run AKM Jettison	91
40	Root Migration as a Function of Loop Gain	95
41	Roll/Yaw s Plane Equations	96
42	G(s) with Roll/Yaw Sensor Feedback	99
43	Yaw Solar Torques	101
44	G(s) with Yaw Solar Torque Effect	103
45	Root Migration as a Function of Yaw Solar Torque	104
46	G(s) Including the Effect of Magnetic Torques	109
47	Root Migration as a Function of Magnetic Torques	110
48	Wheel Orientation	112
49	Root Migration as a Function of Wheel Misalignment	113
50	Run 1 - Sunline 35° - Nominal	132
51	Run 2 - Sunline 86° - Nominal	138

LIST OF FIGURES (continued)

<u>Figure</u>		<u>Page</u>
52	Run 3 - Sunline 0° - Nominal	144
53	Run 1A - Sensed Pitch and Roll Angles in Feed Back Nominal	150
54	Run 1B - Sensed Pitch and Roll Angles in Feed Back Earth Sensor Misaligned	157
55	Run 4 - Sunline 45° - $K_{\phi}/2$	164
56	Run 4A - Sunline 45° - $2K_{\phi}$	170
57	Run 6C - Sunline 12° - $K_4/2$ - Dead Bands Out	176
58	Run 4B - Sunline 45° - 4A + Wheel Misalignments	182
59	Run 4C - Sunline 45° - 4B + CP Shift	188
60	Run 5 - Sunline 86° - Worst Case	194
61	Run 6 - Sunline 0° - Worst Case	200
62	Run 7A - Wheel 1 Failure Compensated - Worst Case - Sunline 0°	206
63	Run 8 - Wheel 2 Failure Uncompensated - Worst Case - Sunline 45°	212
64	Run 9 - Wheel 2 Failure Compensated - Worst Case - Sunline 45°	218
65	Run 10 - Wheel 2 Failure Compensated - Worst Case - Sunline 86°	224
66	Run 19 - Deployment (P.Q.R.) = (.007..007..1) (PHI.THT.PSI) = (0.0.10)	230

LIST OF FIGURES (concluded)

<u>Figure</u>		<u>Page</u>
67	Run 20 - Deployment (P.Q.R.) = (.007.007..05) (PHI.THT.PSI) = (0.0.10)	236
68	Run 21 - Deploy (P.Q.R.) = (.007..007.01) (PHI.THT.P91) = (.25..25.10.0)	242
69	Run 23 - Deploy (P.Q.R.) = (.007..007..01) (PHI.THT.PSI) = (.25..25.10.0) ROD1 and ROD2 Rates Unequal	248
70	Run 24 - Deploy (P.Q.R.) = (.007..007..01) (PHI.THT.PSI) = (.25..25.10.0) ROD1 and ROD2 Rates Unequal KSUB(PSI) = KSUB(PSI)/2	254
71	Run 25 - 2 Second Run 3 Body	260
72	Run 26 - 60 Second Run 3 Body without C. E. Fix	265
73	Run 27 - 60 Second Run 3 Body with C. E. Fix	270
74	Run 27A - 60 Sec 3 Body Run with Locked Up Drive Motor	275
75	Run 28 - 10 Minute Run 3 Body	279
76	Roll Wheel Frequency Response	285
77	Pitch Wheel Frequency Response	286
78	Yaw Wheel Frequency Response	287

LIST OF TABLES

<u>Table</u>		<u>Page</u>
1	Radiation Constants	21
2	Influence Coefficient Matrix for Two-Beam Gravity Gradient Rod	30
3	Damping Matrix for Two-Beam Gravity Gradient Rod (For 1/2 of 1 percent Critical Damping)	32
4	-Y Solar Array (Bending Only)	37
5	+Y Solar Array (Bending Only)	38
6	NTS-2 Solar Arrays	42
7	Comparison of Original and Modified Torsional Mode Frequencies	50
8	Spring Force Displacement and Spring Constant	61
9	Spring Force and Resulting Torque	63
10	Nutation Damper Performance--Launch	87
11	Nutation Damper Performance--Post AKM Burn	88
12	Nutation Damper Performance--Post AKM Jettison	89
13	Satellite Equation Constants	93
14	Effect of Varying Yaw Sensor Output on Root Migration	100
15	Plotting Symbol Definitions	114
16	Run Log	115
17	Tracking Errors--Nominal Conditions	119

LIST OF TABLES (concluded)

<u>Table</u>		<u>Page</u>
18	Tracking Errors--Off Nominal Conditions	119
19	ACE System Stability Margins	129
20	Flexibility Effects Run Table	130
21	Flexibility Run Symbol Definition	131

SECTION I

INTRODUCTION

The results of the NTS-2 independent stability and control analysis will be presented in the following order:

- o Summary of results and recommendations
- o Model development
- o Simulation and supplementary analysis
- o Conclusions

Since much of the modeling had been developed under the NDS study, only those model elements which specifically affect NTS-2 results will be described.

SECTION II

SUMMARY OF RESULTS AND RECOMMENDATIONS

NTS-2 verification results can be summarized as follows.

Nutation Damper Performance

Results: Analysis of nutation damper performance at the post separation, post AKM burn, and post AKM jettison mission time points predicts the following ranges of equivalent time constants.

- Post separation, 300-700 seconds
- Post AKM burn, 120-850 seconds
- Post AKM jettison, 1000-5000 seconds

The ball was observed to hit the end of the tube, particularly at the post separation condition, but with no deleterious effects on nutation damping.

Simulation of the AKM jettison with time varying inertias and worst case disturbance torques indicated an insignificant nutation angle disturbance.

Recommendations: None

On Orbit Performance

Results: Large stability margins were predicted from linear analysis for the effects of solar torques, magnetic torques, yaw sun sensor errors and

wheel misalignments. Simulation of satellite performance at four sun line to orbit plane angles (0° , 12° , 45° , 86°) under nominal and worst case conditions uncovered no instabilities. Wheel failures, if compensated for within six orbits, will cause no problems.

Recommendations: None

Deployment and Acquisition

Results: If reaction wheels are turned on at the start of rod deployment, earth/sun acquisition is possible without earth/sun sensor saturation for the following initial body rates

$$p = .007^\circ/\text{sec} + \dot{\kappa}$$

$$q = .007^\circ/\text{sec} + \dot{\kappa}$$

$$r = .01^\circ/\text{sec} + \dot{\psi}_s$$

where $\dot{\kappa}$ represents earth rate and $\dot{\psi}_s$ represents sun tracking rate.

Recommendations: Use results shown above as guidelines for deployment procedures.

Rod and Panel Flexibility Effects

Results: Large gain and phase margins in the control system should handle any unpredicted rod flexibility effects. Simulation of rod and panel flexibility dynamics with complete satellite model uncovered no instabilities.

Recommendations: None

In general, performance was more than satisfactory. No stability or control problems are anticipated in those areas investigated.

SECTION III

MODEL DEVELOPMENT

III-A. REFERENCE SYSTEM DESCRIPTION

Five coordinate systems were employed in the analysis. The inertial coordinate system (X_I, Y_I, Z_I) has its origin at the center of the earth. Z_I points north, X_I is positive in the direction of vernal equinox, and Y_I makes up a right handed triad. The local vertical coordinate system (X_{LV}, Y_{LV}, Z_{LV}) has its origin at the center of mass of the space vehicle. Z_{LV} points at the earth's center, X_{LV} is in the direction of orbital velocity, and Y_{LV} is normal to the orbit plane. The inertial and local vertical coordinate systems are shown in Figure 1.

The body coordinate system (X_B, Y_B, Z_B) has its origin at the center of mass of the space vehicle. Z_B points in the direction of the vehicle antennae or, equivalently, in the direction of the gravity gradient rod with the smaller tip mass, Y_B is along the solar panel support boom, and X_B completes a right handed triad. This axis system was employed with the NDS analysis and is consistent with Rockwell's definition. A panel coordinate system (X_p, Y_p, Z_p) was also employed. Z_p is normal to the panel surface, Y_p is along the solar panel support boom, and X_p completes the right handed triad. Panel angle is defined to be zero when the panel coordinate system is aligned with the body coordinate system. The body coordinate system and panel coordinate system are pictured in Figure 2.

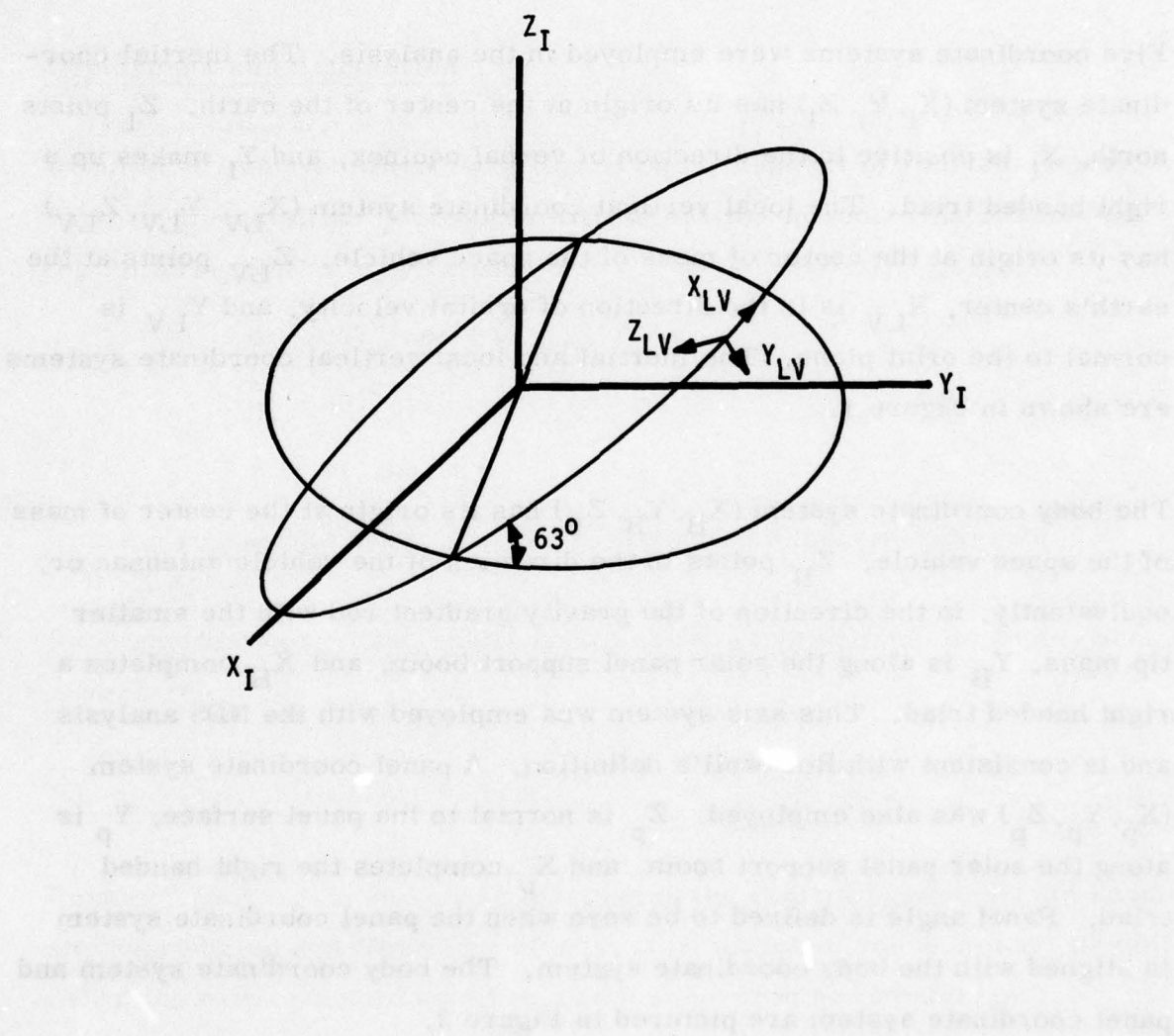


Figure 1. Inertial and Local Vertical Coordinate System

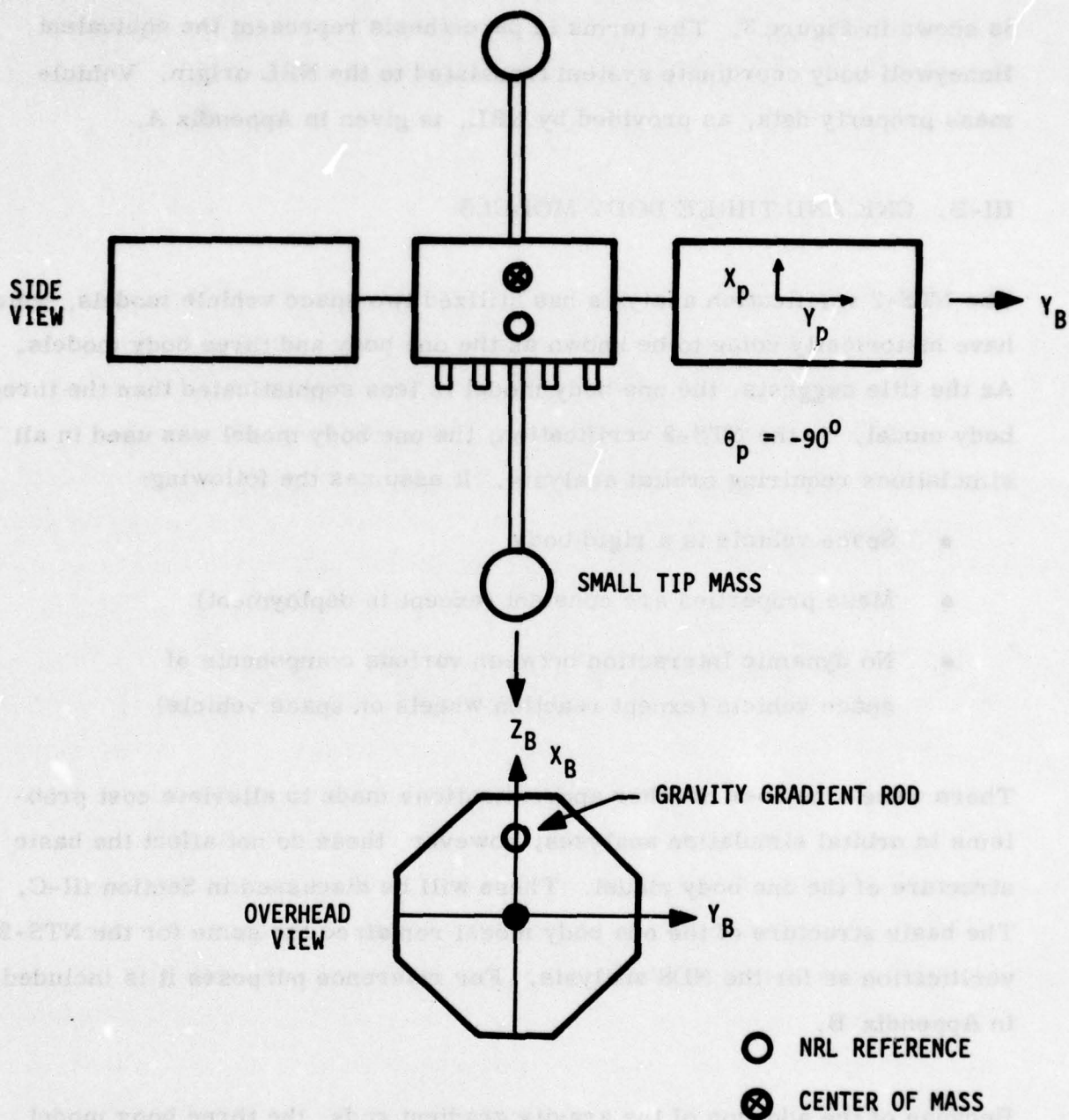


Figure 2. Body and Panel Coordinate System

The vehicle data provided was referenced to the NRL coordinate system which is shown in Figure 3. The terms in parenthesis represent the equivalent Honeywell body coordinate system translated to the NRL origin. Vehicle mass property data, as provided by NRL, is given in Appendix A.

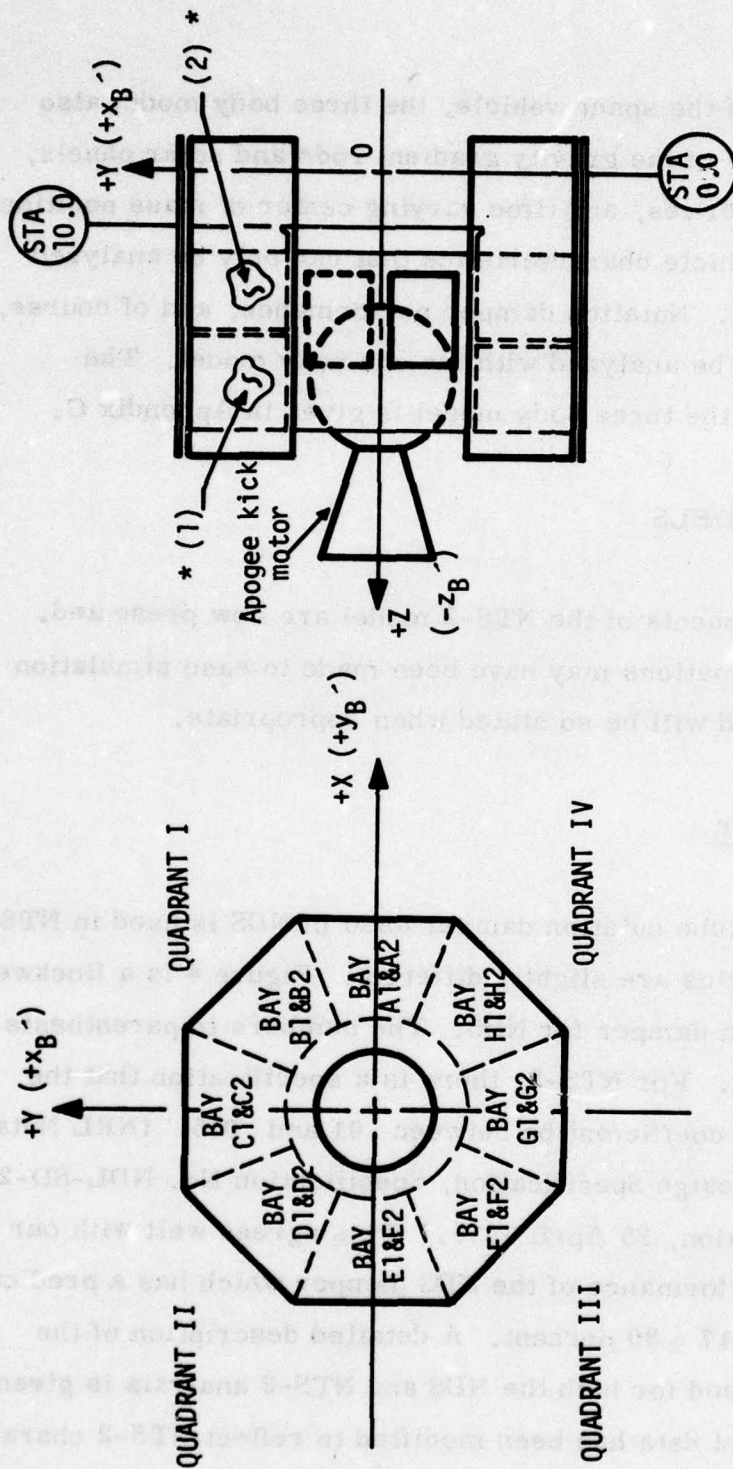
III-B. ONE AND THREE BODY MODELS

The NTS-2 verification analysis has utilized two space vehicle models, which have historically come to be known as the one body and three body models. As the title suggests, the one body model is less sophisticated than the three body model. In the NTS-2 verification, the one body model was used in all simulations requiring orbital analysis. It assumes the following:

- Space vehicle is a rigid body
- Mass properties are constant (except in deployment)
- No dynamic interaction between various components of space vehicle (except reaction wheels on space vehicle)

There were a number of other approximations made to alleviate cost problems in orbital simulation analyses; however, these do not affect the basic structure of the one body model. These will be discussed in Section III-C. The basic structure of the one body model remained the same for the NTS-2 verification as for the NDS analysis. For reference purposes it is included in Appendix B.

Because of the addition of the gravity gradient rods, the three body model was modified from its NDS counterpart. Besides providing interaction



- (1) DESIGNATES UPPER BAY
- (2) DESIGNATES LOWER BAY

Figure 3. NRL/NTS-2 Coordinate System

between all components of the space vehicle, the three body model also contains flexibility effects of the gravity gradient rods and solar panels, time varying inertia properties, and time varying center of mass position. There are some space vehicle characteristics that can only be analyzed with the three body model. Nutation damper performance, and of course, flexibility effects, cannot be analyzed with the one body model. The equation development for the three body model is given in Appendix C.

III-C. COMPONENT MODELS

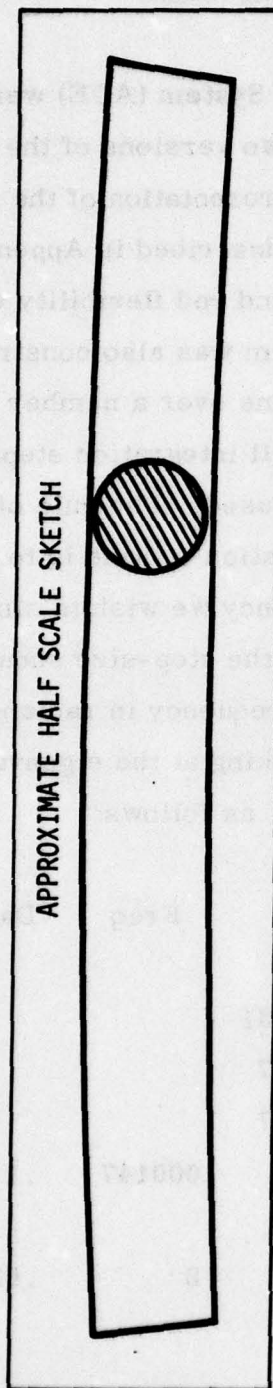
Descriptions of the components of the NTS-2 model are now presented. Assumptions and approximations may have been made to ease simulation computational burdens and will be so stated when appropriate.

III-C-1. Nutation Damper

The same type of ball in tube nutation damper used in NDS is used in NTS-2. The physical characteristics are slightly different. Figure 4 is a Rockwell description of the nutation damper for NDS. The numbers in parenthesis refer to the NTS-2 model. For NTS-2, there is a specification that the nutation damper damping coefficient be between .01 and .015. (NRL Nutation Damper Assembly Design Specification, Specification No. NDL-SD-265498. Ford Aerospace Corporation, 25 April 1975.) This agrees well with our predicted estimate of performance of the NDS damper which has a predicted damping coefficient of $.017 \pm 30$ percent. A detailed description of the nutation damper model used for both the NDS and NTS-2 analysis is given in Appendix D. All pertinent data has been modified to reflect NTS-2 characteristics. As will be discussed under nutation damper performance results, the location of the nutation damper does have a significant effect on performance.

TYPE BALL IN GAS-FILLED TUBE

TUBE CURVED TO PROVIDE CENTRIFUGAL SPRING



TUBE

I.D.: 1.266 INCH (1.009 INCH)

O.D.: 1.566 INCH

LENGTH: 16 INCHES (17 INCHES)

RADIUS OF CURVATURE: 159 INCHES
(13.0 ± 1.0 FT)

MATERIAL: ALUMINUM

BALL

DIAMETER: 1.25 INCH (1.000 INCH)

MATERIAL: TUNGSTEN CARBIDE

GAS

9:1 MIXTURE NITROGEN: HELIUM 1
ATMOSPHERE

WEIGHT

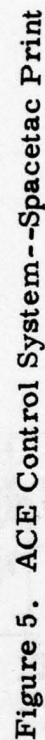
1.75 LBS (0.22 LBS)

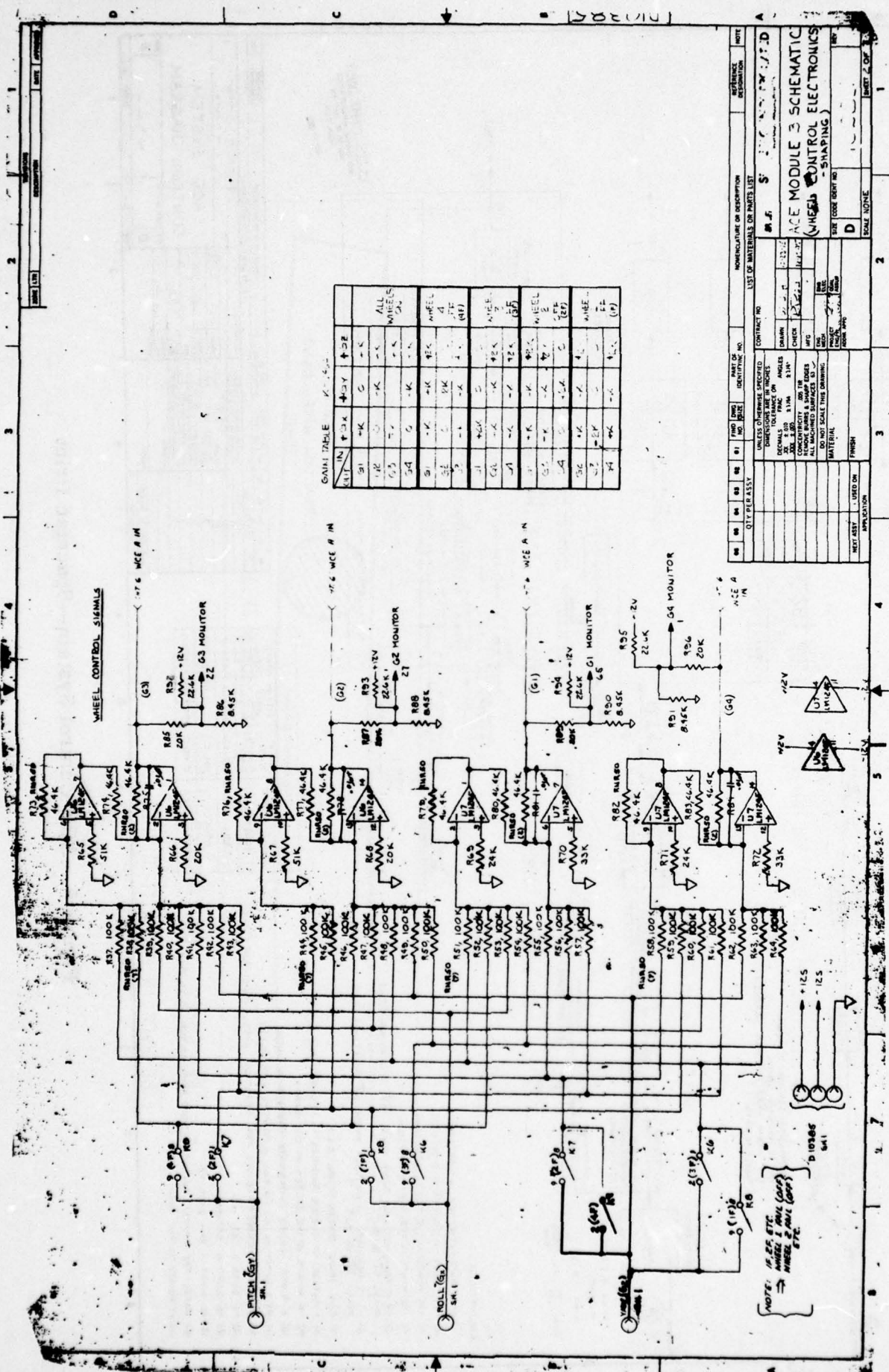
Figure 4. NDS and NTS-2 Nutation Damper Characteristics

III-C-2. Attitude Control Electronics System Model

Models for the Attitude Control Electronics System (ACE) were constructed based on data shown in Figures 5 and 6. Two versions of the ACE system were constructed. One was a complete representation of the ACE system shown in Figures 5 and 6. This system is described in Appendix E. The system was used when the effects of panel and rod flexibility were studied. An approximated version of the actual system was also constructed to provide the capability for making simulation runs over a number of orbits. This was done to avoid the need for the small integration step-size that would be required if the actual system was used. The rule of thumb that we use in choosing step sizes for the integration routine is to select the step-size as a function of the highest frequency we wish to simulate. If there are poorly damped oscillatory roots, the step-size should be no greater than $.1/\omega_{\max}$ where ω_{\max} is the largest frequency in radians/sec. The largest frequency may be determined by looking at the eigenvalues, which in the closed loop case may be represented, as follows:

Source	Real	Freq	Damp
Rigid Body Pitch	-.002		
	-.000031		
Rigid Body Roll/ Yaw	-.00187		
	-.00187		
		.000147	.1
Each Reaction Wheel		.8	.62
Each Structural Filter	-.033		





The required integration steps then would be about 50 seconds for simulating rigid body dynamics, 3.0 seconds if structural filters were included, and .125 seconds if the actual wheel loops were included. Hence if the wheel loop could be approximated (and the structural filters ignored because they are unnecessary if flexibility is not modeled), the step size could be increased 400 times over what is required with the actual control system. The approximation was derived based on the actual intent of the ACE system. Consider the relationship, as shown in Figure 5 between wheel 1 and roll attitude error. This may be represented by Figure 7.

Since the wheel loop is 400 times faster than the dynamics of the rigid body and since we neglect the structural filters, Figure 7 may be reduced to

$$W_1 = K_\phi \phi$$

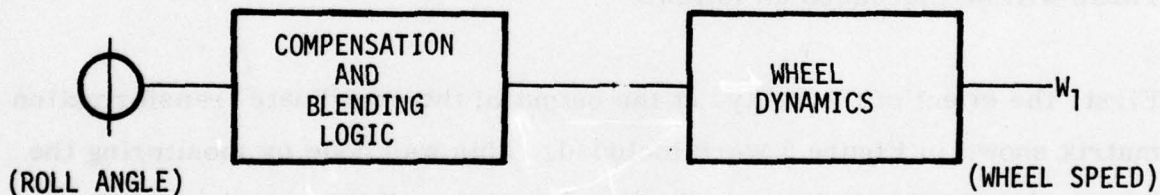


Figure 7. Roll Angle to Wheel 1 Relationship

where K_ϕ is the equivalent transmission gain. However, since the integration is with respect to moment equations, we utilized the relationship between wheel acceleration and wheel torque or

$$T_{W_1} = I_{W_1} \ddot{W}_1 \quad (1)$$

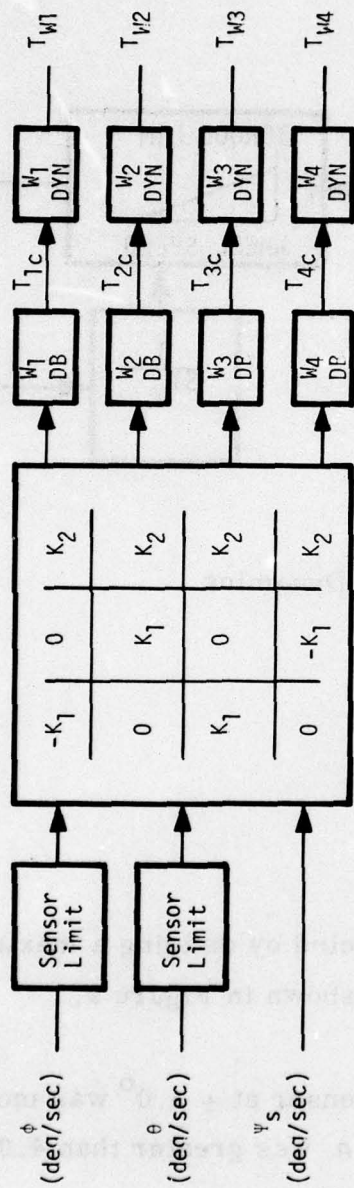
where T_{W_1} is the torque wheel 1 produces, and I_{W_1} is Wheel 1 moment of inertia.

Taking the derivative of equation--and substituting in equation--we obtain

$$T_{W_1} = K_\phi I_{W_1} \dot{\phi} \quad (2)$$

where $K_\phi I_{W_1}$ is the loop gain for that wheel. This describes the basis for the approximated version of the ACE system. Block diagrams of the modified version are given in Figures 8 and 9. As shown, there were several other modifications necessary to handle the non-linearities in the ACE system. These will be discussed as follows:

First, the effect of the relays at the output of the coordinate transformation matrix shown in Figure 5 were included. This was done by monitoring the output of that relay in the actual control system. If the output was zero, which indicates a zero commanded wheel speed, it was assumed that the wheel loop could be unloaded in less than the time of an integration step. In fact, the time constant of that loop would allow a 95 percent reduction in wheel speed in six seconds. This is much less than the 50 second integration steps. The procedure simulated when the output of the relay was zero was to command a torque which would drive the wheel speed to zero within that integration step, or



$$\psi_s = \frac{\psi_s(i) - \psi_s(i-1)}{\Delta t}$$

$$K_1 = .046$$

$$K_2 = .0025$$

$$K_2 = .0075 \text{ IF sun line } 10^\circ \text{ of orbit plane}$$

$$\theta_p < 18^\circ \text{ and } \theta_p > 162^\circ$$

W_i DB - checks output of relay in actual wheel loop

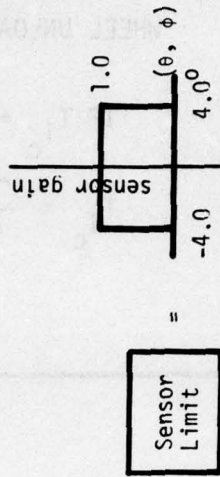


Figure 8. Modified Wheel Control System

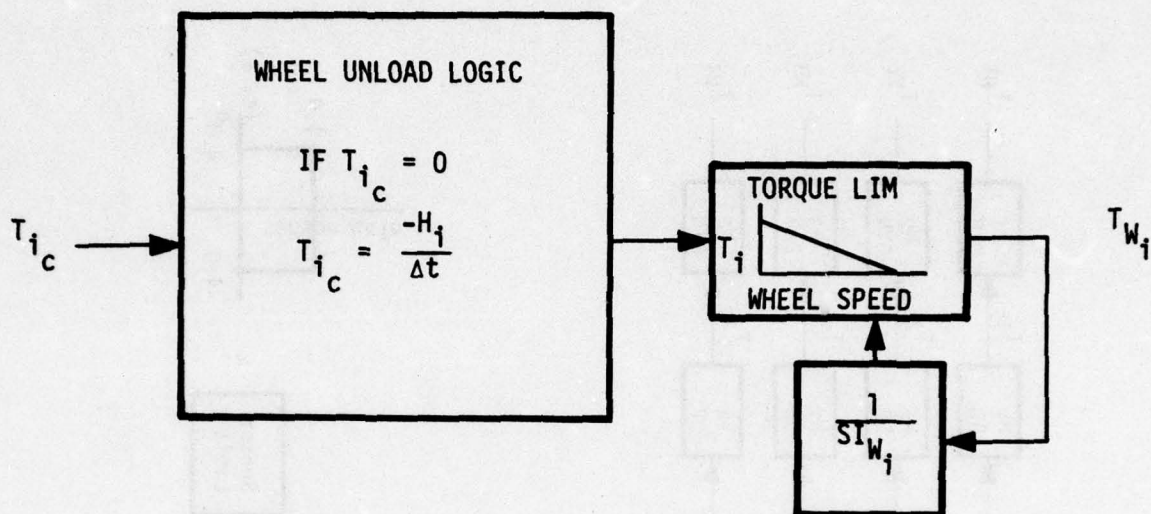


Figure 9. Modified Wheel Dynamics

$$T_{W \text{ commanded}} = - \frac{I_w w}{\Delta T} \quad (3)$$

where ΔT is the integration step.

Second, the effect of rolling friction was modeled by defining a maximum torque limit as a function of wheel speed, as shown in Figure 9.

Third, the saturation of the combined earth sensor at $\pm 4.0^\circ$ was modeled by setting the $\dot{\phi}$ and $\dot{\theta}$ to zero when ϕ and θ was greater than 4.0° .

Fourth, the yaw sun sensor rate signal was obtained by numerically differentiating the output of the yaw sun sensor model.

III-C-3. Magnetic Torques Model

Spacecraft magnetic torques result from the interaction between the magnetic properties of the spacecraft and the ambient magnetic field. The main sources are:

- Permanent magnetism in the spacecraft
- Spacecraft generated current loops
- Magnetism induced by external field
- Currents induced by external fields
- Rotating assemblies

The earth's magnetic field can be represented by an analytical model that defines magnitude and direction as a function of location. Four mathematical models have been developed for representing the earth's magnetic field and are listed below in order of increasing accuracy.

- Spin axis, centered dipole
- Tilted, centered dipole
- Quadripole model
- Spherical harmonic expansion

NASA SP-8018 states that the simple, less accurate models, spin axis and tilted, may be used

- For conceptual or preliminary design studies
- When the magnitude of the spacecraft dipole moment M is an estimated value

- When long-term effects are of primary importance, i.e., average torque or torque impulse is over several orbits, days, or longer
- When the orbit radius (distance from the geocenter) is greater than three Earth radii

In addition, data given in SP-8018 indicate a 5 percent or less deviation in magnitude and direction between a tilted, centered dipole model, and the sophisticated spherical harmonic expansion model at four Earth radii (NTS-2 orbit radius).

Based on these two considerations, it was decided to use a tilted, centered dipole model, to represent the earth's magnetic field. The details of the model are given in Appendix F.

III-C-4. Solar Torque Model

Mathematical models were constructed for estimating the solar torques produced by the solar panels, the gravity gradient rods, and the tip masses. The basic approach was to break up the component of interest into an arrangement of flat surfaces. The solar force on a flat surface may then be computed by

$$\vec{F} = -F_N \vec{N} + F_T \vec{T} \quad (4)$$

where

$$F_N = [(1 + \sigma \rho) \cos \psi + \frac{2}{3} \rho (1 - \sigma)] PA \cos \psi$$

$$F_T = (1 - \sigma \rho) \cos \psi \sin \psi PA$$

F_N = normal component of force

\vec{N} = unit vector normal to surface

F_T = tangential component of force

\vec{T} = unit vector tangent to surface

P = solar pressure constant = 1.0×10^{-7} lb/ft²

A = area of the flat surface

ρ = fraction of incident radiation reflected

σ = fraction of reflected radiation that is specular

(Note: defined another way, specular reflection = $\sigma \rho$, diffuse reflection = $\rho(1 - \sigma)$, and absorbitivity $\geq (1 - \rho)$).

Solar torques are then computed by summing the force-moment arm products with respect to the center of mass. The solar torques are computed as a function of vehicle attitude and panel position each integration step. The nominal value used for the radiation characteristics of the panels, rods, and tip masses are given in Table 1.

Table 1. Radiation Constants

	ρ	σ
Panels	.2	0
Rods	.85	1.0
Tip Masses	0	0

For more details of the solar torque model, refer to Appendix G.

III-C-5. Gravity Gradient Rod Thermal Model

The effect of thermal heating on the gravity gradient rods was analyzed using the computer program MITAS which is a software package provided by Control Data Corporation. MITAS is a general three dimensional finite difference heat transfer program developed to mathematically model thermal characteristics. The approach is based on dividing the physical model into an R-C electrical network mesh analog. Either explicit or implicit finite difference methods can be used for steady state or transient solutions. MITAS can handle all three types of heat transfer, conduction, convection, and radiation.

Deatils of the model can be found in Appendix H. The major results may be summarized as follows:

- For nominal values of absorptivity and emissivity ($\alpha = 0.15$, $\epsilon = 0.05$) the predicted radius of curvature of the gravity gradient rod, assuming the sun line is perpendicular to the rod, is 2300 ft.
- For worst case values of absorptivity and emissivity ($\alpha = 0.30$, $\epsilon = 0.1$) the predicted radius of curvature is 1100 ft.
- Radius of curvature varies as a csc function of incidence angle.
- Dynamics of thermal deflection have time constant on the order of 10 to 60 seconds which can be assumed to be instantaneous for orbital runs.

III-C-6. Gravity Gradient Rod Flexibility Model

A general two-element discrete coordinate structural math model was developed for simulation of a flexible gravity gradient rod for NTS-2 satellite control studies. The model has been verified with STARDYNE finite element static and dynamic check cases. It also allows for cross-axis coupling effects due to small rod curvatures from thermal deflections or manufacturing tolerances on deployed rod straightness.

A series of multiple beam models were analyzed for dynamic responses to solar array drive pulses. These studies are detailed in Appendix I. Based on these studies, it is apparent that using a single flexible beam element with only one node at the tip mass gives considerable error in open-loop transient response simulations. Using four elastic beams and five node points per rod (one attached to the spacecraft), realistic results are obtained, allowing for realistic rod bending modes. Using two beams and three nodes per rod (one attached), almost identical dynamic results are obtained, as shown in Appendix I.

Transient responses (open-loop) are presented in Figure 10 for one tip mass, and in Figure 11 for the spacecraft rotation about the solar array drive axis.

Based on these results, a discrete coordinate math model for the gravity gradient rods was developed. Rod deflections at the tip mass and at a mid-point node are defined in terms of the rod stiffness properties (EI and JG), rod geometry ($2l$ = total rod length), and the applied loads. For deflection in one plane, the model is simply a two by two beam influence coefficient matrix. For cross-axis coupling due to rod curvature, the initial mass point displacements from the rod undeformed centerline must be specified.

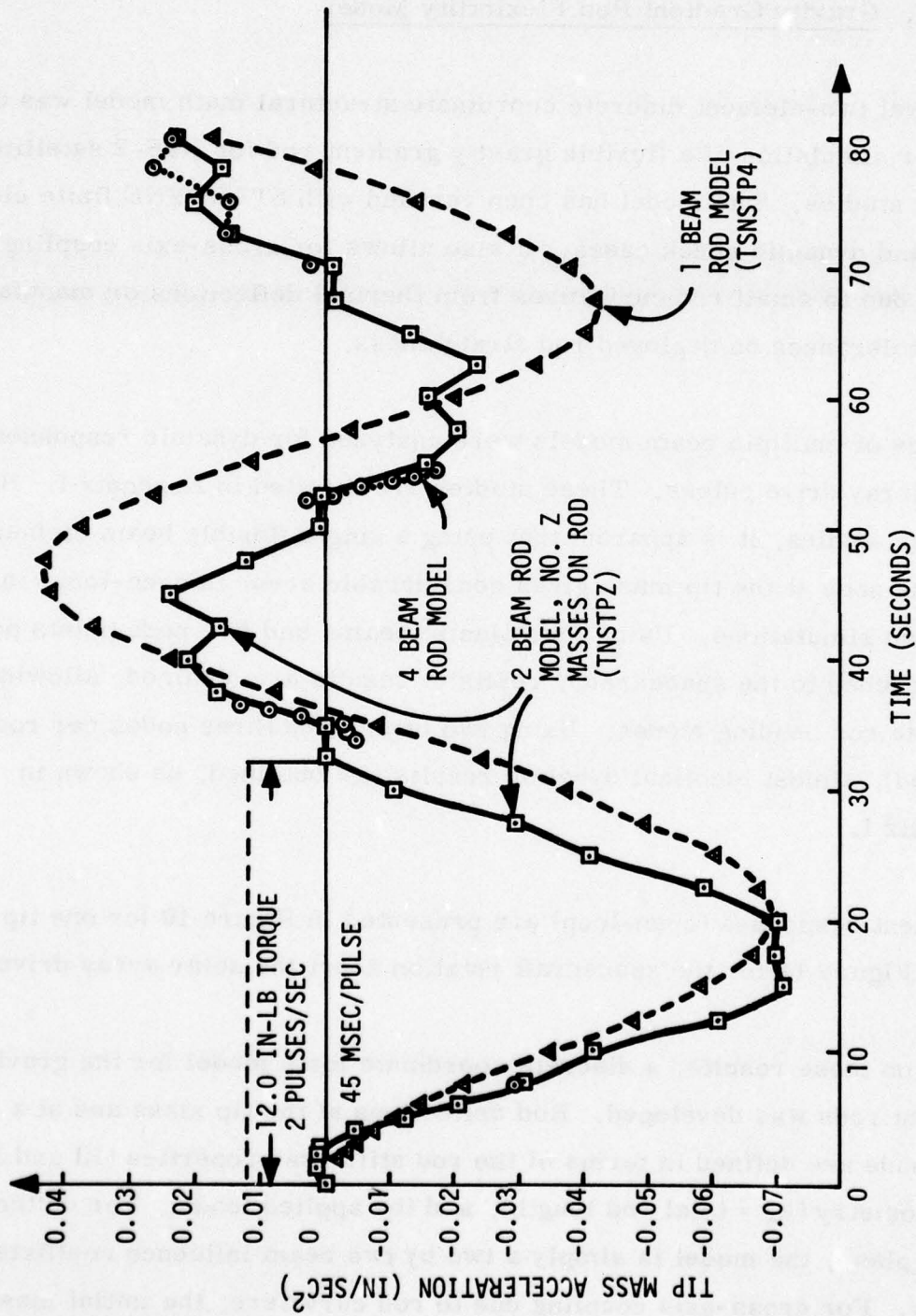


Figure 10. NTS-2 Satellite Tip Mass Acceleration vs. Time

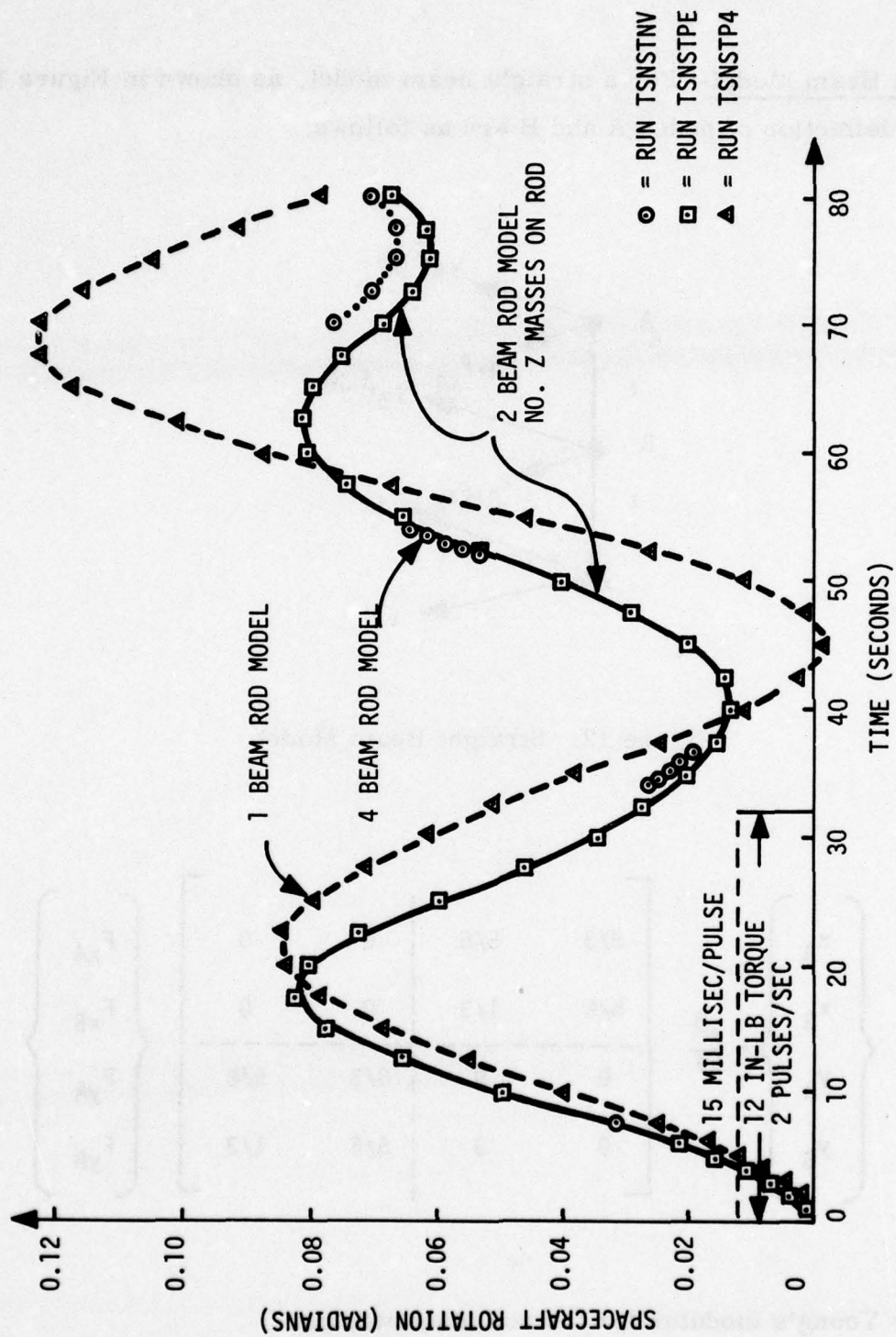


Figure 11. NTS-2 Satellite Rotation vs. Time About Solar Array Drive Axis

Straight Beam Model--For a straight beam model, as shown in Figure 12, the elastic deflection of nodes A and B are as follows:

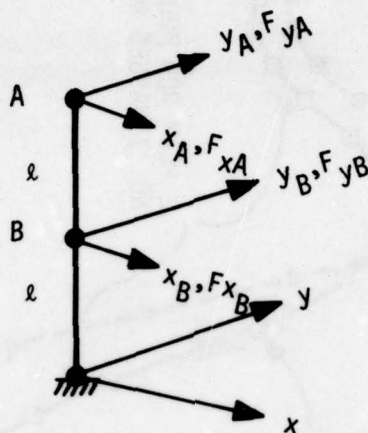


Figure 12. Straight Beam Model

$$\begin{Bmatrix} x_A \\ x_B \\ y_A \\ y_B \end{Bmatrix} = \frac{l^3}{EI} \begin{bmatrix} 8/3 & 5/6 & 0 & 0 \\ 5/6 & 1/3 & 0 & 0 \\ \hline 0 & 0 & 8/3 & 5/6 \\ 0 & 0 & 5/6 & 1/3 \end{bmatrix} \begin{Bmatrix} F_{xA} \\ F_{xB} \\ F_{yA} \\ F_{yB} \end{Bmatrix} \quad (5)$$

where

E = Young's modulus for the rod material, psi

I = rod section bending stiffness, in⁴

l = rod half-length, inches

x, y = elastic displacements in x and y directions respectively, inches

F_x, F_y = panel point loads in x and y directions respectively, lbs.

The above equation assumes the same EI for bending about both axes.

The panel point loads are defined, in any one axis, as follows:

$$F_x = F_{x \text{ applied}} - m \ddot{x}_{\text{relative}}$$

where $F_{x \text{ applied}}$ could be the x component of external loads from solar pressures, or the x direction component of a differential gravity field.

$\ddot{x}_{\text{relative}}$ = the acceleration of the mass point as if it were rigidly attached to the spacecraft.

Basic Equations of Motion--In terms of a simple, one degree of freedom harmonic oscillator subject-to-base excitation + applied forces:

$$M\ddot{X} + C\dot{X} + KX = F(t) - M\ddot{X}_{\text{base}} \quad (6)$$

Rewriting this equation

$$KX \approx -M\ddot{X} - C\dot{X} + F(t) - M\ddot{X}_{\text{base}}$$

$$\ddot{X} = \alpha - \frac{M\ddot{X}}{K} - \frac{CX}{K} + \frac{F(t)}{K} - \frac{M\ddot{X}_{\text{base}}}{K}$$

where $\alpha = 1/K$.

For two degrees of freedom, the basic matrix equation is

$$\begin{bmatrix} m_A & 0 \\ 0 & m_B \end{bmatrix} \begin{bmatrix} X_A \\ X_B \end{bmatrix} + \begin{bmatrix} C_{AA} & C_{AB} \\ C_{BA} & C_{BB} \end{bmatrix} \begin{bmatrix} X_A \\ X_B \end{bmatrix} + \begin{bmatrix} K_{AA} & K_{AB} \\ K_{BA} & K_{BB} \end{bmatrix} \begin{bmatrix} X_A \\ X_B \end{bmatrix} = \text{RHS} \quad (7)$$

It can be shown that the solution to the above equation is

$$\begin{bmatrix} X_A \\ X_B \end{bmatrix} = E \begin{bmatrix} m_A & 0 \\ 0 & m_B \end{bmatrix} \begin{bmatrix} X_A \\ X_B \end{bmatrix} - \begin{bmatrix} C_{AA} & C_{AB} \\ C_{BA} & C_{BB} \end{bmatrix} \begin{bmatrix} X_A \\ X_B \end{bmatrix} + \begin{bmatrix} F_{A \text{ applied}} \\ F_{B \text{ applied}} \end{bmatrix} \\ + \begin{bmatrix} m_A & 0 \\ 0 & m_B \end{bmatrix} T \begin{bmatrix} X_{\text{base}} \\ \theta_{\text{base}} \end{bmatrix}$$

where $[E] = \text{influence coefficient matrix} = [K]^{-1}$

and $[T] = \text{rigid body transformation matrix.}$

Masses are defined as follows:

$$m_{\text{tip}} = \text{tip mass} = (7.5 \text{ lbs/g}_c) \text{ for NTS-2}$$

$$m_{\text{beam}} = \text{rod mass} = (.9 \text{ lbs/g}_c)$$

$$m_A = m_{\text{tip}} + 1/4 m_{\text{beam}}$$

$$m_B = 1/2 m_{\text{beam}}$$

$$\text{lump} = 1/4 m_{\text{beam}} \text{ to attach point on spacecraft}$$

Curved Beam Model--Appendix I contains the details of the curved beam deflection calculations for unit loads. The beam Z axis is considered to be initially aligned along the vehicle body-fixed Z axis but then is displaced to an offset unstressed position with components

X_{oA} = X direction offset at node A

X_{oB} = X direction offset at node B

y_{oA} = y direction offset at node A

y_{oB} = y direction offset at node B

The model is shown in Figure 13.

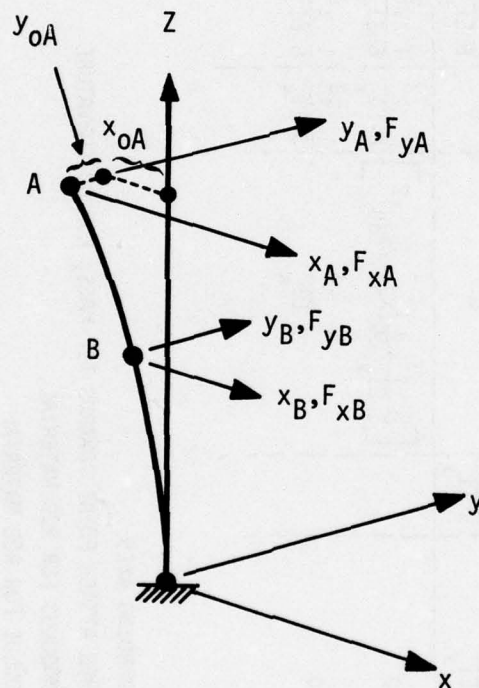


Figure 13. Curved Beam Model

Note that the offsets are considered positive if in the negative direction.
(If +X is toward the sun, the thermal deflection is away from the sun.)

The full influence coefficient matrix is presented in Table 2.

Table 2. Influence Coefficient Matrix for Two-Beam Gravity Gradient Rod

$$\begin{Bmatrix} x_A \\ x_B \\ y_A \\ y_B \end{Bmatrix} \begin{bmatrix} \left[\frac{8}{3} \frac{\ell^3}{EI_y} + \frac{\ell}{JG} (y_{0A} - 2y_{0B})^2 \right] & \frac{5}{6} \frac{\ell^3}{EI_y} & 0 & 0 \\ \frac{5}{6} \frac{\ell^3}{EI_y} & \frac{1}{3} \frac{\ell^3}{EI_y} & 0 & 0 \\ 0 & 0 & \left[\frac{8}{3} \frac{\ell^3}{EI_x} + \frac{\ell}{JG} (x_{0A} - 2x_{0B})^2 \right] & \frac{5}{6} \frac{\ell^3}{EI_x} \\ 0 & 0 & \frac{5}{6} \frac{\ell^3}{EI_x} & \frac{1}{3} \frac{\ell^3}{EI_x} \end{bmatrix} \begin{Bmatrix} F_{xA} \\ F_{xB} \\ F_{yA} \\ F_{yB} \\ F_{zA} \\ F_{zB} \end{Bmatrix}$$

WHERE

x, y ARE ROD BENDING AXES

z IS FROM ROD ATTACH POINT TOWARDS TIP MASS, FOR NO CURVATURE

E = YOUNG'S MODULUS FOR ROD MATERIAL

G = SHEAR MODULUS FOR ROD MATERIAL

I_x, I_y = ROD SECTION BENDING STIFFNESS ABOUT x, y AXES RESPECTIVELY

J = ROD SECTION TORSIONAL STIFFNESS

ℓ = ROD HALF LENGTH

x_0 = INITIAL UNSTRESSED NODE POSITION AWAY FROM $+x$ AXIS

y_0 = INITIAL UNSTRESSED NODE POSITION AWAY FROM $+y$ AXIS

SUBSCRIPT A REFERS TO TIP MASS NODE

SUBSCRIPT B REFERS TO NODE AT MIDDLE OF ROD

For linear analysis with a curved or straight beam, the influence coefficients are computed once. Numerical values are presented in Appendix I. For non-linear analysis, the influence matrix can be periodically updated if the cross-axis coupling terms are updated as follows:

Define new variables

$$X_{oA} = X_{oA} + X_A \text{ (current value)}$$

$$X_{oB} = X_{oB} + X_B \text{ (current value)}$$

using the updated variables in the Table 2 equations.

Damping--In the normal method of calculating structural responses, the damping is often assumed to be equivalent viscous damping, for lightly damped systems. The modal damping is conveniently expressed as $2 \zeta W_n$, where

$$\zeta = c/C_c, \text{ the damping ratio (usually } < .10)$$

$$W_n = \text{the mode's frequency, radians/sec}$$

$$C_c = \text{critical damping ratio}$$

If the modes, frequencies, and generalized weights for an elastic structure are known, it can be shown that the discrete damping matrix can be calculated using the estimated modal damping values (see Appendix I). The calculated damping matrix is

$$C = \left[\phi^T \right]^{-1} \left[2 \right] \left[M_{eq} \right] \left[\phi \right]^{-1} \quad (8)$$

where

$$C = \text{discrete damping matrix}$$

ϕ = square matrix of mode shapes

ϕ^T = transpose of ϕ

ζ = damping ratio, as a fraction of critical viscous damping

$\begin{bmatrix} \diagup & & \\ & \diagdown & \\ & & \diagup \end{bmatrix}$ = denotes a diagonal matrix

M_{eq} = equivalent or generalized mass for each mode

$$= \begin{bmatrix} \phi^T \end{bmatrix} \begin{bmatrix} M \end{bmatrix} \begin{bmatrix} \phi \end{bmatrix}$$

In accordance with previous equations, the 2 by 2 damping matrix, as calculated in Appendix I is

$$\begin{bmatrix} C_{AA} & C_{AB} \\ C_{BA} & C_{BB} \end{bmatrix} = \begin{bmatrix} 201.06 & -.75 \\ -.75 & 12.17 \end{bmatrix} \times 10^{-6} \quad (9)$$

for ζ (or β) = .005

This corresponds to 1/2 of 1 percent critical damping, which is an estimate for a gravity gradient rod. The full damping matrix is given in Table 3 in a form to match the Table 2 influence matrix.

Table 3. Damping Matrix for Two Beam Gravity Gradient Rod
 (For 1/2 of 1 percent Critical Damping)

$$\begin{bmatrix} FD_{xA} \\ FD_{xB} \\ FD_{yA} \\ FD_{yB} \end{bmatrix} = C \begin{bmatrix} 201.06 & -.75 & 0 & 0 \\ -.75 & 12.17 & 0 & 0 \\ 0 & 0 & 201.06 & -.75 \\ 0 & 0 & -.75 & 12.17 \end{bmatrix} \times 10^{-6} \begin{bmatrix} x_A \\ x_B \\ y_A \\ y_B \end{bmatrix} \quad (10)$$

where

FD_{ij} = damping force in the i th direction, at the j th node, lbs

C = a conversion factor to allow for possible scaling of above damping and/or to account for conversion from inch units to feet units.

x_j, y_j = panel point velocities at the j th node due to elastic deflections, inches/sec.

III-C-7. Solar Panel Flexibility Model

A linear structural math model will provide reasonable dynamic simulations of flexible solar array panels for NTS-2 satellite control system analysis.

Bending deflections of the solar arrays are obtained from the discrete mass, damping, and stiffness matrices described in Appendix J. This approach is similar to the method used previously to model the flexible gravity gradient rods. Separate matrix equations are given in Tables 4 and 5 for each array, each consisting of three panels. Part of each array's mass is lumped at the center of the outermost panel. The balance of the array mass is added to the rigid mass of the spacecraft.

The torsional flexure model cannot be simulated very well with a lumped mass model unless a total of 7 torsional masses are used, one for each panel plus one for the drive motor. Therefore, a modal solution is developed whereby only three generalized coordinate responses must be solved instead of seven discrete responses.

The preceeding math models were all developed on the basis of finite element models using the STARDYNE structural analysis program.

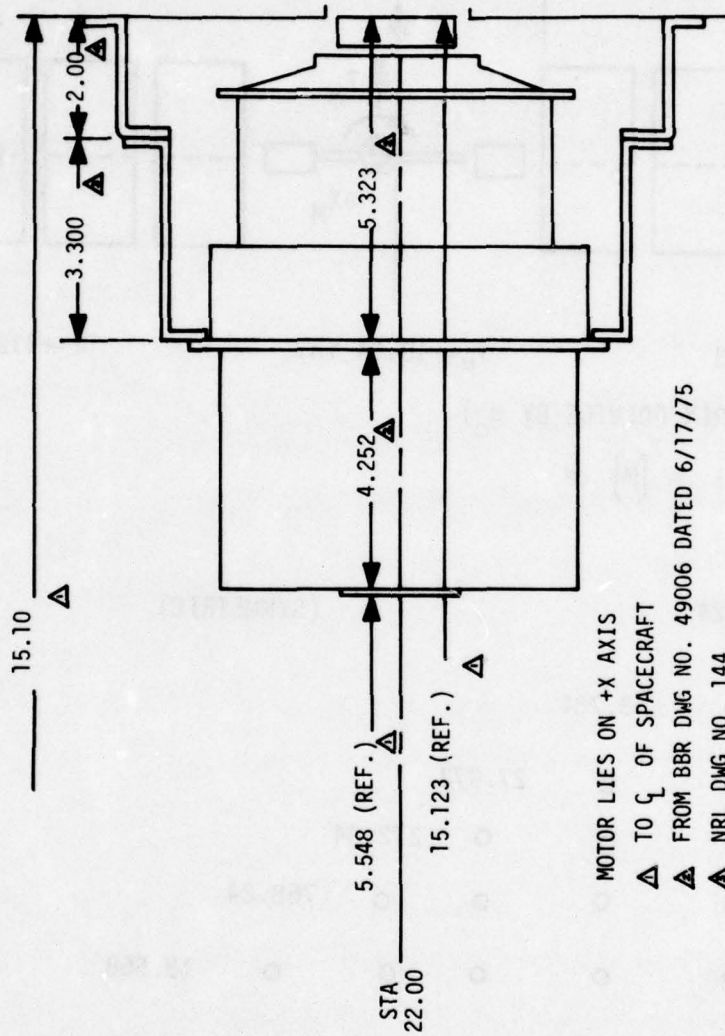
Location of Drive Motor--The bending equations of motion are defined with respect to motion of the solar array drive motor, which is considered centered at 10.3 inches from the CL of the spacecraft, located on the +Y axis (Honeywell coord). As a result, the +Y solar array has short drive tube $L \approx 15$ inches, while the -Y solar array has a drive tube about 35.5 inches long. A sketch provided by NRL is shown in Figure 14. As a result, the bending stiffnesses for the two solar arrays are slightly different.

Bending Stiffness, Mass, and Damping for Solar Arrays--Finite element math models of various levels of complexity for the solar arrays were run on STARDYNE, as reported in Appendix J. A model with a single lumped mass at the center of the outer panel was found to give almost the same transient responses to a step yaw torque input as more complex models.

The general solar array model is shown in Appendix J. Basically, each solar panel has a node at each hinge point and a node at its center. Additional nodes are used at the interfaces with a small 11 inch long honeycomb interface panel and at the drive tube connections. A total of 32 nodes was used to describe the flexible solar array system.

The dynamically equivalent solar array bending model is shown in Figure 15. The corresponding discrete stiffness, mass, and damping matrices are presented in Tables 4 and 5. Note that the x solar panel coordinates are defined to be normal to the plane of the solar panels. As the panels are rotated about the drive axis, the local x and z panel coordinates also rotate.

The slight amount of stiffness coupling between the local x and z panel deflections are attributed to a slight asymmetry in the hinges between the solar panels.



MOTOR LIES ON +X AXIS
 ▲ TO CL OF SPACECRAFT
 ▲ FROM BBR DWG NO. 49006 DATED 6/17/75
 ▲ NRL DWG NO. 144
 ▲ NRL DWG NO. 136

Figure 14. Solar Array Drive Motor

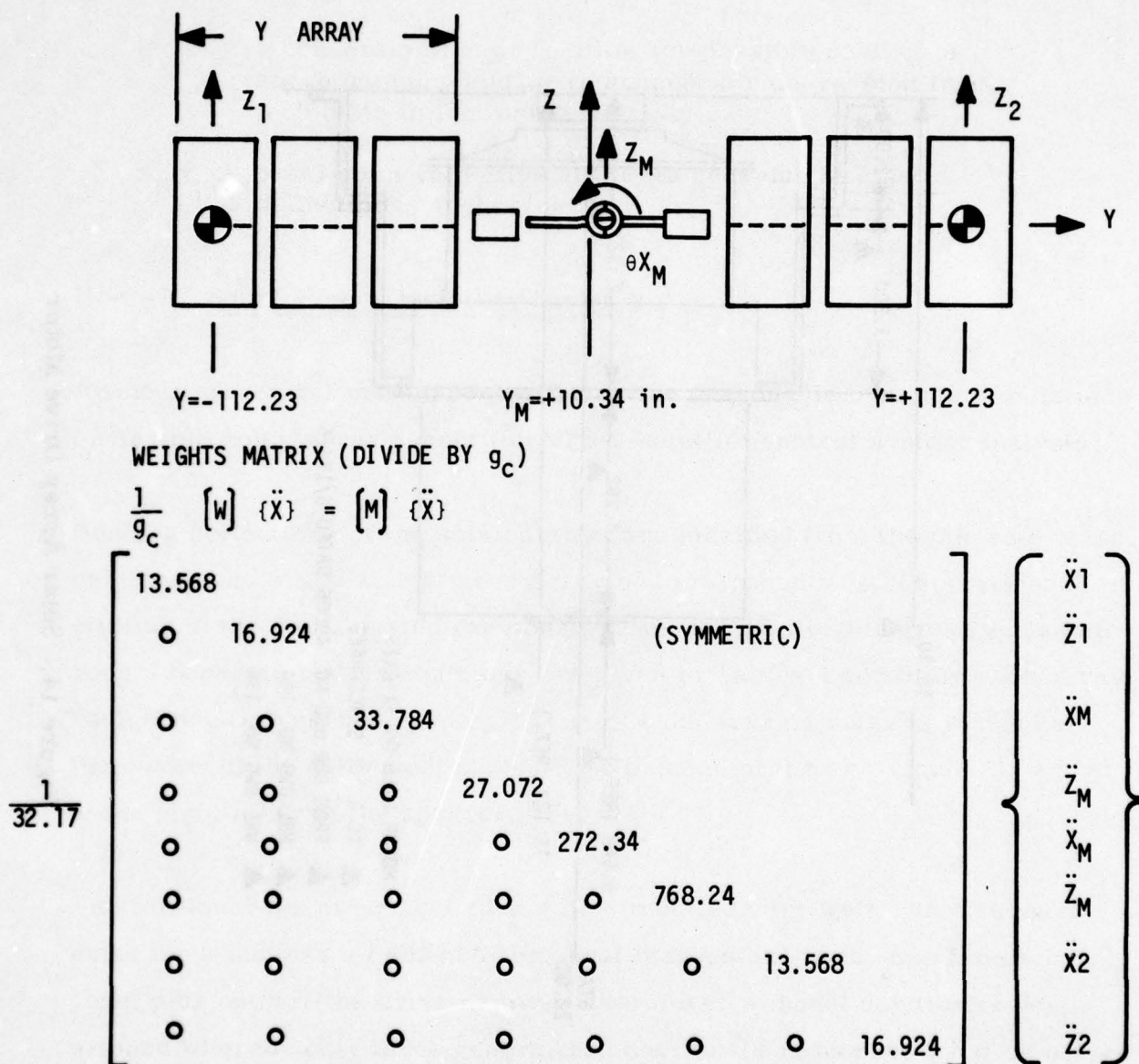


Figure 15. Solar Array Bending Flexure Model

Table 4. -Y Solar Array (Bending Only)

STIFFNESS MATRIX
(units = lbs/ft)

For motion relative to
drive motor

$$[K]\{x\} = \begin{bmatrix} .0085617 & -.004860 \\ -.004860 & .630218 \end{bmatrix} \begin{bmatrix} x_1 \\ z_1 \end{bmatrix}$$

where

x_1 = motion of center of outer panel,
normal to plane of panel

z_1 = motion of center of outer panel,
in plane of the panel

MASS MATRIX
(units = slugs (lb-sec²/ft))

$$[M]\{x\} = \begin{bmatrix} .42176 & 0 \\ 0 & .52608 \end{bmatrix} \begin{bmatrix} \ddot{x}_1 \\ \ddot{z}_1 \end{bmatrix}$$

DAMPING MATRIX $\zeta_R = .005$ (1/2 of 1% critical damping)

$$[C]\{x\} = \frac{\zeta}{.005} \begin{bmatrix} .0006009 & 0 \\ 0 & .005758 \end{bmatrix} \begin{bmatrix} \dot{x}_1 \\ \dot{z}_1 \end{bmatrix}$$

Units of $[C]$ are $\frac{\text{lb-sec}}{\text{ft}}$

Table 5. +Y Solar Array (Bending Only)

STIFFNESS MATRIX
(units = lbs/ft)

For motion relative to
drive motor

$$[K]\{x\} = \begin{bmatrix} .008670 & -.010705 \\ -.010705 & 1.37791 \end{bmatrix} \begin{bmatrix} x_2 \\ z_2 \end{bmatrix}$$

MASS MATRIX
(units = slugs (lb-sec²/ft))

$$[M]\{\ddot{x}\} = \begin{bmatrix} .42176 & 0 \\ 0 & .52608 \end{bmatrix} \begin{bmatrix} \ddot{x}_1 \\ \ddot{z}_2 \end{bmatrix}$$

DAMPING MATRIX
(units = lb-sec/ft)

$$[C]\{\dot{x}\} = \begin{bmatrix} .0006047 & 0 \\ 0 & .008514 \end{bmatrix} \begin{bmatrix} \dot{x}_2 \\ \dot{z}_2 \end{bmatrix}$$

The damping matrices are calculated on the basis of the uncoupled mass and stiffness terms for each direction. For a single DOF system, with mass m and stiffness k , the critical damping coefficient C_c is defined as

$$C_c = 2\sqrt{Km} \quad (11)$$

In terms of the equivalent viscous damping ratio ζ , the discrete damping coefficient is

$$C = 2\zeta C_c \quad (12)$$

$$C = 2\zeta\sqrt{Km}$$

For the math model shown in Figure 16, the STARDYNE model was subjected to a step yaw torque pulse of .04 ft-lbs for 3 seconds, after which time the yaw torque goes to zero instantly. The response of the lumped outer panel mass is shown in Figure 17 in inch units. Table 6 presents summary of the peak x direction displacements of node 2 and the time at which they occur. It demonstrates that the equivalent single bending D. O. F. model is reasonable. Mode shapes for bending and torsion modes are presented in Appendix J.

Solar Array Torsional Dynamic Model--A simplified torsional dynamic model for the solar arrays was attempted, using a torsional inertia, lumped at each outer and inner panel, plus a coordinate at the drive motor location.

The first symmetric solar array torsional mode is calculated @ about 1.05 Hz (see Appendix J). This mode has the inner panels plus drive motor out of phase with the outer panels. This mode is simulated fairly well by the simplified model, which has the same primary torsional mode at 1.088 Hz. However, the second symmetric torsional mode at 1.89 Hz is missing from

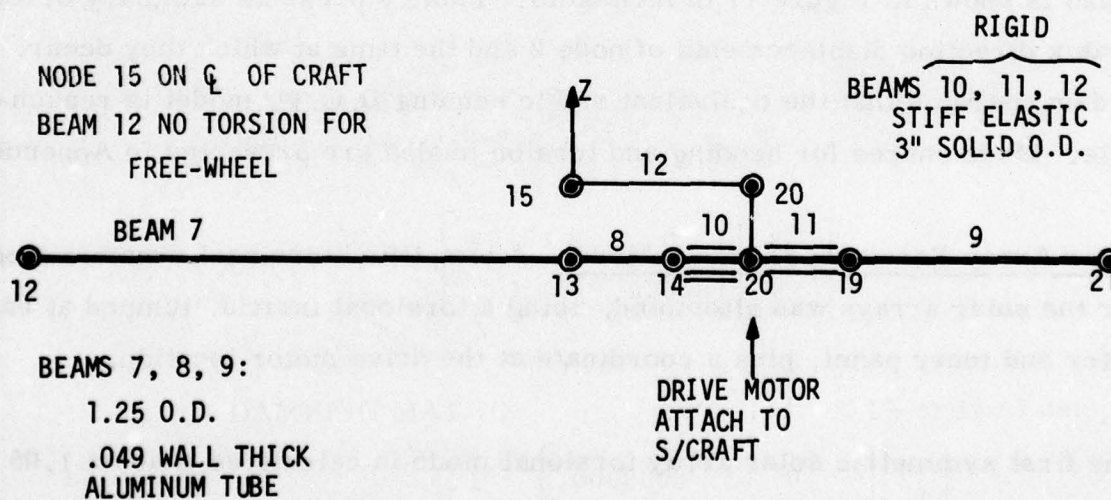
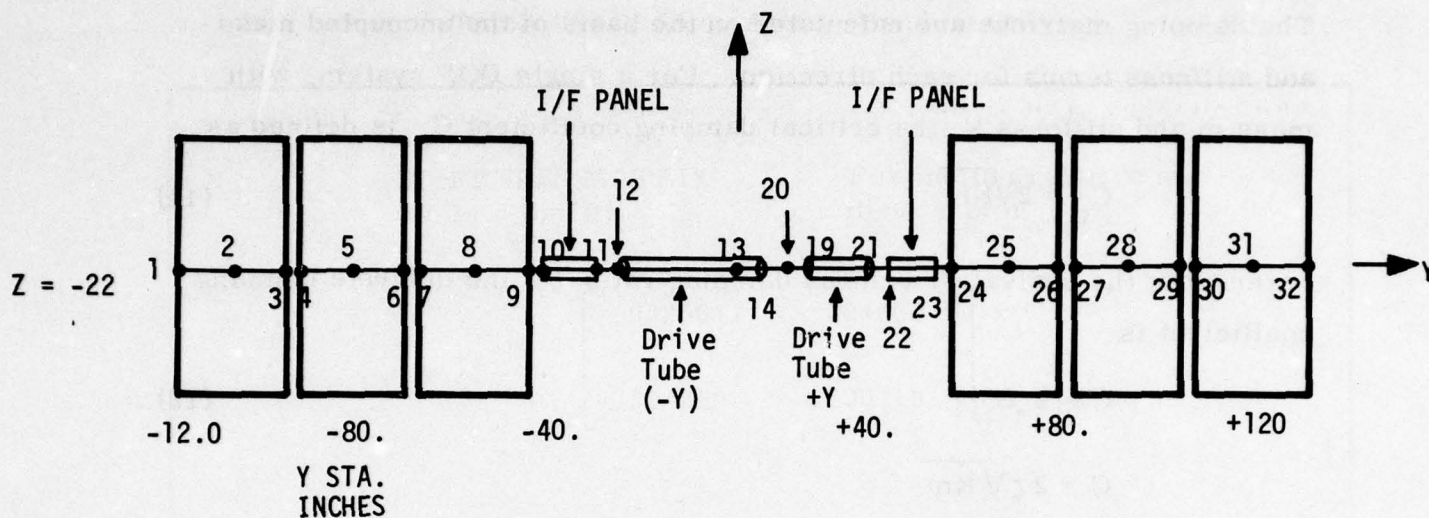


Figure 16. STARDYNE Math Model for Flexible Solar Arrays

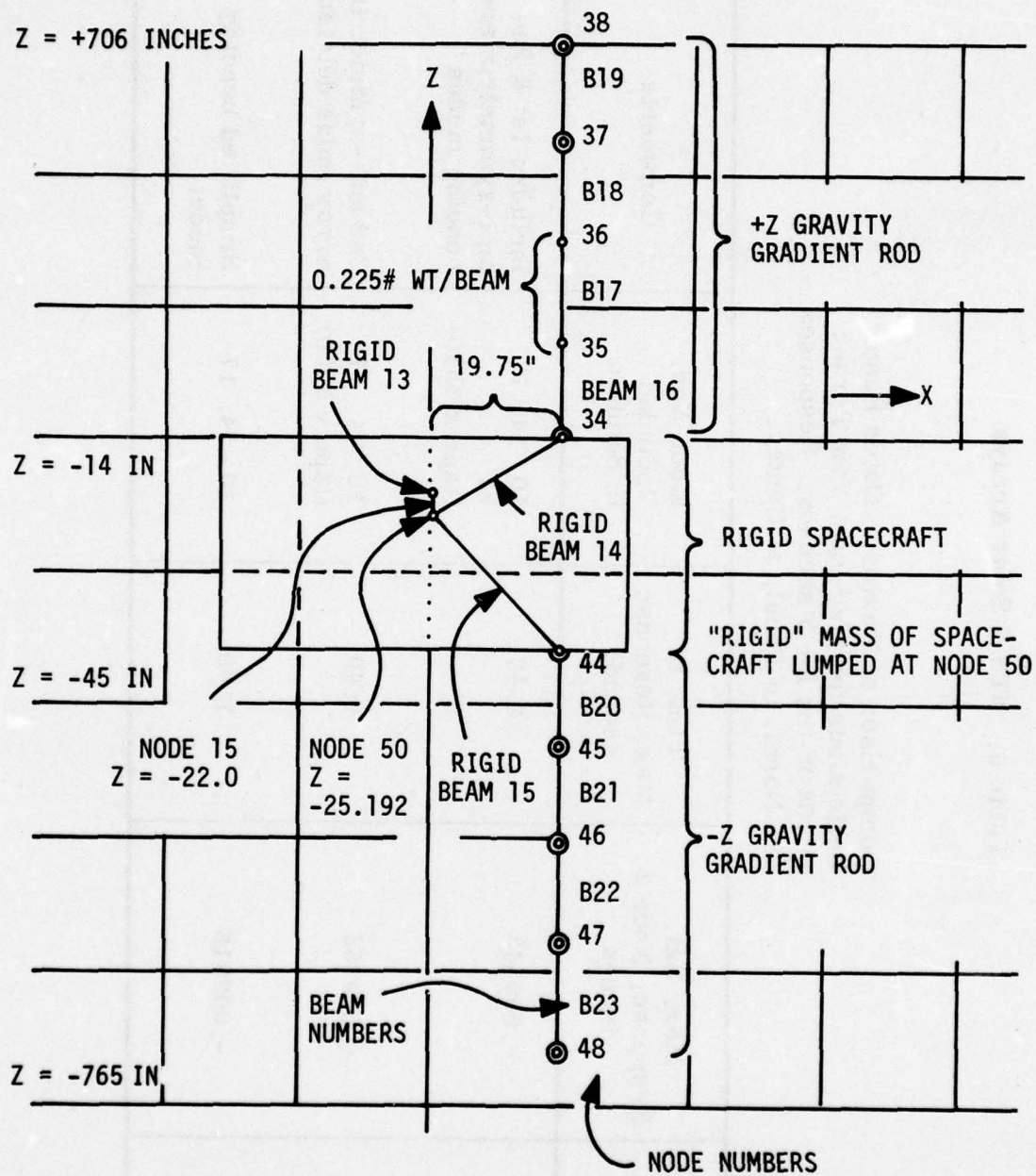


Figure 17. Gravity Gradient Rod and Spacecraft Definition

Table 6. NTS-2 Solar Arrays

Comparison of Maximum Outer Panel Deflections for Step Input Yaw Torque of .04 ft-lbs for 3 seconds. Responses are Norm. to Panel, at Center.

DYNRE1 Run No.	Max. Rel. Response, Node 2 inches	Time of Max. Response seconds	Mode Nos. Included in Solution	Comments
TSNSTC0	-.009843	1.40	10, 14, 17, 24 (tape x 3350)	Includes 1st & 2nd anti-symmetrix array bending modes
TSNSTI1	-.009855	1.40	10, 14, 17 (tape x 3350)	2nd anti-symmetrix array mode deleted
TSNSTJ0	-.009916	1.40	10, 14, 17	Simplified bending model

the simplified model because it has no inertia at the middle panels (nodes 5 and 28). The middle panels have the maximum amplitude in this higher mode.

A series of DYNRE1 runs were made in the complete solar array model, in which the effect of not including the second torsional symmetric mode was compared to a run with all significant modes considered. Results are plotted in Figures 18 through 23.

Therefore a modal coordinate approach was developed. The approach is outlined in Appendix J, with the responses of the generalized coordinate computed using the solution to the basic matrix equation for 2 degrees of freedom. If the discrete torsional response of the drive motor or the center of the outer panel is required, perform the matrix multiplication indicated in the basic matrix equation for 2 degrees of freedom.

Solar Array Torsional Dynamic Model Modifications--The solar array torsional dynamic model was modified from the description given above and in Appendix J. The modification was necessitated by a last minute change in the solar array hardware which significantly increased the torsional stiffness of the array. A complete description of the modification is given in Appendix K. The biggest impact of the modification is in the frequencies of the first two symmetric torsion modes. A comparison between the original and modified mode frequencies is given in Table 7.

Also shown in column 3 of Table 7 is the effect of a grounded drive shaft at the drive motor versus the free wheeling model frequencies given in column 2. Although the shaft is not completely locked or grounded at the drive motor, there are torques (Ball brother braking torque, rolling friction)

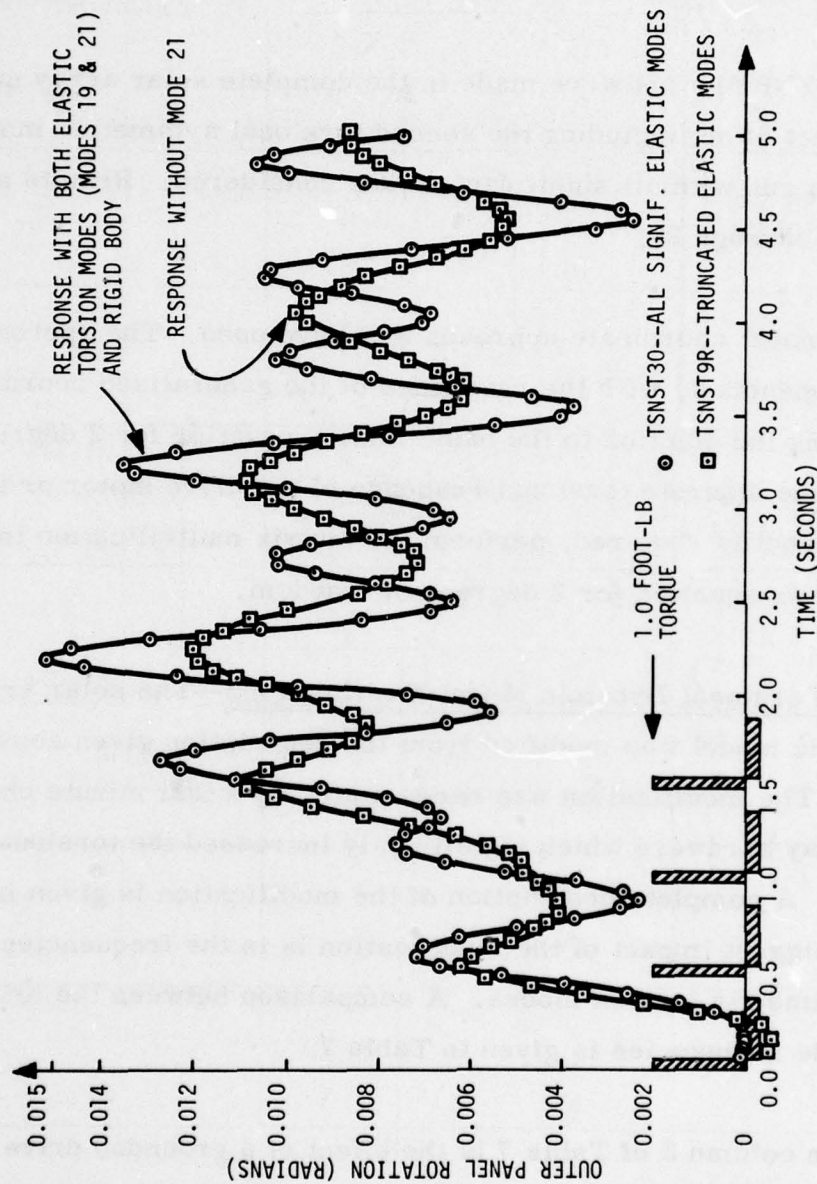
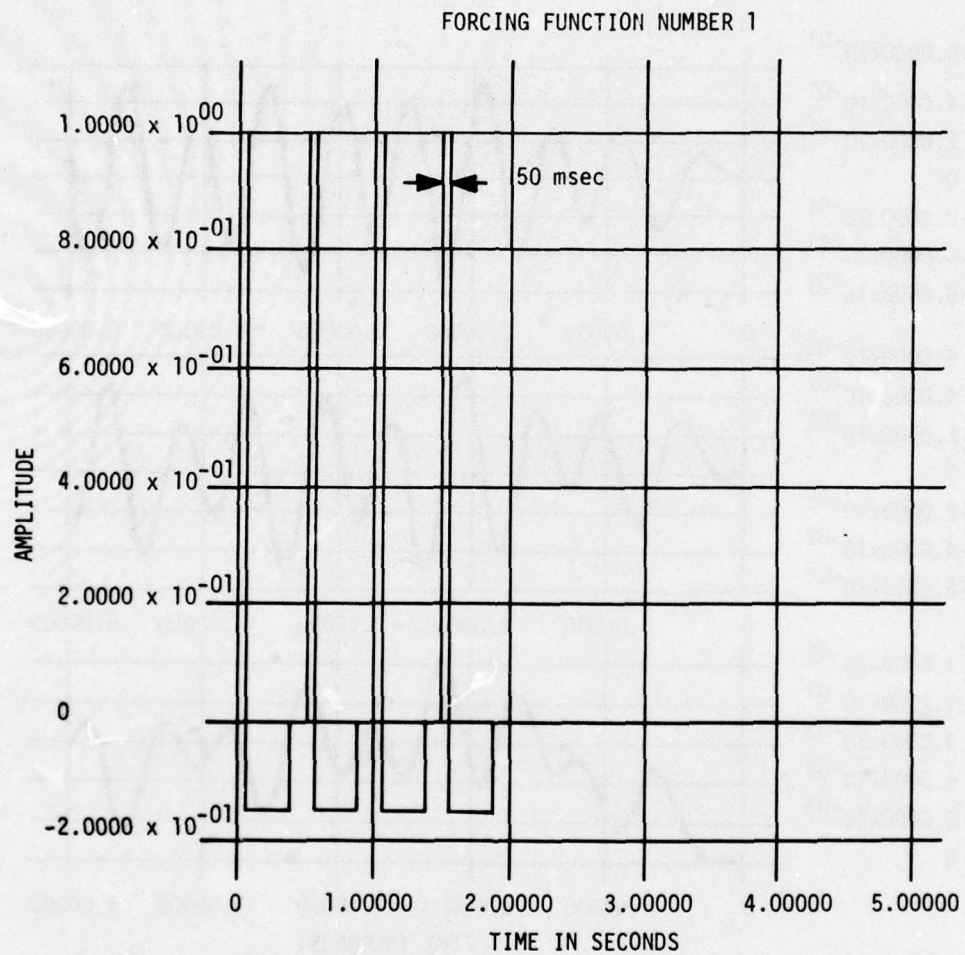


Figure 18. STARDYNE Model Node 2
 θ_Y Response Versus Time



REF. TSNST30
TSNST65

**Figure 19. Solar Array Torsion Model 4 Pulse
Input Forcing Function (Normalized)
(Amplitude of 1.0 = .04 ft-lb)**

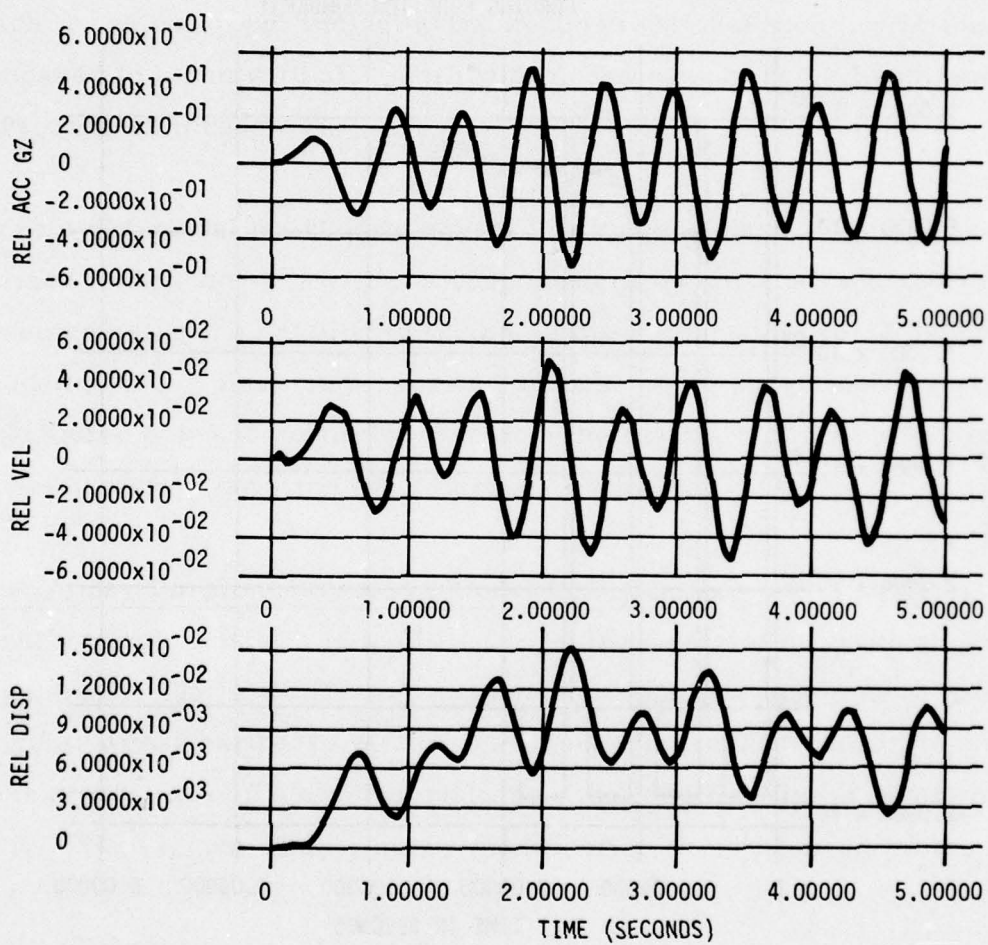


Figure 20. Solar Array Torsion Model, Node 2 = Outer Panel Display, Velocity, Acceleration and Response (in Radian Units) to Four Pulse Excitation

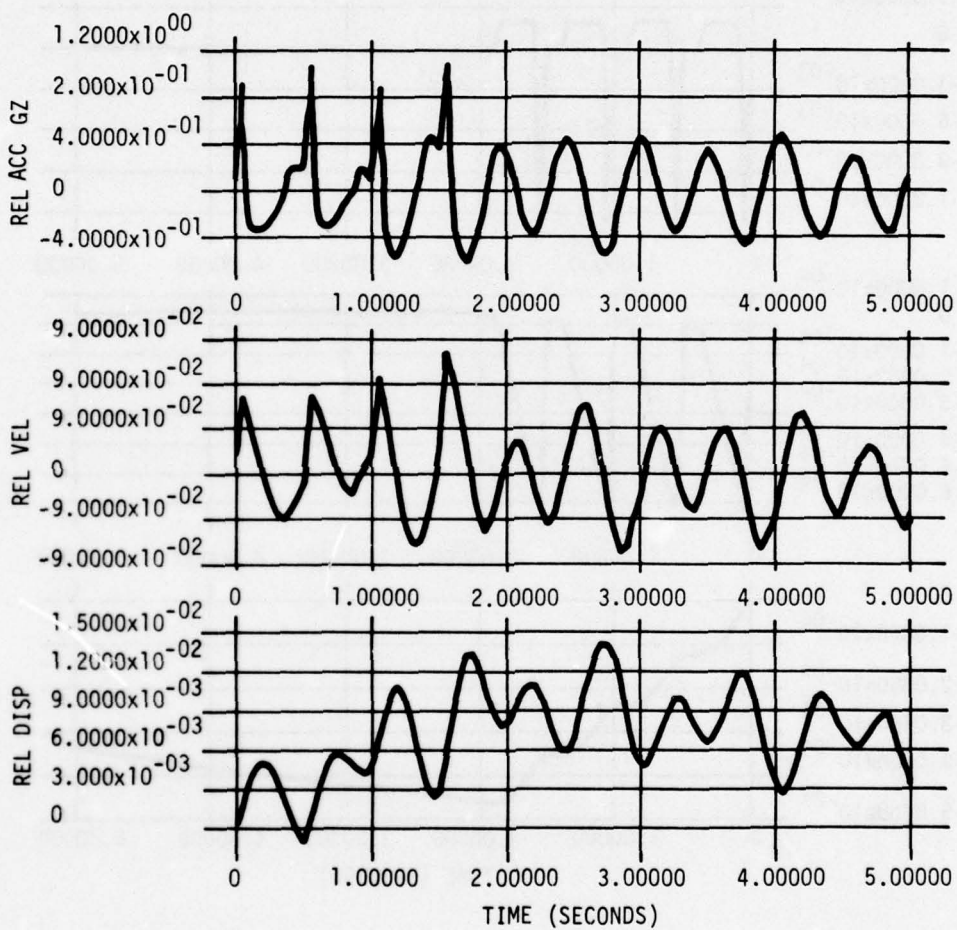


Figure 21. Solar Array Torsion Model Response at Drive Motor to 4 Pulses Applied at Drive Motor

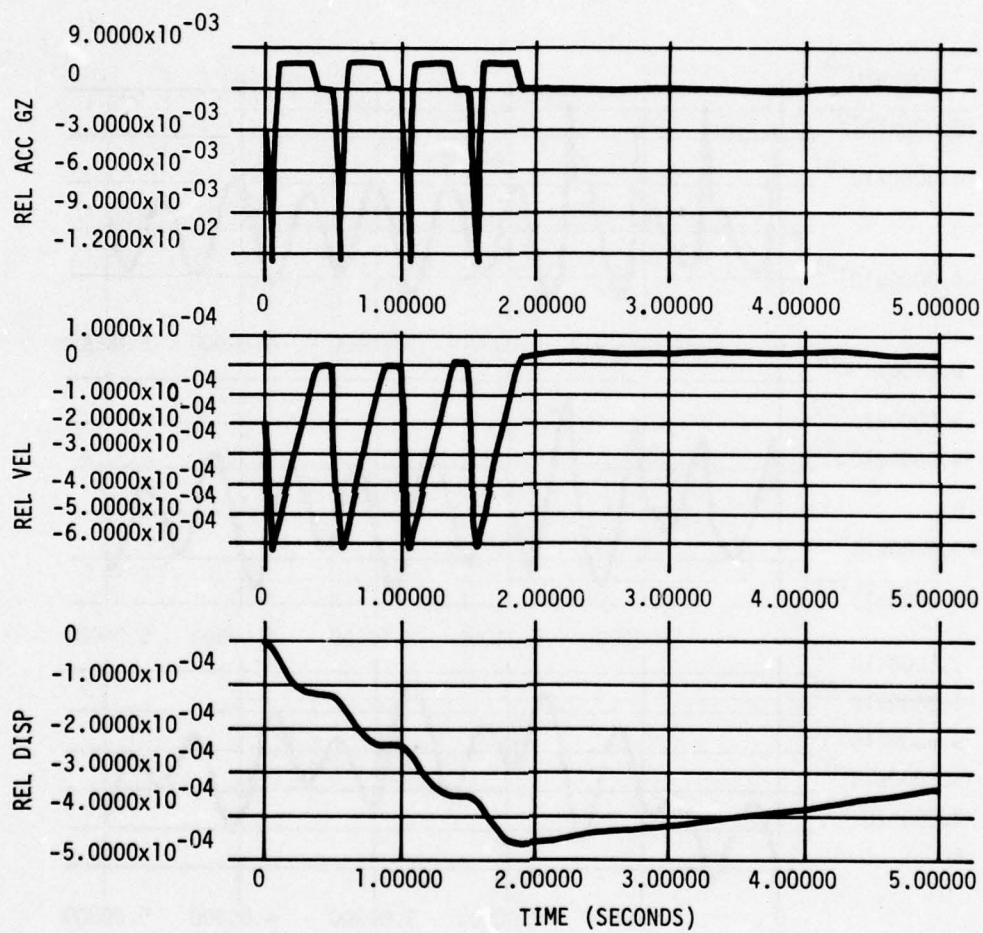
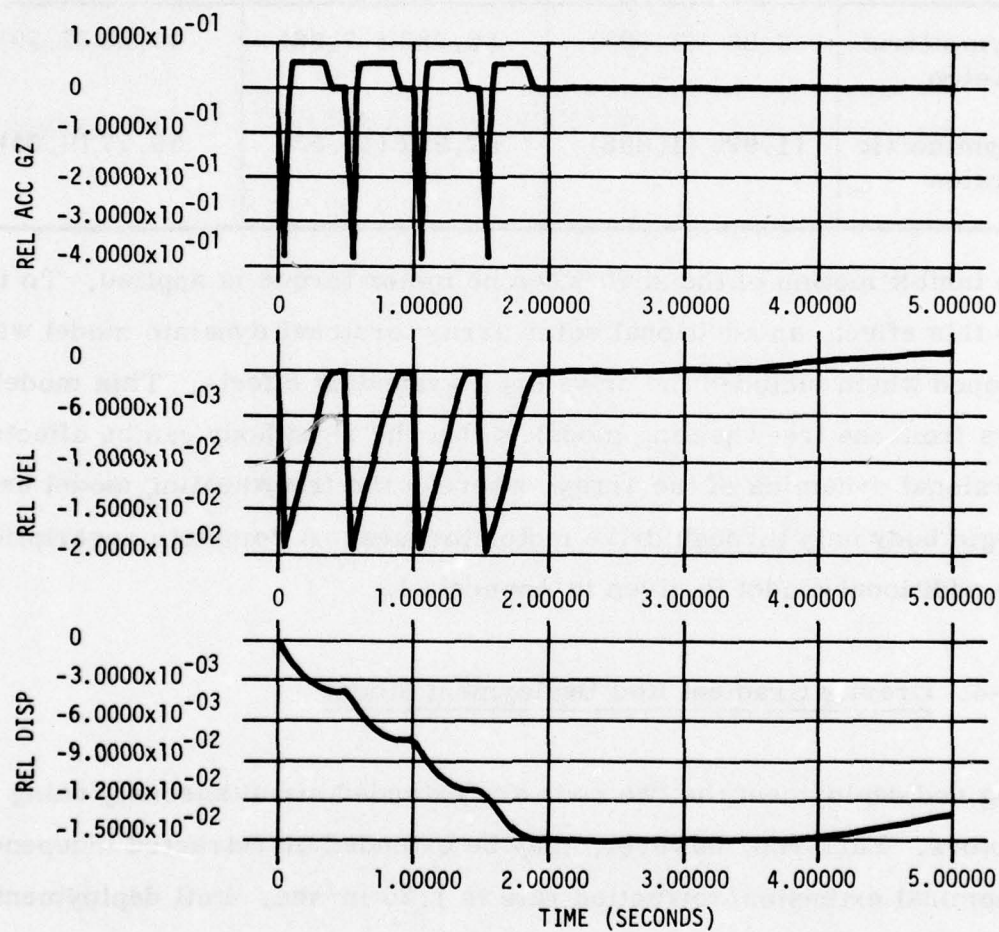


Figure 22. Solar Array Torsion Model Response of Rigid Spacecraft to 4 Pulses



**Figure 23. Response of -Z Gravity Rod Tip Mass (Node 48)
X Direction Response (Inch Units) Relative* to
Spacecraft Attach Point, 4 Pulses on Solar Array
Drive Motor**

***NOTE:** No rigid body contribution for relative response.

Table 7. Comparison of Original and Modified Torsional Mode Frequencies

Mode	Original Model Frequency rad/sec (Hz)	Modified Model Frequency rad/sec (Hz)	Grounded Drive Motor Model rad/sec (Hz)
1st Symmetric Torsion	6.88 (1.095)	50.036 (7.96)	16.28 (2.59)
2nd Symmetric Torsion	11.925 (1.898)	97.907 (15.53)	56.77 (9.04)

which inhibit motion of the shaft when no motor torque is applied. To investigate this effect, an additional solar array torsional dynamic model was developed which included the drive shaft grounding effects. This model differs from the freewheeling model is that the rigid body can be affected by torsional dynamics of the array, whereas the freewheeling model excites the rigid body only through drive motor torques. A complete description of the additional model is given in Appendix L.

III-C-8. Gravity Gradient Rod Deployment Model

During rod deployment the two rods are extended simultaneously using two dc motors. Each rod, however, may be extended or retracted independently. The nominal extension/retraction rate is 1.25 in/sec. Full deployment then would require approximately 9.6 minutes.

Modeling--Deploying the gravity gradient rods produces a large change in the moments of inertia of the vehicle. Hence, the gravity gradient rod deployment model consists of a time varying inertia tensor representation.

The inertia tensor for the total system may be represented by

$$I = I_{RB} + I_{panels} + I_{rod1} + I_{rod2}$$

The first two terms, the rigid body inertia tensor and solar panel inertia tensors are available from the vehicle mass properties data. The inertia tensor of the rods can be computed based on the theorem of parallel axis.

The inertia tensor for a hollow right circular cylinder about its principle axis located at the center of the mass of the cylinder is given by

$$I_{rods} = \begin{bmatrix} \frac{m_r}{12} [r_o^2 + r_i^2 + l^2] & 0 & 0 \\ 0 & \frac{m_r}{12} [r_o^2 + r_i^2 + l^2] & 0 \\ 0 & 0 & \frac{m_r}{2} [r_o^2 + r_i^2] \end{bmatrix} \quad (13)$$

where

r_o = outside radius of rod = .25 in

r_i = inside radius of rod = .248 in

m_r = mass of rod = .028 slugs

l = length of rod = 60 ft (fully extended)

The inertia tensor for a solid sphere about its principal axis about its principal axis about its center of mass is given by

$$I_{\text{Tip mass}}' = \begin{bmatrix} \frac{2}{5} m_s r_s^2 & 0 & 0 \\ 0 & \frac{2}{5} m_s r_s^2 & 0 \\ 0 & 0 & \frac{2}{5} m_s r_s^2 \end{bmatrix} \quad (14)$$

where

m_s = mass of tip mass ($m_{s_1} = m_{s_2} = .233$ slugs)

r_s = radius of tip mass ($r_{s_1} = 2$ in; $r_{s_2} = 3.81$ in)

The principal axis of the tip masses can be chosen so as to be parallel to the principal axes of the gravity gradient rods. These in turn can be considered parallel to the rigid body coordinate system which are approximately vehicle principal axes.

The theorem of parallel axis can now be used to calculate the contribution of the gravity gradient rods to the vehicle inertia tensor with respect to a center of mass coordinate system. The total system inertia is

$$\begin{aligned} I_{xx} = & I_{xx \text{ rigid body}} + I_{xx \text{ panels}} + I'_{xx \text{ rod}_1} + m_{R_1} (r^1)^2 \\ & + I'_{xx \text{ Tip mass}_1} + m_{s_1} (\tilde{r}^1)^2 + I'_{xx \text{ rod}_2} + m_{R_2} (r^2)^2 \\ & + I'_{xx \text{ Tip mass}_2} + m_{s_2} (\tilde{r}^2)^2 \end{aligned} \quad (15)$$

where

r^1 = y component plus z component of distance from center of mass of rigid body to center of mass of rod 1

r^2 = y component plus z component of distance from center of mass of rigid body to center of mass of rod 2

\tilde{r}^1 = y component plus z component of distance from center of mass of rigid body to center of mass of tip mass 1

\tilde{r}^2 = y component plus z component of distance from center of mass of rigid body to center of mass of tip mass 2

Similar expressions can be computed for I_{yy} and I_{zz} .

The products of inertia are defined:

$$I_{xy} = I_{xy \text{ rigid body}} + I_{xy \text{ panels}} - m_{R_1} (r_x^1 r_y^1) - m_{s_1} (\tilde{r}_x^1 \tilde{r}_y^1) - m_{R_2} (r_x^2 r_y^2) - m_{s_2} (\tilde{r}_x^2 \tilde{r}_y^2) \quad (16)$$

$$I_{xz} = I_{xz \text{ rigid body}} + I_{xz \text{ panels}} - m_{R_1} (r_x^1 r_z^1) - m_{s_1} (\tilde{r}_x^1 \tilde{r}_z^1) - m_{R_2} (r_x^2 r_z^2) - m_{s_2} (\tilde{r}_x^2 \tilde{r}_z^2)$$

$$I_{yz} = I_{yz \text{ rigid body}} + I_{yz \text{ panels}} - m_{R_1} (r_y^1 r_z^1) - m_{s_1} (\tilde{r}_y^1 \tilde{r}_z^1) - m_{R_2} (r_y^2 r_z^2) - m_{s_2} (\tilde{r}_y^2 \tilde{r}_z^2)$$

where, for example,

r_x^1 , is the x component of the vector from the center of mass of the vehicle to the center of mass of rod 1

The center of mass vectors can be represented as follows:

$$\mathbf{r}^1 = \rho^1 + \sigma^1 + \xi^1$$

where

ρ^1 = vector from center of mass of rigid body to NRL origin

σ^1 = vector from NRL origin to support point of rod 1

$$\xi^1 = \begin{bmatrix} 0 \\ 0 \\ \xi_3^1 \end{bmatrix} = \text{vector from support point to center of mass of rod 1}$$

$$\xi_3^1 = \frac{l_1}{2}$$

where

$$l_1 = \int \dot{l}_1 dt \quad l_1 \leq l_{1\max} = 60 \text{ ft}$$

$$\dot{l}_1 = \text{constant} = \text{rod 1 extension rate} = 1.25 \text{ in/sec}$$

A similar representation can be given for rod 2.

For the tip masses

$$\tilde{\mathbf{r}}^1 = \mathbf{r}^1 + \begin{bmatrix} 0 \\ 0 \\ r_{s1} + \frac{l}{2} \end{bmatrix} \quad (17)$$

The masses of the spheres in the total system inertia are constant. However, the masses of the rods change as they are extended.

The mass of the rods may be computed as follows:

$$m_{r_1} = \gamma V \quad (18)$$

where

γ = density of the rod material

V = volume of a hollow cylinder

Equation $m_{r_1} = \gamma V$ may be written

$$m_1 = \frac{1}{32.17} \gamma \pi (r_o^2 - r_i^2) l_1$$

where r_o , r_i , and l_1 have been defined previously and

$$\gamma = 690.18 \text{ lbs/cu. ft.}$$

III-C-9. AKM Jettison Disturbance Torque Model

Equipment jettison usually produces a small transient disturbance torque that has a negligible effect on the long-term performance of the control system. In this instance, the magnitude of the disturbance torque effect on spin axis attitude is of prime concern. When the distance between the jettisoned equipment and the spacecraft's mass center is large, the line of action of the separation force should pass as close to mass center as possible.

In the present case, the AKM is a spring-loaded payload. At time of jettison, a retaining band is released, enabling the spring-loaded payload to be ejected. The springs do not expand at identical rates and do not have the exact spring constants.

In addition, it cannot be assumed that all springs will expand exactly. Therefore, there will be a resulting torque acting on the space vehicle.

Figure 24 illustrates the locations of the four springs which attach the AKM to the space vehicle. Important data is

- o Spring constant: 16 lbs/inch \pm tolerance
- o Uncompressed length: 1.5 inch \pm tolerance
- o Compressed on vehicle: .75 inch \pm tolerance
- o Solid length: .65 inch

Figure 25 shows the positioning of the springs with respect to the X-Y coordinates of the space vehicle assuming no AKM misalignment. Figure 26 shows the same positioning assuming the AKM misaligned from both the X and Y axes. Figure 27 illustrates the geometry involved in calculating the displacement of the springs from the space vehicle X-Y axis, assuming no misalignment (positioning assuming misalignment can be easily calculated from these base calculations). Table 8 contains these spring force locations.

From

$$F = kx$$

the force created by a spring expanding .75 in. with $k = 16 \text{ lb/in}$ is 12 lbs. The resultant force of the four springs is 48 lbs. The weight of the AKM is 64 lbs. Its mass is $64/32.2 = 1.99$ slugs. Calculation of the AKM acceleration gives

$$F = ma$$

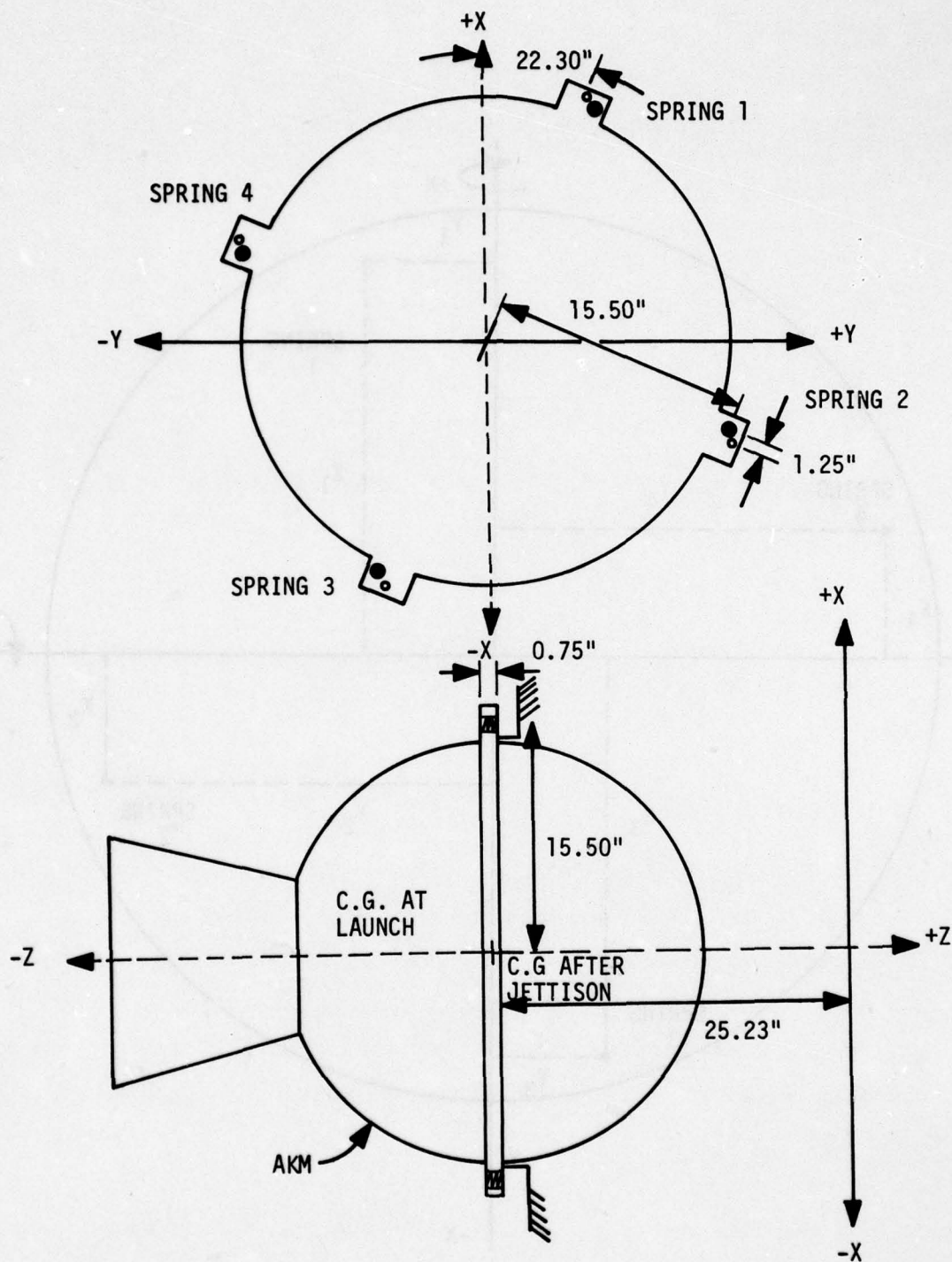


Figure 24. Spring Location

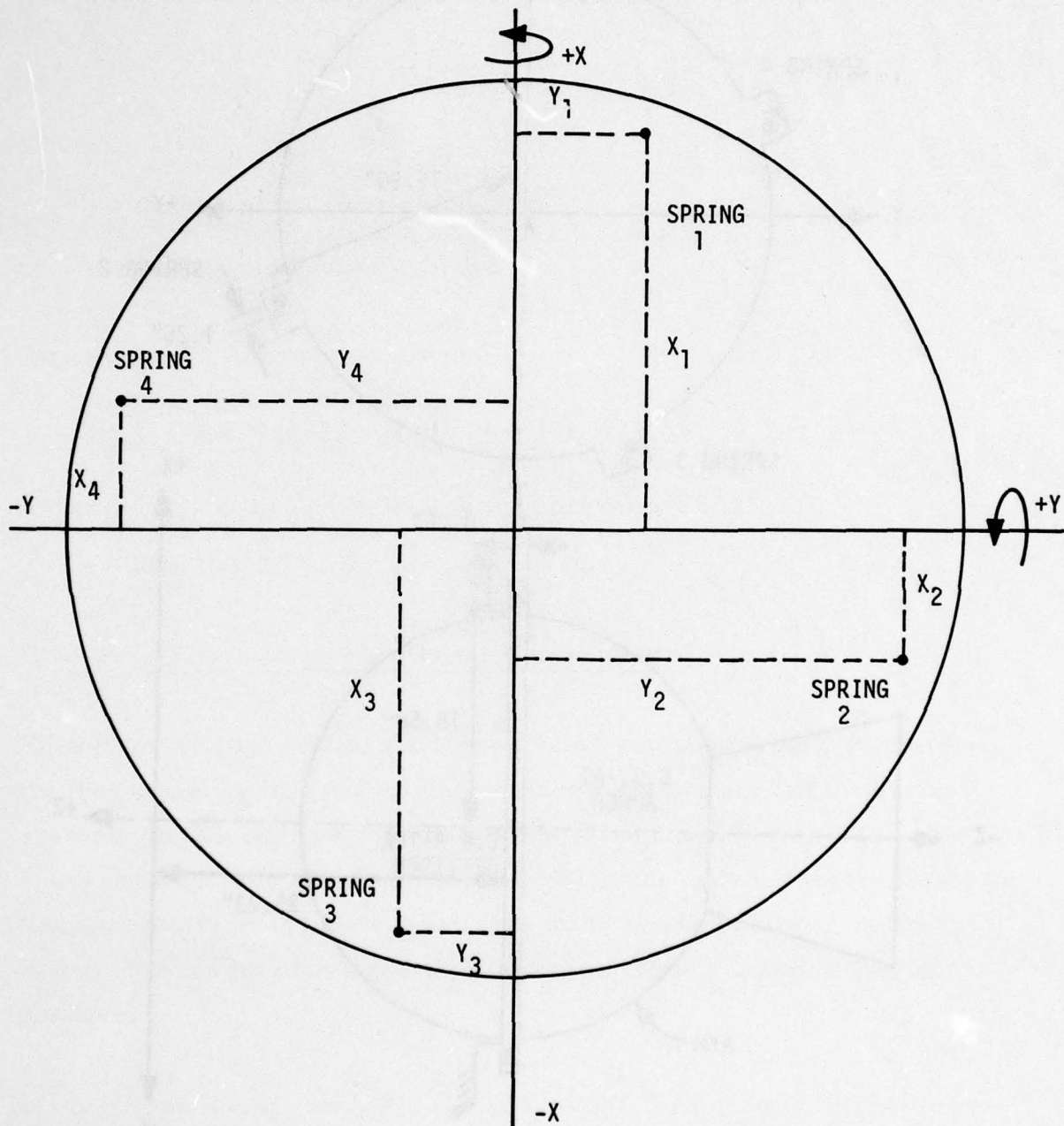


Figure 25. Spring Location--No Misalignment

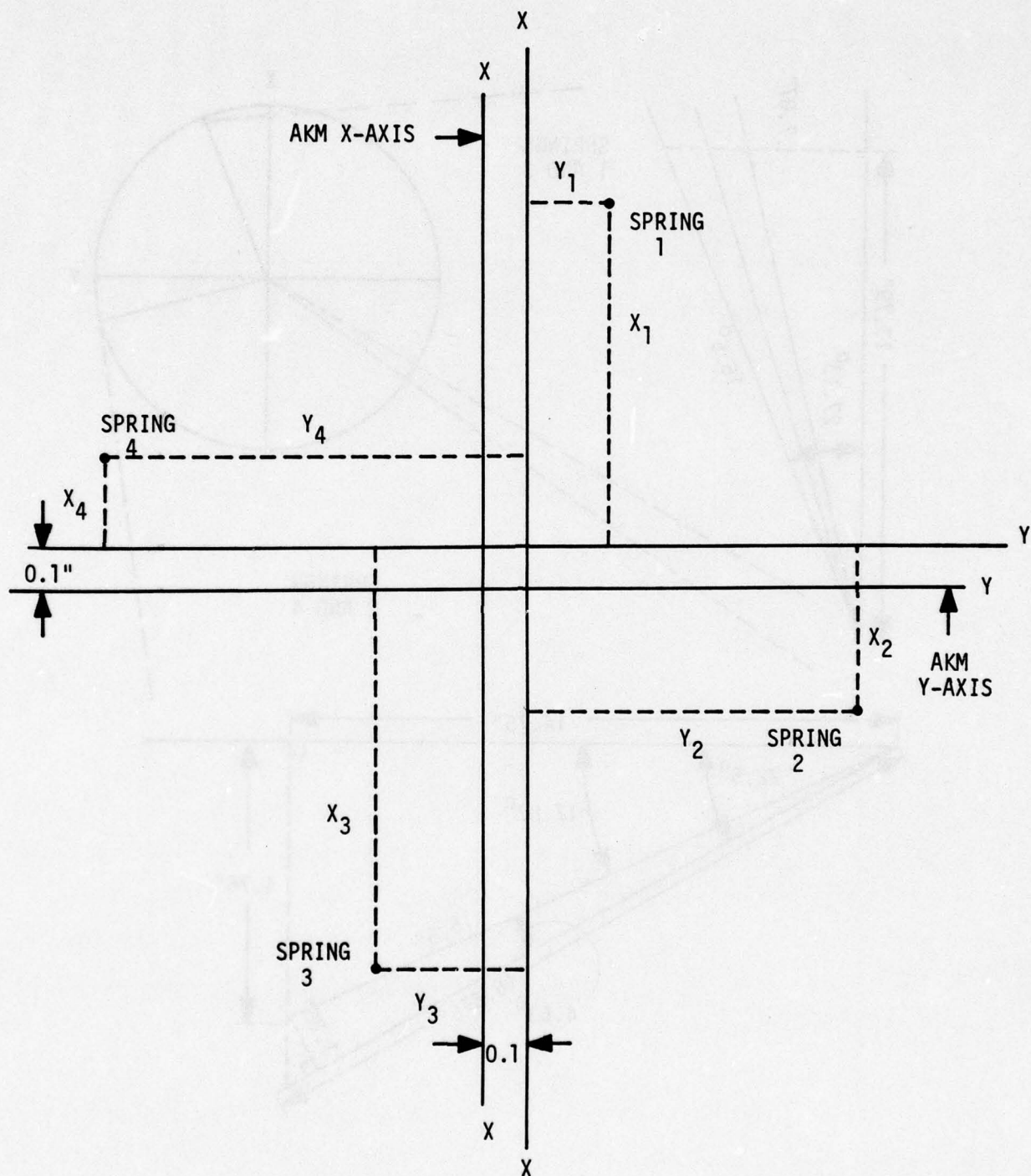


Figure 26. Spring Location--Misalignment as Shown

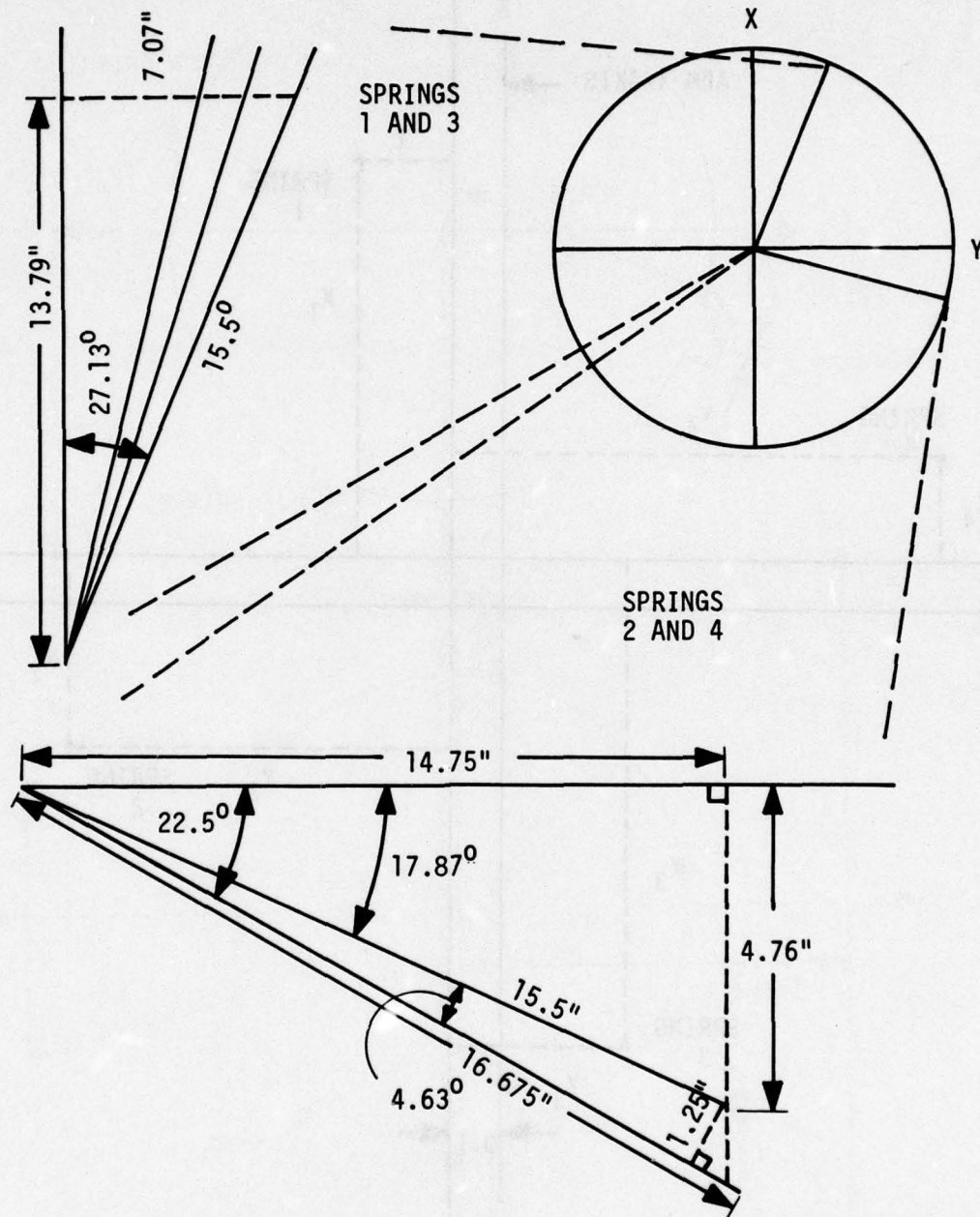


Figure 27. Spring Force Displacement Calculation

Table 8. Spring Force Displacement and Spring Constant

Case Number	SPRING FORCE DISPLACEMENT (in)								SPRING CONSTANT (lb/in)			
	X ₁	X ₂	X ₃	X ₄	Y ₁	Y ₂	Y ₃	Y ₄	1	2	3	4
1	13.79	-4.76	-13.79	4.76	7.07	14.75	-7.07	-14.75	14.4	16	17.6	16
2	13.69	-4.86	-13.89	4.66	7.07	14.75	-7.07	-14.75	14.4	16	17.6	16
3	13.69	-4.86	-13.89	4.66	7.07	14.75	-7.07	-14.75	16	17.6	16	14.4
4	13.79	-4.76	-13.79	4.76	6.97	14.65	-7.17	-14.85	16	14.4	16	17.6
5	13.79	-4.76	-13.79	4.76	6.97	14.65	-7.17	-14.85	14.4	16	17.6	16
6	13.69	-4.86	-13.89	4.66	6.97	14.65	-7.17	-14.85	14.4	16	17.6	16
7	13.69	-4.86	-13.89	4.66	6.97	14.65	-7.17	-14.85	14.4	17.6	17.6	14.4
8	13.69	-4.86	-13.89	4.66	6.97	14.65	-7.17	-14.85	14.4	17.6	17.6	17.6
9	13.69	-4.86	-13.89	4.66	6.97	14.65	-7.17	-14.85	16	16	14.4	17.6

$$48 = 1.99 a$$

$$a = 24.12 \text{ ft/sec}^2$$

From

$$d = \frac{1}{2}at^2$$

We have

$$.75/12 = \frac{1}{2}(24.12)t^2$$

$$t = .072 \text{ sec}$$

and

$$v = at = 24.12 \times .072 = 1.74 \text{ ft/sec}$$

The resulting velocity of the AKM is calculated to be approximately 1.74 ft/second.

Torque Computation--Assuming that the spring constants vary by no more than 10 percent, the resulting forces can be calculated and, from these forces, the disturbance torques can be easily computed.

Nine cases were chosen to be evaluated. Case 1 involved no AKM misalignment. Cases 2, 3, 4, and 5 assumed Y axis misalignment and X axis misalignment respectively. Cases 6 through 9 assumed both X and Y axis misalignment. Table 8 lists each spring constant (including a ± 10 percent tolerance).

Table 9 lists the computed torques about the X and Y axis of the space vehicle.

NOTE: There was no disturbance about the Z axis.

Table 9. Spring Force and Resulting Torque

Case Number	SPRING FORCE (lb)				X axis mis-align-ment	Y axis mis-align-ment	(ft-lb) $\Sigma \Gamma x$	(ft-lb) $\Sigma \Gamma x$
	1	2	3	4				
1	10.8	12	13.2	12	0	0	-1.414	-2.158
2	10.8	12	13.2	12	0	0.1"	-1.414	-3.158
3	12	13.2	12	10.8	0	0.1"	2.95	-1.352
4	12	10.8	12	13.2	0.1"	0	-3.35	.952
5	10.8	12	13.2	12	0.1"	0	-1.814	-2.598
6	10.8	12	13.2	12	0.1"	0.1"	-1.814	-3.158
7	10.8	13.2	13.2	10.8	0.1"	0.1"	1.136	-4.11
8	10.8	13.2	13.2	13.2	0.1"	0.1"	-1.834	-3.178
9	12	12	10.8	13.2	0.1"	0.1"	-1.168	1.455

III-C-10. Solar Array Drive Model

The solar array drive torque model is based on data generated by the Ball Brothers Research Corporation. The data is in the form of handwritten notes labeled "Equations for Simulating the Rockwell GPS Solar Array Drive by Glen King and Lew Martin." It is dated February 5, 1976. The pulse frequency modulator logic is as described in a memo to Honeywell from Samso (P. Talley, October 22, 1975).

General Description--A functional block diagram of the solar array positioning loop is given in Figure 28. Shown is a block for the modification developed by GE which will be described in the flexibility analysis section.

Motor Torques--As given in the Ball Brothers data there are five sources of torque associated with the solar array drive motor. These are:

- Mechanical torque T_M
- Coulomb friction torque T_{CL}
- Cogging torque T_{CG}
- Magnetic hysteresis torque T_D
- Flex cable torque* T_{FC}

In addition, Ball Brothers has modeled the interaction between the motor shaft and array as a torsional spring mass damper system as shown in Figure 29.

* This term relates only to the NTS-2 version of the model.

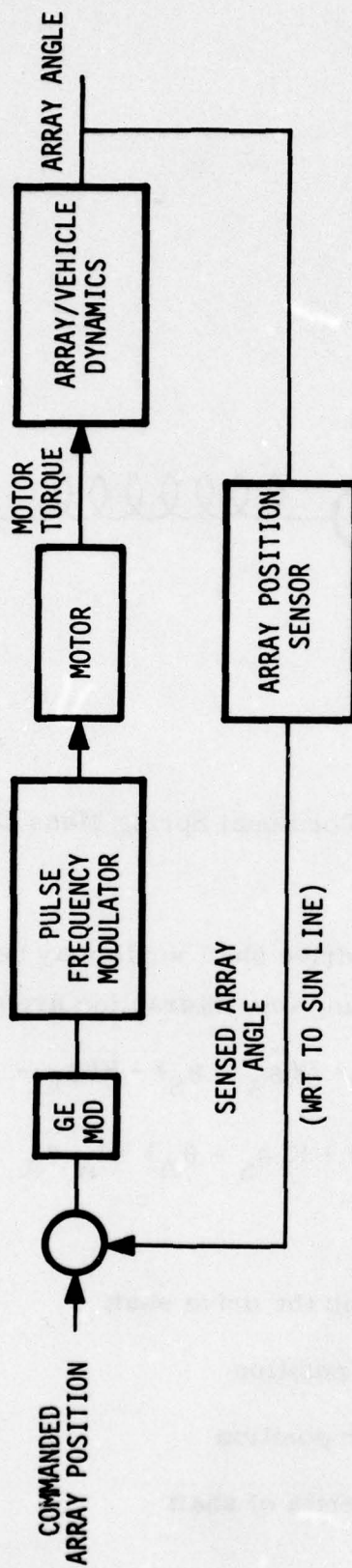


Figure 28. Solar Array Drive Functional Block Diagram

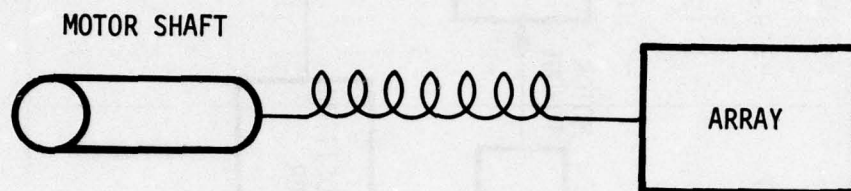


Figure 29. Torsional Spring Mass Damper System

With this model, motor drive shaft angle may be different from array angle. The dynamics representing this interaction are given by

$$\begin{aligned} T_S &= I_S \ddot{\theta}_S - D(\dot{\theta}_A - \dot{\theta}_S) - K(\theta_A - \theta_S) \\ D(\dot{\theta}_S - \dot{\theta}_A) + K(\theta_S - \theta_A) &= I_A \ddot{\theta}_A \end{aligned} \quad (19)$$

where

T_S = Total torque on the drive shaft

θ_S = Shaft angular position

θ_A = Array angular position

I_S = Moment of inertia of shaft

I_A = Moment of inertia of array

D = Equivalent damping coefficient

K = Spring constant

The total torque on the shaft is

$$T_S = T_M - T_{CL} - T_{CG} - T_D - T_{FC} \quad (20)$$

The torque producing components of this equation have been modeled by Ball Brothers from experimental data.

They are (oz - in)

Motor Torque

$$T_M = (25 - 1.44 \theta_S) \left(\frac{8.48}{1/800 S + 1} \right) \\ \approx 8.48 (25 - 1.44 \theta_S)$$

Coulomb Friction Torque

$$T_{CL} = 30.0 \text{ For } \dot{\theta}_S > 0.0007 \text{ rad/sec} \\ = 36.0 \text{ For } \dot{\theta}_S < 0.0007 \text{ rad/sec (during pulse)} \\ = 0. \text{ For } \dot{\theta}_S < 0.0007 \text{ rad/sec (no pulse)}$$

Cogging Torque

$$T_{CG} = \{2.3933 [\sin 97 \theta_S + \sin (97 \theta_S + 0.803)] \\ + 0.3506 \sin (16 \theta_S + 1.57)\} \{0.0385 + 0.964 \sin^2 (0.5 \theta_S)\}$$

Magnetic Hysteresis Torque

$$T_D = \int T_D dt \\ T_D = 14.6 [T_D \text{ SGN } \theta_S - 10.0]^2 \dot{\theta}_S$$

Flex Cable Torque

$$T_{FC} = 4.0 \sin(0.9 \theta_S) \quad (21)$$

Model Simplification--Values for the spring constant ($K = 1.905 \times 10^5$ oz - in/rad) and equivalent damping coefficient ($D = 352$ oz-in-sec)* are equivalent to a torsional mode frequency of 230.46 rad/sec (36.68 Hz) and a damping coefficient of .213. Preliminary analysis indicated that this frequency is much higher than the highest significant structural mode-frequency of the panels (less than 20 rad/sec). Thus we assumed a rigid connection between the motor and array. A comparison of array angular response for the motor drive model as given by Ball Brothers and the rigid approximation is given in Figure 30.

Array Angle Definition and Limits--NRL defines array angle to be zero when the array is in the yz plane (HI coordinate system) and with the solar cell surface pointing in the +x direction. Positive rotation is about +y. For GPS, zero array angle is panels in the xy plane, solar cell surface pointing in the +z direction. Thus for panel angle θ ,

$$\theta_{HI} = \theta_{NRL} + 90^\circ \quad (22)$$

The limits in rotation in the NRL system is $\pm 100^\circ$. In our system, therefore,

$$-10 \leq \theta_{HI} \leq +190^\circ \quad (23)$$

* Since the motor drive is not situated at the center of the drive shaft, our structural analysis indicates that this is an average value for the two arrays.

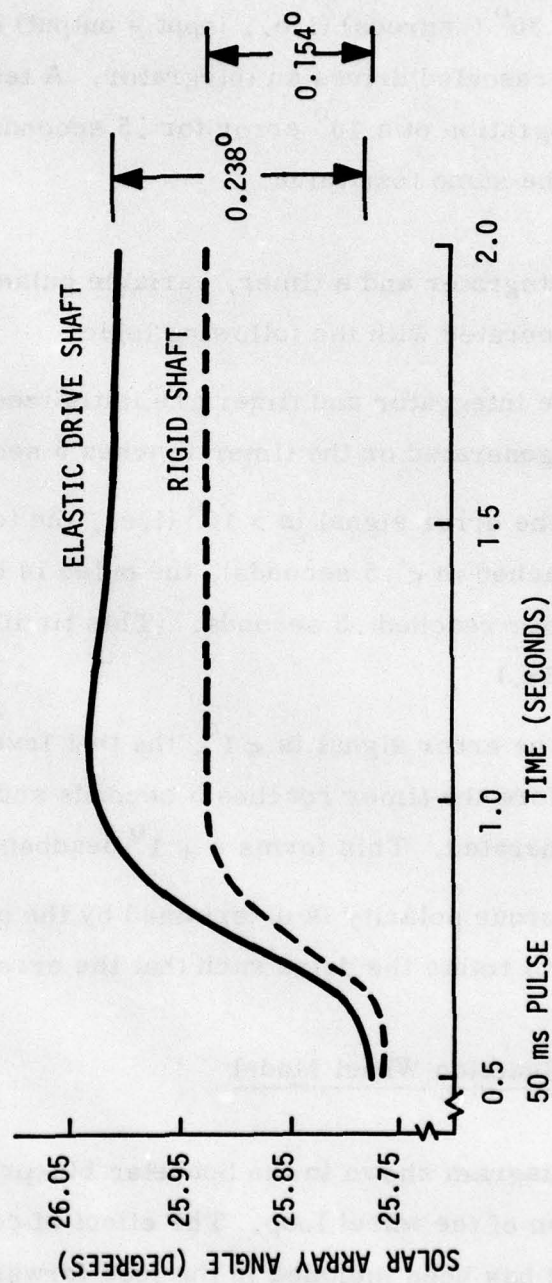


Figure 30. Solar Array Response

Pulse Frequency Modulator--The pitch sun sensor signal which is proportional for $\pm 30^\circ$ (degrees) (i.e., input = output) is scaled at $7.2 \mu \text{ amp/degree}$. This signal rescaled drives an integrator. A test level is established such that the integration of a 10° error for .5 seconds or a 1° error for 5 seconds will reach the same test value.

Using the integrator and a timer, variable pulse rates between .2 Hz and 2 Hz are generated with the following logic:

- The integrator and timer are initialized each time a pulse is generated or the timer reaches 5 seconds.
- If the error signal is $> 10^\circ$ (i.e., the test level would be reached in $< .5$ seconds), the pulse is inhibited until the timer reached .5 seconds. (This limits the pulse rate to 2 Hz.)
- If the error signal is $< 1^\circ$, the test level will not be reached before the timer reaches 5 seconds and, hence, no pulse is generated. This forms a $\pm 1^\circ$ deadband around null.

The pulse torque polarity is determined by the pitch sun sensor polarity and is directed to rotate the drive such that the error signal is reduced.

III-C-11. Reaction Wheel Model

The block diagram shown in the Spacetac blueprint given in Figure 5 includes a description of the wheel loop. The effect of coulomb friction is not explicit. However, it has been included in the feed forward block containing the first order lag term $K\tau/(\tau S+1)$. A more realistic approach is shown in Figure 31.

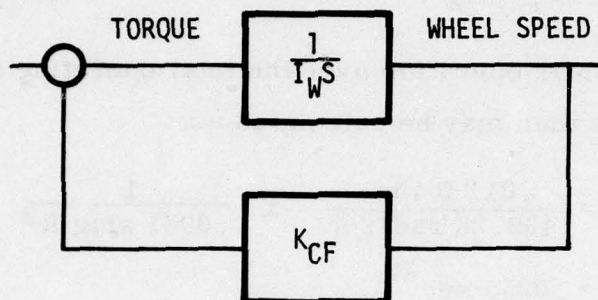


Figure 31. Coulomb Friction Effect

The time constant τ , or in our notation, τ_w is then a function of Coulomb friction and wheel inertia.

The time constant τ_w of the wheel may be calculated as follows: The torque the wheel produces is a function of applied voltage and wheel speed or

$$T(w, v) = I_w \ddot{w} \quad (24)$$

Linearizing this equation, we obtain

$$I_w \ddot{\delta w} = \frac{\partial T}{\partial w} \ddot{\delta w} + \frac{\partial T}{\partial v} \ddot{\delta v}$$

Assuming a constant applied voltage, equation may be written

$$\ddot{\delta w} = \frac{1}{I_w} \left[\frac{\partial T}{\partial w} \right] \ddot{\delta w}$$

$\frac{\delta T}{\delta W}$ may be approximated with data shown in Figure 32 which was taken from Bendix test data* or

$$\frac{\delta T}{\delta W} = \frac{T_1 - T_2}{W_1 - W_2} = \frac{2.1 \text{ in oz}}{-1330 \text{ rpm}} \quad (25)$$

which assumes linear operation over the total operating speed of the wheel. The time constant then may be calculated as

$$\begin{aligned} \frac{1}{\tau_W} &= \frac{.011 \text{ ft lbs}}{139.28 \text{ rad/sec}} \times \frac{1}{.0031 \text{ slug ft}^2} \\ &= .0255 \text{ sec}^{-1} \end{aligned} \quad (26)$$

or

$$\tau_W = 39.25 \text{ sec}$$

The lines labeled +20% linearity is equivalent to a 33 second time constant and the -20% linearity is equivalent to a 52 second time constant. Thus τ_W could vary between 30 and 50 seconds.

III-C-12. Combined Earth Sensor Model

A mathematical model of the combined earth sensor which includes both a horizon crossing indicator for use in the spin phase and an earth radiation detector for on orbit generation was developed for the NDS verification. The model includes a filter with a 1.4 second time constant representing thermopile image processor fade lag. The sampling strategy for computing pitch

*NRL reaction wheel type No. 3890003-1, Bendix Navigation and Control Division, 28 August 1974.

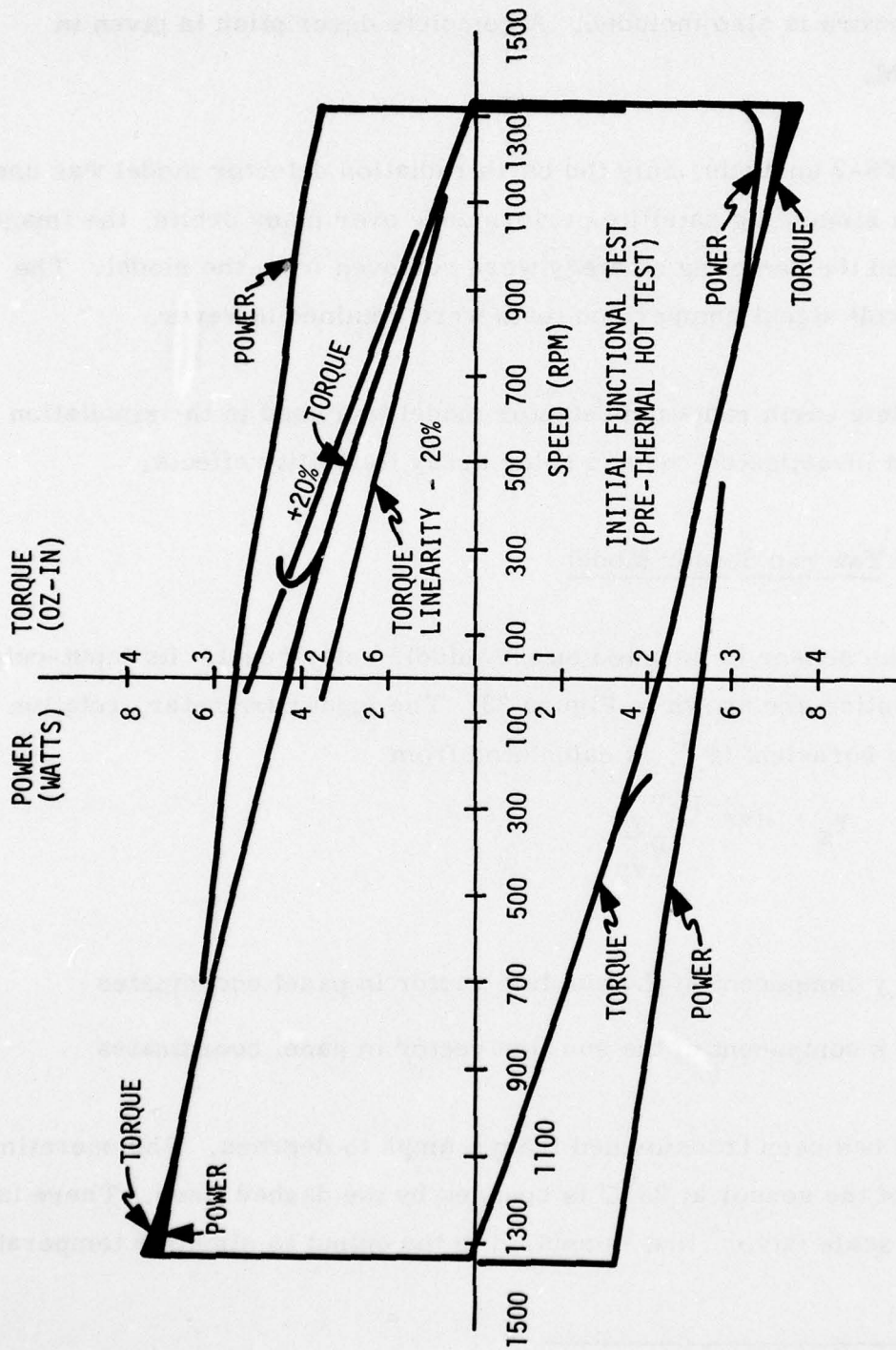


Figure 32. Bendix Test Data

and roll errors is also included. A complete description is given in Appendix M.

For the NTS-2 analysis, only the earth radiation detector model was used. For use in simulating satellite performance over many orbits, the image fade lag and the sampling strategy were removed from the model. The pitch and roll signal comparison tests were retained however.

The complete earth radiation detector model was used in the simulation runs which investigated rod and solar array flexibility effects.

III-C-13. Yaw Sun Sensor Model

The yaw sun sensor is mounted on the middle solar panel. Its input-output characteristics are shown in Figure 33. The input parameter, rotation angle from boresight (ψ_s), is calculated from

$$\psi_s = -\tan^{-1} \frac{V_{yp}}{V_{zp}}$$

where

V_{yp} = y component of the sun line vector in panel coordinates

V_{zp} = z component of the sun line vector in panel coordinates

The output has been transformed from μ amps to degrees. The operating accuracy of the sensor at 25°C is bounded by the dashed lines. There is an additional scale factor* that is applied to the output to simulate temperature

* Scale factor range suggested by Rockwell.

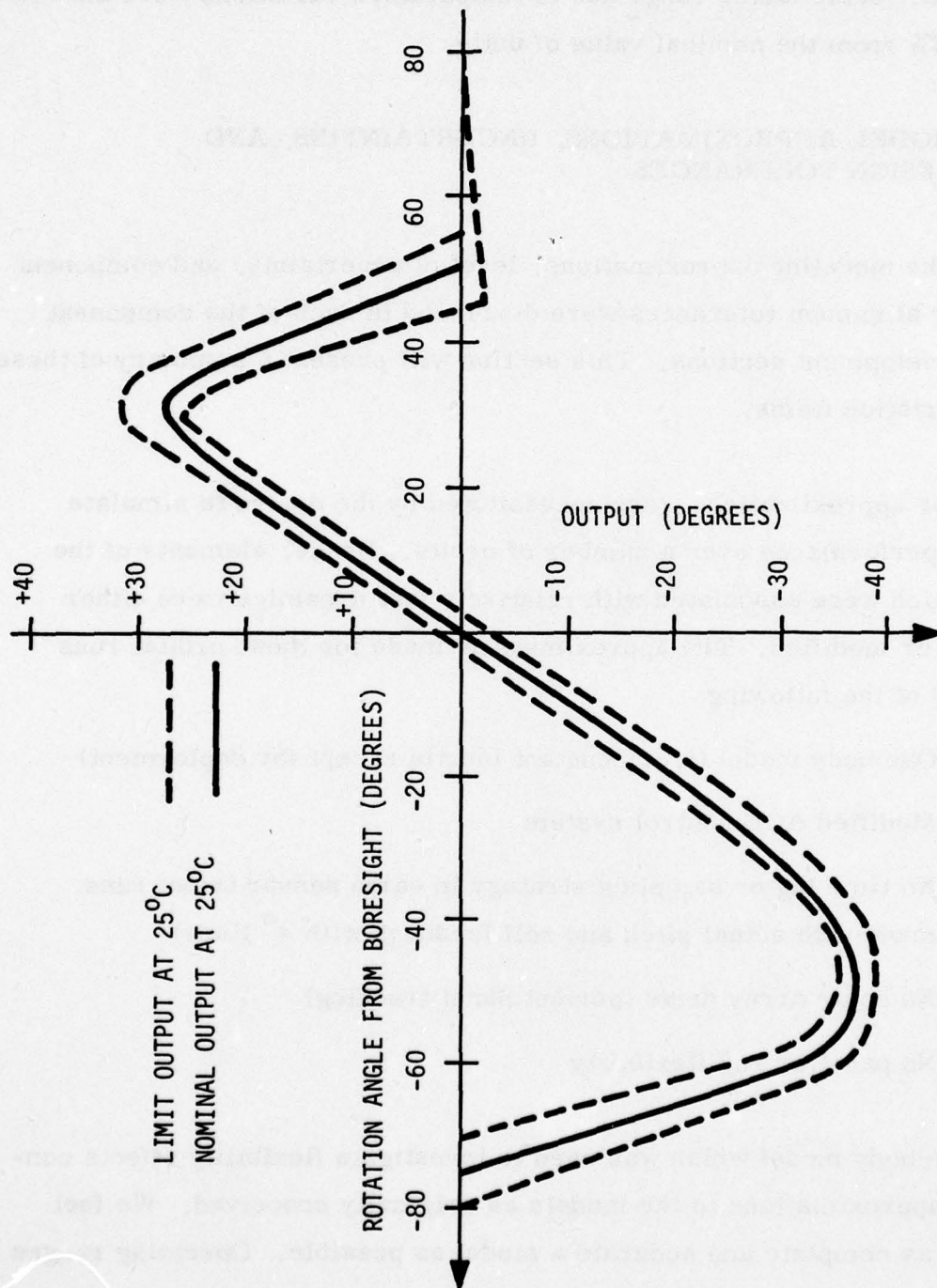


Figure 33. Yaw Sun Sensor Characteristics

variations. Scale factor range due to temperature variations were assumed to be $\pm 50\%$ from the nominal value of unity.

III-D. MODEL APPROXIMATIONS, UNCERTAINTIES, AND DESIGN TOLERANCES

Most of the modeling approximations, level of uncertainty, and component design or alignment tolerances were discussed in each of the component model development sections. This section will present a summary of these model variation items.

The major approximations were necessitated by the desire to simulate satellite performance over a number of orbits. Hence, elements of the model which were associated with relatively fast dynamics were either removed or modified. The approximations made for these orbital runs consisted of the following:

- One body model (i.e. constant inertia except for deployment)
- Modified ACE control system
- No time lag or sampling strategy in earth sensor (most runs made with actual pitch and roll feedback with 4° limit)
- No solar array drive (perfect panel tracking)
- No panel or rod flexibility

The three body model which was used to investigate flexibility effects contains no approximations to the models as originally conceived. We feel that it is as complete and accurate a model as possible. Operating ranges

of pertinent component models will now be summarized. Sources of design tolerances or alignment specs will be noted when applicable.

Nutation Damper

- Damper coefficient 0.01 - 0.015 (NRL Spec)
- Radius of curvature 13 ± 1 ft (NRL Spec)

Magnetic Torques

- Spacecraft dipole moment 500 - 2000 pole-cm

Rod Thermal Curvature

- Min radius of curvature 1100 - 2300 ft

Earth Sensor Errors

- Gross error 0.25° (NRL)
- Fine errors as discussed in Appendix M

Yaw Sun Sensor Errors

- Gain variation $\pm 50\%$ (Rockwell)
- Envelope as discussed previously

Vehicle Mass Properties

- CM misalignment $\Delta x = \Delta y = .05$ in, $\Delta z = .1$ in
- Inertia variation I_{xx}, I_{yy}, I_{zz} 2.2 slug ft² (NRL)
 I_{xy} 0.9 slug ft²

Wheel Misalignment

- 1° in cant and yaw (NRL)

Panel Center of Pressure Shift

- 0.5 inches

Rod Deployment Rates

- ± 10 percent

AKM Jettison Springs

- - Spring constant ± 10 percent

SECTION IV

PRESENTATION OF RESULTS

IV-A. NTS-2 Independent Stability and Control Analysis

- Nutation damper performance
- On orbit performance
- Deployment and acquisition
- Rod and panel flexibility effects

The results of each of these topics will now be analyzed.

IV-A-1. Nutation Damper Performance

Nutation damper performance is a function primarily of satellite inertia ratio, nutation damper dissipation coefficient, and location of the nutation damper with respect to the spin axis. As shown in Appendix D, the motion of the ball in the tube can be modeled with spring damper equations where the frequency of the response is given by

$$\omega_{nd} = \frac{5}{7} \frac{l}{R} \omega_z \quad (28)$$

where

l = distance of nutation damper from center of mass

R = radius of curvature of the tube

ω_z = spin rate

Optimum performance of the nutation damper will occur where the nutation damper frequency is tuned to the nutation frequency which is given by:

$$\omega_n \approx \left(\frac{I_{zz}}{I_{xx}} - 1 \right) \omega_z \quad (29)$$

Equating () and ()

$$\frac{5}{7} \frac{l}{R} \omega_z = \left(\frac{I_{zz}}{I_{xx}} - 1 \right) \omega_z$$

we see that tuning the damper is independent of the spin rate. Although nutation damper satellite dynamics are, at a minimum, fifth order, nutation performance has been expressed as an equivalent first order time constant. Figure 34 presents plots of equivalent time constant versus l/R for different inertia ratios. The time constants were computed using the "energy sink" approximation described in Appendix D. Also shown is the location of the NTS-2 damper at 1.5 feet from the spin axis. At that location, the nutation damper will perform optimally for an inertia ratio of

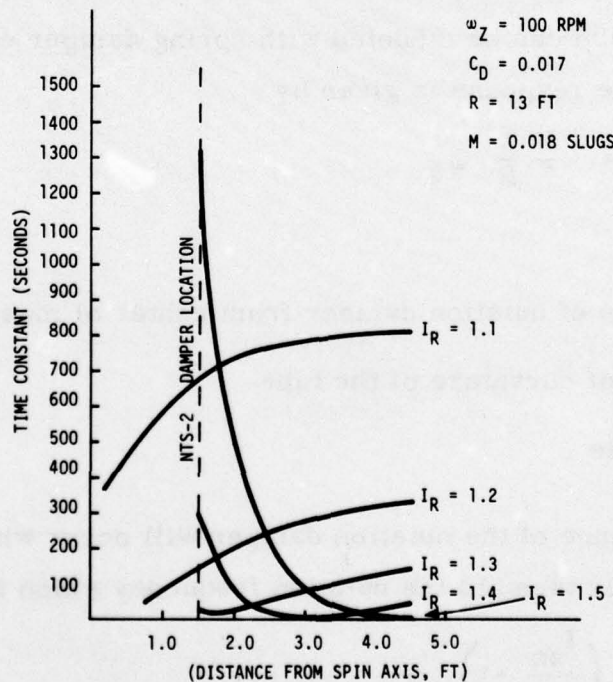


Figure 34. Damper Position

1.3. For inertia ratios greater than 1.3, performance will deteriorate much more rapidly than for those less than 1.3.

For NTS-2, nutation damper performance was investigated at three mission time points: 1) post separation, 2) post AKM burn, and 3) post AKM jettison. This represents an inertia ratio spread of 1.17 at post separation to 1.54 after the AKM has been jettisoned. Nutation damper performance was simulated at these three time points under nominal and worst case conditions for spin rates of 90 RPM (nominal), 100 RPM (maximum expected), and 40 RPM (minimum allowable). The worst case conditions chosen were:

- o Damper dissipate coefficient -0.01
- o Inertia ratios $\Delta I_{xx} = \Delta I_{yy} = \Delta I_{zz} = \pm 2.2 \text{ slug ft}^2$
- o Cm misalignment $\Delta x = \Delta y = 0.1'' \quad \Delta z = 0.2''$

The sign on the inertia ratio variation was chosen such that the time constant variation was largest as estimated from Figure 34. The sign on was chosen to increase the distance of the center of mass of the nutation damper from the center of mass of the satellite.

Nutation damper performance in terms of nutation angle time history for the post separation configuration, and nominal conditions at 90 RPM is shown in Figure 35. As shown, the estimated equivalent time constant is approximately 300 seconds. (Note: as discussed in Appendix D, the nutation damper model assumed perfect elastic collisions when the ball hit the end of the tube. The response shown in Figure 35 was for a model which assumed the other extreme, an inelastic collision. A comparison of per-

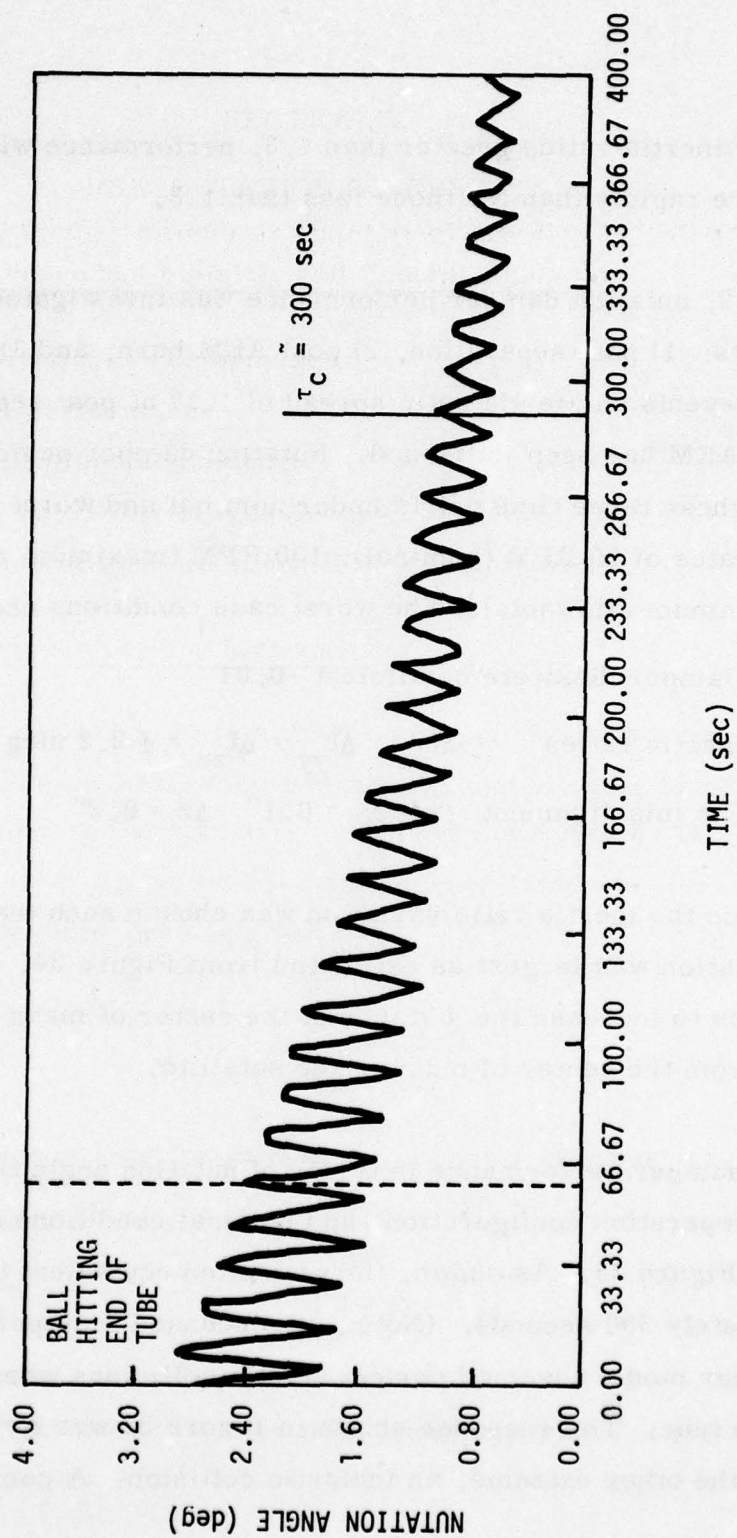


Figure 35. Nutation Damper Run Launch 90 RPM,
3 Deg Nutation Angle Inelastic

formance will be discussed shortly.) The results of nutation damper performance evaluation at the remaining mission time points is given in Figures 36 through 38 and in Tables 10 through 12. These conditions were simulated at the Air Force Academy, where it was not possible to generate plots of the form shown in Figure 35. Hence only the numerical results are given.

Equivalent time constants estimated using two other techniques are also shown. τ_{es} is the predicted time constant using "energy sink" approximations. τ_l is the time constant computed from eigenvalues generated at selected points in the simulation via a numerical linearization/root fender procedure. The latter values were used as a check on simulation efficacy. Time constants calculated using the energy sink approximations generally predict pessimistic performance particularly at the larger inertia ratios.

Since there is no defined performance specification applied to the nutation damper, the results shown in Figures 36 through 38 and Tables 10 through 12 do not in themselves indicate satisfactory or unsatisfactory performance. That evaluation is a function of mission time line constraints. To aid in making those evaluations, a summary of the results is as follows:

	Time Constant (sec)	
	Nom	Worst Case
Post Separation	300	700
Post AKM Burn	150	850
Post AKM Jettison	1100	5000

In addition, the ball does hit the end of the tube for initial nutation angles of 3° or more (post separation). This does not appear to have a significant effect on damping whether the tube collision is assumed to be elastic or inelastic. The elastic collision model, which was used in all simulation

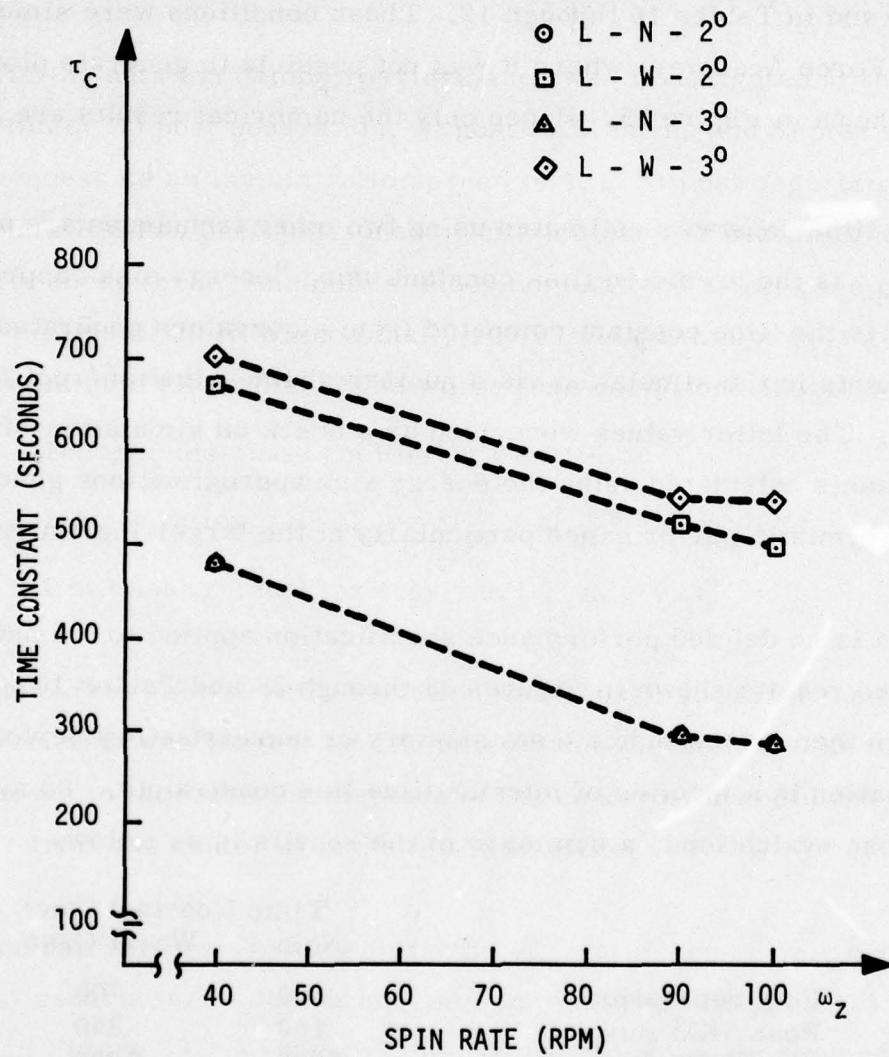


Figure 36. Damper Performance, Post Separation

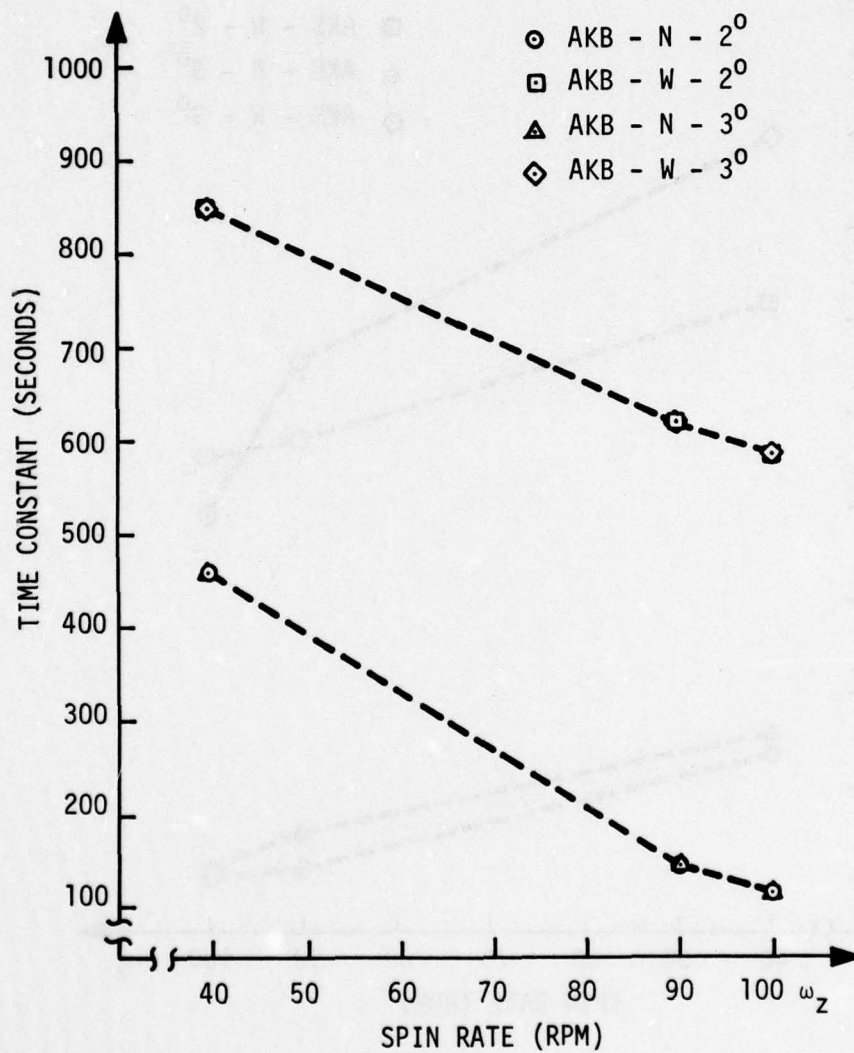


Figure 37. Damper Performance, Post AKM Burn

AD-A052 633 HONEYWELL INC MINNEAPOLIS MINN SYSTEMS AND RESEARCH --ETC F/6 22/2
NTS-2 INDEPENDENT STABILITY AND CONTROL ANALYSIS. VOLUME I. TEC--ETC(U)
MAR 77 R E POPE, M D WARD, S M SCHWANTES

HONEYWELL INC MINNEAPOLIS MINN SYSTEMS AND RESEARCH --ETC F/G 22/2
NTS-2 INDEPENDENT STABILITY AND CONTROL ANALYSIS. VOLUME I. TEC--ETC(U)
MAR 77 R E POPE, M D WARD, S M SCHWANTES

77SRC17-VOL-1

NL

2 OF 4
AD
A052633

Sub	1	2	3	4	5	6	7	8	9	10	11	12	13	14	15	16	17	18	19	20	21	22	23	24	25	26	27	28	29	30	31	32	33	34	35	36	37	38	39	40	41	42	43	44	45	46	47	48	49	50	51	52	53	54	55	56	57	58	59	60	61	62	63	64	65	66	67	68	69	70	71	72	73	74	75	76	77	78	79	80	81	82	83	84	85	86	87	88	89	90	91	92	93	94	95	96	97	98	99	100
Sub	1	2	3	4	5	6	7	8	9	10	11	12	13	14	15	16	17	18	19	20	21	22	23	24	25	26	27	28	29	30	31	32	33	34	35	36	37	38	39	40	41	42	43	44	45	46	47	48	49	50	51	52	53	54	55	56	57	58	59	60	61	62	63	64	65	66	67	68	69	70	71	72	73	74	75	76	77	78	79	80	81	82	83	84	85	86	87	88	89	90	91	92	93	94	95	96	97	98	99	100

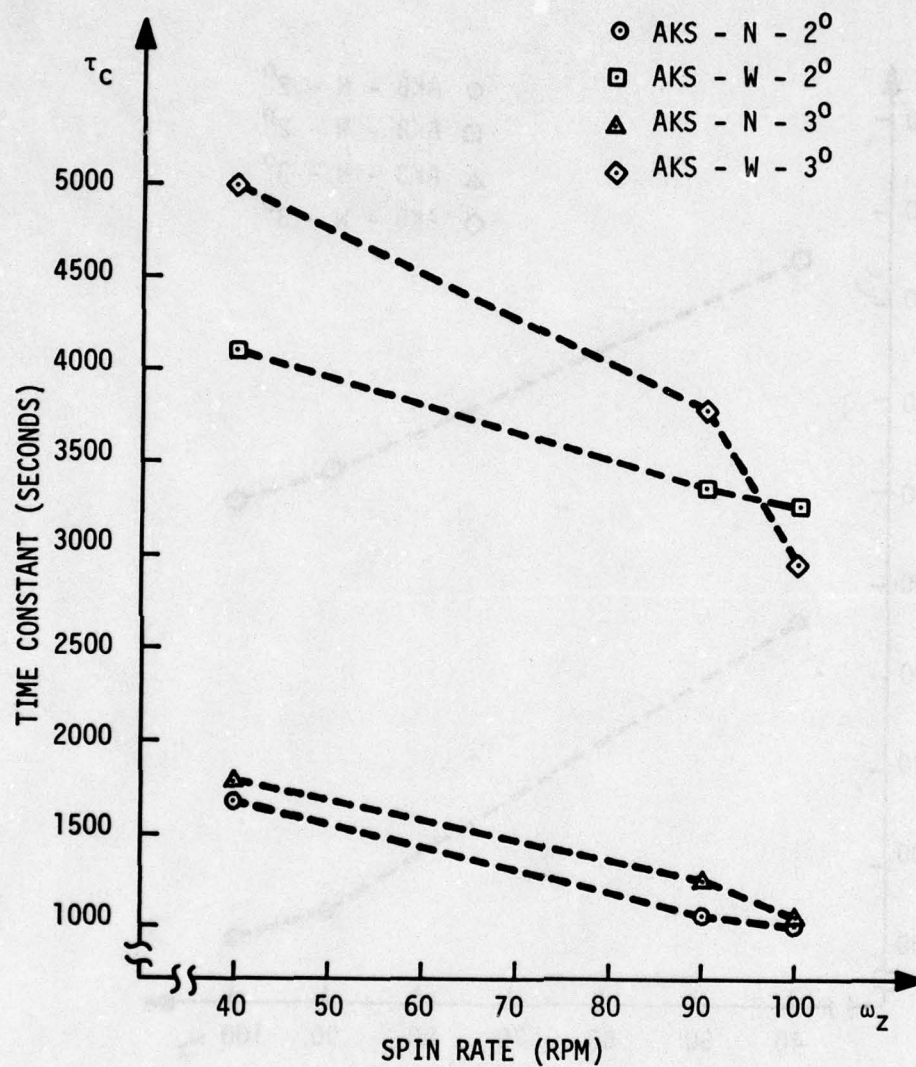


Figure 38. Damper Performance, Post AKM Jettison

Table 10. Nutation Damper Performance--Launch

ω_z (RPM)	η_{IC} (DEG)	τ_p (SEC)	τ_L (SEC)	τ_{ES} (SEC)	Ball Hits End of Tube?
40	2	480	-	349	No
90	2	300	-	304	No
100	2	290	-	302	No
40	3	425	400	349	Yes
90	3	300	-	304	Yes (80)
100	3	300	-	302	Yes (80)
90	3	296	-	304	Yes (60)

NOMINAL

INERTIA RATIO = 1.17

inelastic collision \rightarrow

40	2	670	670	857	No
90	2	525	570	835	Yes
100	2	500	-	834	Yes
40	3	700	670	857	Yes
90	3	600	-	835	Yes
100	3	600	-	834	Yes

WORST CASE

INERTIA RATIO = 1.13

Table 11. Nutation Damper Performance--Post AKM Burn

ω_z (RPM)	η_{IC} (DEG)	τ_p (SEC)	τ_L (SEC)	τ_{ES} (SEC)	Ball Hits End of Tube?
40	2	460	480	319	No
90	2	150	170	205	No
100	2	120	150	200	No
40	3	460	490	319	No
90	3	150	170	205	No
100	3	120	150	200	No

NOMINAL

INERTIA RATIO = 1.38

40	2	850	820	1169	No
90	2	620	570	1062	No
100	2	590	500	1057	No
40	3	820	720	1169	No
90	3	620	520	1062	No
100	3	590		1057	No

WORST CASE

INERTIA RATIO = 1.45

Table 12. Nutation Damper Performance--Post AKM Jettison

ω_z (RPM)	η_{IC} (DEG)	τ_p (SEC)	τ_L (SEC)	τ_{ES} (SEC)	Ball Hits End of Tube?
40	2	1700	-	2413	No
90	2	1100	-	2181	No
100	2	1050	-	2170	No
40	3	1800	-	2413	No
90	3	1300	-	2181	No
100	3	1100	-	2170	No

NOMINAL

INERTIA RATIO = 1.54

40	2	4100	-	8270	No
90	2	3400	-	8026	No
100	2	3300	-	8015	No
40	3	5000	-	8270	No
90	3	3800	-	8026	No
100	2	3000	-	8015	No

WORST CASE

INERTIA RATIO = 1.62

runs, was verified to be worst case. Although the difference in equivalent time constant between the elastic and inelastic models for identical runs was small, the ball hits the end of the tube twenty seconds longer into the run with the elastic model than with the inelastic model.

IV-A-2. AKM Jettison

In order to determine what effect jettisoning the AKM would have on nutation angle, the jettison was simulated using the worst case disturbance torques selected from Table 9. These were

$$\Delta T_x = -1.834$$

$$\Delta T_y = -3.178$$

These torques were applied over .075 seconds, that is, the time it takes the springs to expand to their uncompressed length. Time varying off nominal inertia properties were also included in the simulation. The results are shown in Figure 39. As can be seen, peak nutation angle due to the AKM jettison is approximately $.006^\circ$, an insignificant amount. It is concluded that the AKM jettison should produce no undesirable effects.

IV-B-1. On Orbit Stability Analysis

The closed loop control system is a combination of active and passive control. The passive control moment producers are the pitch and roll gravity gradient torques. The active control moment producers are four reaction wheels aligned to give decoupled three axis control. As discussed in the modeling section, the ACE system commands wheel momentum proportional

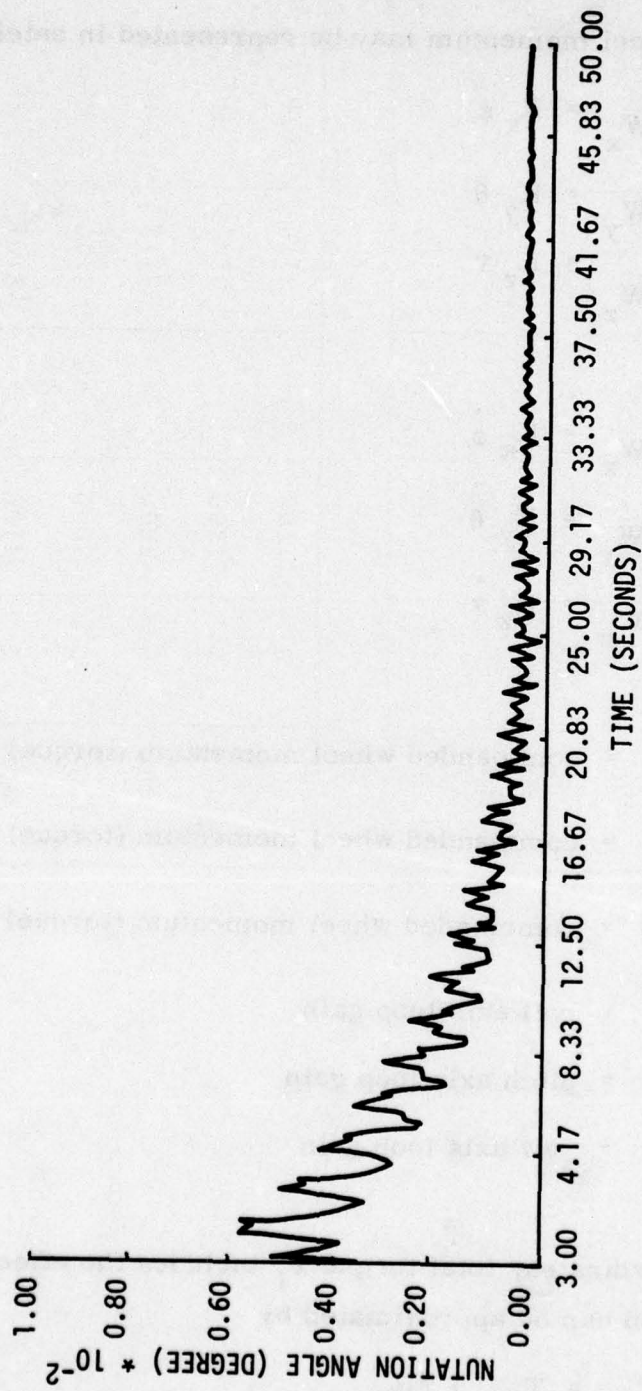


Figure 39. Nutation Damper Run AKM Jettison

to attitude error, or equivalently, wheel torque proportional to attitude rate. Commanded wheel momentum may be represented in satellite axes as follows:

$$\begin{aligned} H_{W_x} &= K_x \dot{\phi} \\ H_{W_y} &= K_y \dot{\theta} \\ H_{W_z} &= K_z \dot{\psi} \end{aligned} \quad (30)$$

and similarly

$$\begin{aligned} T_{W_x} &= K_x \ddot{\phi} \\ T_{W_y} &= K_y \ddot{\theta} \\ T_{W_z} &= K_z \ddot{\psi} \end{aligned}$$

where

$$\begin{aligned} H_{W_x}(T_{W_x}) &= \text{commanded wheel momentum (torque) in roll axis} \\ H_{W_y}(T_{W_y}) &= \text{commanded wheel momentum (torque) in pitch axis} \\ H_{W_z}(T_{W_z}) &= \text{commanded wheel momentum (torque) in yaw axis} \\ K_x &= \text{roll axis loop gain} \\ K_y &= \text{pitch axis loop gain} \\ K_z &= \text{yaw axis loop gain} \end{aligned}$$

In inertial coordinates, total torque T_I includes the effects of satellite orbital rate and can be approximated by

$$T_{I_x} = T_{W_x} + \eta H_{W_z} \quad (31)$$

$$\begin{aligned} T_{I_y} &= T_{W_y} \\ T_{I_z} &= T_{W_z} - \dot{\eta} H_{W_x} \end{aligned}$$

Substituting equations H_W and T_W into T_I , we get

$$\begin{aligned} T_{I_x} &= K_x \dot{\phi} + \dot{\eta} K_y \psi \\ T_{I_y} &= K_y \dot{\theta} \\ T_{I_z} &= K_z \dot{\psi} - \dot{\eta} K_x \phi \end{aligned} \quad (32)$$

For closed loop dynamics this equation is combined with the solid sphere inertial tensor equation to form

$$\begin{aligned} I_{xx} \ddot{\phi} - K_x \dot{\phi} - 4\dot{\eta}^2 (I_{zz} - I_{yy}) \phi + (I_{zz} + I_{xx} - I_{yy}) \dot{\eta} \dot{\psi} - \dot{\eta} K_z \psi &= 0 \\ I_{yy} \ddot{\theta} - K_y \dot{\theta} + 3\dot{\eta}^2 (I_{xx} - I_{zz}) \theta &= 0 \\ I_{zz} \ddot{\psi} - K_z \dot{\psi} + \dot{\eta}^2 (I_{yy} - I_{xx}) \psi - (I_{yy} - I_{xx} - I_{zz}) \dot{\eta} \dot{\phi} + \dot{\eta} K_x \phi &= 0 \end{aligned} \quad (33)$$

The nominal values of the constant in the above equation are given in Table 13.

Table 13. Satellite Equation Constants

I_{xy}	1998 slug ft ²
I_{yy}	1914 slug ft ²
I_{zz}	205 slug ft ²
K_x	3.75 ft-lbs/rad
K_y	3.75 ft-lbs/rad
K_z	.4 ft-lbs/rad
η	.000145 rad/sec

The nominal eigenvalues of the satellite have been listed previously. Eigenvalue migration for the three axes is shown in Figure 40 as a function of loop gain. Since roll and yaw are coupled the loci are for each axis with the other axis closed at the nominal loop gain.

In the pitch axis, the roots migrate from the open-wheel loop, neutrally-stable, gravity-gradient, oscillatory pair to a pair of real roots at $-.002$ and $-.000031$. These roots result from a loop gain that is four times larger than that required for critical damping.

The roll and yaw loops are characterized by a low frequency poorly damped oscillatory pair which is due to the coupling in the control loop through the orbital rate term as shown in the above equation. This coupling is relied upon for stability. This can be seen more clearly if we look at the s plane representation of the solid sphere inertial tensor equation in matrix form as shown in Figure 41. The characteristic equation of the system shown in Figure 41 may be found by forming the determinant of $G(s)$. The characteristic equation will have the form

$$s^4 + a_3 s^3 + a_2 s^2 + a_1 s + a_0 = 0 \quad (34)$$

The importance of the roll yaw control coupling can be seen by looking at a_0 which is

$$a_0 = \left(4\dot{\eta}^2 \frac{(I_{yy} - I_{zz})}{I_{xx}} \right) \left(\dot{\eta}^2 \frac{(I_{yy} - I_{xx})}{I_{zz}} \right) + \left(\frac{K_z \dot{\eta}}{I_{xx}} \right) \left(\frac{K_x \dot{\eta}}{I_{zz}} \right) \quad (35)$$

The first term of this equation is independent of reaction wheel control. The second term is a direct result of the coupling in roll and yaw wheel

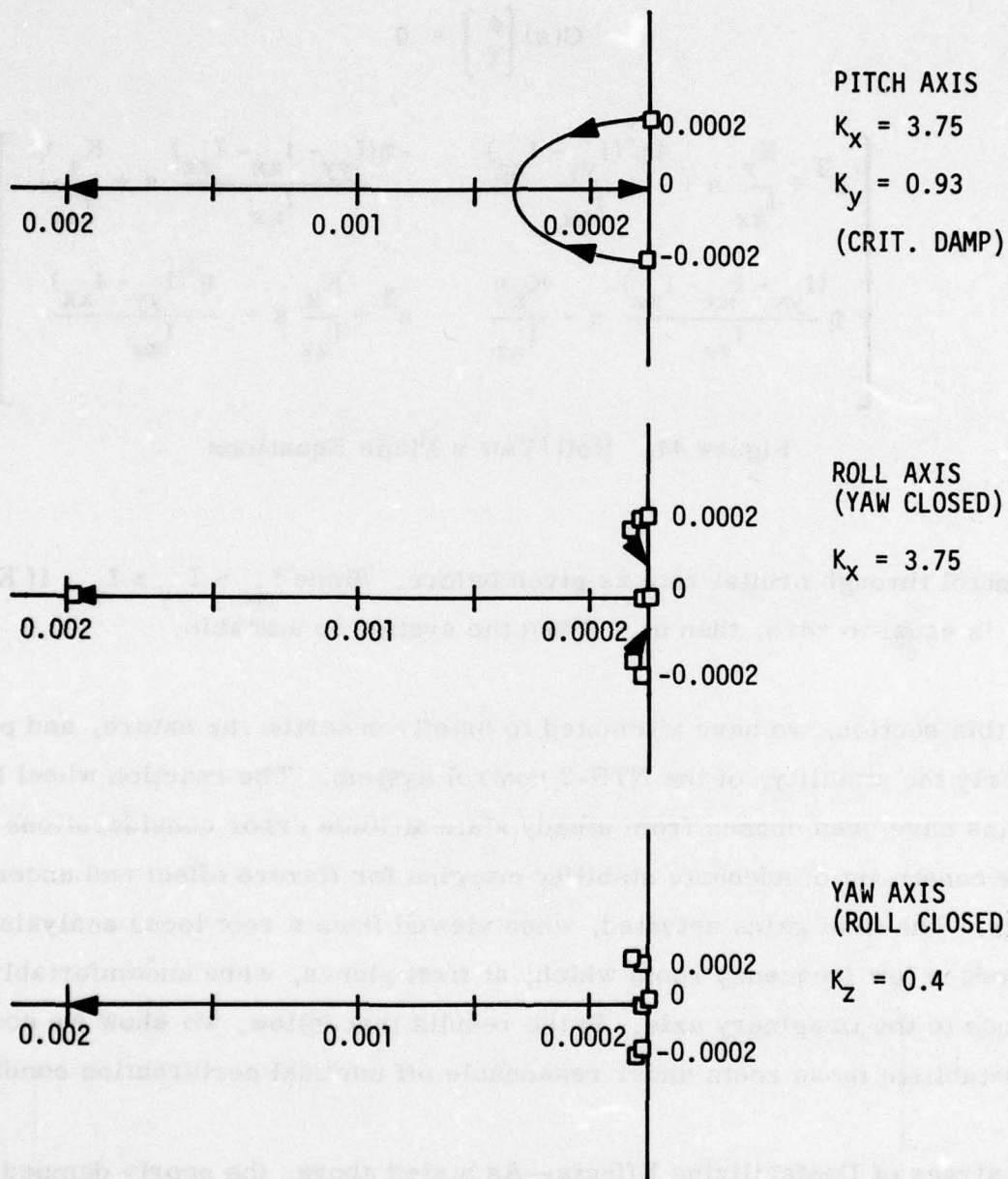


Figure 40. Root Migration as a Function of Loop Gain

$$G(s) \begin{bmatrix} \phi \\ \psi \end{bmatrix} = 0$$

$$\begin{bmatrix} s^2 + \frac{K_x}{I_{xx}} s + \frac{4\eta^2(I_{yy} - I_{zz})}{I_{xx}} & -\frac{\eta(I_{yy} - I_{xx} - I_{zz})}{I_{xx}} s + \frac{K_z \eta}{I_{xx}} \\ \eta \frac{(I_{yy} - I_{xx} - I_{zz})}{I_{zz}} s - \frac{K_x \eta}{I_{zz}} & s^2 + \frac{K_z}{I_{zz}} s + \frac{\eta^2(I_{yy} - I_{xx})}{I_{zz}} \end{bmatrix}$$

Figure 41. Roll/Yaw s Plane Equations

control through orbital rate as given before. Since $I_{xx} > I_{yy} > I_{zz}$, if K_x or K_z is equal to zero, then $a_0 < 0$ and the system is unstable.

In this section, we have attempted to briefly describe the nature, and particularly the stability, of the NTS-2 control system. The reaction wheel loop gains have been chosen from steady state attitude error considerations under the constraint of adequate stability margins for flexure effect and uncertainties. The final gains selected, when viewed from a root locus analysis, produce low frequency roots which, at first glance, were uncomfortably close to the imaginary axis. In the results that follow, we show we could not destabilize those roots under reasonable off nominal perturbation conditions.

Analyses of Destabilizing Effects--As stated above, the poorly damped nature of the pair of oscillatory roots in the roll/yaw equations caused concern. We tried to establish whether or not there were destabilizing effects that could force those roots into the right half plane. The destabilizing effects that were investigated were

- o Yaw sun sensor errors
- o Yaw solar torques
- o Magnetic torques
- o Wheel misalignments

We will now discuss the results of that investigation.

Yaw Sun Sensor Errors--The control equations described previously assumed that the yaw sun sensor sensed pure yaw rotations. There are only two points in each orbit where this is the case, assuming perfect sun tracking on array pitch control. Since the yaw sun sensor is mounted on the solar array and measures yaw as the angle between the sun line and the array rotation axis in the plane defined by the array rotation axis and the array normal, the sensed yaw angle is a function of array angle with respect to the satellite body. The sensor senses pure yaw only when the array normal is perpendicular to the satellite yaw axis. A derivation of what the sensor sees for the case of the array normal being tilted 45° to the yaw axis now follows.

The sensed yaw angle is given by

$$\psi_s = \tan^{-1} \frac{V_{yp}}{V_{zp}} \quad (36)$$

where

V_{yp} = y (array axis of rotation) component of sun line in panel coordinates

$$= E_{21} R_x + E_{22} R_y + E_{23} R_z$$

$$\begin{aligned}
 V_{yp} &= z \text{ component (array normal) of sun line in panel coordinates} \\
 &= \sin \theta_p V_{xB} + \cos \theta_p V_{zB}
 \end{aligned} \tag{37}$$

where

E_{ij} ($i=1,3$ $j=1,3$) = components of inertial to body transformation

R_x, R_y, R_z = sun line in inertial coordinates

V_{xB} = x component of sun line in body coordinates

V_{zB} = z component of sun line in body coordinates

To force $\theta_p = 45^\circ$ $R_x = -.707$, $R_y = 0$, $R_z = -.707$. The sun line in panel coordinates then becomes

$$V_{yp} = -(.707) (E_{21} + E_{23}) \tag{38}$$

$$V_{zp} = .707(-.707) (E_{11} + E_{13} - E_{31} - E_{33})$$

To first order,

$$\psi_s = \tan^{-1} \frac{V_{yp}}{V_{zp}} \approx \frac{V_{yp}}{V_{zp}} \tag{39}$$

or

$$\psi_s = - \frac{(+ \cos \psi \sin \theta \sin \phi - \sin \psi \cos \phi + \cos \theta \sin \phi)}{.707 (\cos \theta \cos \psi - \sin \theta + \cos \psi \sin \theta \cos \phi + \sin \psi \sin \phi + \cos \theta \cos \phi)}$$

Assuming small angle approximation

$$\psi_s = \frac{1}{1.414} (\psi - \phi) \tag{40}$$

It is seen from this equation that when the solar array is tilted 45° with respect to the satellite yaw axis, the sun sensor senses an equal combination

of roll and yaw. At other array angles the sensor will sense different proportions of yaw and roll. This effect was investigated by modeling the sensor output ψ_s as

$$\psi_s = a\psi + b\phi \quad (41)$$

where the coefficients a and b represent the effect of array rotation angle. Substituting this equation for ψ in the solid sphere inertial tensor equation and ignoring the pitch component, we obtain

$$\begin{aligned} T_{I_x} &= K_x \phi + \eta K_z (a\psi + b\phi) \\ T_{I_z} &= K_z (a\psi + b\phi) - \eta K_x \phi \end{aligned} \quad (42)$$

The $G(s)$ matrix which includes this effect is shown in Figure 42.

$$\begin{bmatrix} s^2 + \frac{K_x}{I_{xx}} & s + 4\dot{\eta}^2 \frac{(I_{yy} - I_{zz})}{I_{xx}} + \frac{K_z b \dot{\eta}}{I_{xx}} & -\dot{\eta} \frac{(I_{yy} - I_{xx} - I_{zz})}{I_{xx}} s + \frac{K_z a \dot{\eta}}{I_{xx}} \\ \left(\dot{\eta} \frac{(I_{yy} - I_{xx} - I_{zz})}{I_{zz}} + \frac{K_z b}{I_{zz}} \right) s - \frac{K_x \phi}{I_{zz}} & s^2 + \frac{K_z a s}{I_{zz}} + \dot{\eta}^2 \frac{(I_{yy} - I_{xx})}{I_{zz}} \end{bmatrix}$$

Figure 42. $G(s)$ with Roll/Yaw Sensor Feedback

We again form the characteristic equation to look at the effect of the yaw sensor feedback on stability. It is particularly interesting to look at the a_1 coefficient.

$$\begin{aligned}
a_1 &= \frac{K_z a}{I_{zz}} \left(4\dot{\eta}^2 \frac{(I_{yy} - I_{zz})}{I_{xx}} + \frac{K_z b \dot{\eta}}{I_{xx}} \right) + \frac{K_x}{I_{xx}} \dot{\eta}^2 \frac{(I_{yy} - I_{xx})}{I_{zz}} \quad (43) \\
&\quad - \frac{K_z a \dot{\eta}}{I_{xx}} \left(\dot{\eta} \frac{(I_{yy} - I_{xx} - I_{zz})}{I_{zz}} + \frac{K_z b}{I_{zz}} \right) - \frac{K_x \dot{\eta}}{I_{zz}} \frac{(I_{yy} - I_{xx} - I_{zz})}{I_{xx}} \\
&= \frac{K_z a}{I_{zz}} \left(4\dot{\eta}^2 \frac{(I_{yy} - I_{zz})}{I_{xx}} \right) + \frac{K_x}{I_{xx}} \left(\dot{\eta}^2 \frac{(I_{yy} - I_{xx})}{I_{zz}} \right) \\
&\quad - \frac{K_z a \dot{\eta}}{I_{xx}} \left(\dot{\eta} \frac{(I_{yy} - I_{xx} - I_{zz})}{I_{zz}} \right) - \frac{K_x \dot{\eta}}{I_{zz}} \frac{(I_{yy} - I_{xx} - I_{zz})}{I_{xx}}
\end{aligned}$$

As can be seen here, the two terms which include the effects of the component of yaw sensor feedback cancel out. Hence the only effect of the coupled yaw sensor output is a factor of a gain reduction.

Although the same cancellation effect does not occur in the other coefficients, it is the rate coefficient that has the most impact on the location of the oscillatory pair. Table 14 shows the effect of varying b on the location of the oscillatory pair. No effect can be seen.

Table 14. Effect of Varying Yaw Sensor Output on Root Migration

a	b	Oscillatory Damping Ratio	Pair Frequency
1.0	0	.1033	.0001465
1.0	0.2	.1033	.0001465
1.0	1.0	.1033	.0001465

The effect of gain reduction can be seen in the root locus of Figure 39. The major effects is on the location of the real root. There is little impact on the location of the oscillatory pair.

Yaw Solar Torques--The most significant effect of solar pressure is a yaw moment which is produced because of the offset of gravity gradient rods from the center of mass of the satellite. This is shown schematically in Figure 43. The rods are normal to the paper. As can be seen, if the x axis of the satellite is perfectly aligned with the sun line, there is no torque. However, as the vehicle yaws there is a destabilizing yaw torque created due to the offset of the rods on the x axis. This can be modeled for stability analysis purposes as follows:

The force on the rods is approximately given by

$$F = (1 + \rho) PA \quad (44)$$

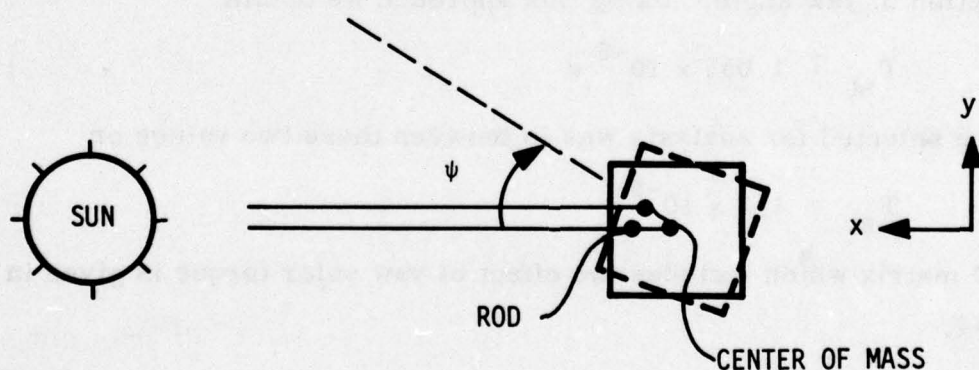


Figure 43. Yaw Solar Torques

where

$$\rho = \text{solar reflectivity constant} = .85$$

$$p = \text{solar radiation pressure constant} = 1 \times 10^{-7} \text{ lbs/ft}^2$$

$$A = \text{area of rods} = 2 \times 60 \times \frac{5}{12} = 5 \text{ ft}^2$$

The torque generated, T_{st} , is then

$$T_{st} = F \times l \sin \psi \quad (45)$$

where l is the rod offset = 19.75 in. \approx 1.65 ft.

Assuming small yaw angles

$$\begin{aligned} T_{st} &= F \times l \psi \\ &= 9.25 \times 10^{-7} \times 1.65 \psi \\ &= 1.5263 \times 10^{-6} \psi \end{aligned} \quad (46)$$

This value was also computed in the program by computing yaw solar torques as a function of yaw angle. Using this approach we obtain

$$T_{st} \approx 1.055 \times 10^{-6} \psi \quad (47)$$

The value selected for analysis was in between these two values or

$$T_{st} = 1.3 \times 10^{-6} \psi \quad (48)$$

The $G(s)$ matrix which includes the effect of yaw solar torque is given in Figure 44.

Root loci were then computed as a function of yaw solar torque magnitude for different levels of control system gains. These results are shown in Figure 45a through 45d.

$$\begin{aligned}
 s^2 + \frac{K_x s}{I_{xx}} + 4\eta^2 \frac{(I_{yy} - I_{zz})}{I_{xx}} - \eta \frac{(I_{yy} - I_{xx} - I_{zz})}{I_{xx}} s + \frac{K_z \eta}{I_{xx}} & \quad (49) \\
 \eta \frac{(I_{yy} - I_{xx} - I_{zz})}{I_{zz}} s - \frac{K_x \eta}{I_{zz}} & \quad s^2 + \frac{K_z s}{I_{zz}} + \eta^2 \frac{(I_{yy} - I_{xx})}{I_{zz}} - \frac{T_{st}}{I_{zz}}
 \end{aligned}$$

Figure 44. $G(s)$ with Yaw Solar Torque Effect

As seen in Figure 45a for nominal yaw and roll control system gains, a solar torque 10 times larger than nominal would be needed to cause the oscillatory pair to move into the right half plane. If the yaw gain was halved, the solar torque would have to be 2 to 4 times larger than nominal. This is shown in Figure 45b. Halving the roll gain with the yaw gain halved increases the margin to 10 times nominal as shown in Figure 45c. Finally, doubling the roll gain with nominal yaw gain would require a solar torque 4 times nominal to produce an instability.

In summary, the yaw torque due to solar pressure on the rods is insufficient to generate an instability. The magnitude of the variables in the force equation cannot be varied realistically to produce no more than a 20 percent increase in solar force which is far below the 200 percent increase necessary for instability.

A solar force generated rolling moment due to yaw is also present due to the imbalance between the upper and lower rods; however, it is two orders of magnitude less than the yaw moment and consequently insignificant.

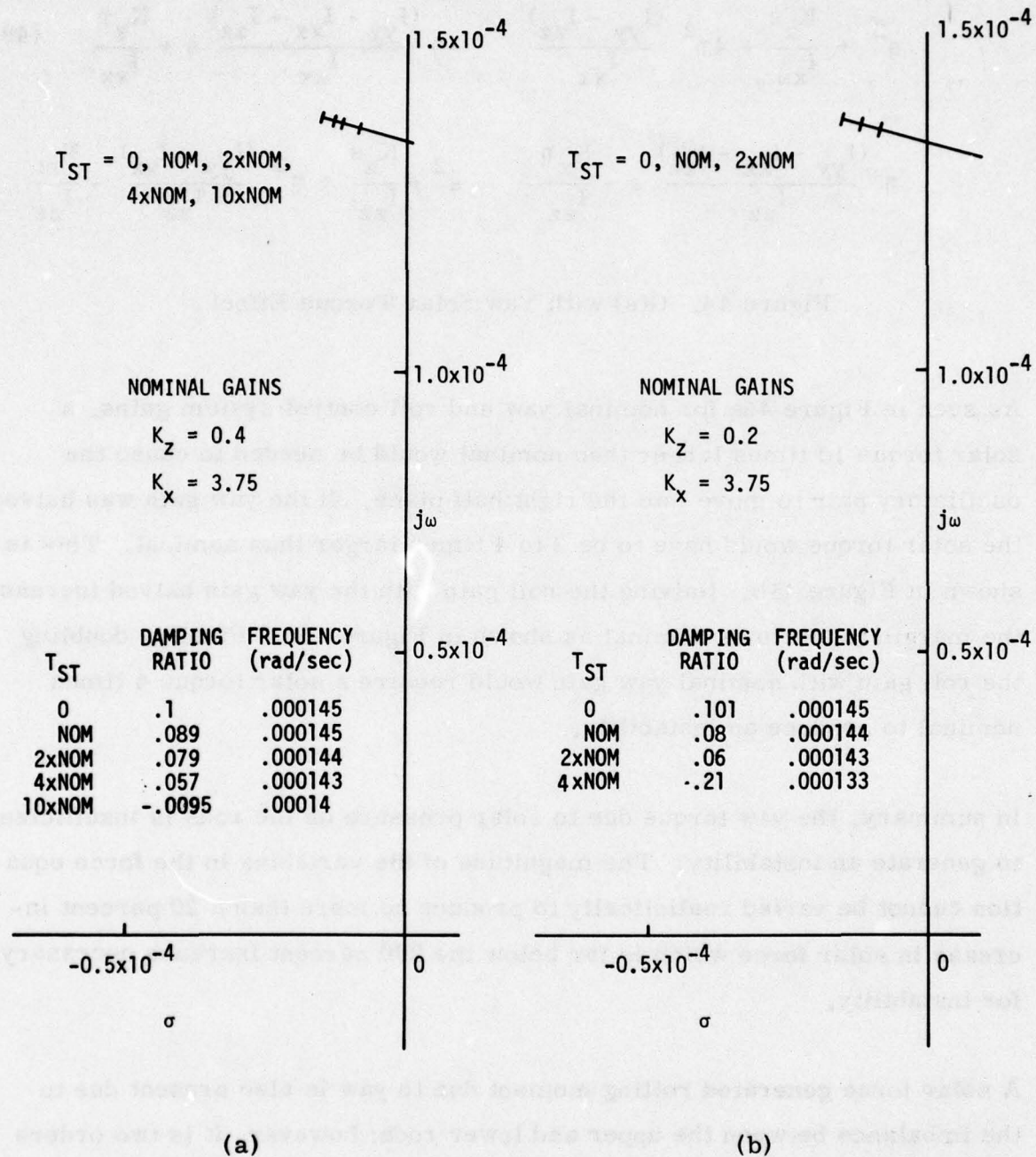


Figure 45. Root Migration as a Function of Yaw Solar Torque

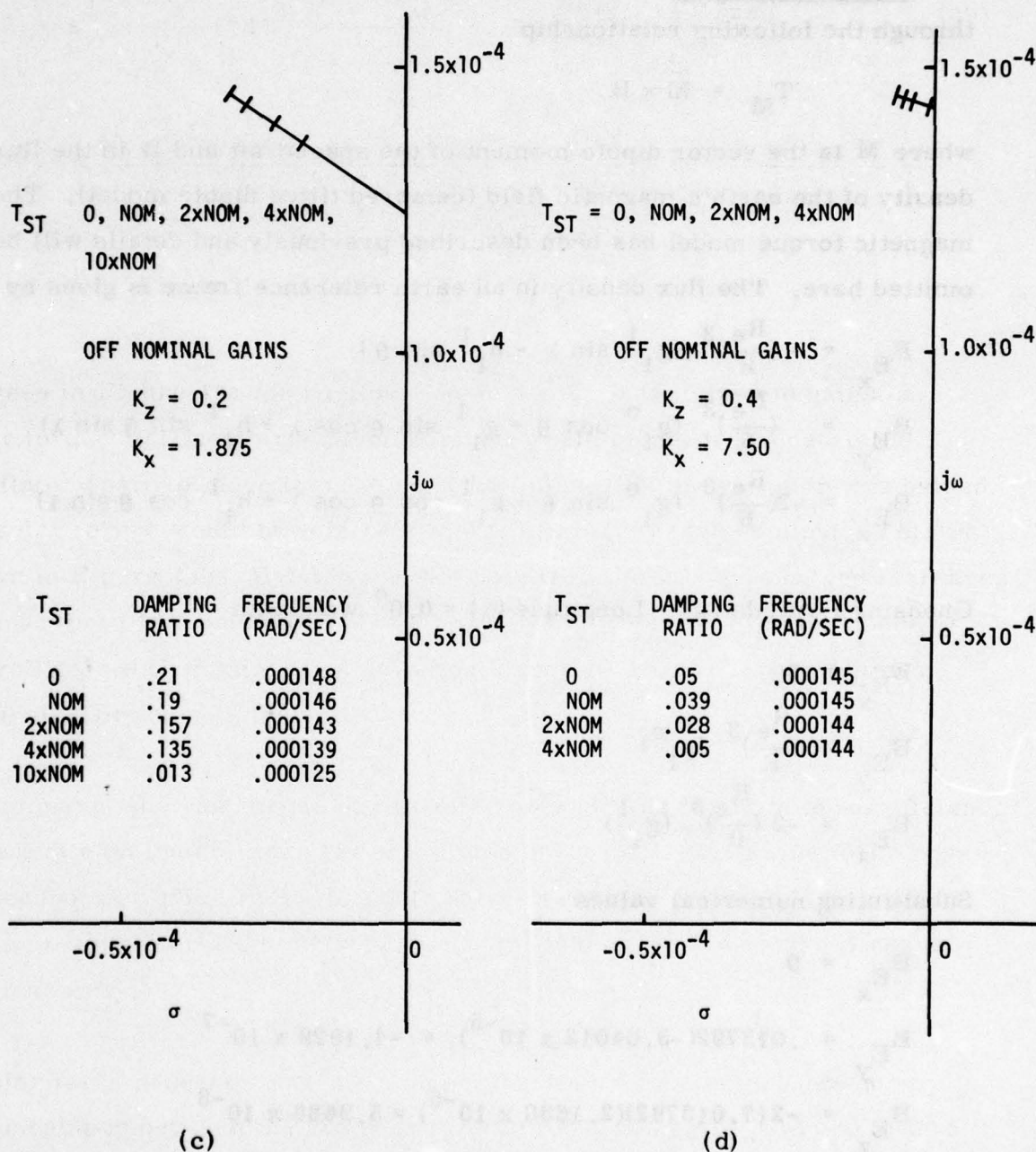


Figure 45. Root Migration as a Function of Yaw Solar Torque (concluded)

Magnetic Torques--Magnetic torques are generated on the spacecraft through the following relationship

$$\mathbf{T}_M = \tilde{\mathbf{M}} \times \mathbf{B} \quad (50)$$

where \mathbf{M} is the vector dipole moment of the spacecraft and \mathbf{B} is the flux density of the earth's magnetic field (centered tilted dipole model). The magnetic torque model has been described previously and details will be omitted here. The flux density in an earth reference frame is given by

$$\begin{aligned} B_{E_x} &= -\left(\frac{R_e}{R}\right)^3 (g_1^1 \sin \lambda - h_1^1 \sin \theta) \\ B_{E_y} &= \left(\frac{R_e}{R}\right)^3 (g_1^0 \cos \theta + g_1^1 \sin \theta \cos \lambda + h_1^1 \sin \theta \sin \lambda) \\ B_{E_z} &= -2\left(\frac{R_e}{R}\right)^3 (g_1^0 \sin \theta + g_1^1 \cos \theta \cos \lambda + h_1^1 \cos \theta \sin \lambda) \end{aligned} \quad (51)$$

Choosing Latitude (θ) = Longitude (λ) = 0.0° we obtain

$$\begin{aligned} B_{E_x} &= 0 \\ B_{E_y} &= \left(\frac{R_e}{R}\right)^3 (g_1^0) \\ B_{E_z} &= -2\left(\frac{R_e}{R}\right)^3 (g_1^1) \end{aligned} \quad (52)$$

Substituting numerical values

$$B_{E_x} = 0 \quad (53)$$

$$B_{E_y} = .013792(-3.04012 \times 10^{-5}) = -4.1929 \times 10^{-7} \quad (54)$$

$$B_{E_z} = -2(7.013792)(2.1638 \times 10^{-6}) = 5.9686 \times 10^{-8} \quad (55)$$

Now transforming from earth reference frame to the local vertical and from the local vertical to the body frame or

$$B_B = T_{LV/B} T_{E/LV} B_E \quad (56)$$

$$B_{LV} = \begin{bmatrix} \sin 63^\circ & -\cos 63^\circ & 0 \\ \cos 63^\circ & \sin 63^\circ & 0 \\ 0 & 0 & 1 \end{bmatrix} \begin{bmatrix} 0 \\ -4.1929 \times 10^{-7} \\ 5.9686 \times 10^{-8} \end{bmatrix}$$

$$= \begin{bmatrix} +1.9035 \times 10^{-7} \\ 3.7359 \times 10^{-7} \\ 5.9686 \times 10^{-8} \end{bmatrix}$$

$$B_B = \begin{bmatrix} \cos \theta \cos \psi & \cos \theta \sin \psi & -\sin \theta \\ \cos \psi \sin \theta \sin \phi & \cos \psi \cos \theta + \sin \psi & \cos \theta \sin \phi \\ -\sin \psi \cos \phi & \sin \theta \sin \phi & \\ \cos \psi \sin \theta \cos \phi & \sin \psi \sin \theta \cos \phi & \cos \theta \cos \phi \\ +\sin \psi \sin \phi & -\cos \psi \sin \phi & \end{bmatrix} B_{LV}$$

Assuming small angles and neglecting second order effects

$$\begin{bmatrix} 1.0 & \psi & -\theta \\ -\psi & 1.0 & \phi \\ \theta & -\phi & 1.0 \end{bmatrix} \quad (57)$$

$$B_{B_x} = 1.9035 \times 10^{-7} + 3.7359 \times 10^{-7} \psi - 5.9686 \times 10^{-8} \theta$$

$$B_{B_y} = -1.9035 \times 10^{-7} \psi + 3.7359 \times 10^{-7} + 5.9686 \times 10^{-8} \phi$$

$$B_{B_z} = 1.9035 \times 10^{-7} \theta - 3.7359 \times 10^{-7} \phi + 5.9686 \times 10^{-8}$$

Now calculating magnetic torques in the body axis

$$\mathbf{T}_B = \begin{bmatrix} i & j & k \\ K_{m_x} & K_{m_y} & K_{m_z} \\ B_{B_x} & B_{B_y} & B_{B_z} \end{bmatrix} \quad (58)$$

$$\begin{aligned} T_{B_x} = & K_{m_y} (1.9035 \times 10^{-7} \theta - 3.7359 \times 10^{-7} \phi + 5.9686 \times 10^{-8}) \\ & - K_{m_z} (-1.9035 \times 10^{-7} \psi + 3.7359 \times 10^{-7} + 5.9686 \times 10^{-8} \phi) \end{aligned}$$

$$\begin{aligned} T_{B_y} = & -K_{m_x} (1.9035 \times 10^{-7} \theta - 3.7359 \times 10^{-7} \phi + 5.9686 \times 10^{-8}) \\ & + K_{m_z} (1.9035 \times 10^{-7} + 3.7359 \times 10^{-7} \psi - 5.9686 \times 10^{-8} \theta) \end{aligned}$$

$$\begin{aligned} T_{B_z} = & K_{m_y} (-1.9035 \times 10^{-7} \psi + 3.7359 \times 10^{-7} + 5.9686 \times 10^{-8} \phi) \\ & K_{m_x} (1.9035 \times 10^{-7} + 3.7359 \times 10^{-7} \psi - 5.9686 \times 10^{-8} \theta) \end{aligned}$$

where K_m equals a scaling factor on the magnitude of the spacecraft dipole moment.

Ignoring the pitch component, $G(s)$ which includes the effect of magnetic torques is given in Figure 46.

A root locus was computed as a function of spacecraft dipole moment assuming $K_{m_x} = K_{m_z}$. The results are shown in Figure 47. As can be seen, a spacecraft dipole moment 40 times the value of spacecraft limitation is required for an instability.

$$\left[\begin{array}{l}
 \frac{s^2 + \frac{K_\phi}{I_{xx}} + 4\dot{\eta} \frac{(I_{yy} - I_{zz})}{I_{xx}} + \frac{K_y \dot{\eta}}{-\dot{\eta} \frac{(I_{yy} - I_{xx} - I_{zz})}{I_{xx}} s + \frac{K_y \dot{\eta}}{I_{xx}}} \\
 \\
 \frac{K_{m_y} (3.7359 \times 10^{-7})}{I_{xx}} + \frac{K_{m_z} (5.9686 \times 10^{-8})}{I_{xx}} \\
 \\
 \frac{\dot{\eta} \frac{(I_{yy} - I_{xx} - I_{zz})}{I_{zz}} s}{s^2 + \frac{K_y}{I_{zz}} + \eta \frac{(I_{yy} - I_{xx})}{I_{zz}} - T_{sT}} \\
 \\
 -\frac{K_\phi \dot{\eta}}{I_{zz}} - \frac{K_{m_x} (5.9686 \times 10^{-8})}{I_{zz}} + \frac{K_{m_x} (1.9035 \times 10^{-7})}{I_{zz}} + \frac{K_{m_x} (3.7359 \times 10^{-7})}{I_{zz}}
 \end{array} \right]$$

Figure 46. G(s) Including the Effect of Magnetic Torques

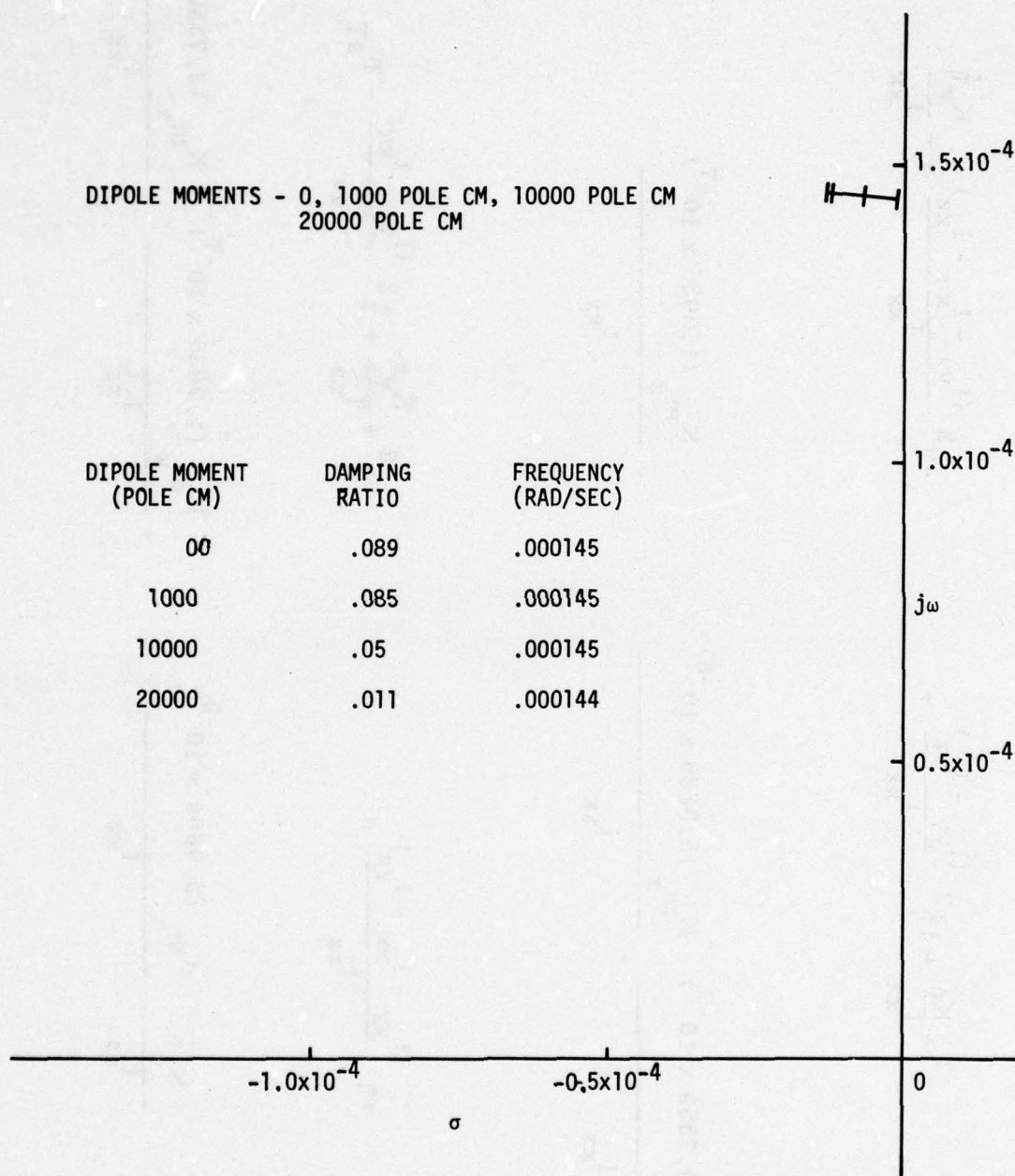


Figure 47. Root Migration as a Function of Magnetic Torques

In summary, no stability problems are expected from the effect of magnetic torques.

Wheel Misalignments--As shown in Figure 48, wheel alignment is defined by a cant angle α , and a wheel yaw angle, ψ_W , which defines the wheel position in the satellite x-y plane. The momentum of the wheels in body axes is given by

$$H_{W_x} = -H_{W_1} \cos \psi_{W_1} \cos \alpha_1 - H_{W_2} \cos \psi_{W_2} \cos \alpha_2 - H_{W_3} \cos \psi_{W_3} \cos \alpha_3 - H_{W_4} \cos \psi_{W_4} \cos \alpha_4 \quad (59)$$

$$H_{W_z} = -H_{W_1} \cos \alpha_1 - H_{W_2} \cos \alpha_2 - H_{W_3} \cos \alpha_3 - H_{W_4} \cos \alpha_4$$

The alignment specification requires alignment errors of no greater than 1° with respect to α and ψ_W . In analyzing the effect of wheel misalignment, it can be shown that the control equations reduce to

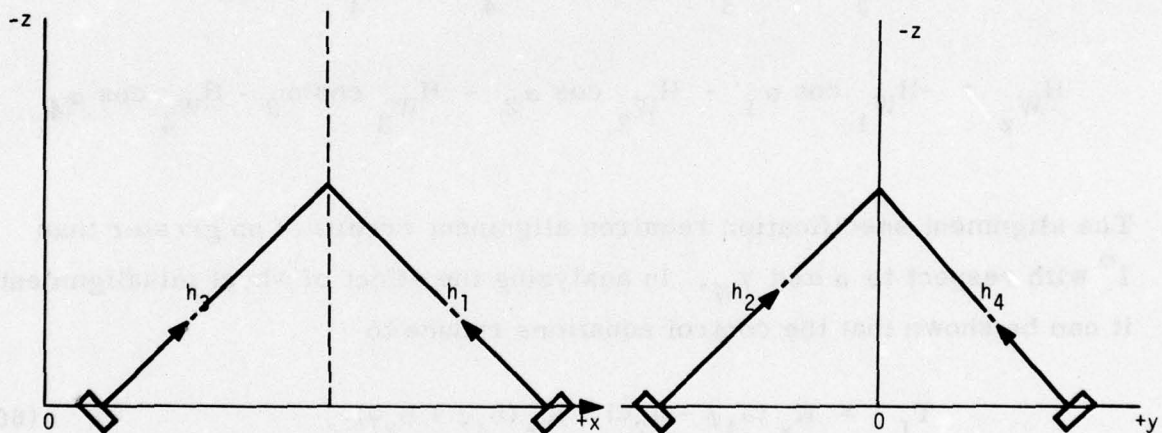
$$T_{I_x} = K_x (a_1 \dot{\phi} + a_2 \dot{\psi}) + K_z (b_1 \phi + b_2 \psi) \quad (60)$$

$$T_{I_z} = K_z (b_1 \dot{\phi} + b_2 \dot{\psi}) - K_x (a_1 \phi + a_2 \psi) \quad (61)$$

where the coefficient a_1 , a_2 , b_1 , b_2 , represented the effect of wheel misalignment. As can be seen, these equations are very similar to those

obtained analyzing yaw sun sensor coupling. The effect on the a_1 coefficient of the characteristic equation is also identical.

Since the effect of coupling is almost completely cancelled out, the combination of wheel misalignment angles were chosen which reduced the yaw loop gain and increased the roll loop gain. A root locus was then computed as a function of magnitude of misalignment angles at this configuration. The results are shown in Figure 49. As can be seen, even a 5° misalignment has an insignificant effect on the location of the oscillatory pair.



Alignment

	ψ_w	α
Wheel 1	0°	45°
Wheel 2	270°	45°
Wheel 3	180°	45°
Wheel 4	90°	45°

Figure 48. Wheel Orientation

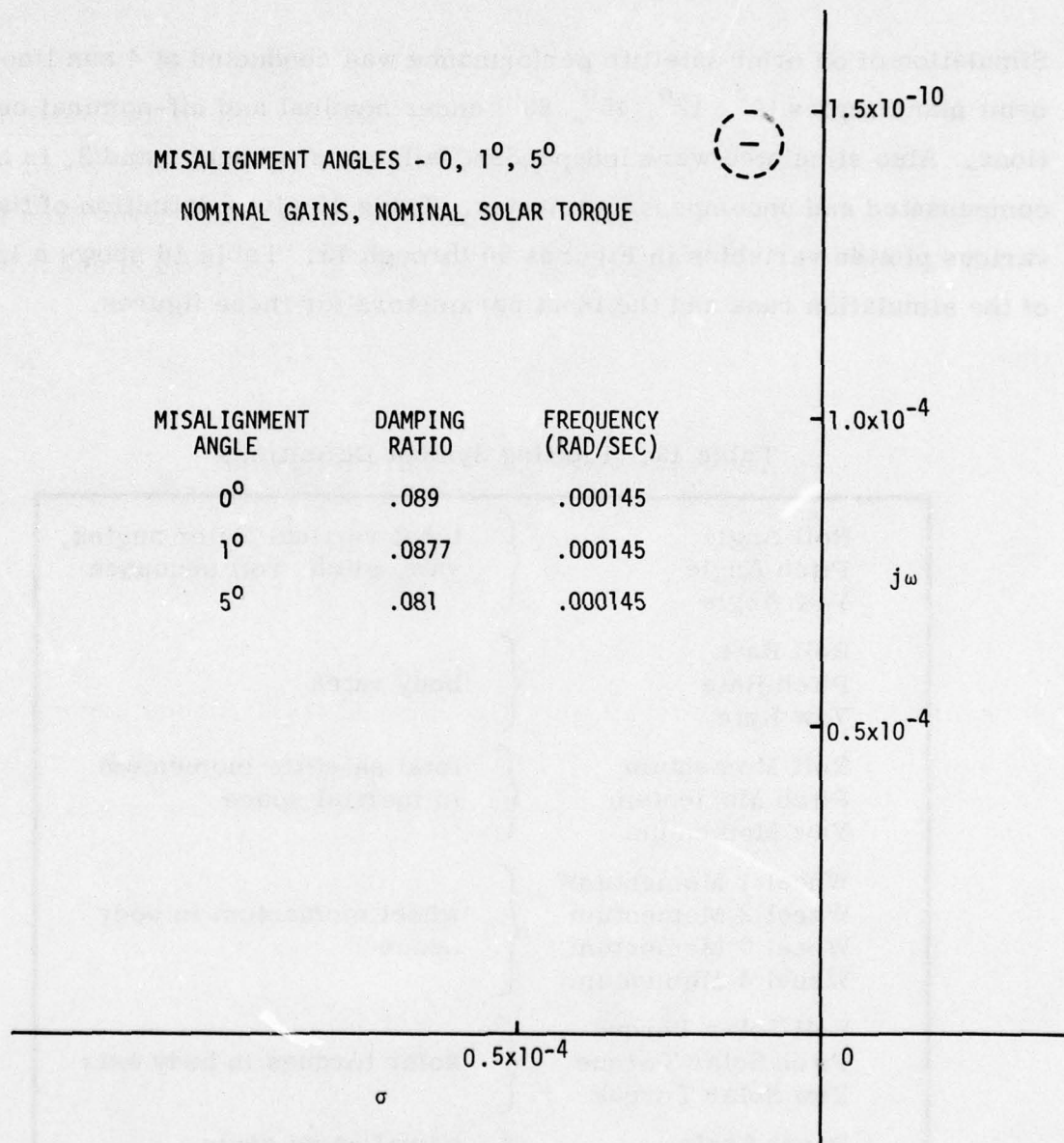


Figure 49. Root Migration as a Function of Wheel Misalignment

IV-B-2. On Orbit Simulation Results

Simulation of on orbit satellite performance was conducted at 4 sun line to orbit plane angles (0° , 12° , 45° , 86°) under nominal and off-nominal conditions. Also simulated were independent failures of wheels 1 and 2, in both compensated and uncompensated modes. Table 15 gives definition of the various plotted variables in Figures 50 through 75. Table 16 shows a log of the simulation runs and the input parameters for these figures.

Table 15. Plotting Symbol Definitions

Roll Angle	{	local vertical Euler angles, yaw, pitch, roll sequence
Pitch Angle		
Yaw Angle		
Roll Rate	{	body rates
Pitch Rate		
Yaw Rate		
Roll Momentum	{	total satellite momentum in inertial space
Pitch Momentum		
Yaw Momentum		
Wheel 1 Momentum*	{	wheel momentum in body space
Wheel 2 Momentum		
Wheel 3 Momentum		
Wheel 4 Momentum		
Roll Solar Torque	{	solar torques in body axis
Pitch Solar Torque		
Yaw Solar Torque		
Panel Angle	(actual panel angle
Sensed Yaw Angle	(output of yaw sun sensor

*Replaced in later runs with wheel momentum by axis

Table 16. Run Log

Run #/AIN Index	257 Sun Mean Anomaly (deg)	251 Satellite Mean Anomaly (deg)	876-878 Dipole Moment Vector (scale factor)	825-827 Center of Gravity (ft)	75-75 Initial Attitude (deg)	72-74 Initial Attitude Rates (deg/sec)	870-872 Initial Lat., Lon., Head (deg)
Nominal	1 310	0	(.73, .73, .73)	(0, 0, -2.0854)	(0, 0, 0)	(0, 0, 0)	(0, 0, 27 ⁰)
	2 176	0	(-.73, .73, .73)	(0, 0, -2.0854)	(0, 0, 0)	(0, 0, 0)	(0, 0, 27)
	3 88	0	(-.73, .73, .73)	(0, 0, -2.0854)	(0, 0, 0)	(0, 0, 0)	(0, 0, 27)
Worst Case	4 310	0	(.73, .73, .73)	(0, 0, -2.0854)	(0, 0, 0)	(0, 0, 0)	(0, 0, 27)
	4A 310	0	(1.47, 1.47, 1.47)	(.008, .008, -2.1204)	(0, 0, 0)	(0, 0, 0)	(0, 0, 27)
	4C 310	0	(1.47, 1.47, 1.47)	(.008, .008, -2.1204)	(0, 0, 0)	(0, 0, 0)	(0, 0, 27)
	5 176	0	(1.47, 1.47, 1.47)	(.008, .008, -2.1204)	(0, 0, 0)	(0, 0, 0)	(0, 0, 27)
	6 88	0	(1.47, 1.47, 1.47)	(.008, .008, -2.1204)	(0, 0, 0)	(0, 0, 0)	(0, 0, 27)
	6A 100	0	(.73, .73, .73)	(0, 0, -2.0854)	(0, 0, 0)	(0, 0, 0)	(0, 0, 27)
	6B 100	0	(1.47, 1.47, 1.47)	(.008, .008, -2.1204)	(0, 0, 0)	(0, 0, 0)	(0, 0, 27)
	6C 100	0	(1.47, 1.47, 1.47)	(.008, .008, -2.1204)	(0, 0, 0)	(0, 0, 0)	(0, 0, 27)
Wheel Failure	7 88	0	(1.47, 1.47, 1.47)	(.008, .008, -2.1204)	(0, 0, 0)	(0, 0, 0)	(0, 0, 27)
	7A 88	0	(1.47, 1.47, 1.47)	(.008, .008, -2.1204)	(0, 0, 0)	(0, 0, 0)	(0, 0, 27)
	8 310	0	(1.47, 1.47, 1.47)	(.008, .008, -2.1204)	(0, 0, 0)	(0, 0, 0)	(0, 0, 27)
	9 310	0	(1.47, 1.47, 1.47)	(.008, .008, -2.1204)	(0, 0, 0)	(0, 0, 0)	(0, 0, 27)
Deployment	11 310	90	(.73, .73, .73)	(0, 0, -2.1025)	(0, 0, 0)	(0, 0, 0)	(63, 90, 90)
	19 176	90	(.73, .73, .73)	(0, 0, -2.1025)	(0, 0, 0)	(0, 0, 0)	(63, 90, 90)
	20 176	90	(.73, .73, .73)	(0, 0, -2.1025)	(0, 0, 0)	(0, 0, 0)	(63, 90, 90)
	21 176	90	(.73, .73, .73)	(0, 0, -2.1025)	(.25, .25, .25)	(.007, .007, .01)	(63, 90, 90)
	22 176	0	(.73, .73, .73)	(0, 0, -2.1025)	(.25, .25, .25)	(.007, .007, .01)	(63, 90, 90)
	23 176	90	(.73, .73, .73)	(0, 0, -2.1025)	(.25, .25, .25)	(.007, .007, .01)	(63, 90, 90)
	24 176	90	(.73, .73, .73)	(0, 0, -2.1025)	(.25, .25, .25)	(.007, .007, .01)	(63, 90, 90)
1A	31	0	(.73, .73, .73)	(0, 0, -2.0854)	(0, 0, 0)	(0, 0, 0)	(0, 0, 27)
1B	31	0	(.73, .73, .73)	(0, 0, -2.0854)	(0, 0, 0)	(0, 0, 0)	(0, 0, 27)

Table 16. Run Log (continued)

293	898	899	981-982	991	816	810-811	812	011
Wheel	Time To	Time To Turn	Rod	YAM Gain	Panel	Scale Factor	Curve # for	Integration
Failure Switch	Start Deploy	On Wheels	Deployment Rate	(ft-lb/deg)	Angle Bias	YAM Sensor	YAM Sensor	Step Size
(sec)	(sec)	(sec)	(ft/sec)	(ft-lb/deg)	(deg)			(sec)
0	0	0	0	.0025	0	(6.33, 6.33)	2	100
0	0	0	0	.0025	0	(6.33, 6.33)	2	100
0	0	0	0	.0025	0	(6.33, 6.33)	2	25
0	0	0	0	.0025	1	(12.66, 12.66)	1	100
0	0	0	0	.0025	1	(4.22, 4.22)	3	100
0	0	0	0	.0025	1	(4.22, 4.22)	3	100
0	0	0	0	.0025	1	(4.22, 4.22)	1	100
0	0	0	0	.0025	1	(4.22, 4.22)	1	100
0	0	0	0	.0025	1	(12.66, 12.66)	1	25
0	0	0	0	.0025	0	(6.33, 6.33)	2	25
0	0	0	0	.0025	1	(12.66, 12.66)	1	25
0	0	0	0	.00125	1	(6.33, 6.33)	3	25
-1	0	0	0	.0025	1	(4.22, 4.22)	3	25
+1	0	0	0	.0025	1	(4.22, 4.22)	3	10
-2	0	0	0	.0025	1	(4.22, 4.22)	3	25
+2	0	0	0	.0025	1	(4.22, 4.22)	3	25
0	10	10	(.10417, -.10417)	.0025	0	(6.33, 6.33)	2	10
0	2	2	(.10417, -.10417)	.0025	0	(6.33, 6.33)	2	2
0	2	2	(.10417, -.10417)	.0025	0	(6.33, 6.33)	2	2
0	2	2	(.10417, -.10417)	.0025	0	(6.33, 6.33)	2	2
0	2	2	(.1145, -.09375)	.0025	0	(6.33, 6.33)	2	2
0	2	2	(.1145, -.09375)	.0025	0	(6.33, 6.33)	2	2
0	2	2	(.1145, -.09375)	.0025	0	(12.66, 12.66)	3	2
0	0	0	(0)	.0075	0	(6.22, 6.22)	2	50
0	0	0	(0)	.0075	0	(6.22, 6.22)	2	50

Table 16. Run Log (concluded)

[illegible]

Runs 1, 2, 3, and 6A present satellite performance under nominal conditions at the 45° , 86° , 0° and 12° sun line to orbit plane angles respectively. As shown in Figures 50 through 52, satellite behavior is stable for the first three. There was no calcomp plot made for 6A. Tracking errors are given in Table 17. Run 6A was made as a check against the analytical results which, while not indicating a problem, show reduced margin to yaw solar torques at reduced yaw gains. The 12° sun line to orbit plane angle was chosen for simulation since we incorrectly believed that the yaw gain increase switch was only enabled when the sun line to orbit plane angle was less than 10° . Hence the yaw gain was kept at its nominal value of .4 ft-lb/rad. This admittedly is an unrealistic run; however, it does demonstrate that even with very low yaw gains, no instability was observed. The dead bands were also removed since they appear to add stability. As can be seen tracking errors in pitch and roll are comparable to the other cases. Yaw error is larger which is expected.

The remaining runs were made with off nominal conditions which will now be described.

Earth Sensor Misalignments--Two runs (1A, 1B) were made with the modified version of the earth sensor as described in the modeling section. Run 1A shown in Figure 53 is a rerun of Run 1 with the only difference being use of approximated earth sensor feedback in the control system. Run 1B, Figure 54, contains a 1° misalignment in the pitch and roll axes of the earth sensor. Tracking errors are summarized in Table 18. Run 2A could also be interpreted as perfect earth sensor alignment but with a 1° misalignment of the gravity gradient rods in pitch and roll.

Table 17. Tracking Errors--Nominal Conditions

Run No.	Sun Line	Roll Error	Pitch Error	Yaw Sun Tracking Error
1	45°	.35°	.37°	7.0°
2	86°	.22°	.24°	4.0°
3	0°	.23°	.37°	-
6A	12°	.2°	.34°	10.9°

Table 18. Tracking Errors--Off Nominal Conditions

Run No.	Sun Line	Peak Roll Error	Peak Pitch Error	Peak Yaw Sun Tracking Error	Comments
1A	45°	.40°	.46°	7.0°	with CES 1° CES mis- alignment
1B		1.66°	1.04°	7.0°	
4	45°	.47°	.45°	14.0°	
4A	45°	.48°	.425°	4.47°	
4B	45°	.47°	.47°	4.8°	
4C	45°	.495°	.476°	4.8°	
5	86°	.306°	.39°	3.2°	
6	0°			-	
6B	12°	.366°	.585°	25.0°	
6C	12°	.334°	.494°	18.6°	
7	0°	Lost earth after six orbits			no deadbands no deadbands
7A	0°	.813°	2.72°	-	
8	45°	.433°	.804°	7.5°	
9	45°	.52°	.46°	3.3°	
10	86°	.302°	.375°	2.87°	

Yaw Sun Sensor Errors--As discussed in the modeling section, yaw sun sensor accuracy is bounded by an accuracy envelope at 25°C and also by a gain variation as a function of temperature. In the simulation program, the nominal or either boundary of the sensor curves may be used. In Table 14, these curves have been designated as curve 1, 2, or 3 as follows:

Curve 1 - lower than nominal

Curve 2 - nominal

Curve 3 - higher than nominal

In addition, the temperature variation can cause as much as a ± 50 percent variation in sensor output. The nominal scale factor in transforming the sensor output (microamps) into degrees is $1/6.33$. Hence $1/4.22$ represents a 50 percent increase in the sensor output and $1/12.66$ represents a 50 percent decrease. Run 4, Figure 55, shows the effect of a 50 percent reduction in sensor output. The plot labeled "sensed yaw" is approximately half the actual yaw tracking error. Tracking error is shown in Table 18. Run 4A, Figure 56, shows the effect of increasing the yaw gain by 50 percent. As shown in Table 18, pitch and roll tracking error are close to the nominal performance for the two runs. Yaw performance varies proportionally with the gain.

Run 6B is with the worst case conditions applied to Run 6A under the same incorrect yaw gain procedure. Yaw gain is reduced by 50 percent of its nominal value over the whole run. Again the dead bonds have been removed. Performance is degraded as shown in Table 18, but still stable. Run 6C, Figure 57, shows the effect of the correct yaw gain implementation. Performance is improved slightly.

Wheel Misalignments--The NRL specifications permit a 1° misalignment of the reaction wheels in yaw and cant angle. The alignment angles that were used in the simulation, as given in Table 15, were determined to be worst case combinations for the NDS satellite. The analysis shown in the previous section indicates they may not be the worst case for NTS-2; however, they do effect a degree of nonlinear coupling not accounted for in the linear analysis.

Run 4B, Figure 58, shows the results of appending these misalignments onto the conditions of 4A. As shown in Table 18, performance is not significantly affected.

Solar Array Center of Pressure Shift--A 0.5" location uncertainty was assumed to exist in the center of pressure on the solar arrays. The combination of signs of the cp shift were chosen to create a yaw solar torque and a further imbalance in pitch solar torque. The results are shown in Run 4C, Figure 59, and Table 18. Again performance is not significantly affected.

The effects of a satellite center of mass variation ($\Delta x = \Delta y = .1"$, $\Delta z = -.2"$), a doubling of the spacecraft magnetic dipole moment, and a 1° solar array tracking error were also included in Runs 4, 4A, 4B, and 4C. The Δz sign was chosen to increase the pitch solar torque imbalance. The dipole moment variation is implemented through a scale factor parameter for changing Newton-meters to ft-lbs. For a dipole moment of 1,000 pole cm, the scale factor is .73. Since the one body simulation used in orbit runs assumes perfect panel-tracking, a 1° tracking error was inserted to simulate the 1° dead band in the solar array drive. All of these perturbations contributed

to the slight degradation in tracking performance as shown in Table 18. The remaining runs contained all the above described perturbations for generating "worst case" conditions. Run 5, Figure 60, is a repeat of Run 4C at the 86° sun line condition. Slightly better performance is shown in Table 18. Run 6, Figure 61, shifts the simulation to noon turn and puts the yaw gain to 50 percent of its nominal value.

The final five runs simulate the result of wheel failures, both compensated and uncompensated under worst case condition. Run 7 has an uncompensated wheel 1 failure at the noon turn condition. Only line printer plots are available for this run and have not been included. The satellite did lose the earth at approximately 6 orbit into the run. Run 7A, Figure 62, presents the same condition as Run 7 however, with the compensation logic included. Performance does degrade seriously as shown in Table 18. The large attitude excursion in pitch at one point in the run is felt to be due to an instantaneous wheel unloading. Wheel 2 failures at two less demanding mission conditions were also simulated. Run 8, Figure 63, shows uncompensated wheel 2 failure response. Performance is surprisingly good. Run 9, Figure 64, shows the effect of adding compensation. Performance does improve, particularly in yaw tracking. Run 10, Figure 65, is identical to Run 9 except at the 86° sun line condition. Again performance is slightly better.

Summary --There appears to be no problem in orbit performance of the satellite. Tracking error is generally less than $.5^{\circ}$ in pitch and roll and stable in yaw. An uncompensated wheel 1 failure will lead to the earth falling out of the field of view of the earth sensor if not compensated for in 6 orbits. Compensated wheel failure performance under worst case conditions indicates transient attitude errors of 2.70° . These do not appear to be a problem.

IV-C. DEPLOYMENT AND ACQUISITION

In determining permissible initial attitudes and rates from which acquisition can be achieved after deployment of the rods, it is necessary to specify an acquisition requirement. One reasonable requirement is that the initial rates and attitudes be such that acquisition be achieved without saturating the earth sensor and yaw sun sensor. If this requirement is to be met, the satellite wheels must be able to absorb the momentum in the satellite due to attitude rates. In addition, the wheels must provide the satellites with the orbital rate components necessary for tracking the earth, and the sun tracking rates for tracking the sun. This latter requirement is a function of sun line position and consequently the yaw angle necessary for sun pointing. If the yaw angle is 0° , the orbital rate component must be built up in the satellite pitch axis. If the yaw angle is 90° , then the satellite roll axis will see the effect of orbital rate. Between 0° and 90° yaw angles, it is a combination of the two. The momentum transfer procedure may be analyzed as follows. The ACE system commands wheel momentum as a function of attitude. Hence the maximum wheel momentum that can be commanded will be when the sensors are at the saturation point, or

$$Hw_{x_{\max}} = K_x \times 4^\circ = 3.75 \times \frac{4}{57.3} = .26 \text{ ft-lb-sec}$$

$$Hw_{y_{\max}} = K_y \times 4^\circ = 3.75 \times \frac{4}{57.3} = .26 \text{ ft-lb-sec}$$

$$Hw_{z_{\max}} = K_z \times 30^\circ = 0.4 \times \frac{4}{57.3} = .21 \text{ ft-lb-sec}$$

These relationships assume no initial attitude error.

Allowable rates for achieving acquisition can then be computed from

$$\begin{aligned} p_{\max} &= H w_{x_{\max}} / I_{xx} \\ q_{\max} &= H w_{y_{\max}} / I_{yy} \\ r_{\max} &= H w_{z_{\max}} / I_{zz} \end{aligned}$$

If the acquisition procedure was not to be initiated until after the rods were fully deployed, the allowable for nominal conditions would then be

$$p_{\max} \text{ (post deployment)} = .0075^{\circ}/\text{sec}$$

$$q_{\max} \text{ (post deployment)} = .0078^{\circ}/\text{sec}$$

$$r_{\max} \text{ (post deployment)} = .06^{\circ}/\text{sec}$$

Since orbit rate is $.008^{\circ}/\text{sec}$, these results indicate that it would be difficult at yaw angles of 0° or 90° to acquire without saturating the earth sensor and that assuming no initial body rates.

In the runs we simulated, we engaged wheel control at the start of deploying the rods. At that condition the allowable rates are

$$p_{\max} \text{ (pre deployment)} = .09^{\circ}/\text{sec}$$

$$q_{\max} \text{ (pre deployment)} = .191^{\circ}/\text{sec}$$

$$r_{\max} \text{ (pre deployment)} = .06^{\circ}/\text{sec}$$

Hence, if the wheels are to be turned on at the same time as the rods begin deployment, the permissible rates will fall somewhere in between the two sets of values. (Note: permissible yaw rate is the same.) This result was verified in simulation and will now be discussed.

Five runs were made to investigate rod deployment and acquisition conditions. These are listed with their pertinent input parameters in Table 15. The 86° sun line was chosen since the orbital rate component appears almost entirely in the roll axis at this condition. Run 19, Figure 66, and Run 20, Figure 67, show acquisition problems for initial yaw rates of $.1^\circ/\text{sec}$ and $.05^\circ/\text{sec}$ respectively. The $.05^\circ/\text{sec}$ rate is less than the maximum permissible. However, with a 10° initial offset in yaw only 20° of the 30° sensor range was available. For that condition, the permissible yaw rate is on the order of $.04^\circ/\text{sec}$. Run 21, Figure 68, did acquire without sensor saturation. The roll attitude response shows the effect of the additional orbit rate term. Roll attitude approaches 4° whereas pitch attitude reaches approximately 1.7° . When orbit rate is added to the initial roll body rate, the equivalent initial roll rate would be $.015^\circ/\text{sec}$.

Run 23, Figure 69, shows the effect of varying the rod deployment rate +10 percent for rod 1 and -10 percent for rod 2. There is no measurable effect.

Run 24, Figure 70, adds a 50 percent reduction in yaw gain to the conditions of Run 23. Acquisition is still achieved.

In summary, it has been demonstrated that initial conditions of

	$p = .007^\circ/\text{sec}$
body rates	$q = .007^\circ/\text{sec}$
	$r = .01^\circ/\text{sec}$
Euler	$\phi = .25^\circ$
angles	$\theta = .25^\circ$
Sun mis- alignment	$\phi = .10^\circ$

will permit deployment and acquisition without sensor saturation. Margins for acquisition at different sun line conditions have also been provided.

IV-D. ROD AND PANEL FLEXIBILITY EFFECTS

The effects of rod and panel flexibility were investigated by 1) determining three axis gain and phase margins via frequency response analysis, and 2) computer simulation which included the actual ACE system and the complete three body dynamics model.

Gain and phase plots for the roll, pitch and yaw axes are given in Figures 76, 77, and 78 respectively. The first and second unsymmetric rod bending modes are visible in both the roll and pitch plots, however, because of the fifth order filtering, their magnitude is very small. (Note: a structural damping ratio of $.0005 \text{ sec}^{-1}$ was assumed in this analysis.) No elastic modes were observed in the yaw axis because of the small magnitude of the yaw excitation moment. A summary of the gain and phase margin characteristics is given in Table 19.

Five computer runs were made which by varying the run length investigated both the effect of torsional flexibility of the solar panels and also the bending effects of the rods. These runs are described in Table 20 and the response histories are given in Figures 71 through 75. Symbol definition is given in Table 21.

Run 25, Figure 71, simulated two seconds of satellite performance with the most complete dynamic model. No instabilities were observed. Because the run was so short, it is possible to see the 8 Hz panel torsional mode

dynamics both in the modal coordinate plot itself and also in the panel motion at the drive motor and at the pitch sun sensor. This run was made without the GE modification in the solar array drive and the motor torque pulses can be seen at their maximum 2 pulse per second frequency. The torsional mode is excited at each pulse; however, damping can be observed between pulses.

Runs 26 and 27, Figures 72 and 73, are extensions in time of Run 25 to 60 seconds. Run 27 includes the GE modification in the solar array drive loop. No instabilities were observed in either simulation. It is interesting to note that even after 60 seconds running the wheels have still not come on. This is because of the deadbands in the wheel loop and the fifth order filters which have equivalent first order time interval of six minutes. Attitude response shows the effect of orbital rate which because of the 86° sun line condition appears almost entirely in roll. Run 26 contains a plot of sensed angle error showing that the 10° error has been reduced within the 1° deadband in approximately 40 seconds. Run 27 contains a similar plot except that the output of the 20 second filter is plotted. Response is much smoother as can be seen. Because of the lag and the pulse frequency reduction, panel error was still 1.96° at 60 seconds.

Run 27A, Figure 74, is a repeat of run 26, assuming, however, that the solar array is grounded at the drive motor instead of free wheeling. This implies that the rigid body can now be excited by the panel torsion motion which was not possible in the free wheeling model. As discussed in the modeling section, the frequency of the first symmetric torsion mode is reduced from 8 Hz to 2.6 Hz for this model. There is very little difference between the two runs. Rigid body pitch attitude is just slightly larger. In runs 26, 27 and 27A, only one period of rod bending effects are observable.

Tip mass deflections in the x and y directions are plotted and show peak magnitude on the order of .1 - .15 feet. In order to see the effects of the rod bending, Run 28, Figure 75, was made. In this run the solar array torsion mode was deleted; however, the solar array drive model was still retained. The GE modification was included in this run.

The effect of the first antisymmetric rod bending mode at .12 rad/sec can be observed on the rigid body pitch attitude response. Again no instabilities were observed. Wheel activity was apparent at about 70 seconds into the run. One interesting point is that roll attitude has reached 3.74° in 600 seconds and appears to be growing. This is in direct agreement with the results previously presented on deployment which stated that at post deployment inertias the maximum permissible rate is $.007^{\circ}/\text{sec}$. Orbital rate which in this case appears almost entirely in the roll axis is $.008^{\circ}/\text{sec}$. Observation of the roll rate plot will show that roll rate has very nearly reached the $.008^{\circ}/\text{sec}$ required which is consistent with the 500 second time constant of the roll rate dynamics. Hence roll attitude should be flattening and gradually through gravity gradient torques return to zero. These results indicate that despite using a modified version of the control system in the deployment simulation analysis, the results are reasonable.

In summary, no problems were detected in the analysis of rod and panel flexibility effects. There are very large stability (gain and phase) margins in the design and the simulation could detect no instabilities due to nonlinear effects.

Table 19. ACE System Stability Margins

Pitch Wheel Loop	<p>Crossover - .0016 rad/sec</p> <p>Gain margin - 19db at .001 rad/sec</p> <p>Phase margin - 76°</p> <p>Gain at first unsymmetric - -88db bending mode</p>
Roll Wheel Loop	<p>Crossovers - .000158 rad/sec</p> <p>- .0023 rad/sec</p> <p>Gain margins - 14db at .000144 rad/sec</p> <p>- 16db at .011 rad/sec</p> <p>Phase margins - 87°</p> <p>- 70°</p> <p>Gain at first unsymmetric - -76db bending mode</p>
Yaw Wheel Loop	<p>Crossover - .0019 rad/sec</p> <p>Gain margin - 17db at .011 rad/sec</p> <p>Phase margin - 74°</p>

Table 20. Flexibility Effects Run Table

Run #	Length of Run	Array Torsional Modes Included	Attay Drive Motor Characteristic	Ge Model Included
25	2 sec	Yes	Free wheeling	No
26	60 sec	Yes	Free wheeling	No
27	60 sec	Yes	Free wheeling	Yes
27A	60 sec	Yes	Grounded	No
28	600 sec	No	Free wheeling	Yes

Table 21. Flexibility Run Symbol Definition

Roll angle Pitch angle Yaw angle	Euler angles in the local vertical
Roll rate Pitch rate Yaw rate	body rates
Sensed yaw angle	output of yaw sun sensor
First symmetric panel	first symmetric torsional mode in modal coordinates
Theta at DM	position of the solar array shaft at the drive motor
UAX tip mass	deflection of tip mass in the x direction
UAY tip mass	deflection of tip mass in the y direction
Theta at sensor	position of the solar array shaft at the pitch sun sensor
Panel angle error	pitch sun sensor output
Panel angle error sensed lag	pitch sun sensor output filtered through Ge lag

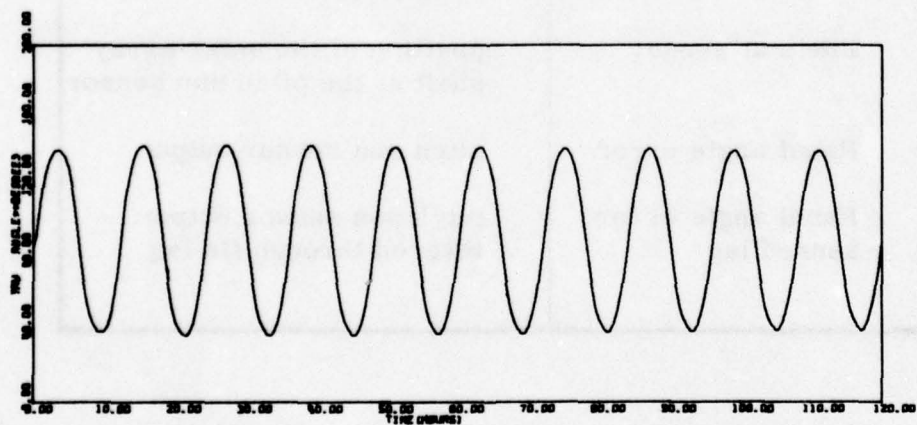
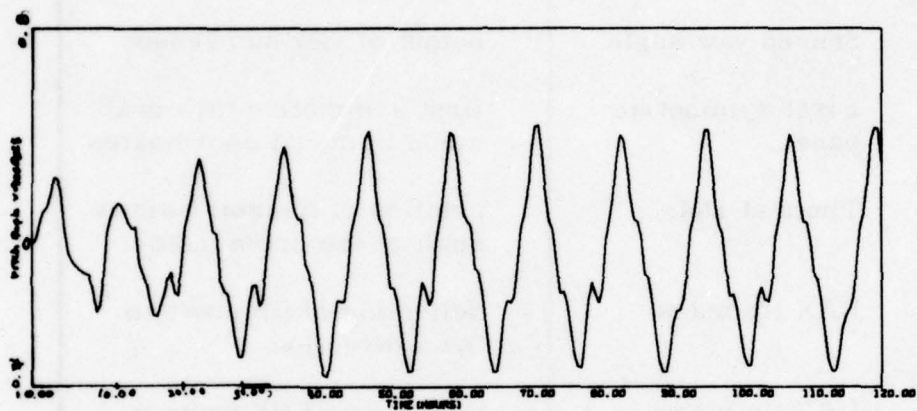
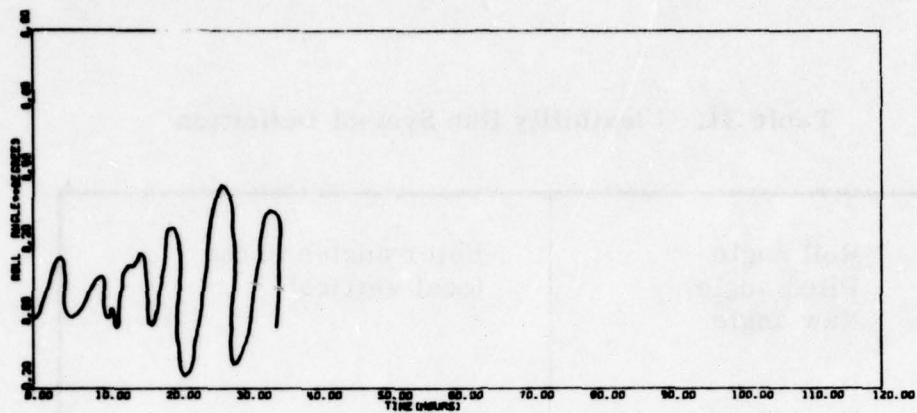


Figure 50. Run 1 - Sunline 35° - Nominal

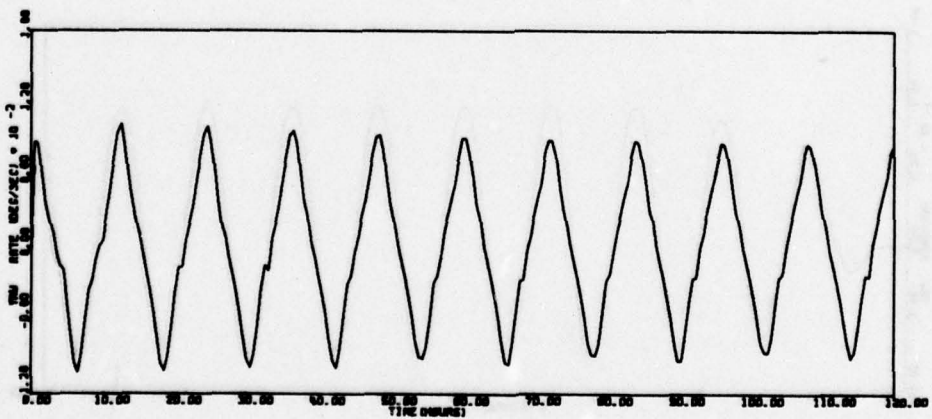
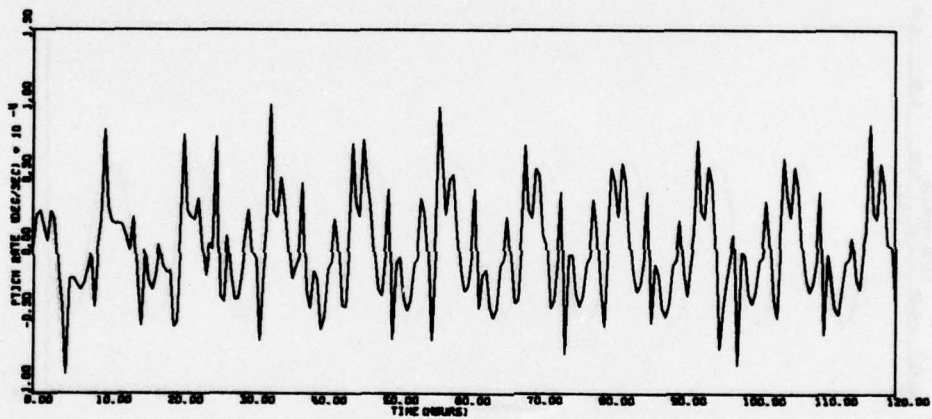
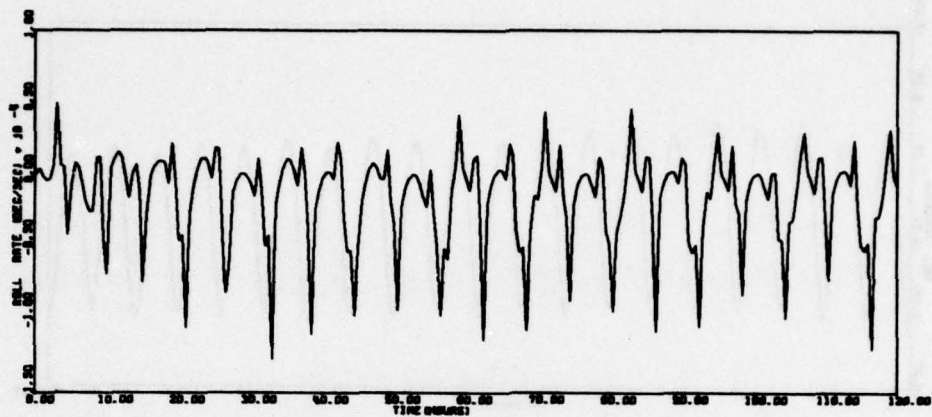


Figure 50. Run 1 - Sunline 35⁰ - Nominal (continued)

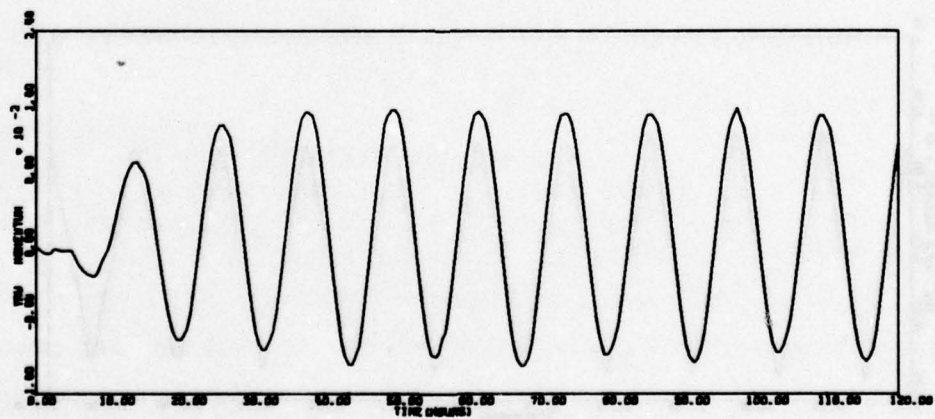
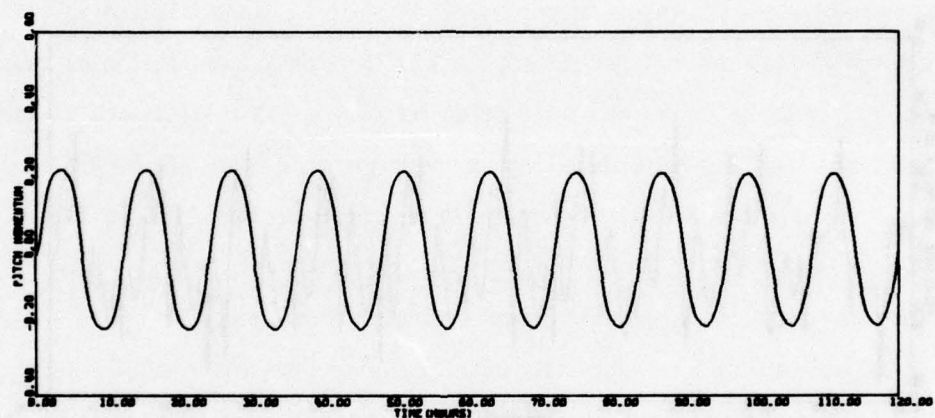
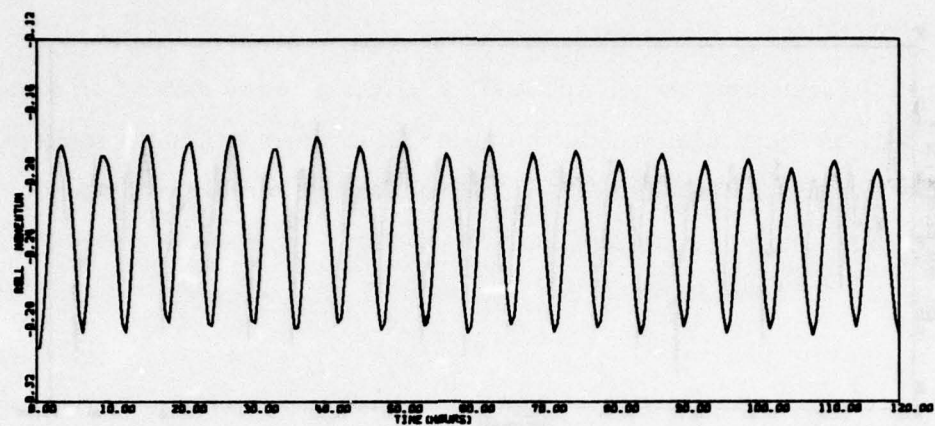


Figure 50. Run 1 - Sunline 35⁰ - Nominal (continued)

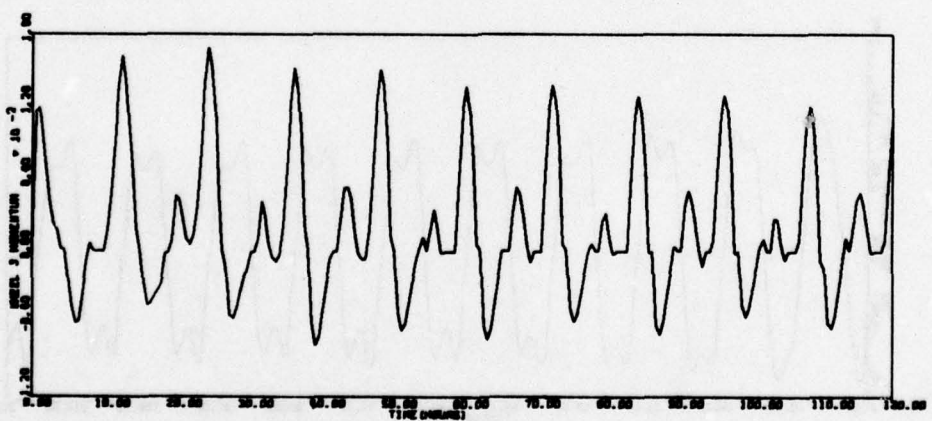
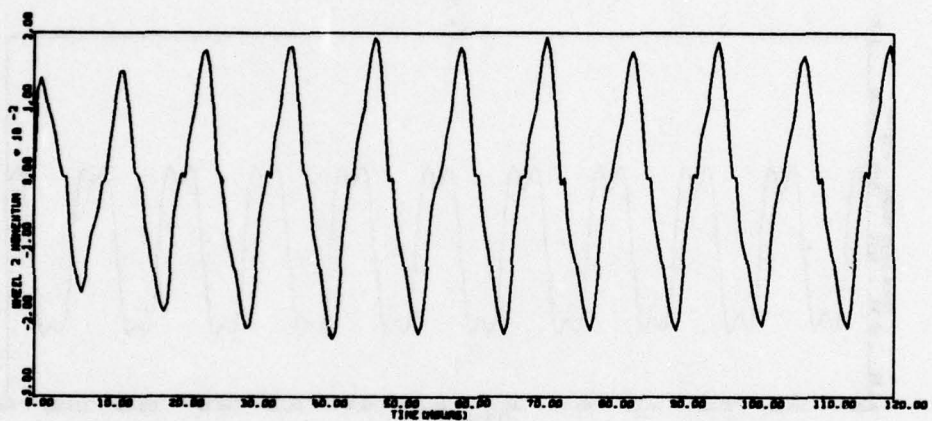
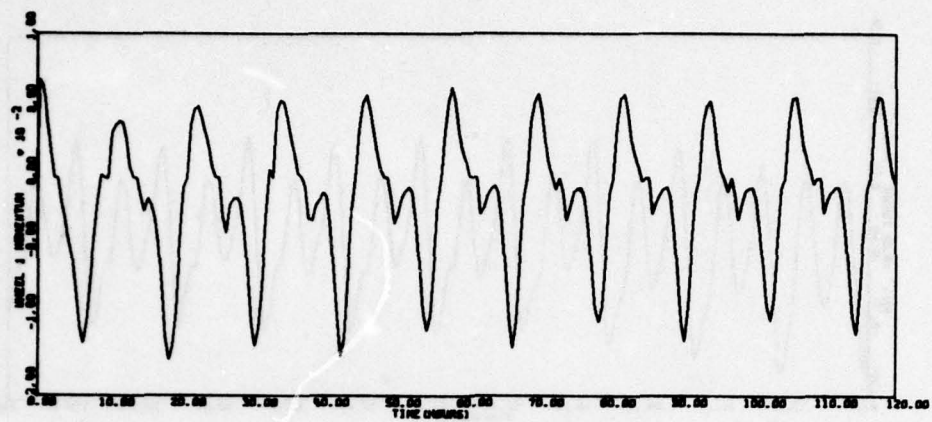


Figure 50. Run 1 - Sunline 35° - Nominal (continued)

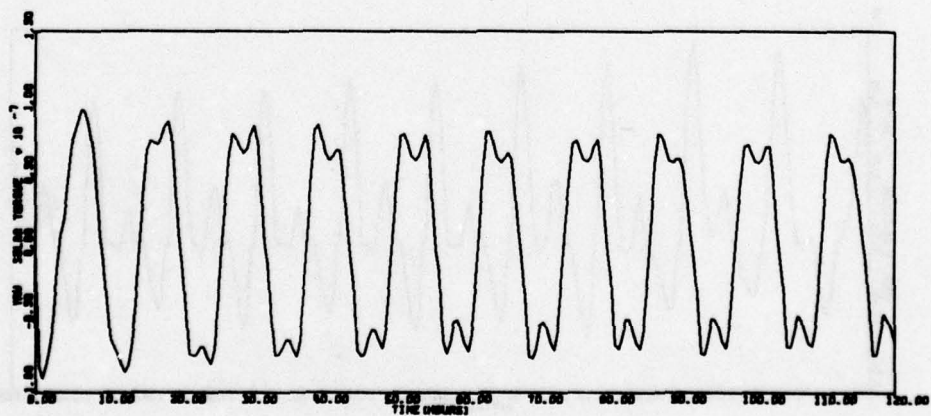
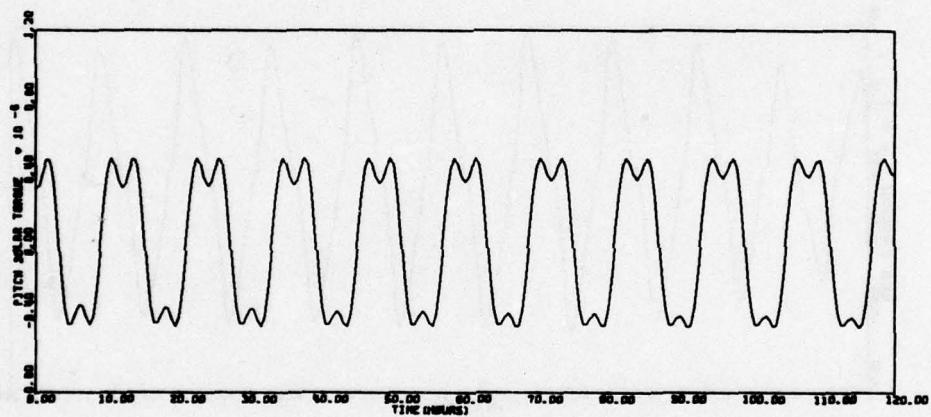
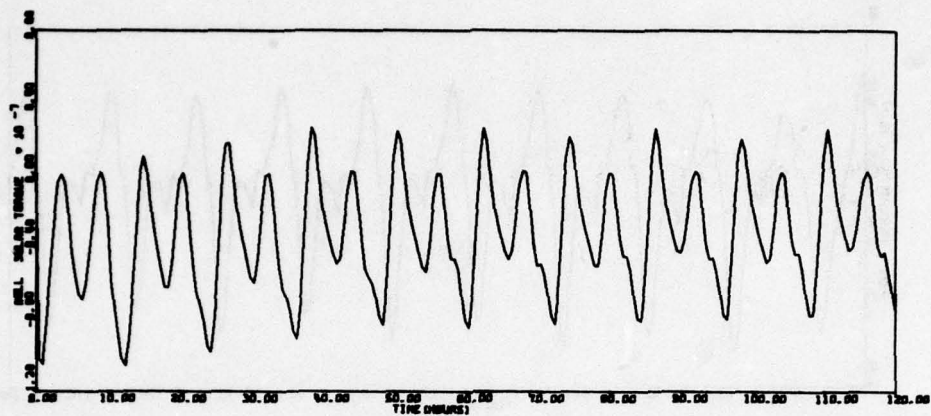


Figure 50. Run 1 - Sunline 35° - Nominal (continued)

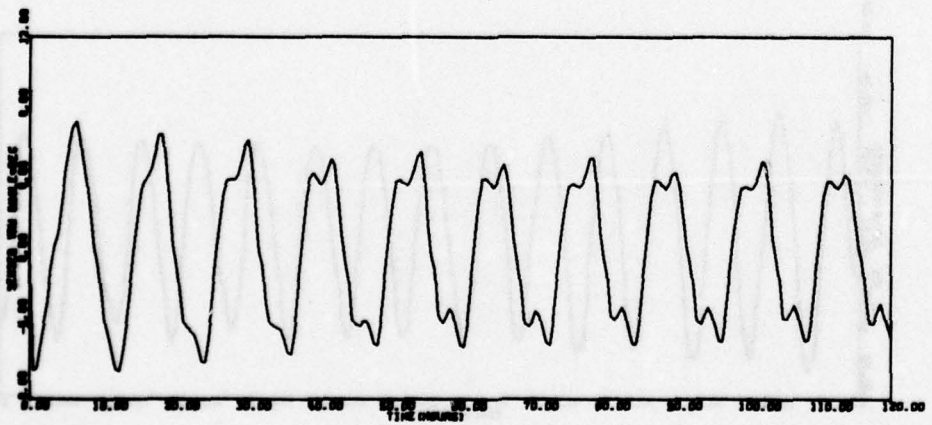
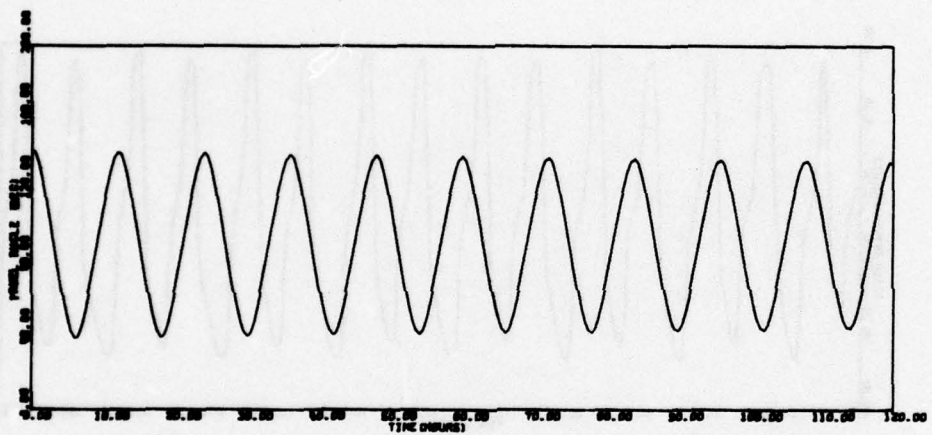
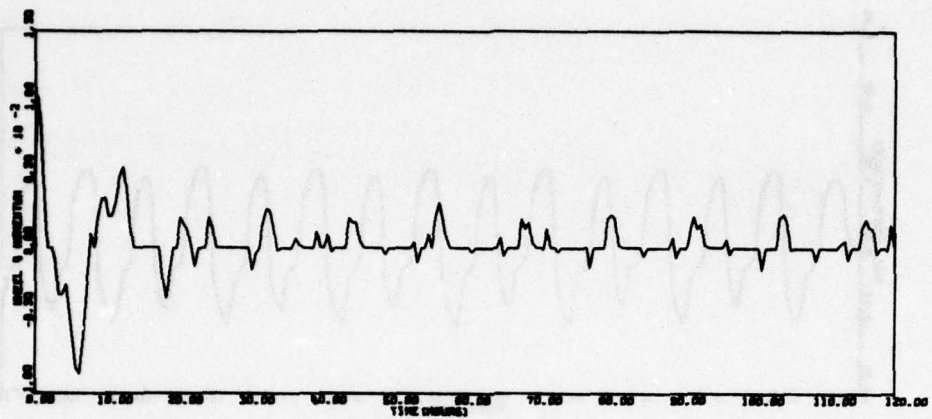


Figure 50. Run 1 - Sunline 35° - Nominal (concluded)

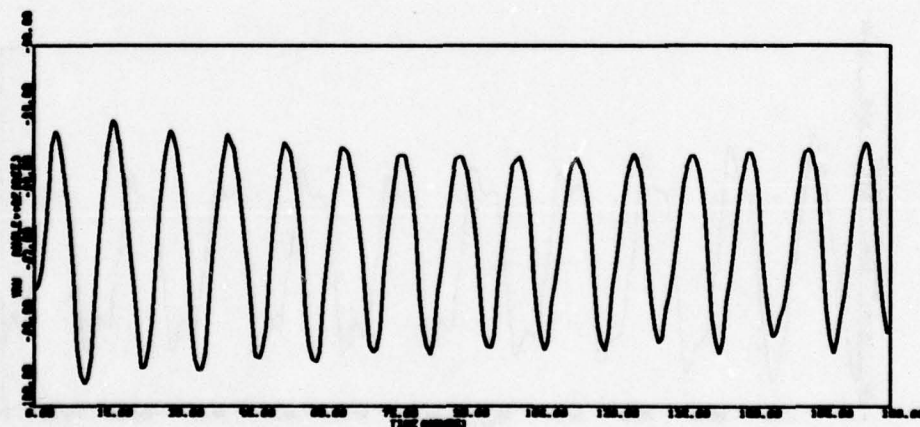
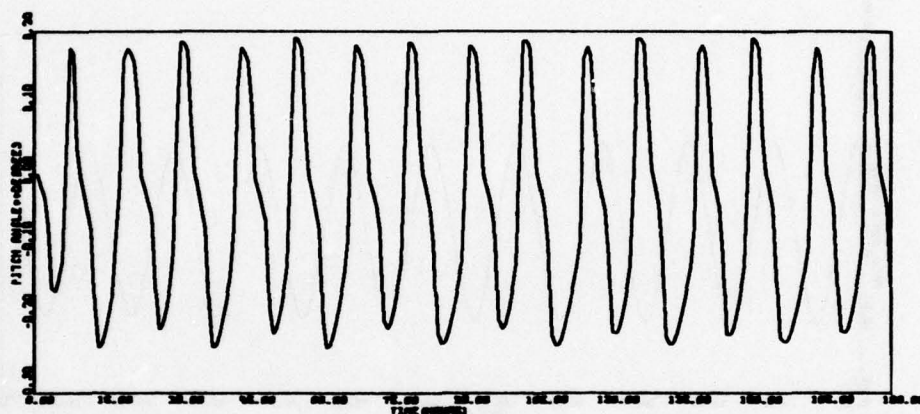
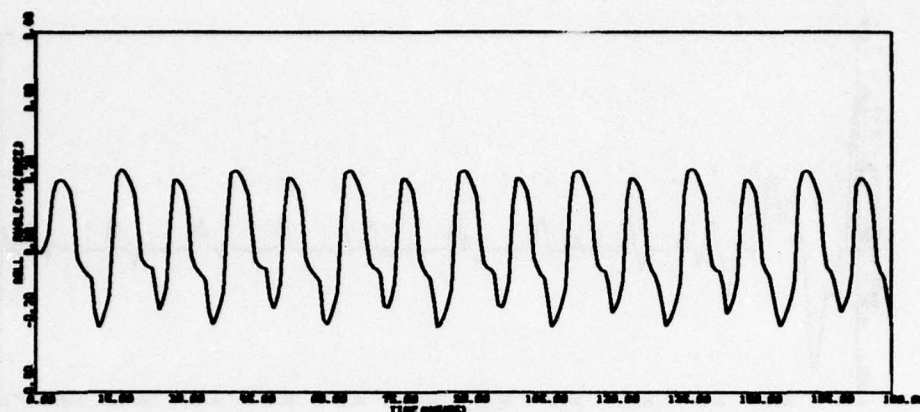


Figure 51. Run 2 - Sunline 86° - Nominal

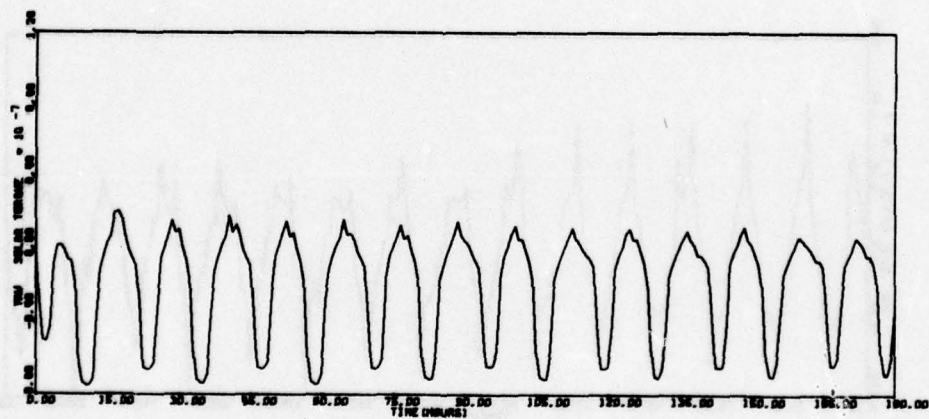
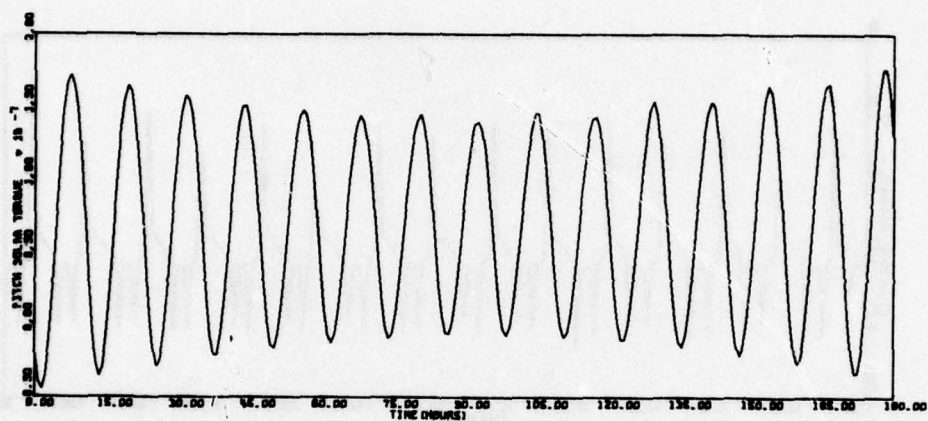
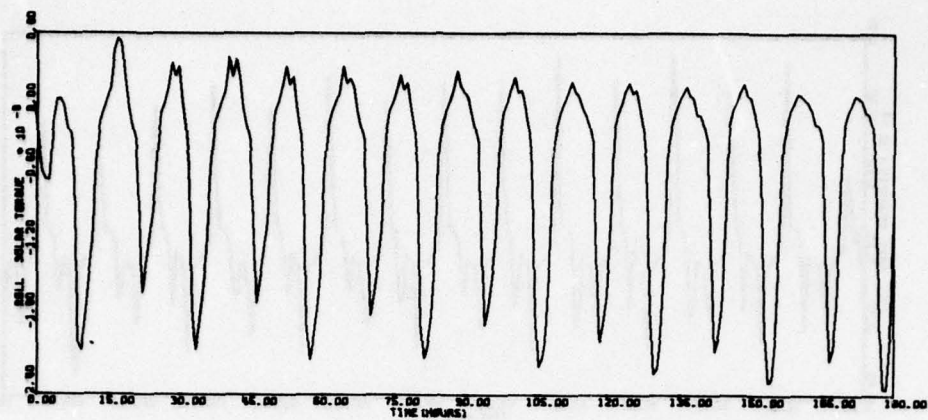


Figure 51. Run 2 - Sunline 86° - Nominal (continued)

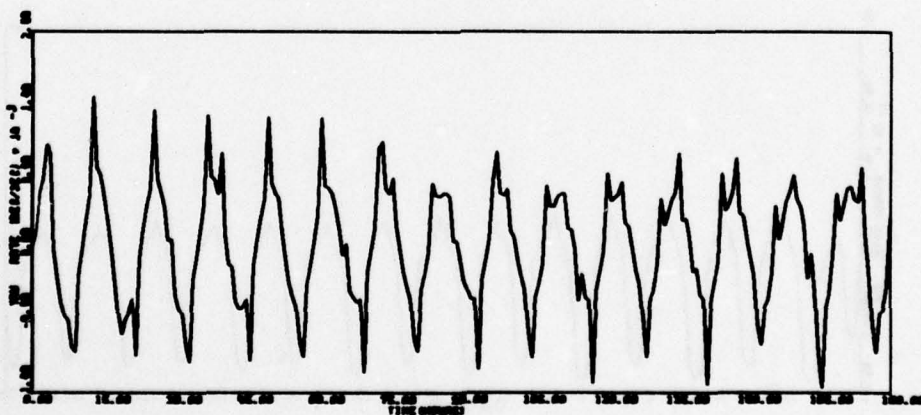
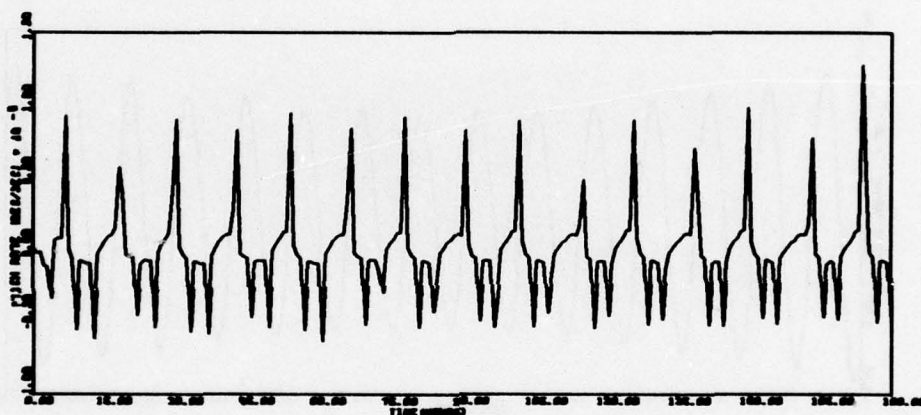
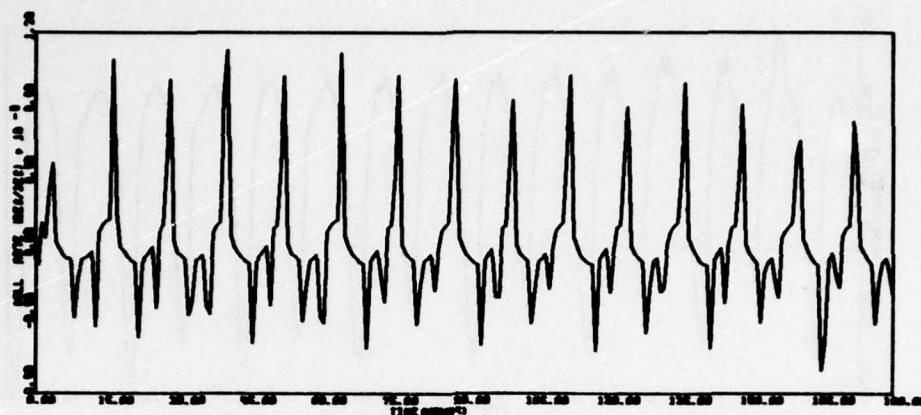


Figure 51. Run 2 - Sunline 86⁰ - Nominal (continued)

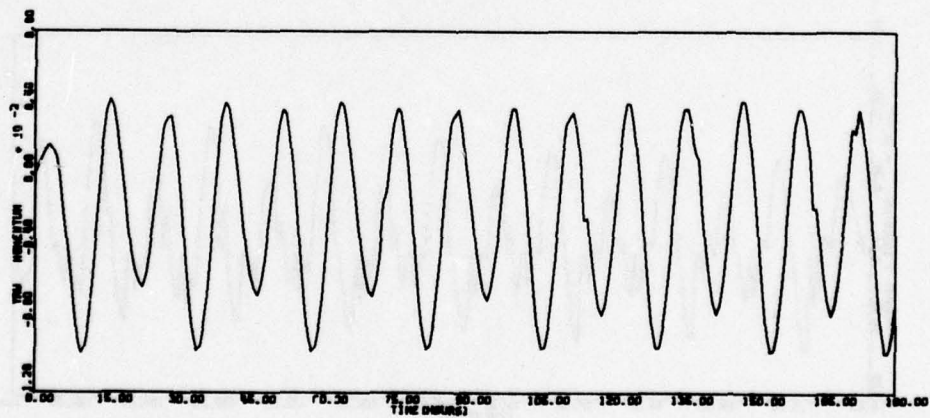
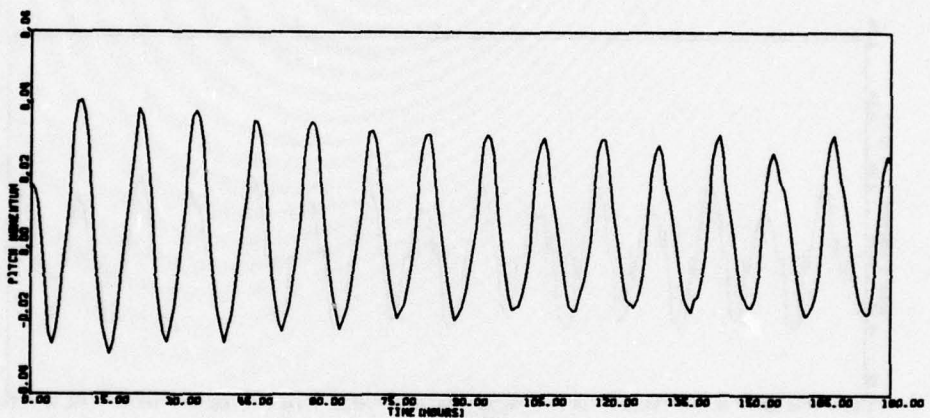
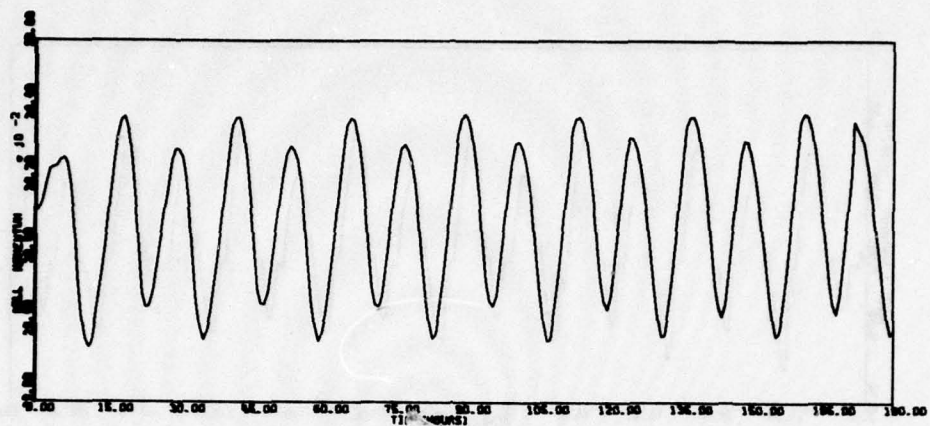


Figure 51. Run 2 - Sunline 86° - Nominal (continued)

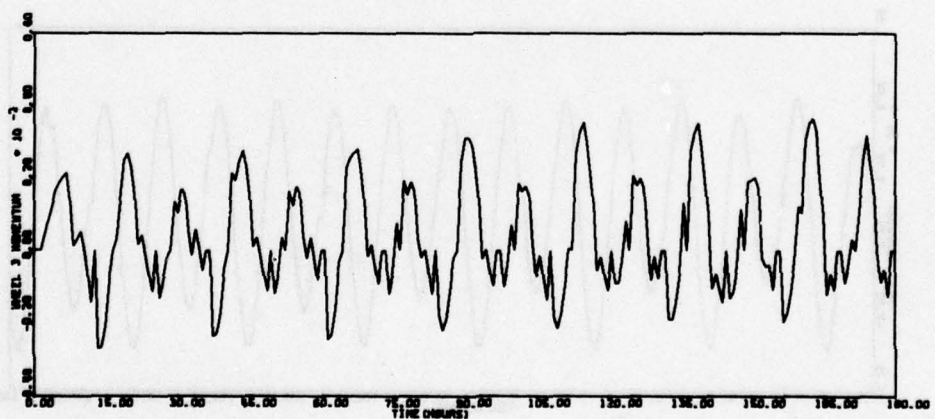
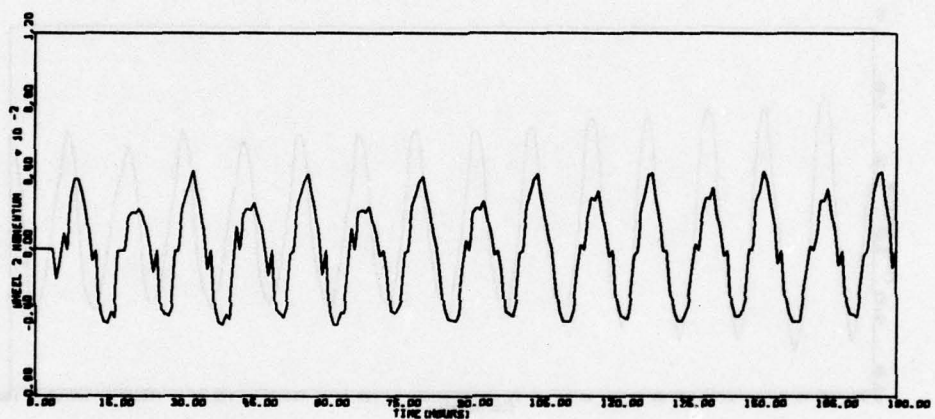
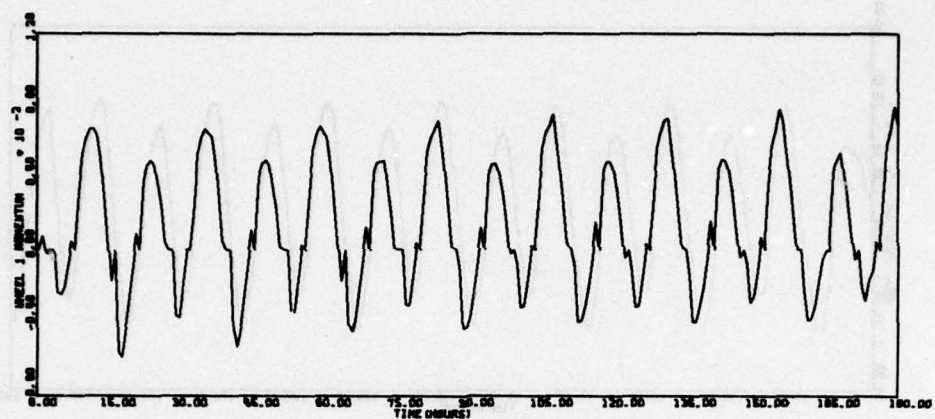


Figure 51 Run 2 - Sunline 86° - Nominal (continued)

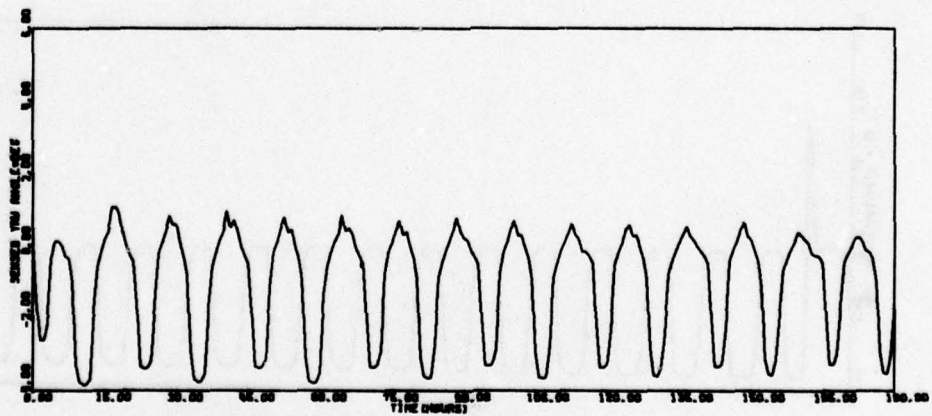
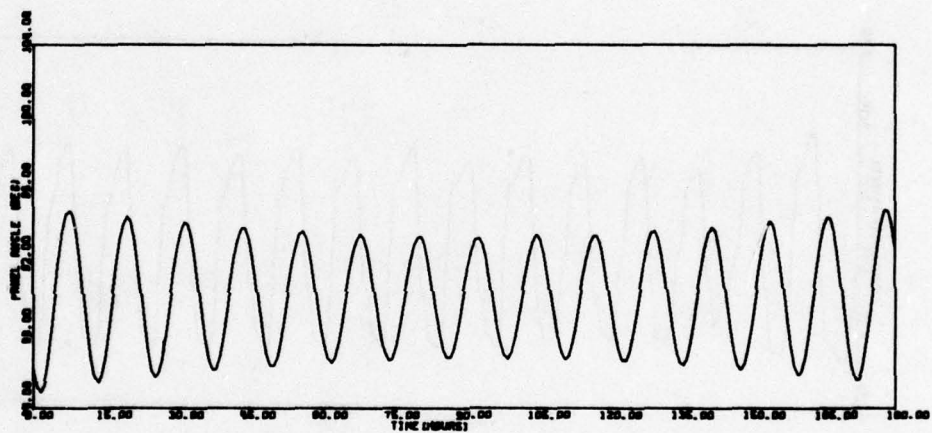
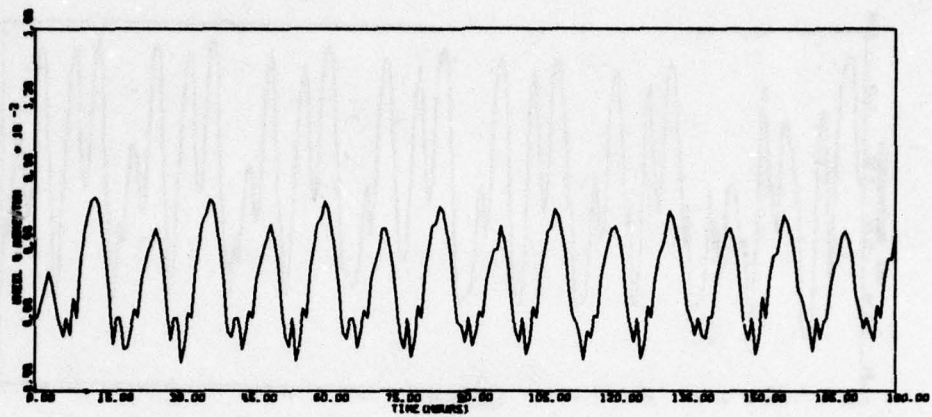


Figure 51. Run 2 - Sunline 86⁰ - Nominal (concluded)

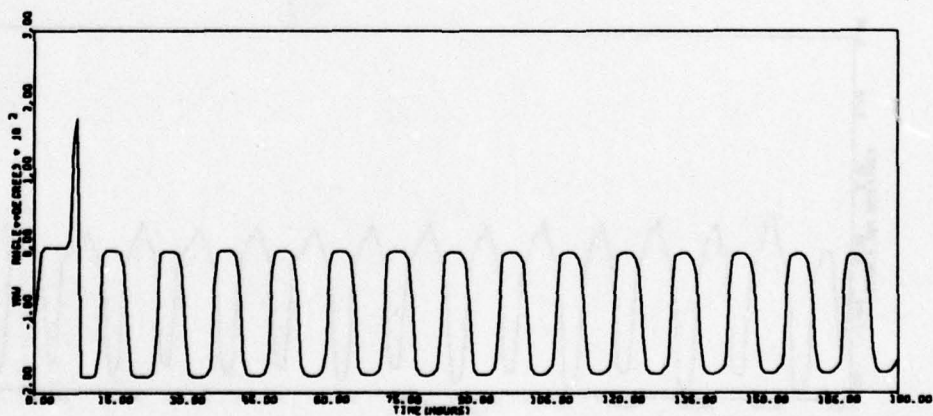
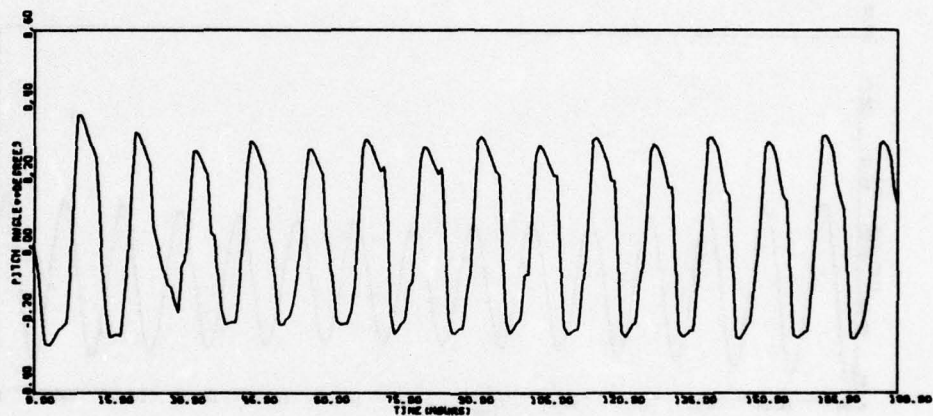
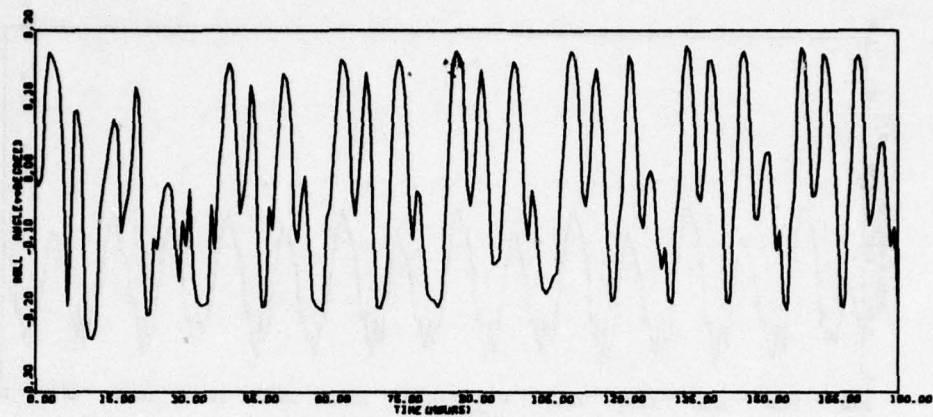


Figure 52. Run 3 - Sunline 0° - Nominal

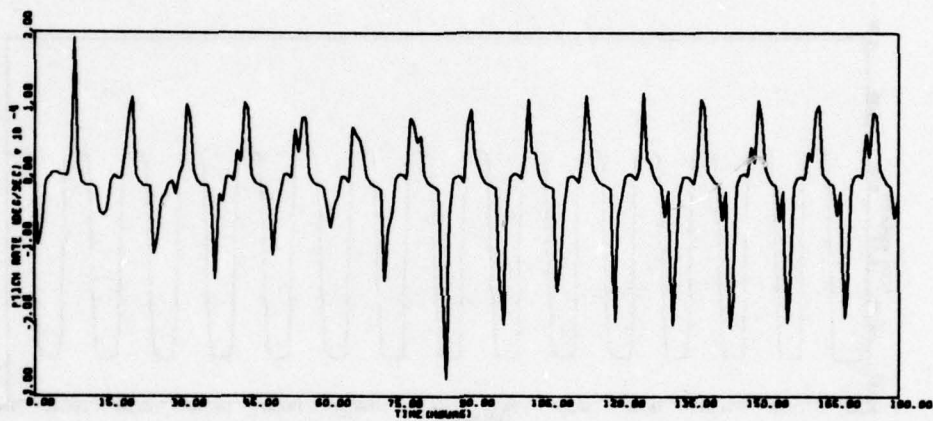
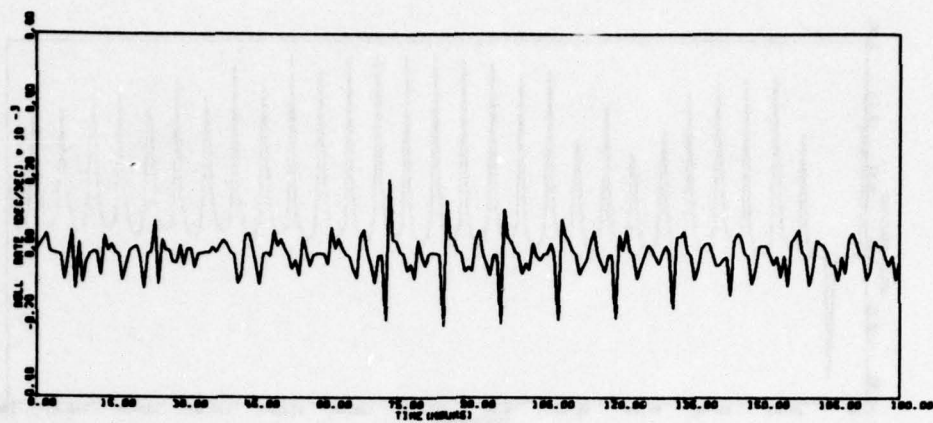


Figure 52. Run 3 - Sunline 0° - Nominal (continued)

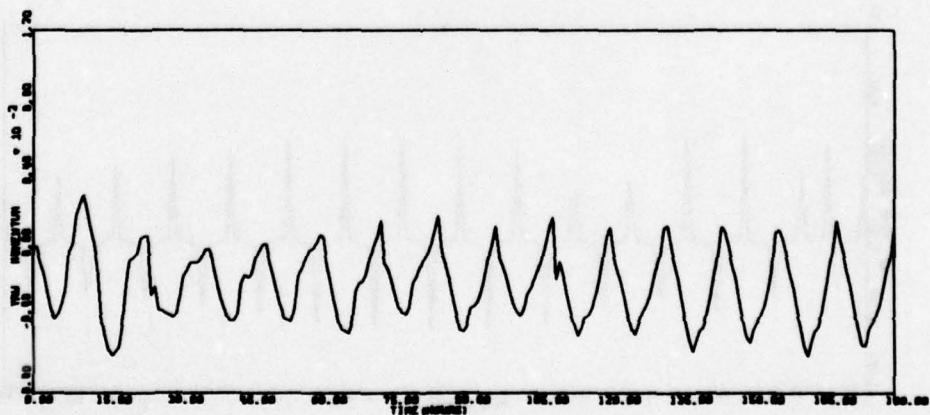
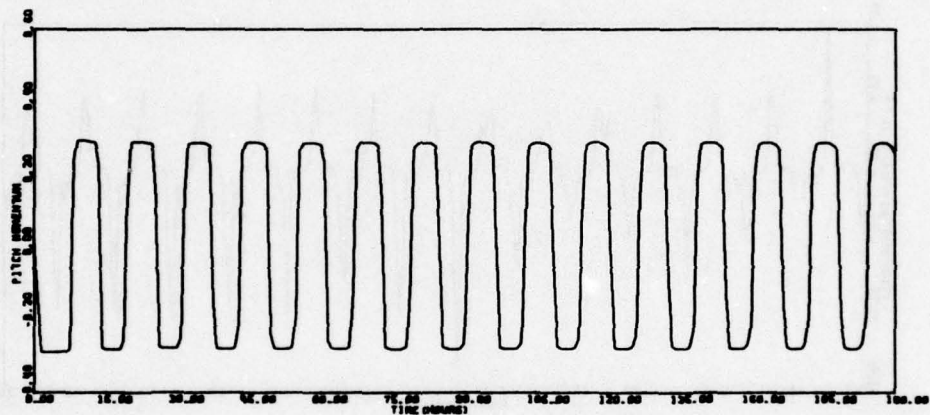
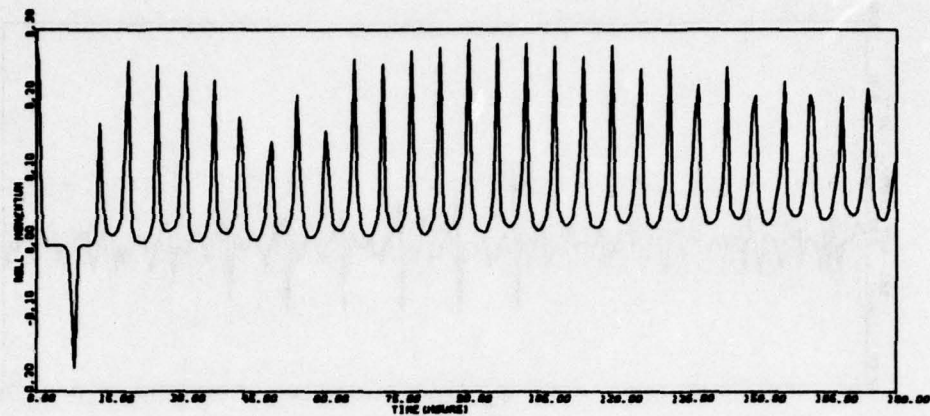


Figure 52. Run 3 - Sunline 0° - Nominal (continued)

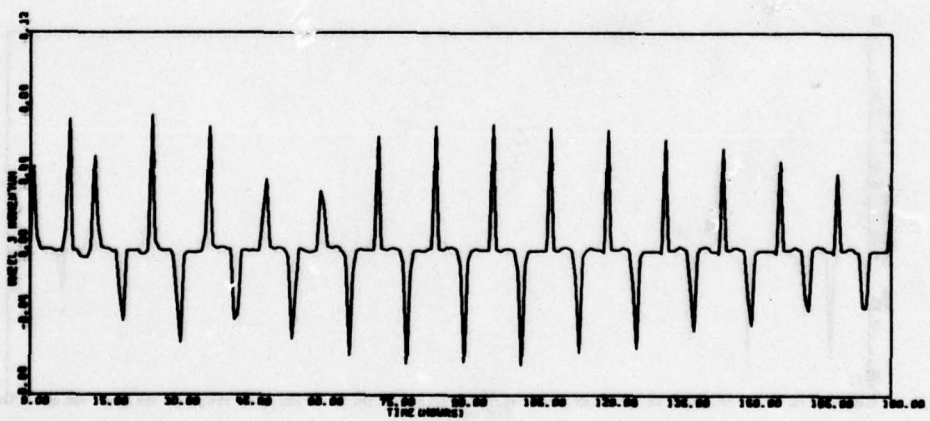
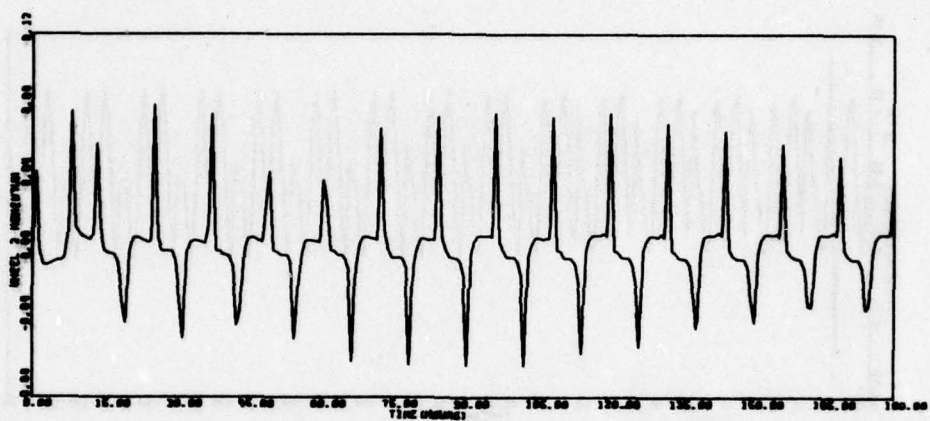
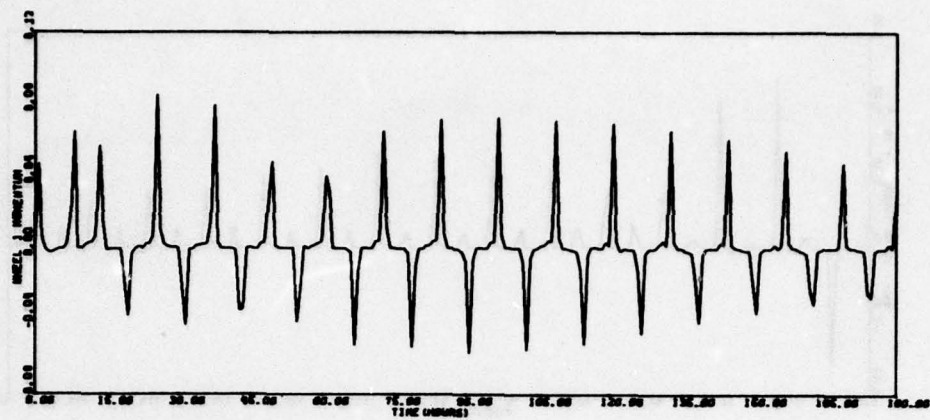


Figure 52. Run 3 - Sunline 0° - Nominal (continued)

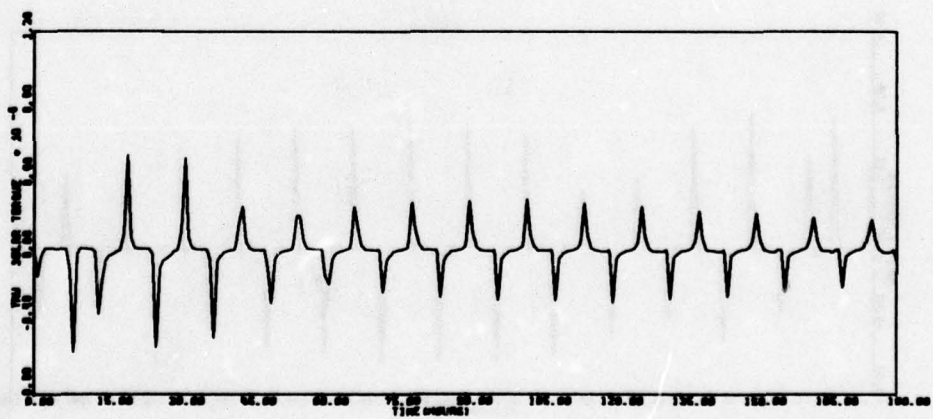
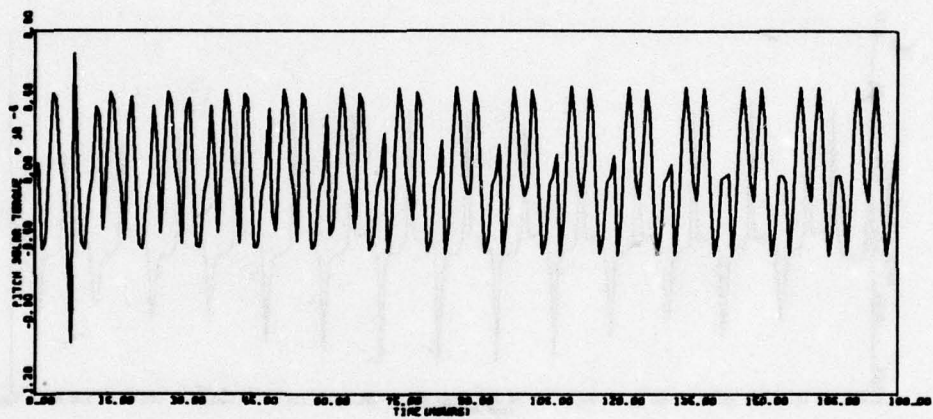
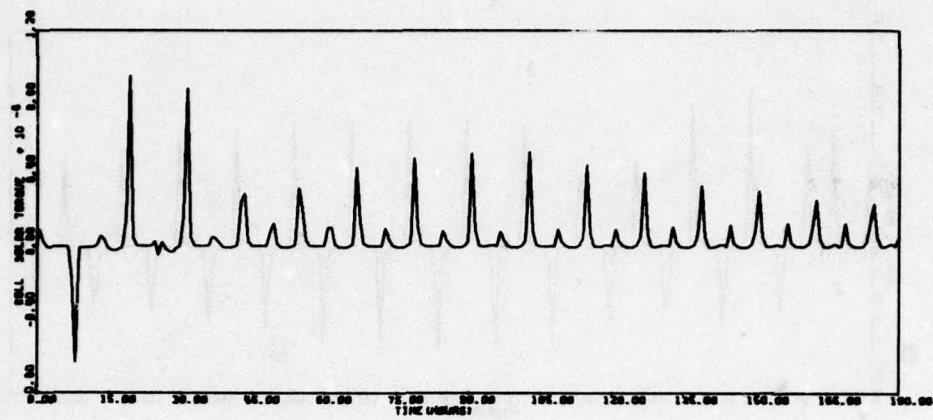


Figure 52. Run 3 - Sunline 0⁰ - Nominal (continued)

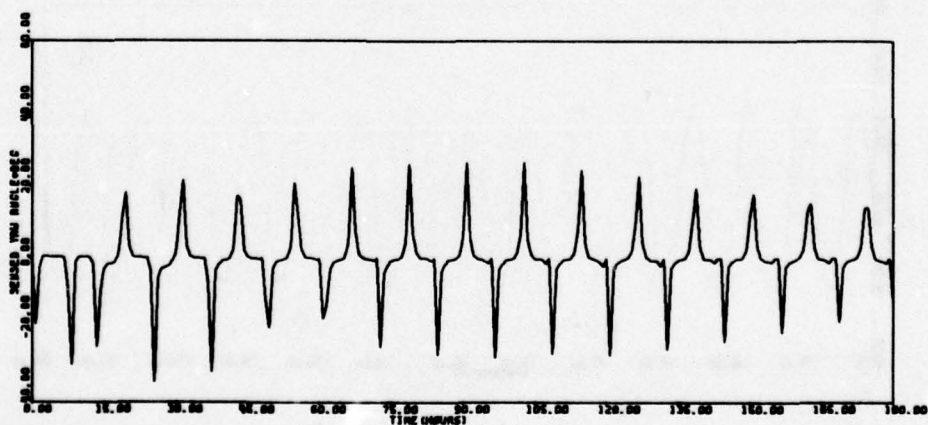
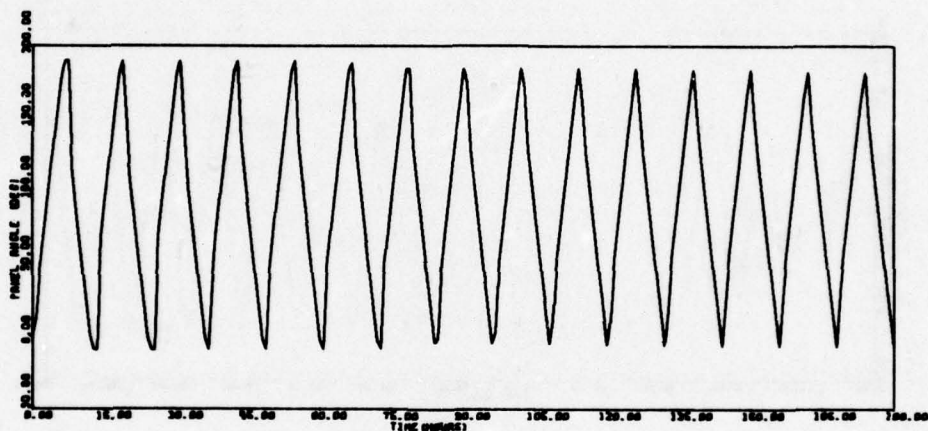


Figure 52. Run 3 - Sunline 0° - Nominal (concluded)

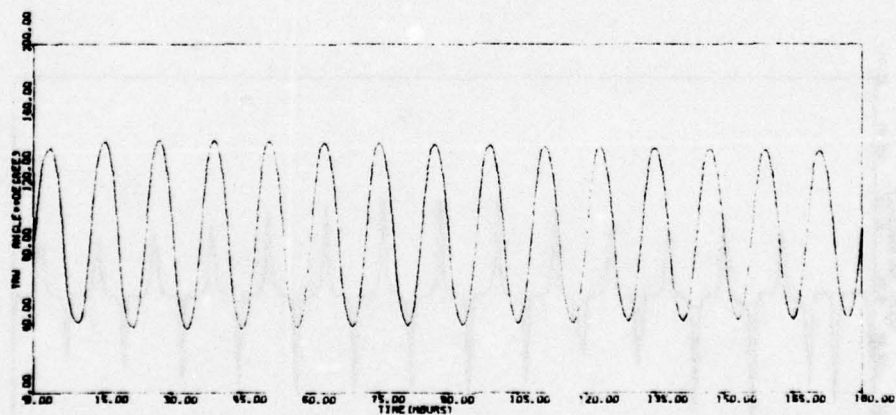
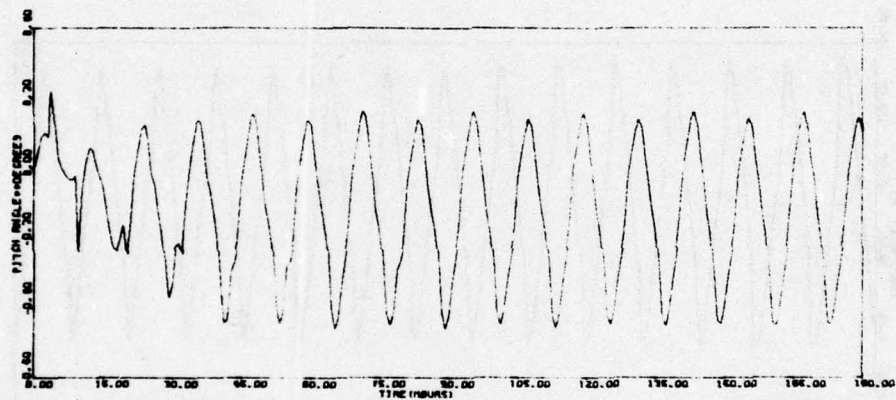
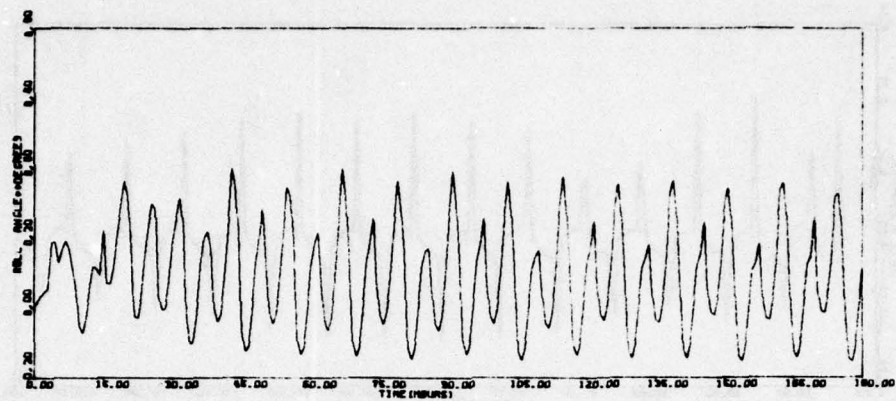


Figure 53. Run 1A - Sensed Pitch and Roll Angles
in Feed Back Nominal

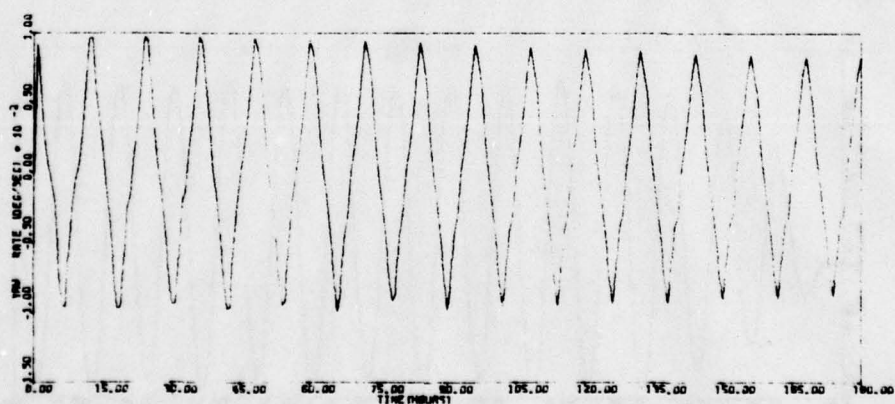
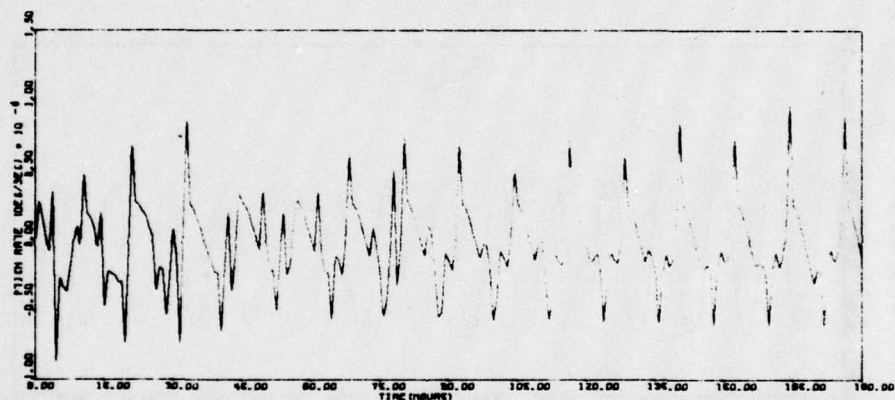
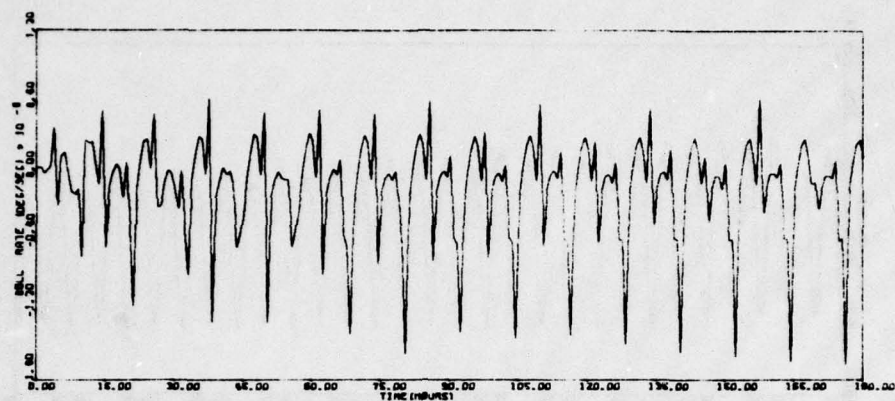


Figure 53. Run 1A - Sensed Pitch and Roll Angles in Feed Back Nominal (continued)

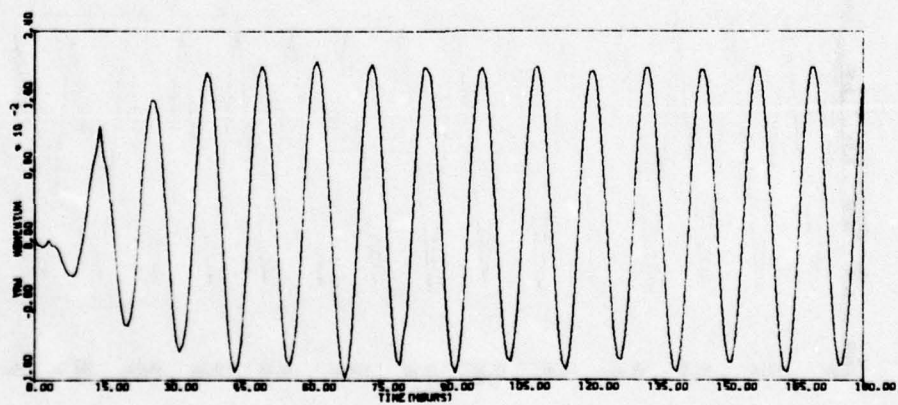
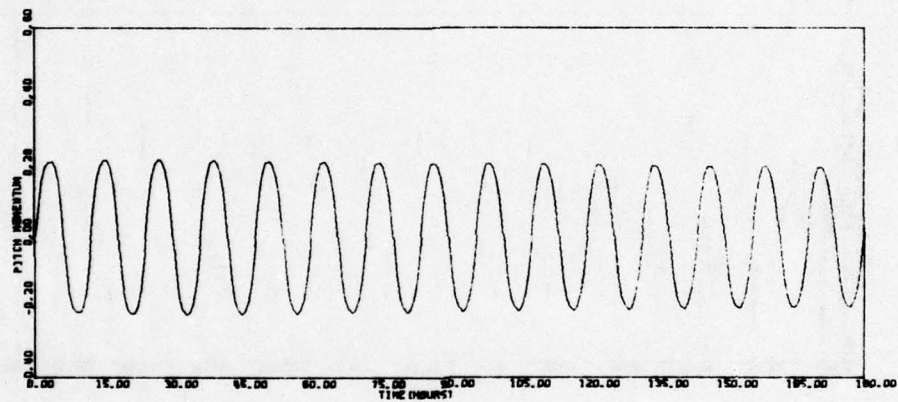
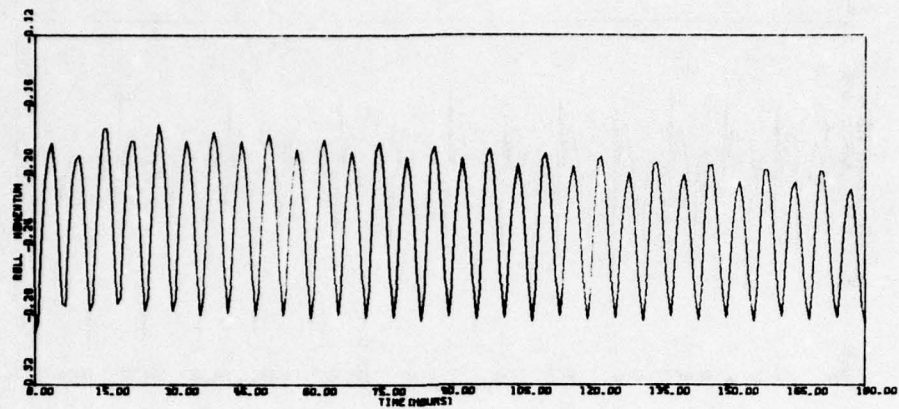


Figure 53. Run 1A - Sensed Pitch and Roll Angles
in Feed Back Nominal (continued)

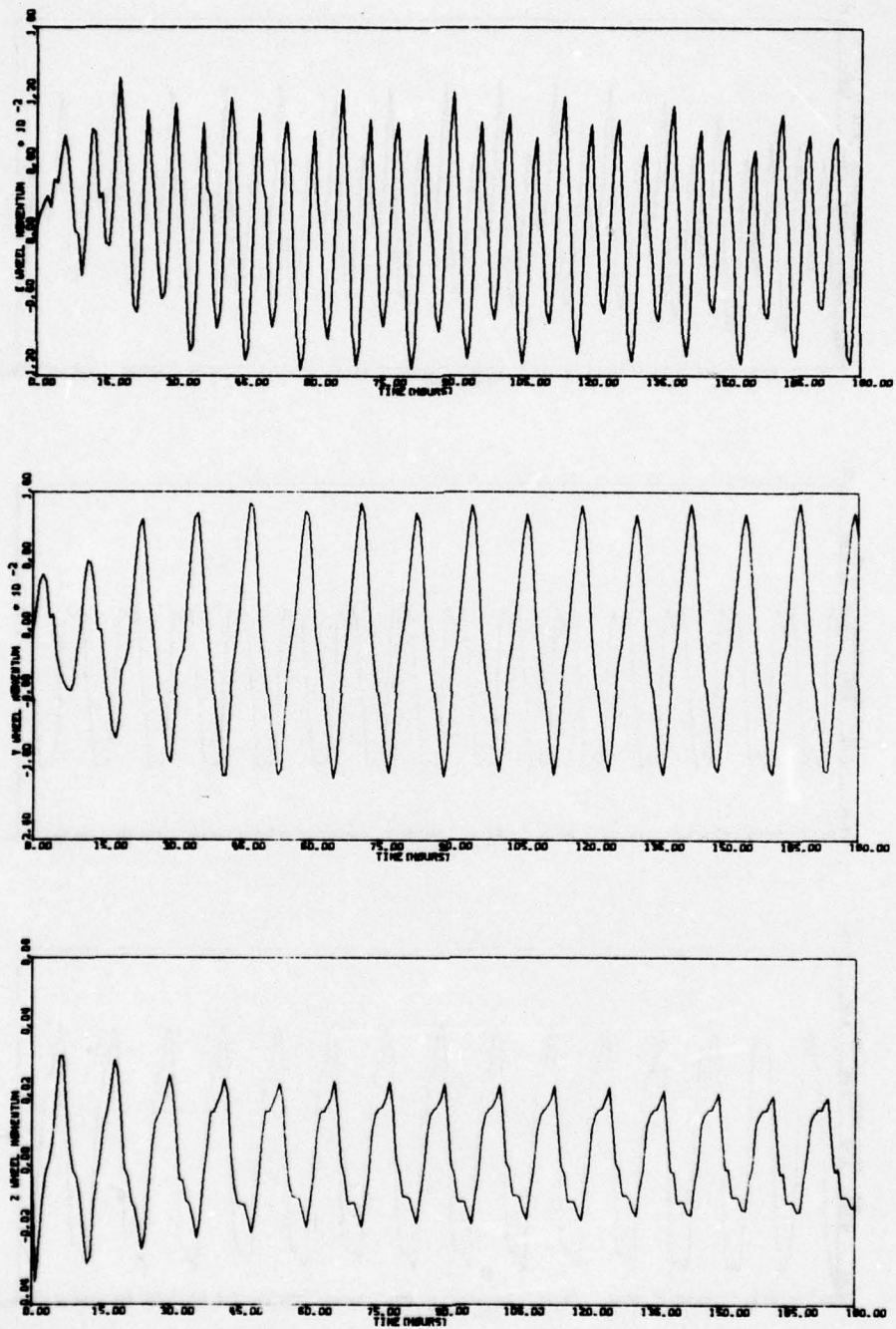


Figure 53. Run 1A - Sensed Pitch and Roll Angles
in Feed Back Nominal (continued)

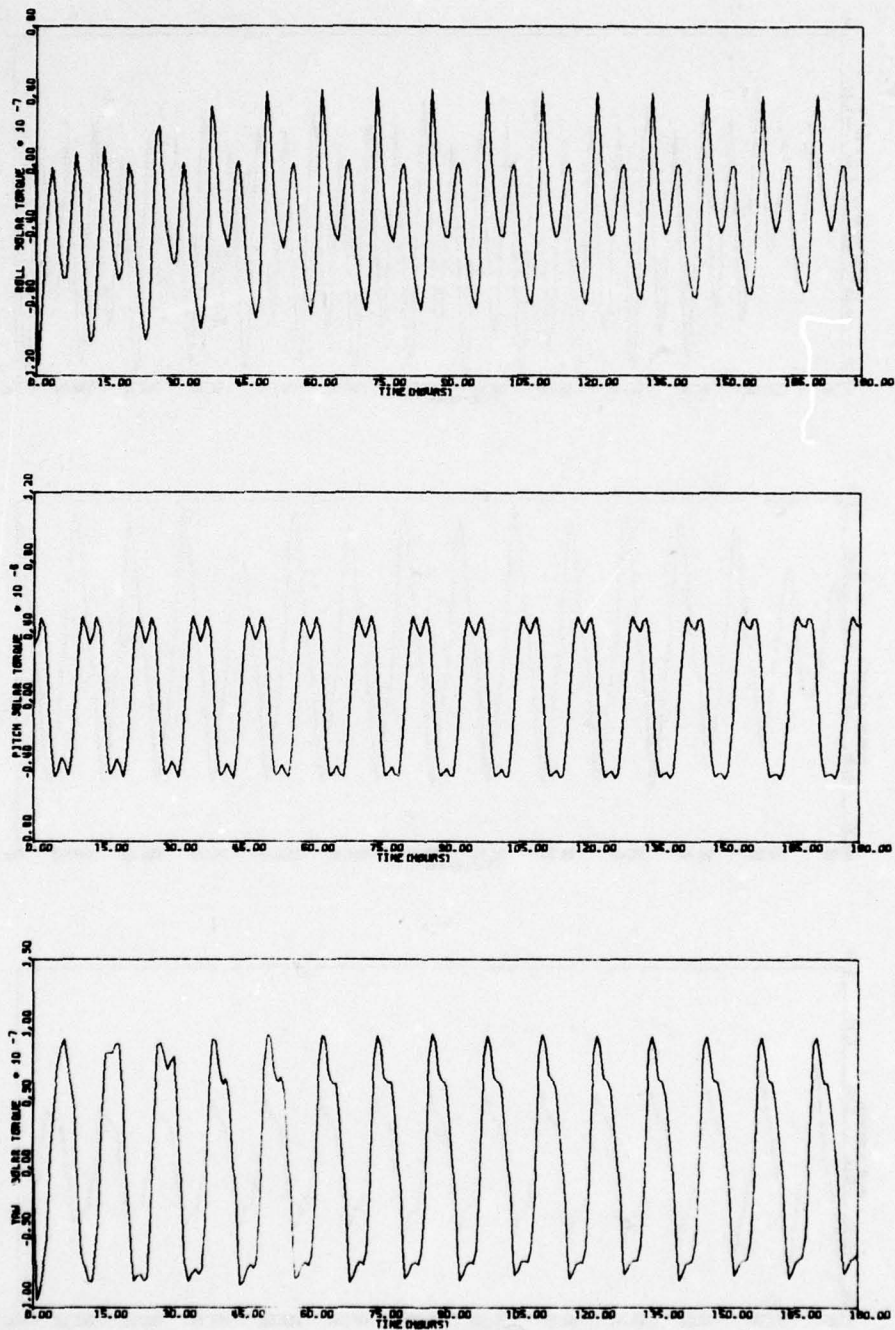


Figure 53. Run 1A - Sensed Pitch and Roll Angles in Feed Back Nominal (continued)

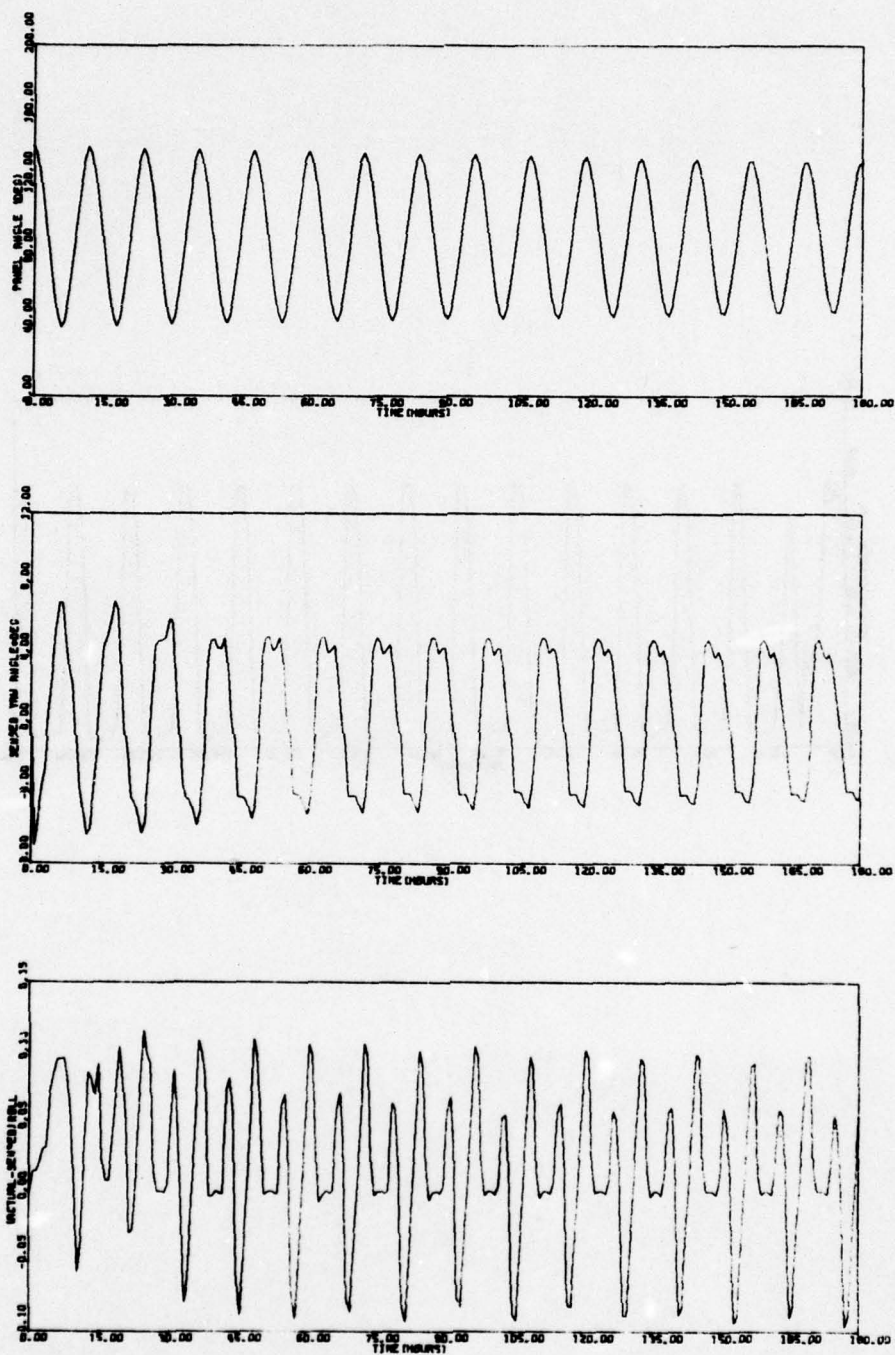


Figure 53. Run 1A - Sensed Pitch and Roll Angles in Feed Back Nominal (continued)

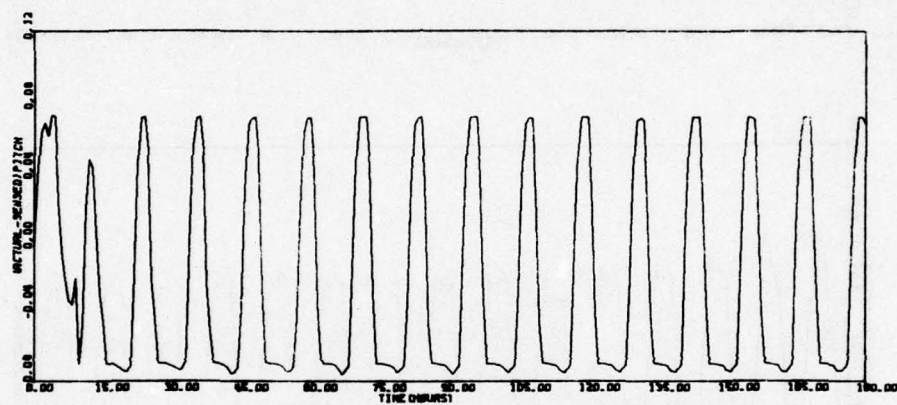


Figure 53. Run 1A - Sensed Pitch and Roll Angles
in Feed Back Nominal (concluded)

BEST AVAILABLE COPY

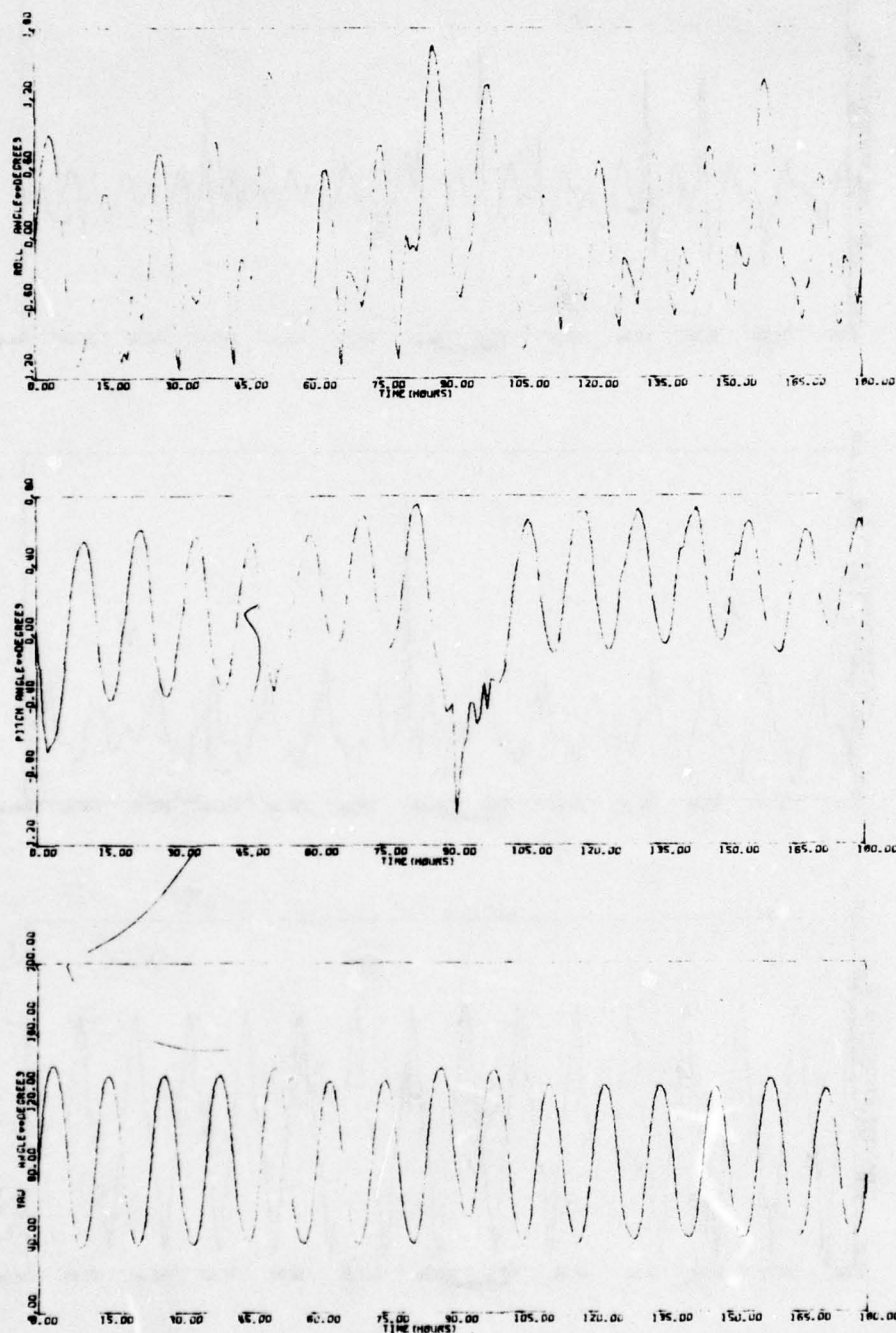


Figure 54. Run 1B - Sensed Pitch and Roll Angles
in Feed Back Earth Sensor Misaligned

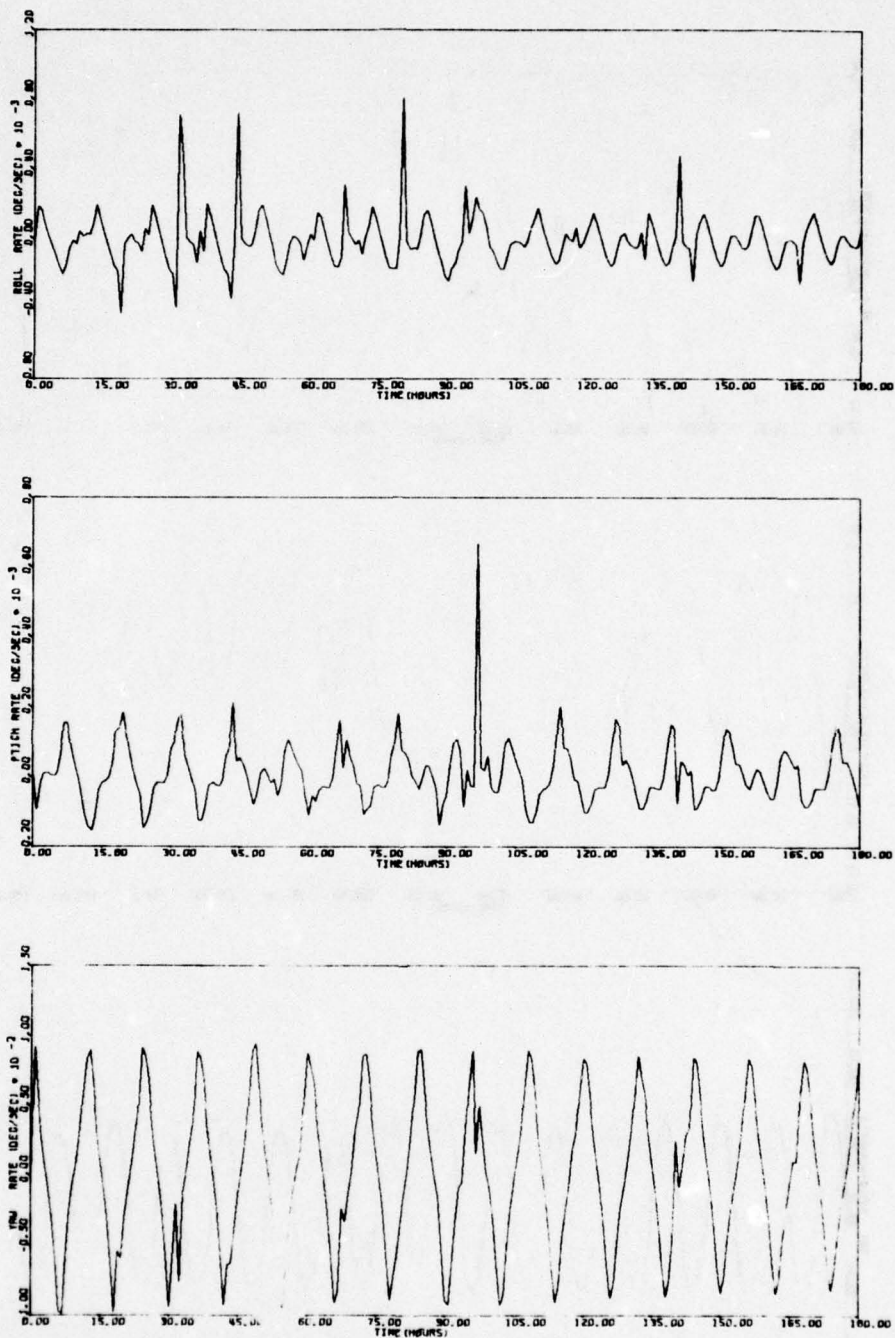


Figure 54. Run 1B - Sensed Pitch and Roll Angles in Feed Back Earth Sensor Misaligned (continued)

BEST AVAILABLE COPY

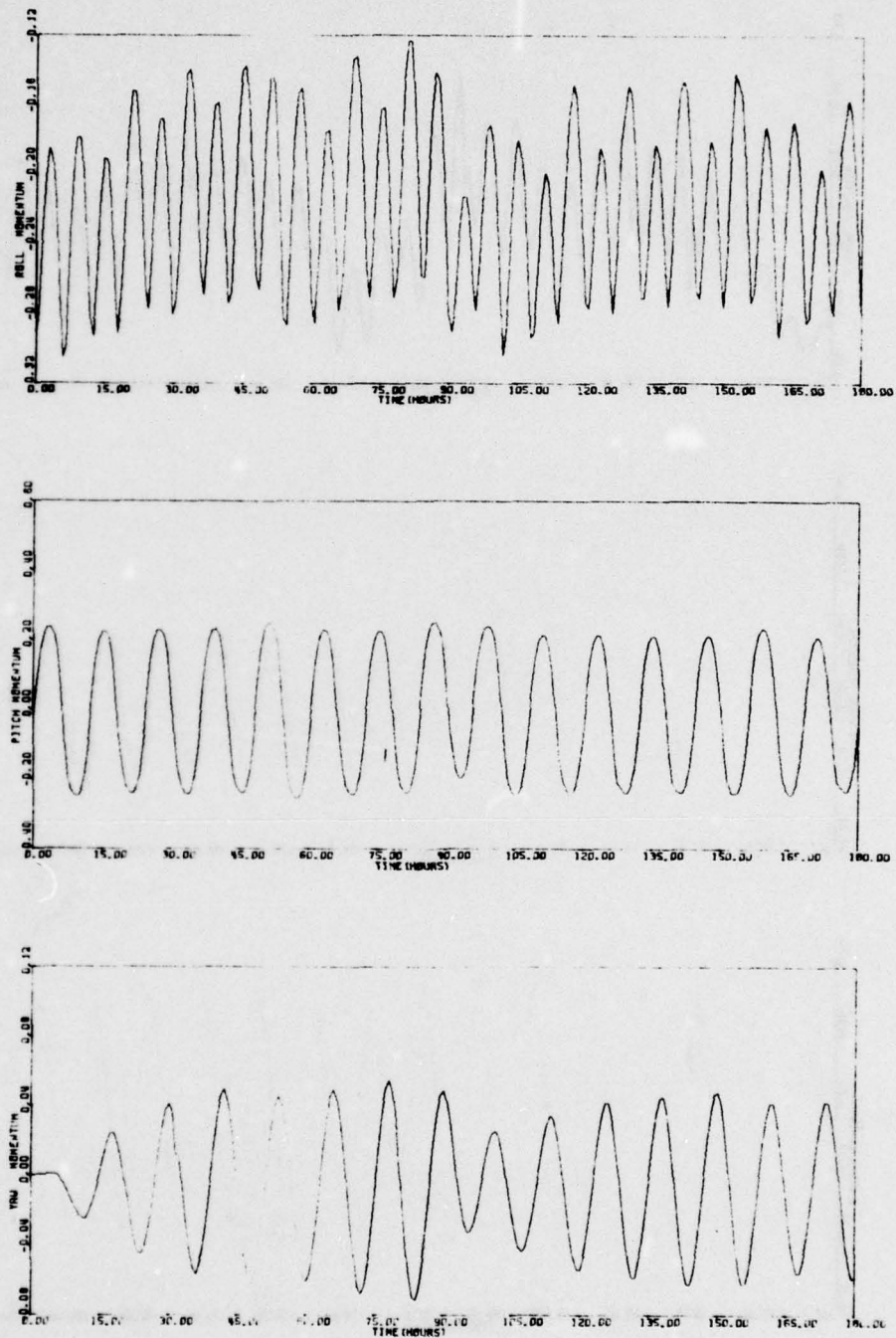


Figure 54. Run 1B - Sensed Pitch and Roll Angles in Feed Back Earth Sensor Misaligned (continued)

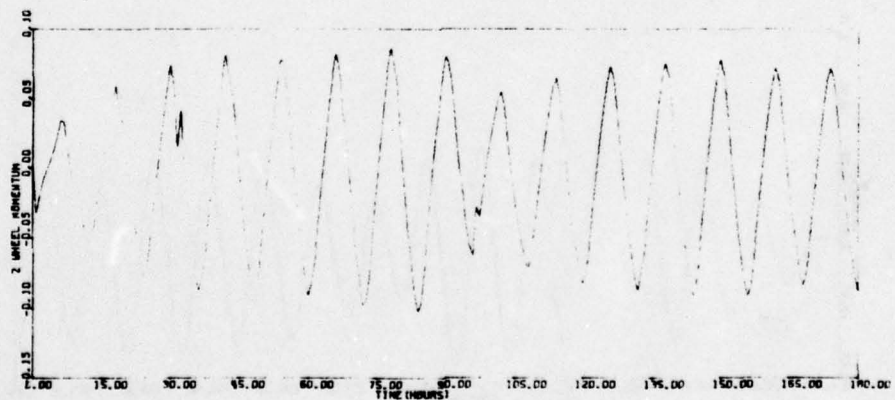
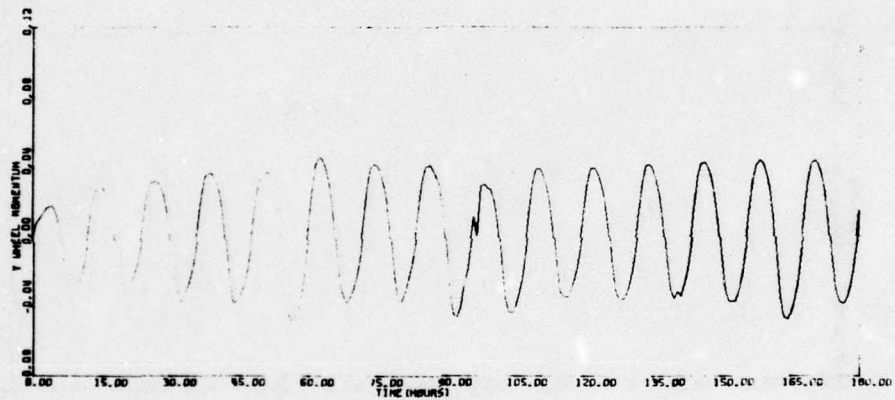
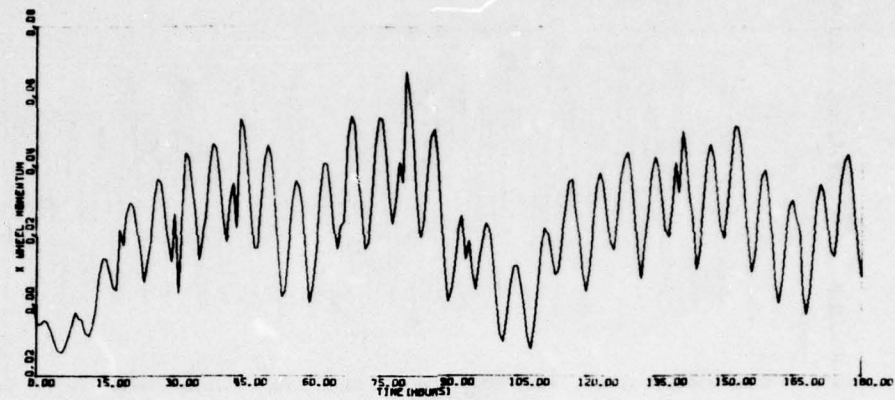


Figure 54. Run 1B - Sensed Pitch and Roll Angles in Feed Back Earth Sensor Misaligned (continued)

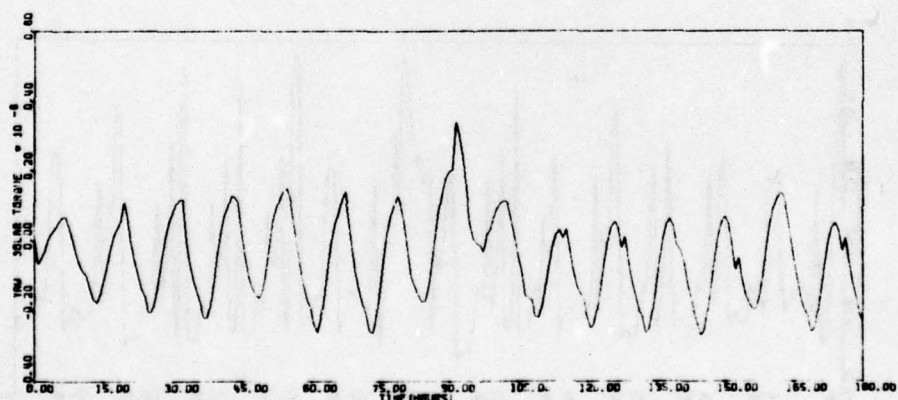
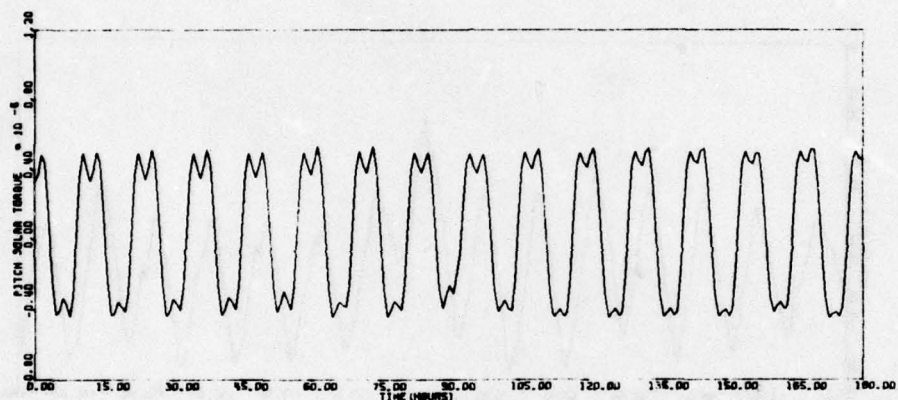
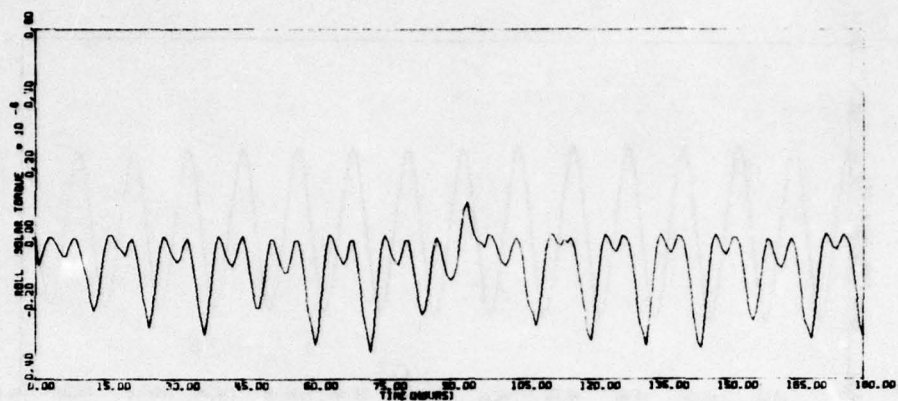


Figure 54. Run 1B - Sensed Pitch and Roll Angles in Feed Back Earth Sensor Misaligned (continued)

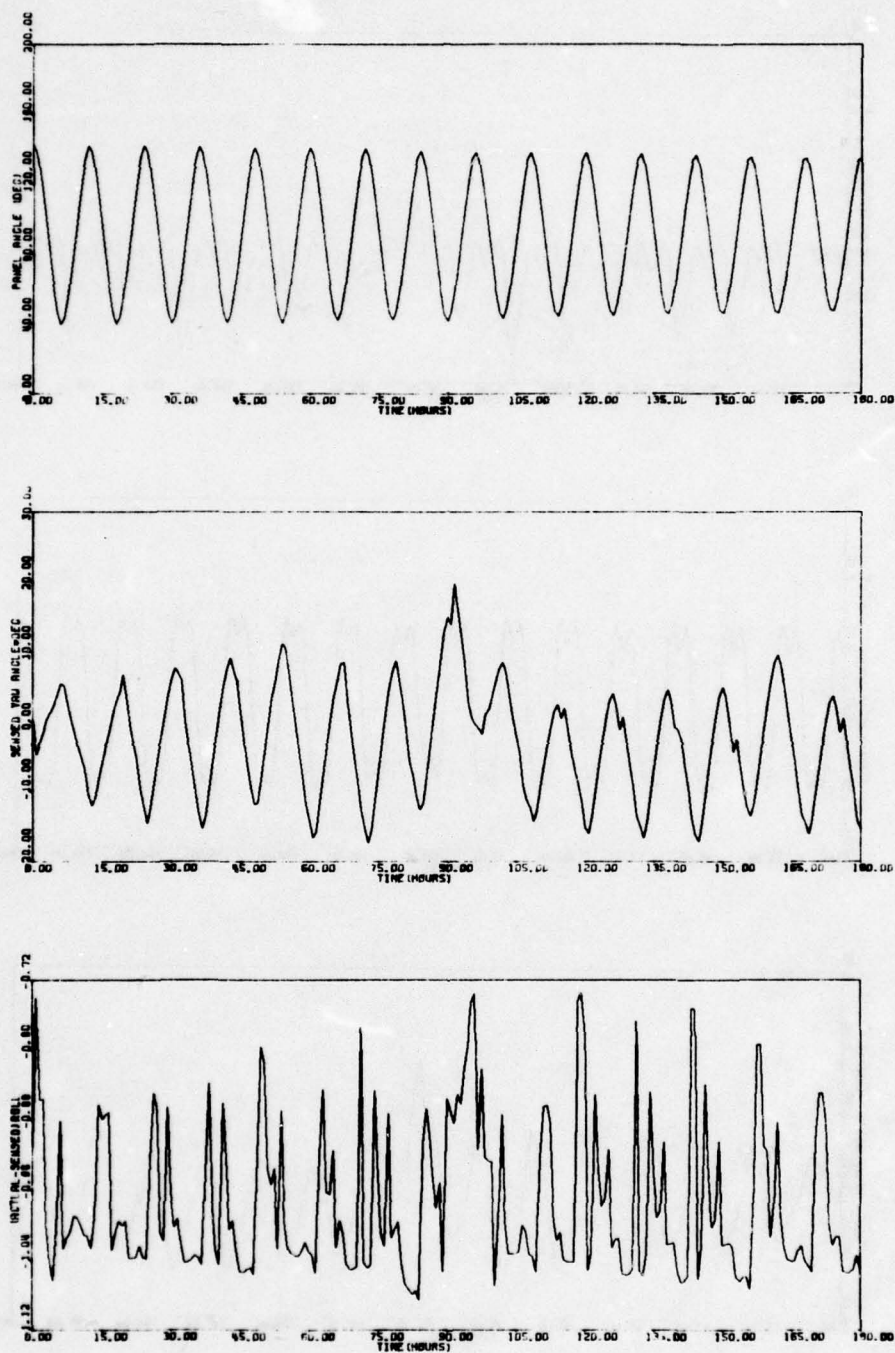


Figure 54. Run 1B - Sensed Pitch and Roll Angles in Feed Back Earth Sensor Misaligned (continued)

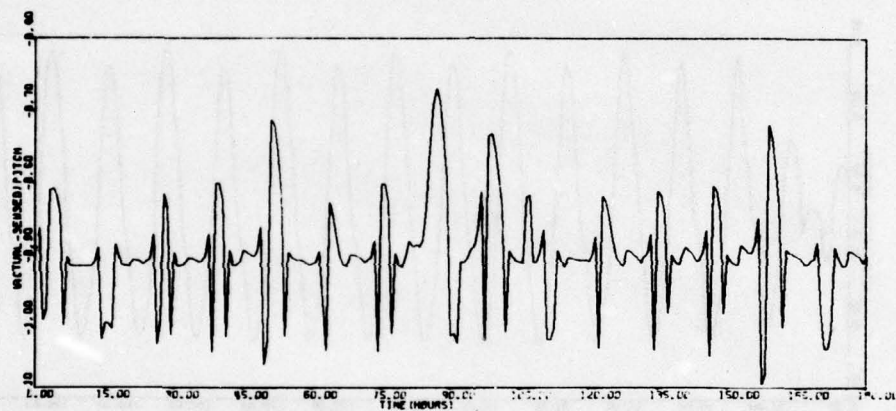


Figure 54. Run 1B - Sensed Pitch and Roll Angles in Feed Back Earth Sensor Misaligned (concluded)

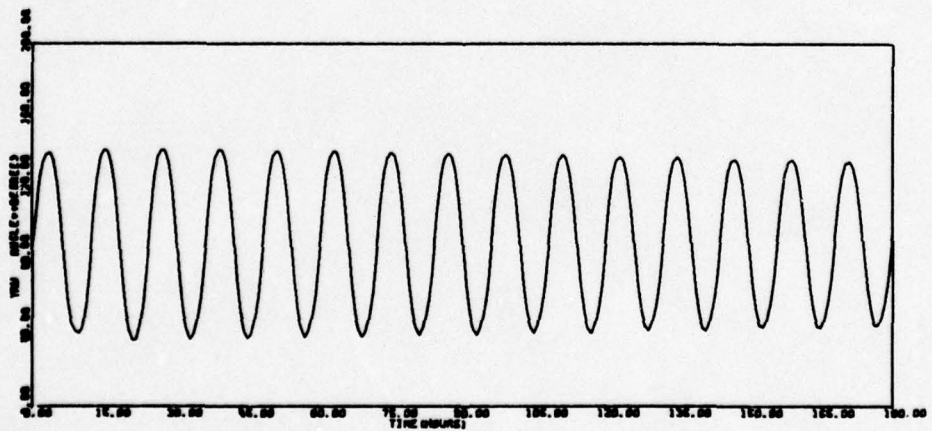
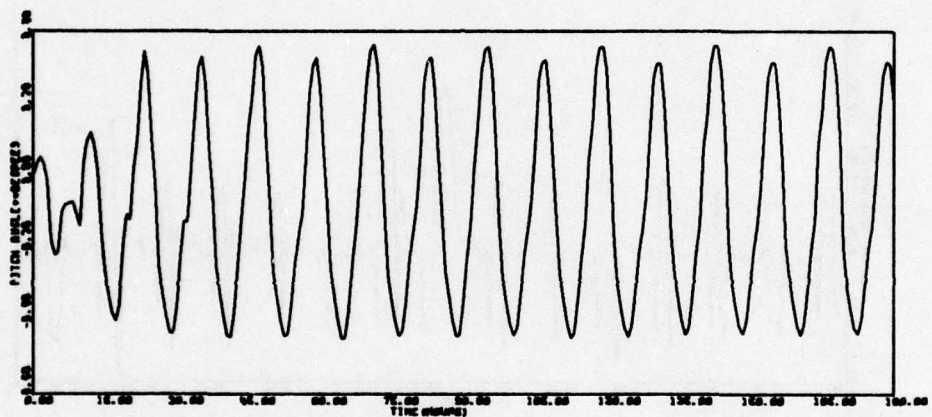
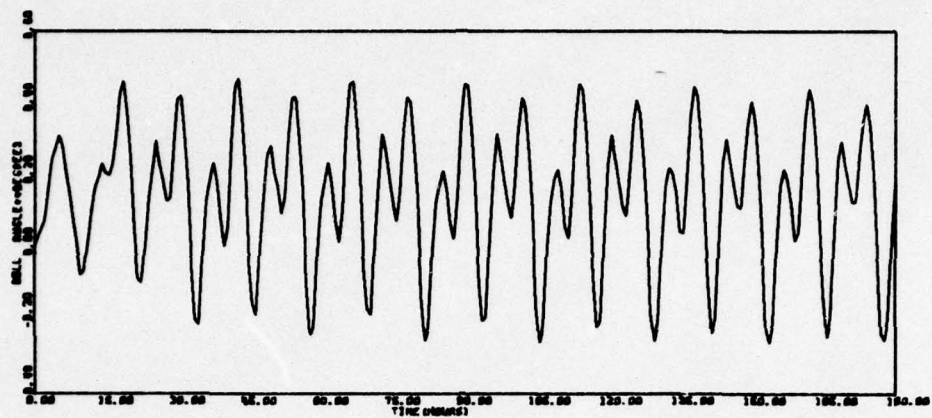


Figure 55. Run 4 - Sunline 45° - $K_{\phi}/2$

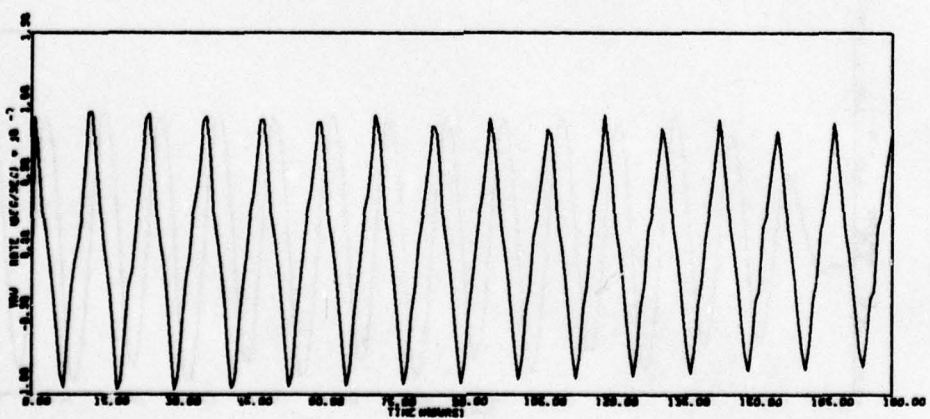
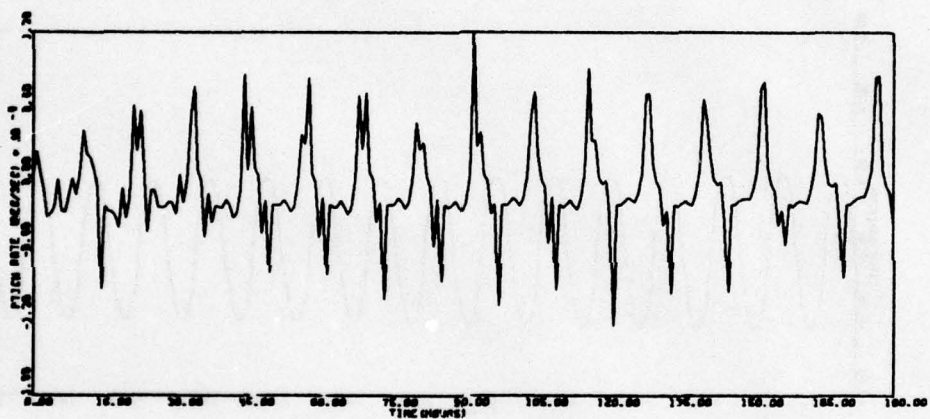
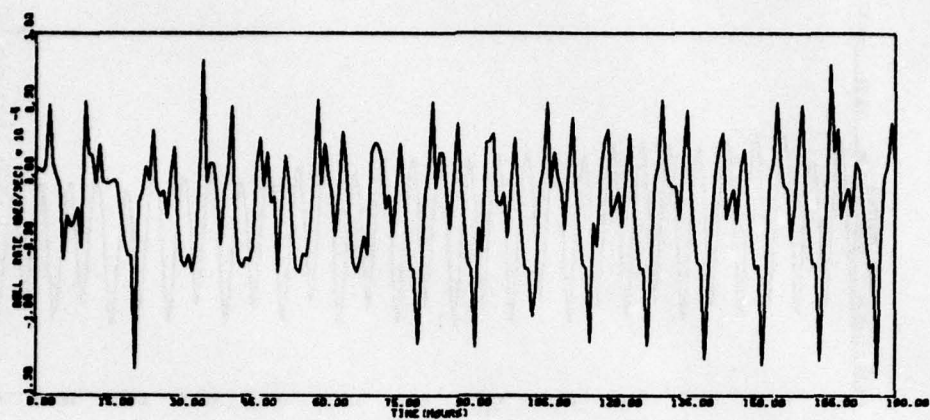


Figure 55. Run 4 - Sunline 45° - $K_{\phi}/2$ (continued)

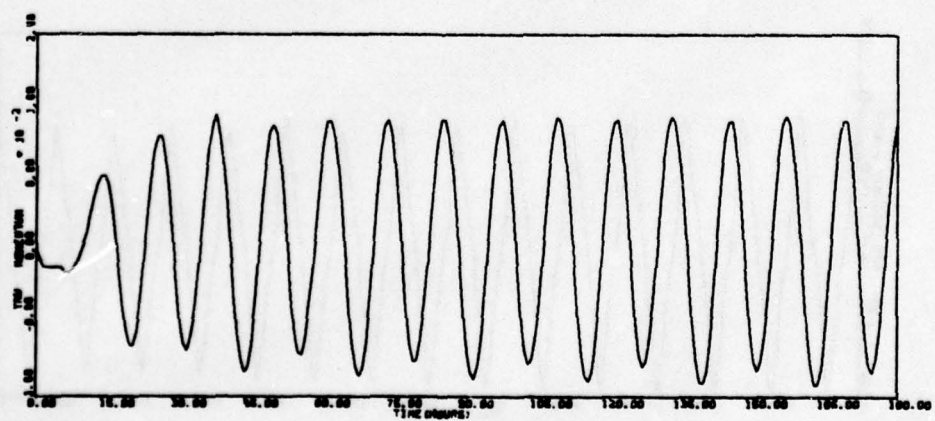
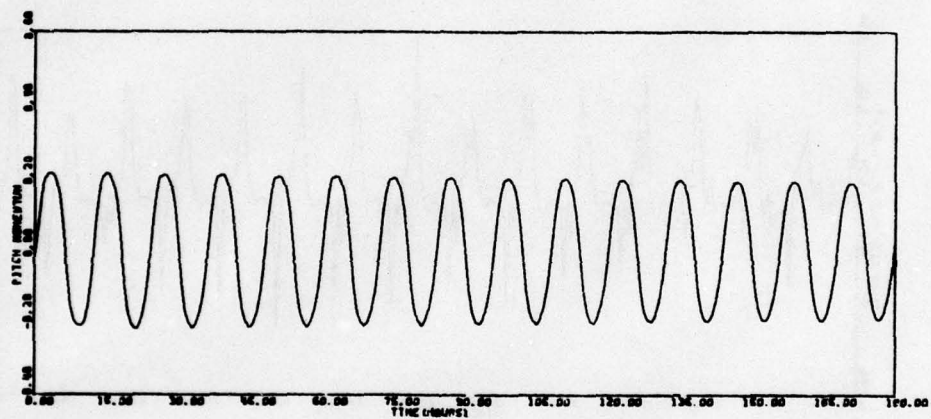
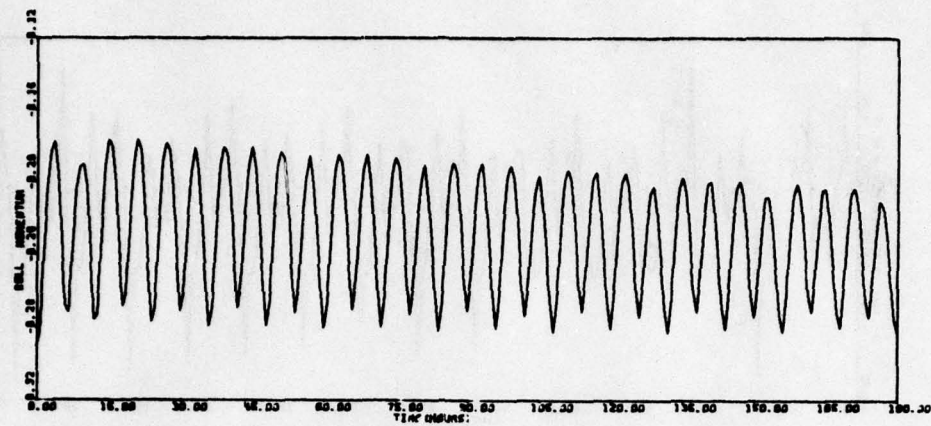


Figure 55. Run 4 - Sunline 45° - $K_{\phi}/2$ (continued)

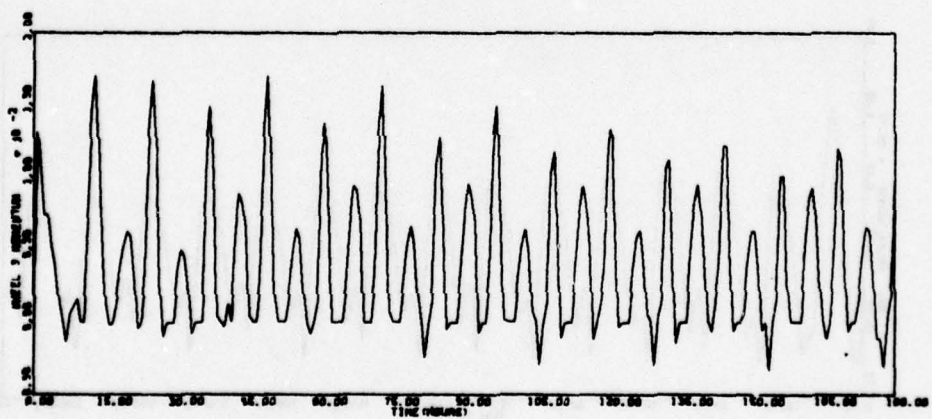
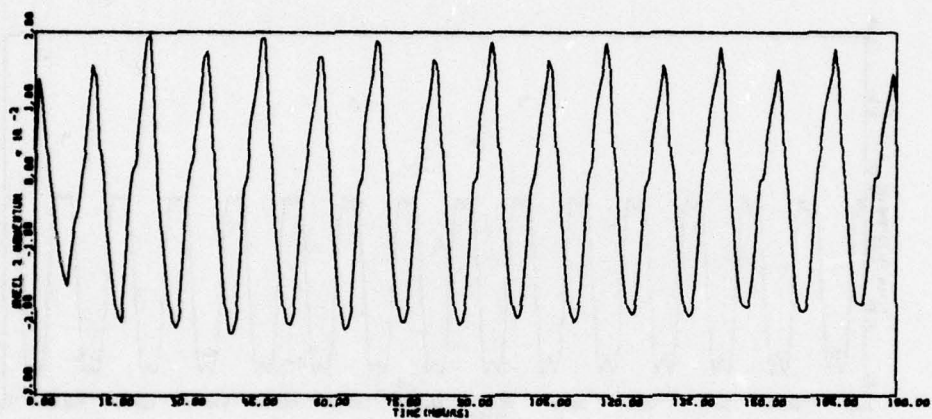
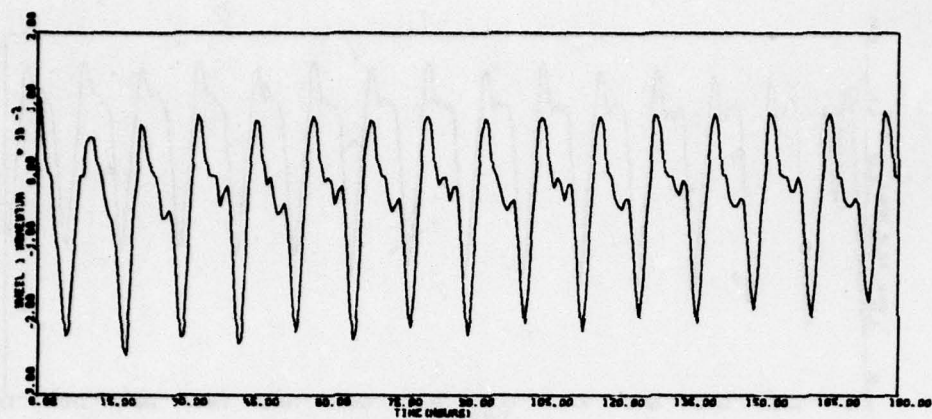


Figure 55. Run 4 - Sunline 45° - $K_\phi/2$ (continued)

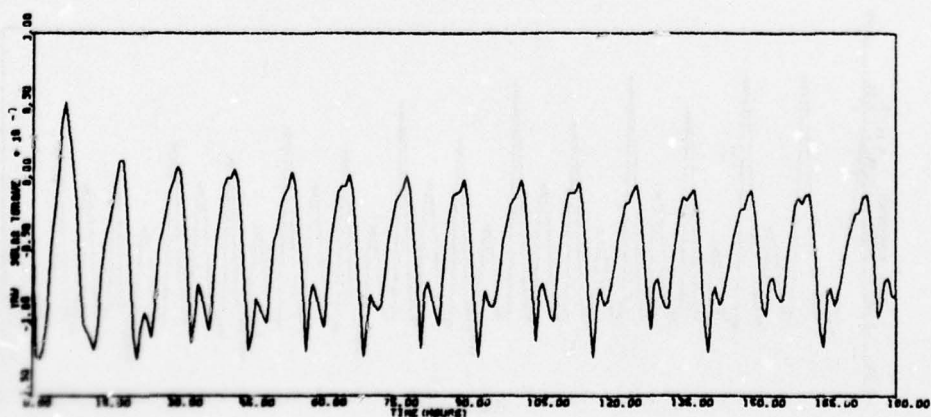
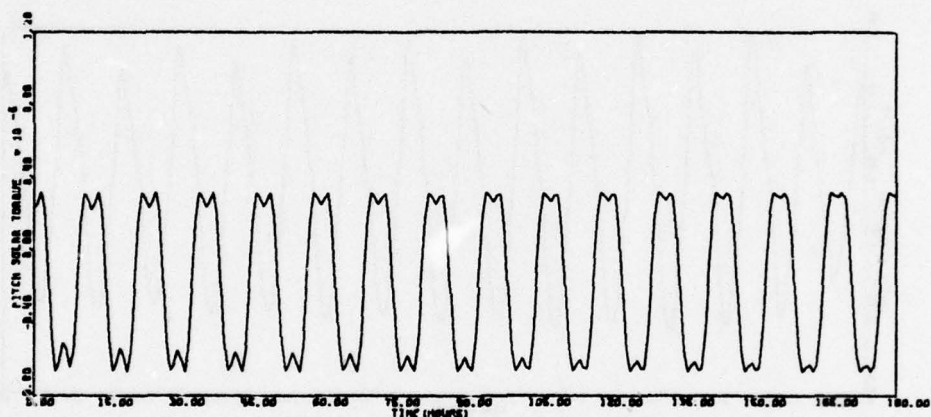
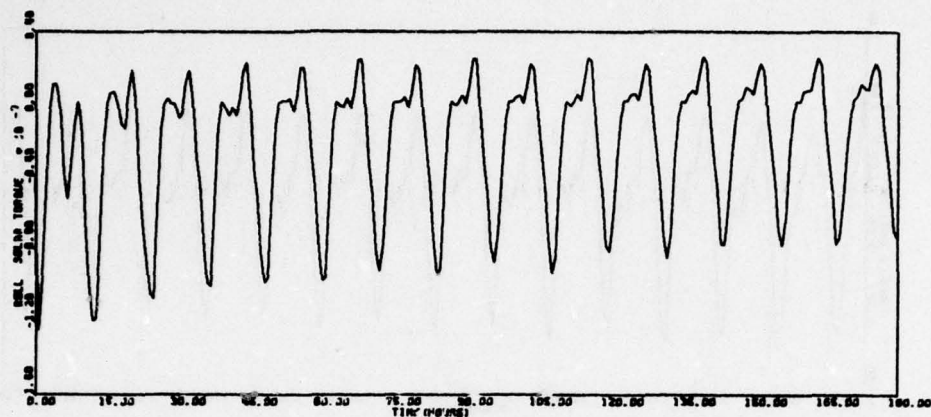


Figure 55. Run 4 - Sunline 45° - $K_{\phi}/2$ (continued)

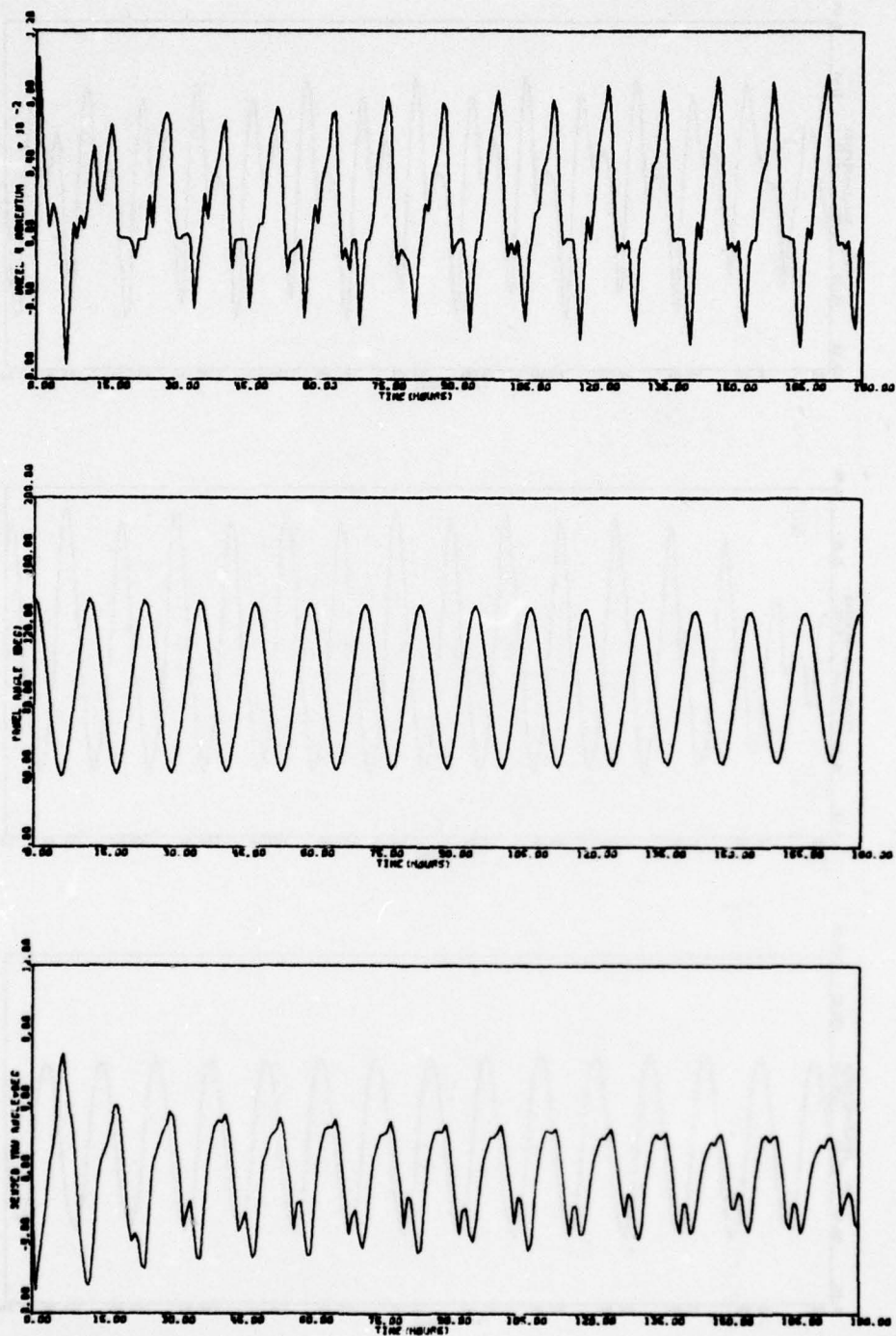


Figure 55. Run 4 - Sunline 45° - $K_{\phi}/2$ (concluded)

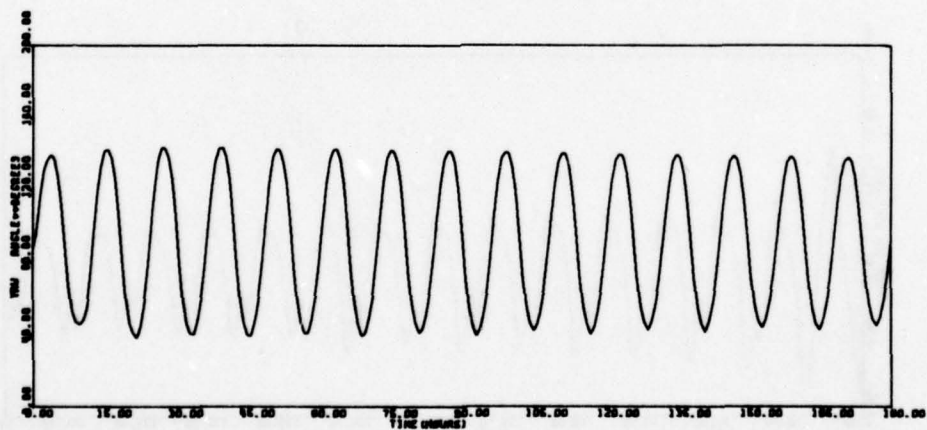
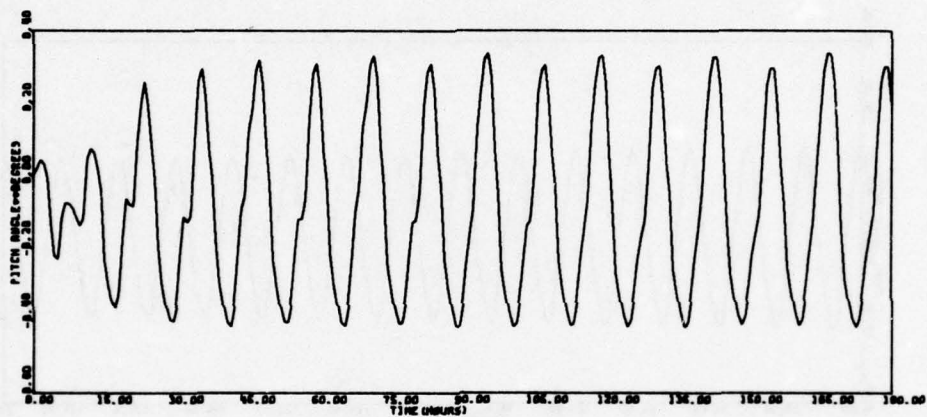
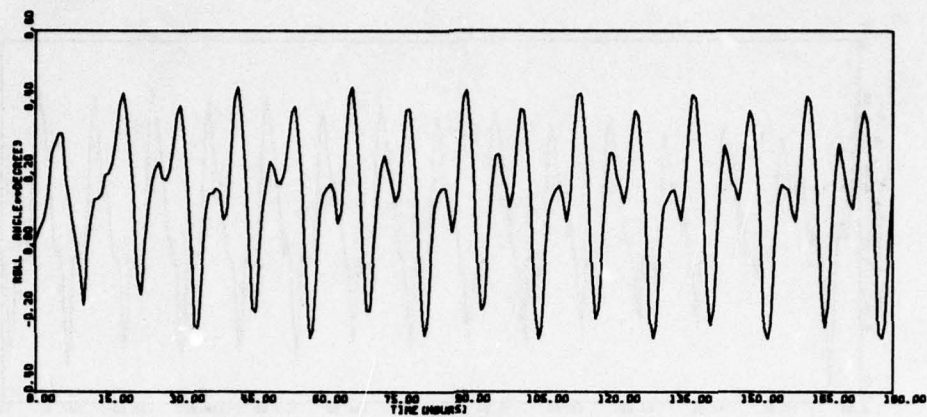


Figure 56. Run 4A - Sunline 45° - $2K_{\varphi}$

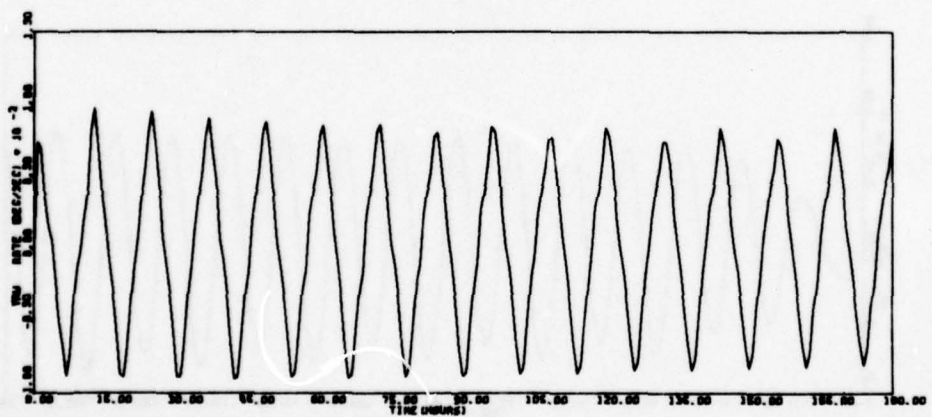
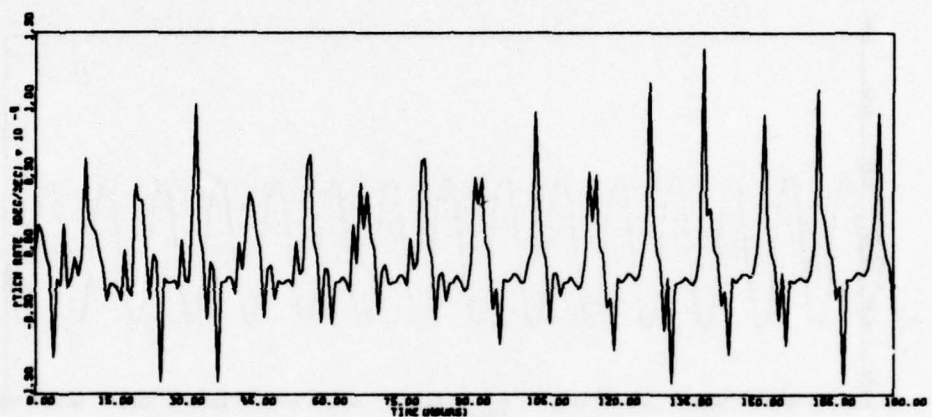
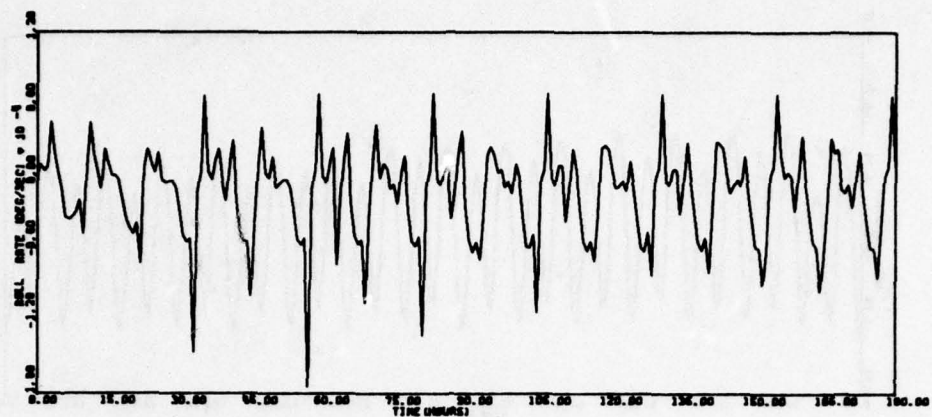


Figure 56. Run 4A - Sunline 45° - $2K_{\phi}$ (continued)

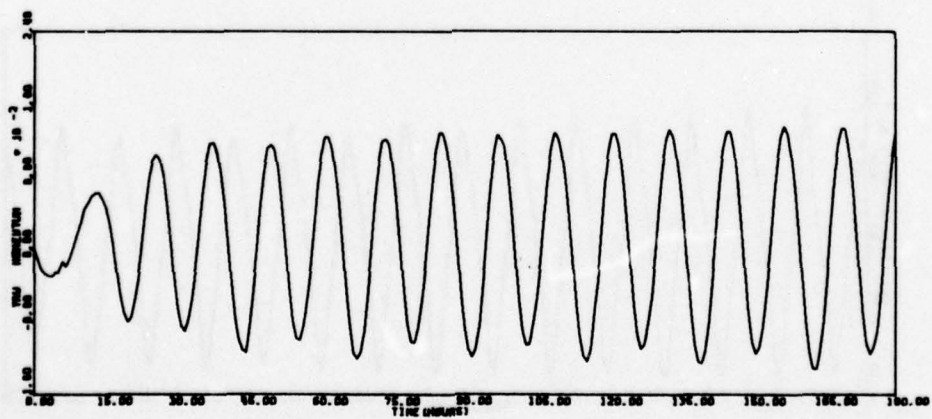
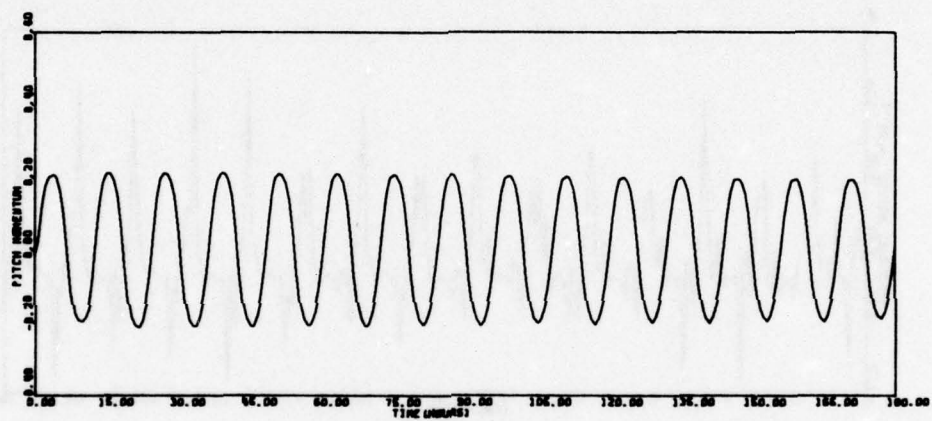
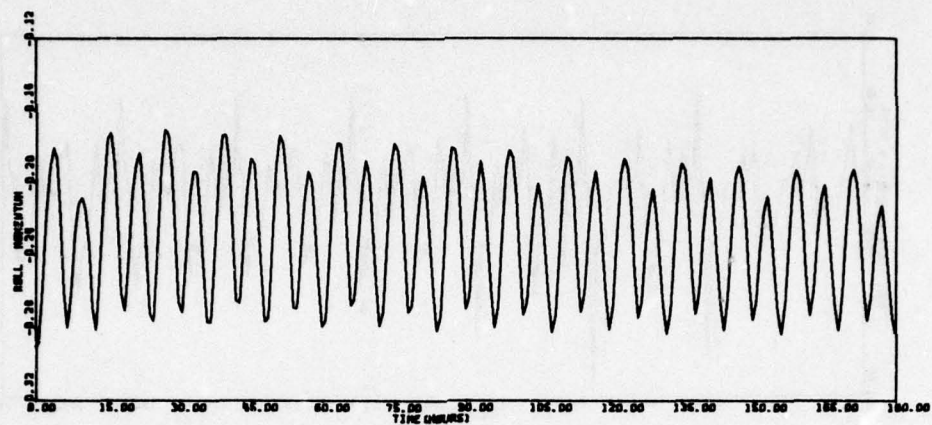


Figure 56. Run 4A - Sunline 45° - $2K_{\varphi}$ (continued)

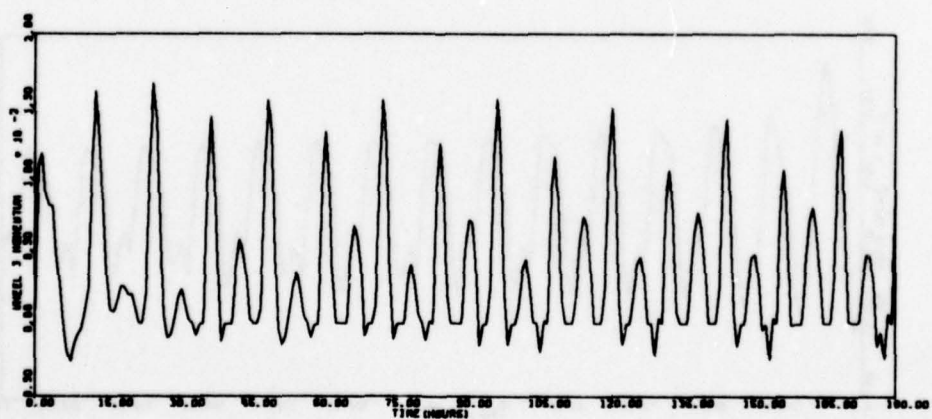
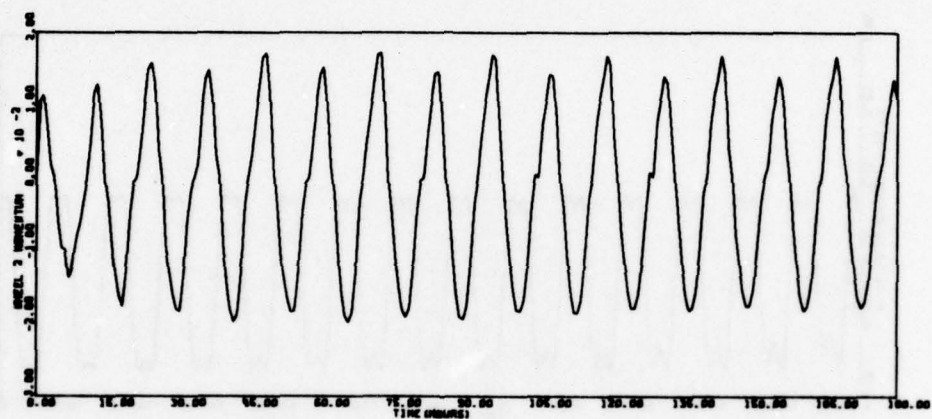
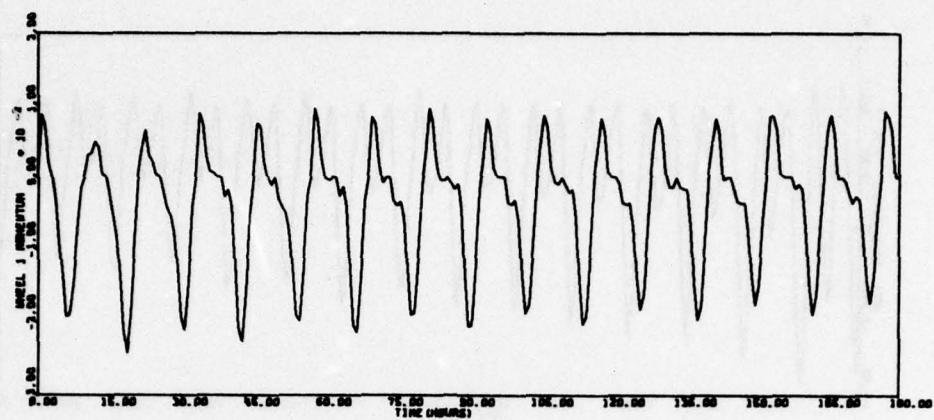


Figure 56. Run 4A - Sunline 45° - $2K_{\phi}$ (continued)

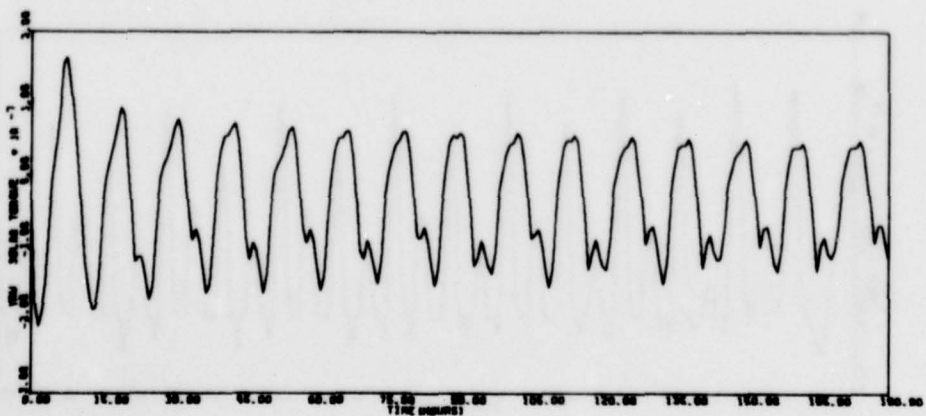
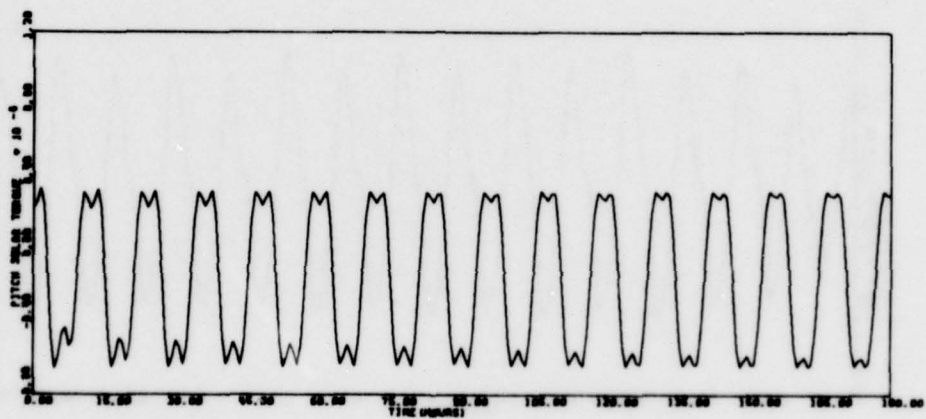
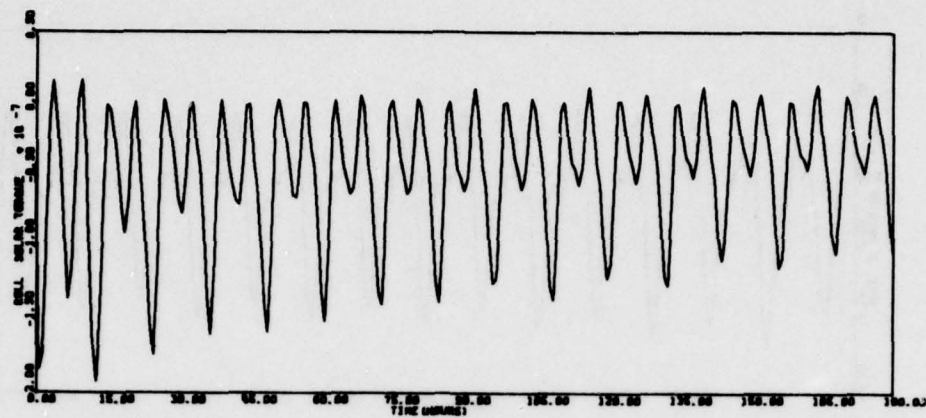


Figure 56. Run 4A - Sunline 45⁰ - 2K_φ (continued)

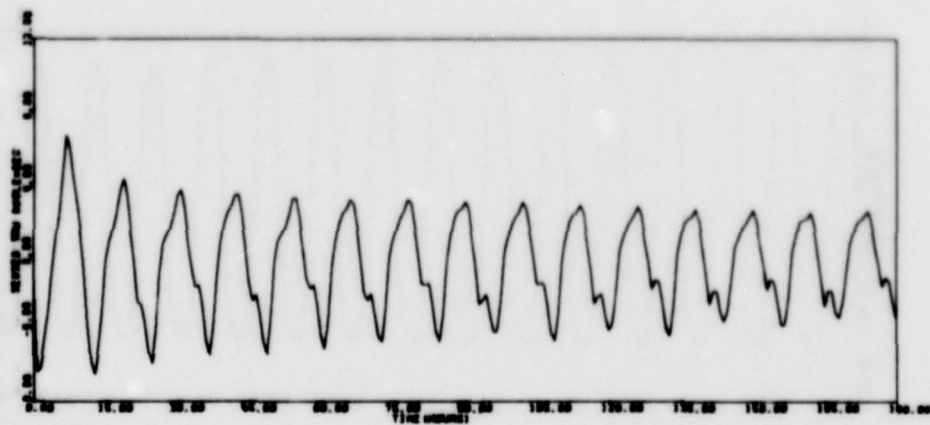
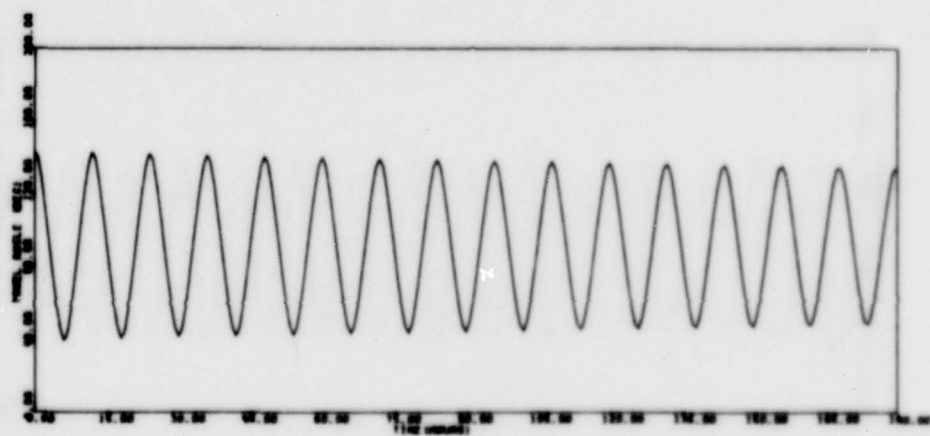
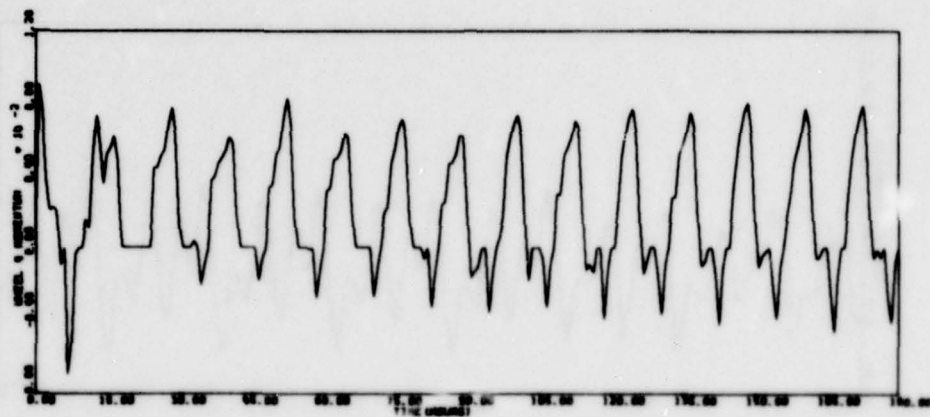


Figure 56. Run 4A - Sunline 45° - $2K_{\phi}$ (concluded)

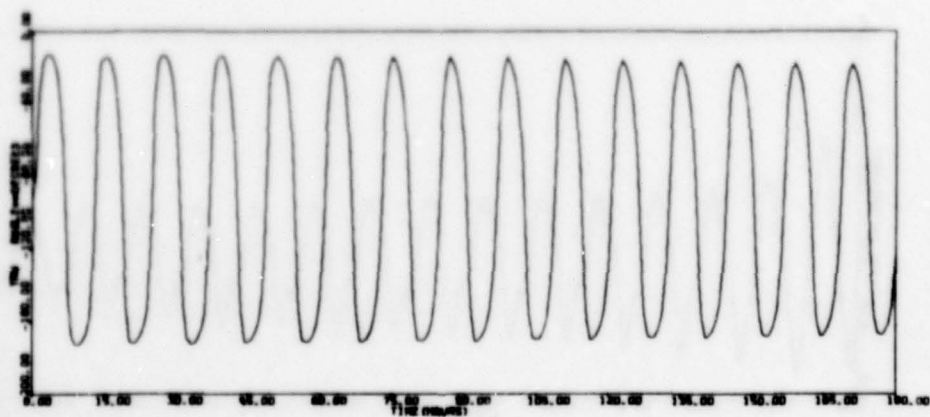
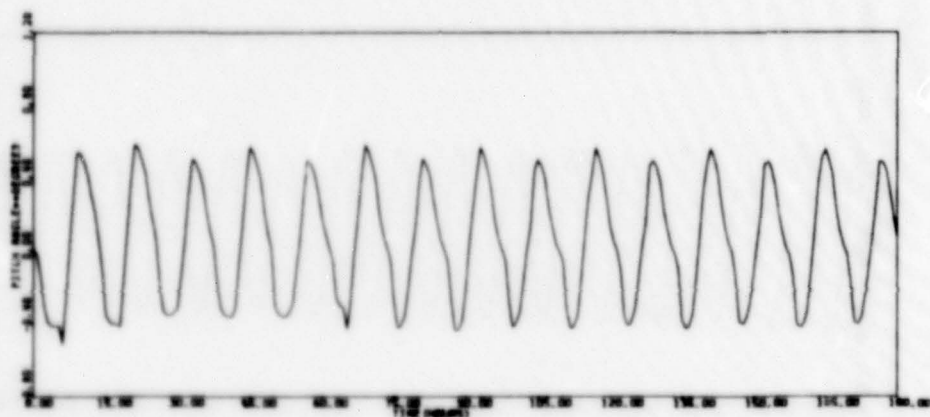
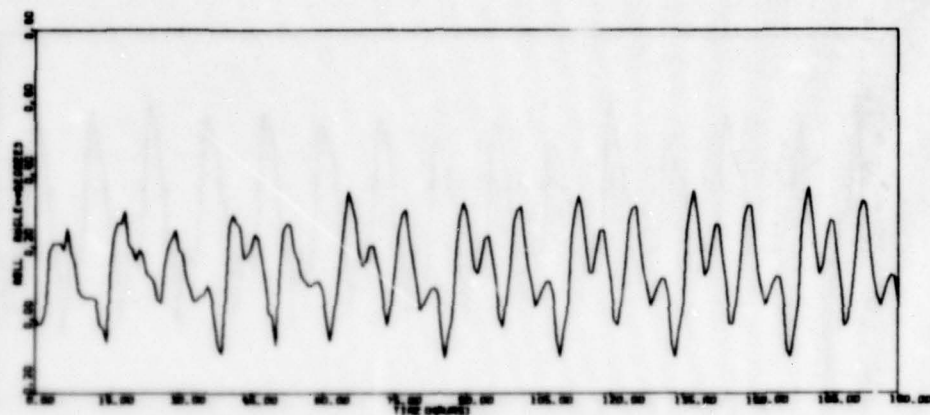


Figure 57. Run 6C - Sunline 12⁰ - K₄/2 - Dead Bands Out

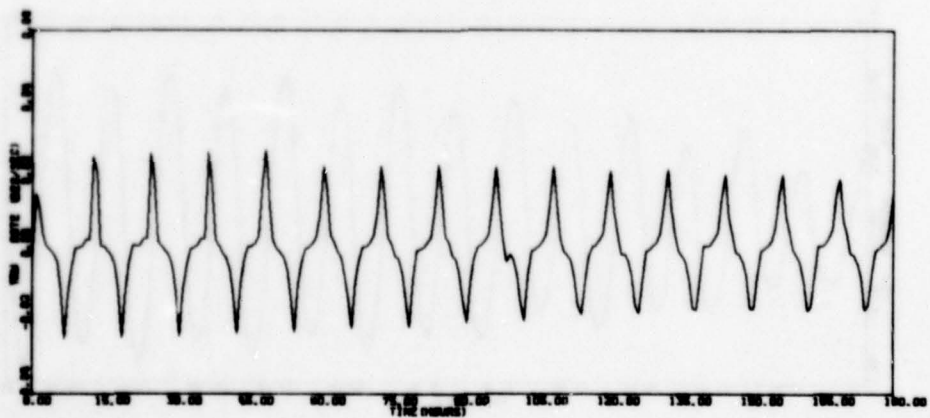
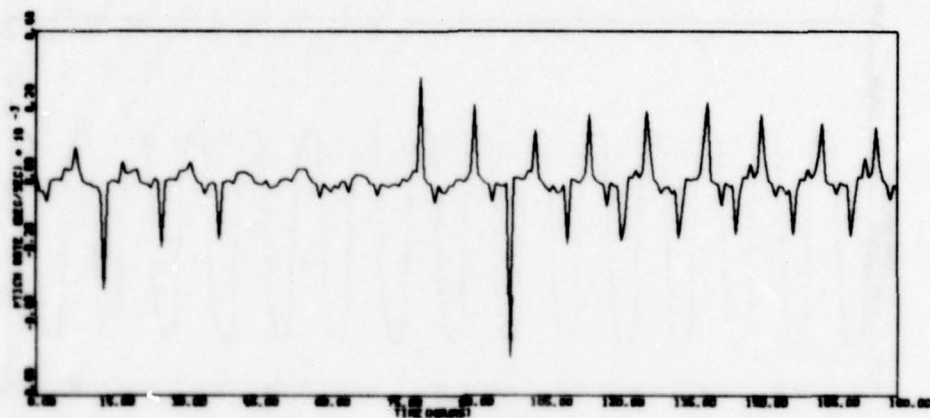
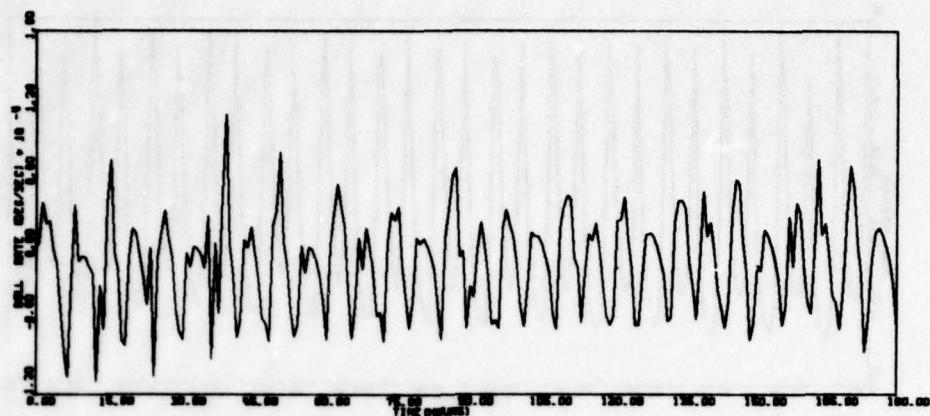


Figure 57. Run 6C - Sunline 12⁰ - K₄/2 - Dead
Bands Out (continued)

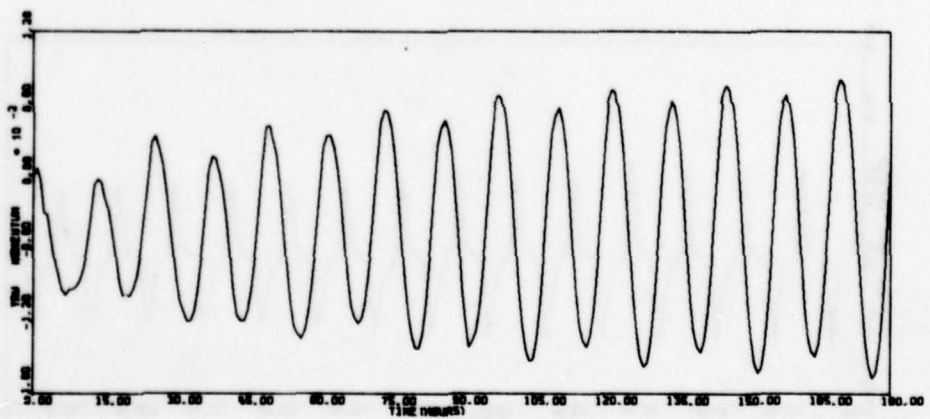
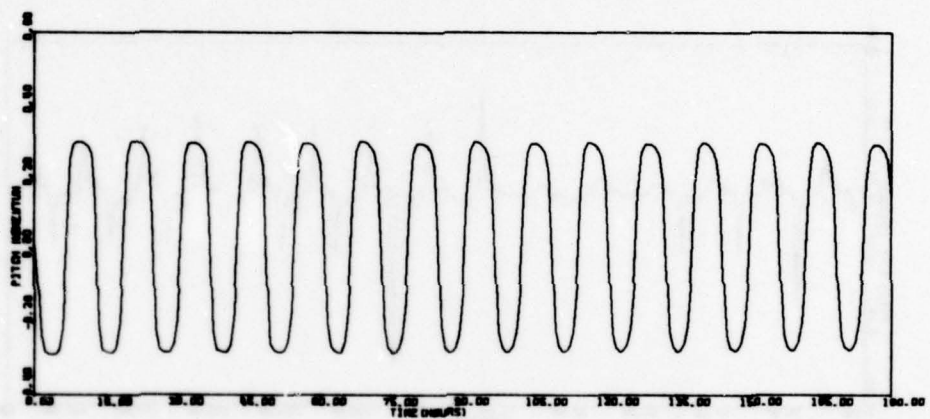
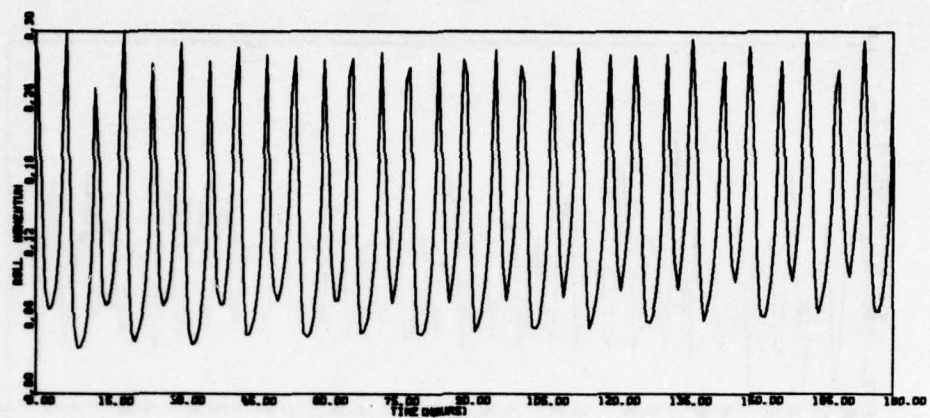


Figure 57. Run 6C - Sunline 12⁰ - K₄/2 - Dead Bands Out (continued)

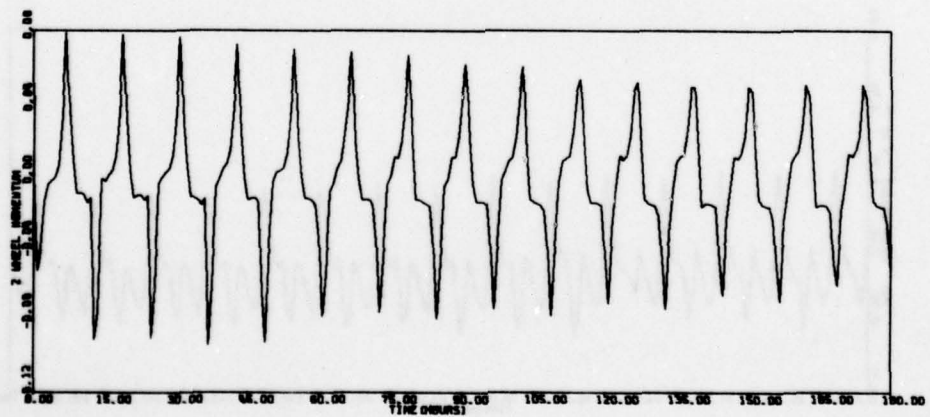
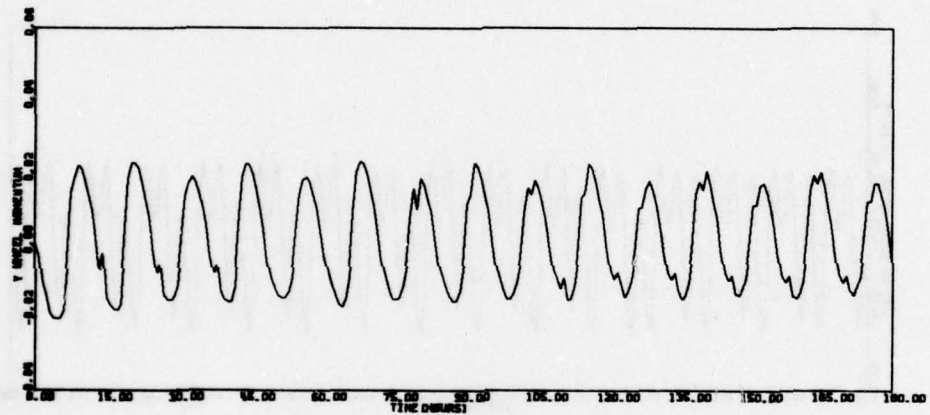
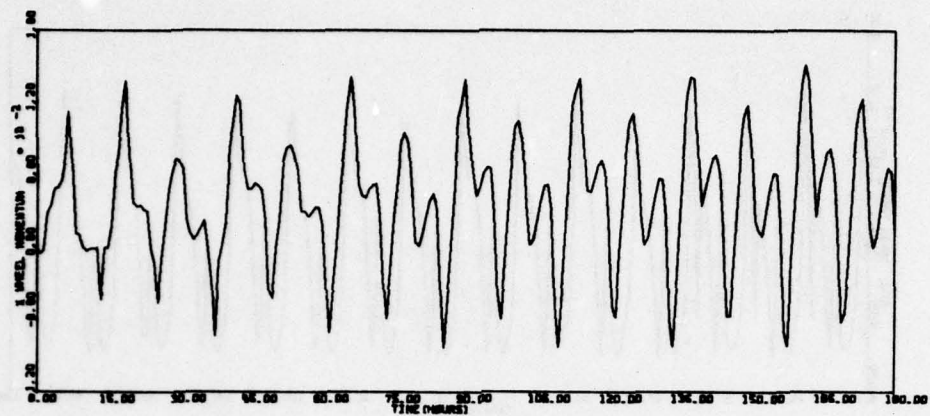


Figure 57. Run 6C - Sunline 12° - $K_4/2$ - Dead Bands Out (continued)

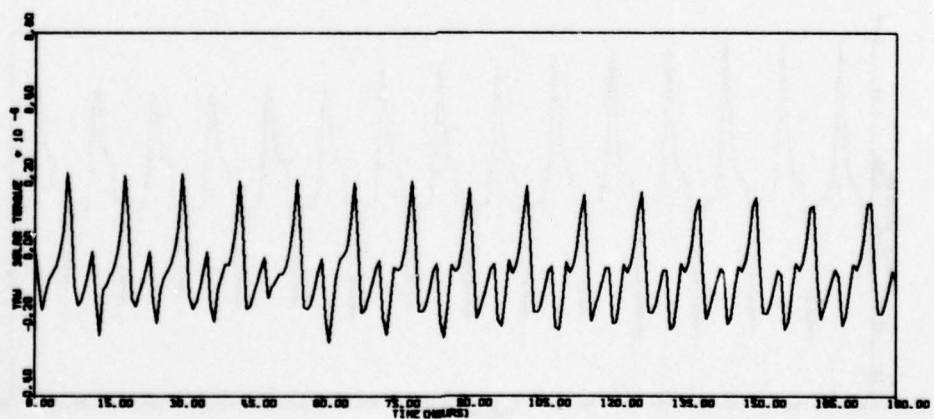
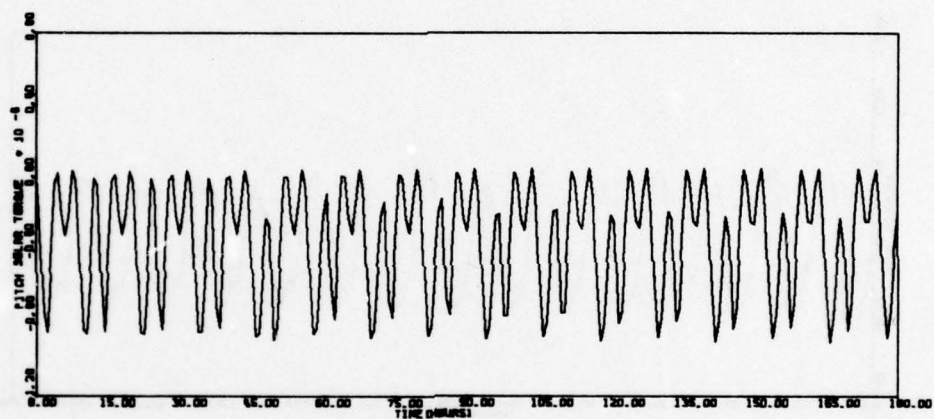
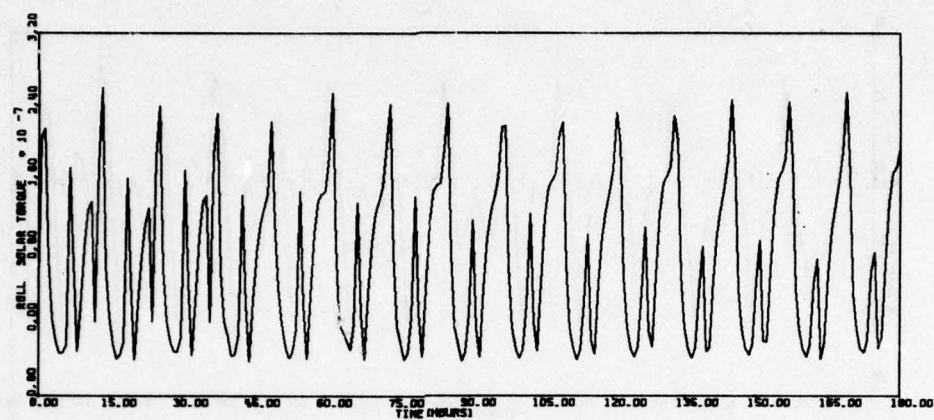


Figure 57. Run 6C - Sunline 12⁰ - K₄/2 - Dead Bands Out (continued)

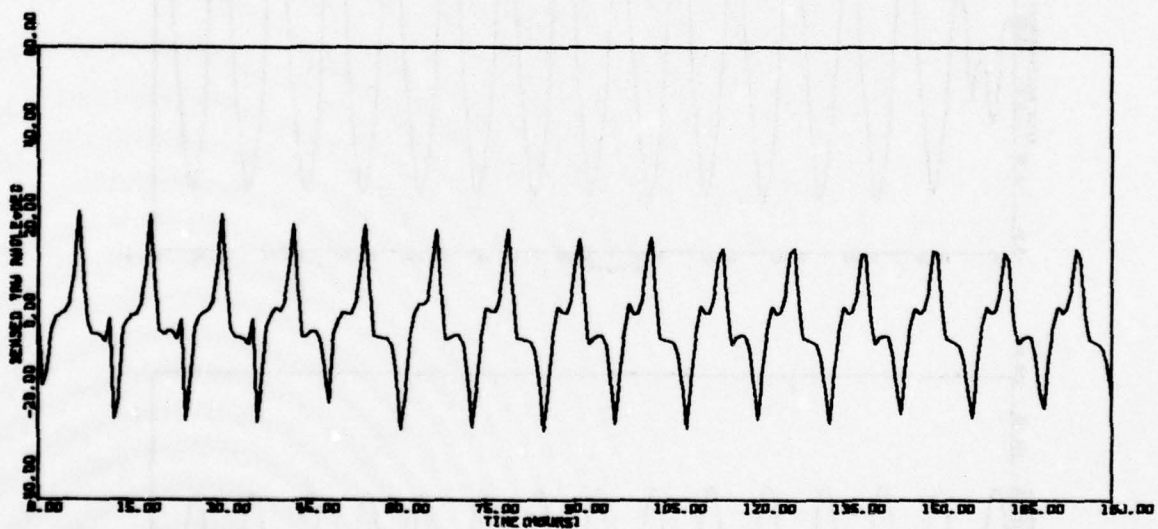
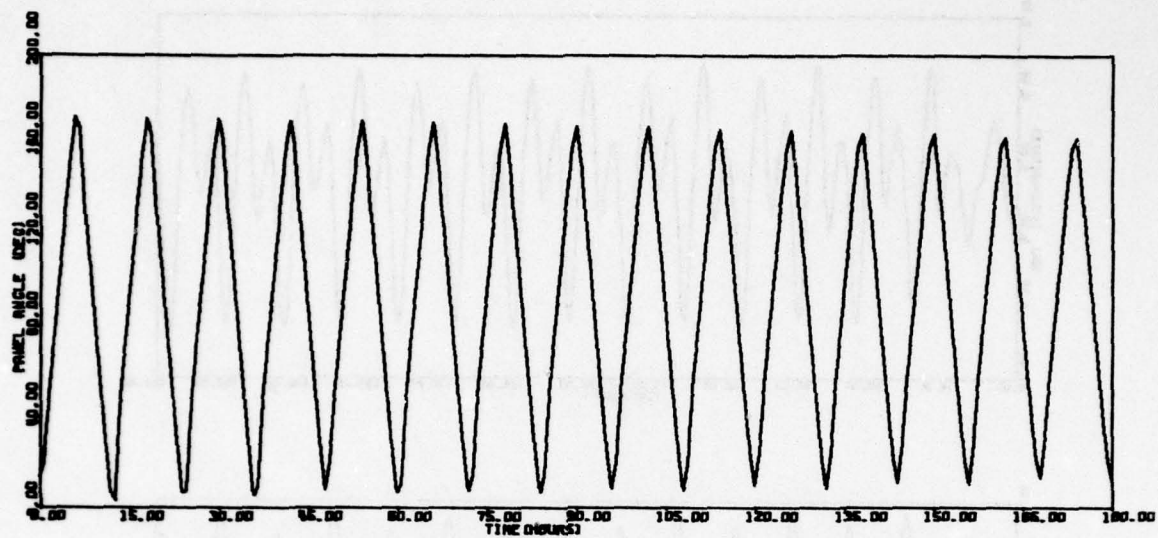


Figure 57. Run 6C - Sunline 12° - $K_4/2$ - Dead Bands Out (concluded)

AD-A052 633

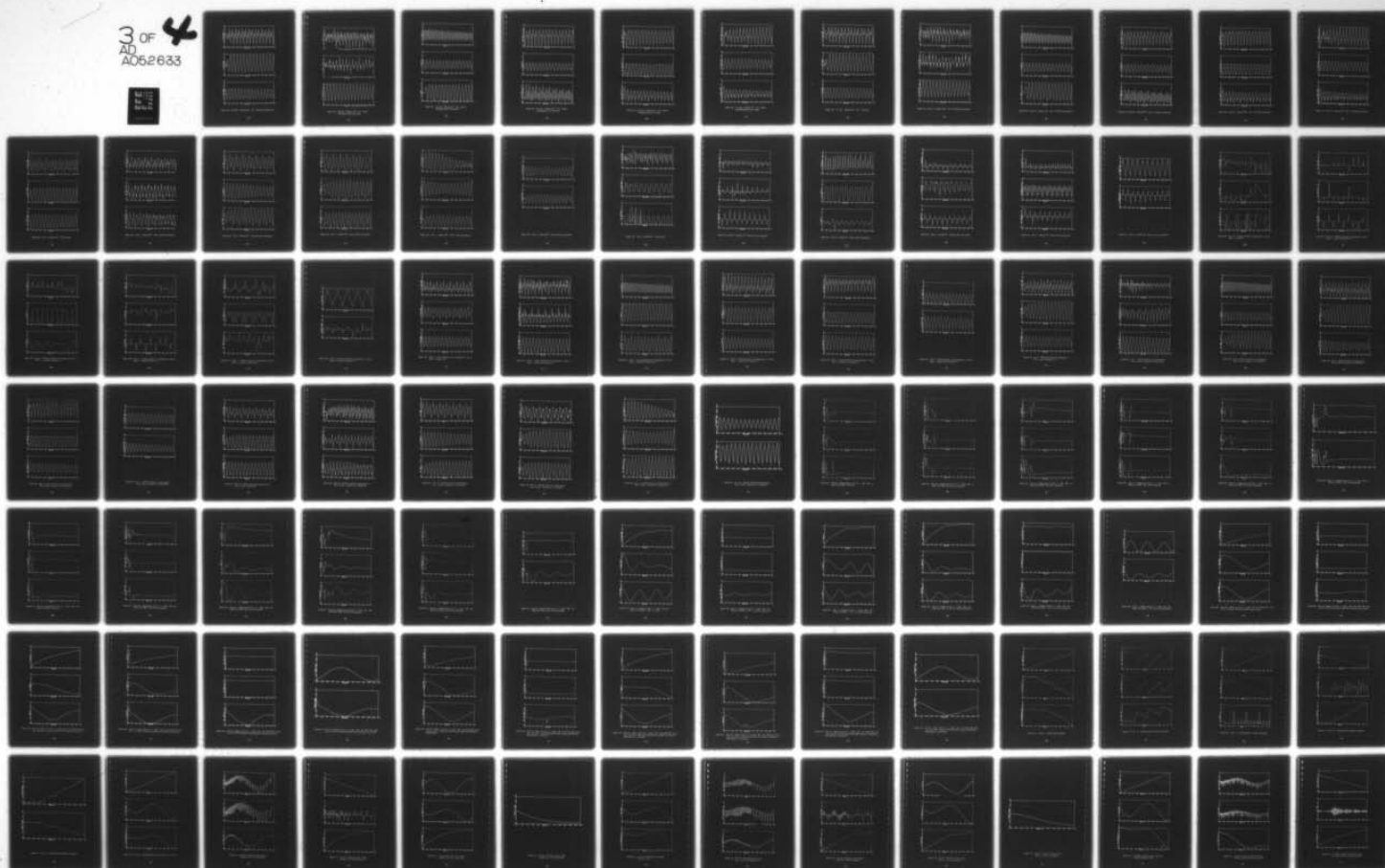
HONEYWELL INC MINNEAPOLIS MINN SYSTEMS AND RESEARCH --ETC F/G 22/2
NTS-2 INDEPENDENT STABILITY AND CONTROL ANALYSIS. VOLUME I. TEC--ETC(U)
MAR 77 R E POPE, M D WARD, S M SCHWANTES

UNCLASSIFIED

77SRC17-VOL-1

NL

3 OF 4
AD
A052633



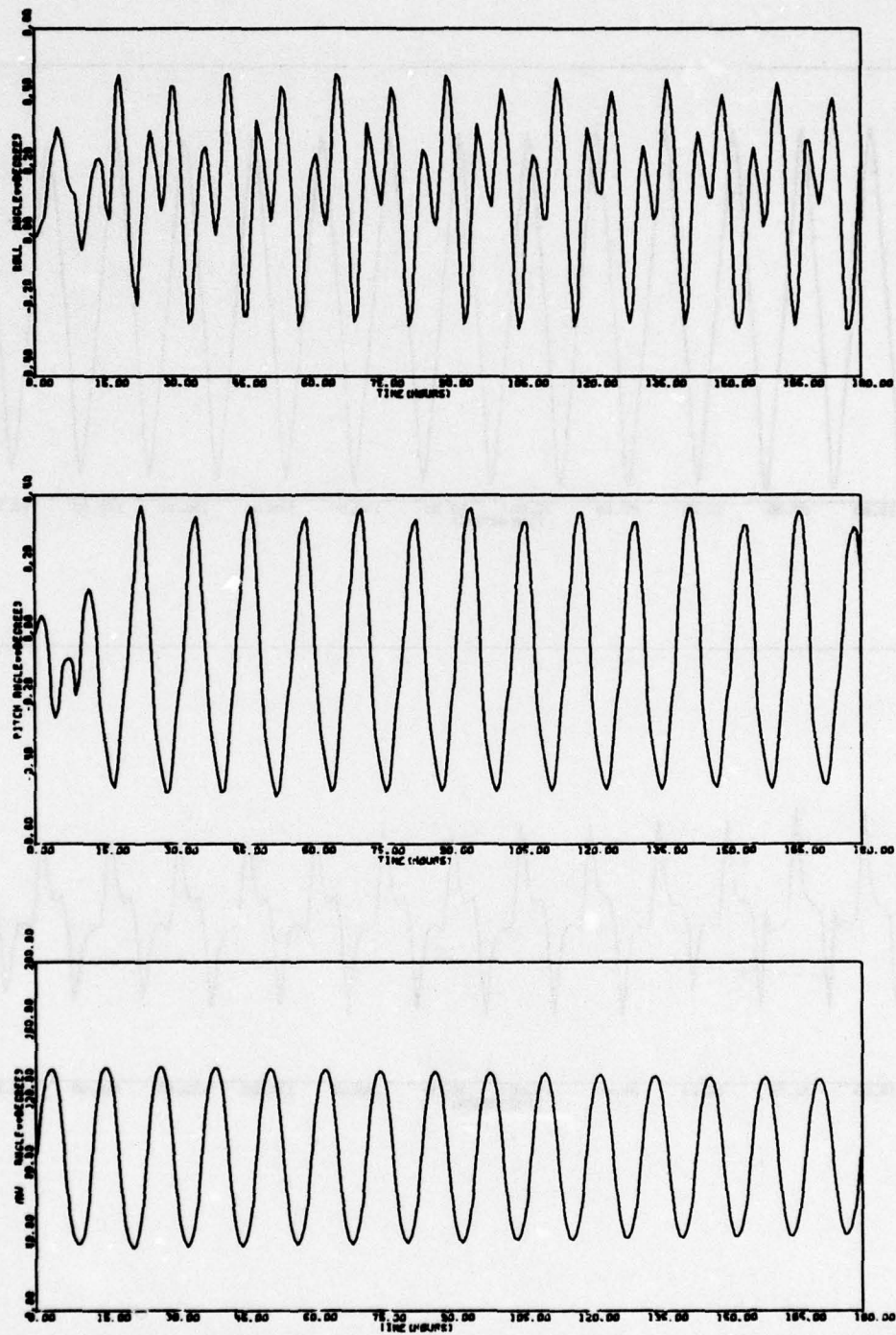


Figure 58. Run 4B - Sunline 45⁰ - 4A + Wheel Misalignments

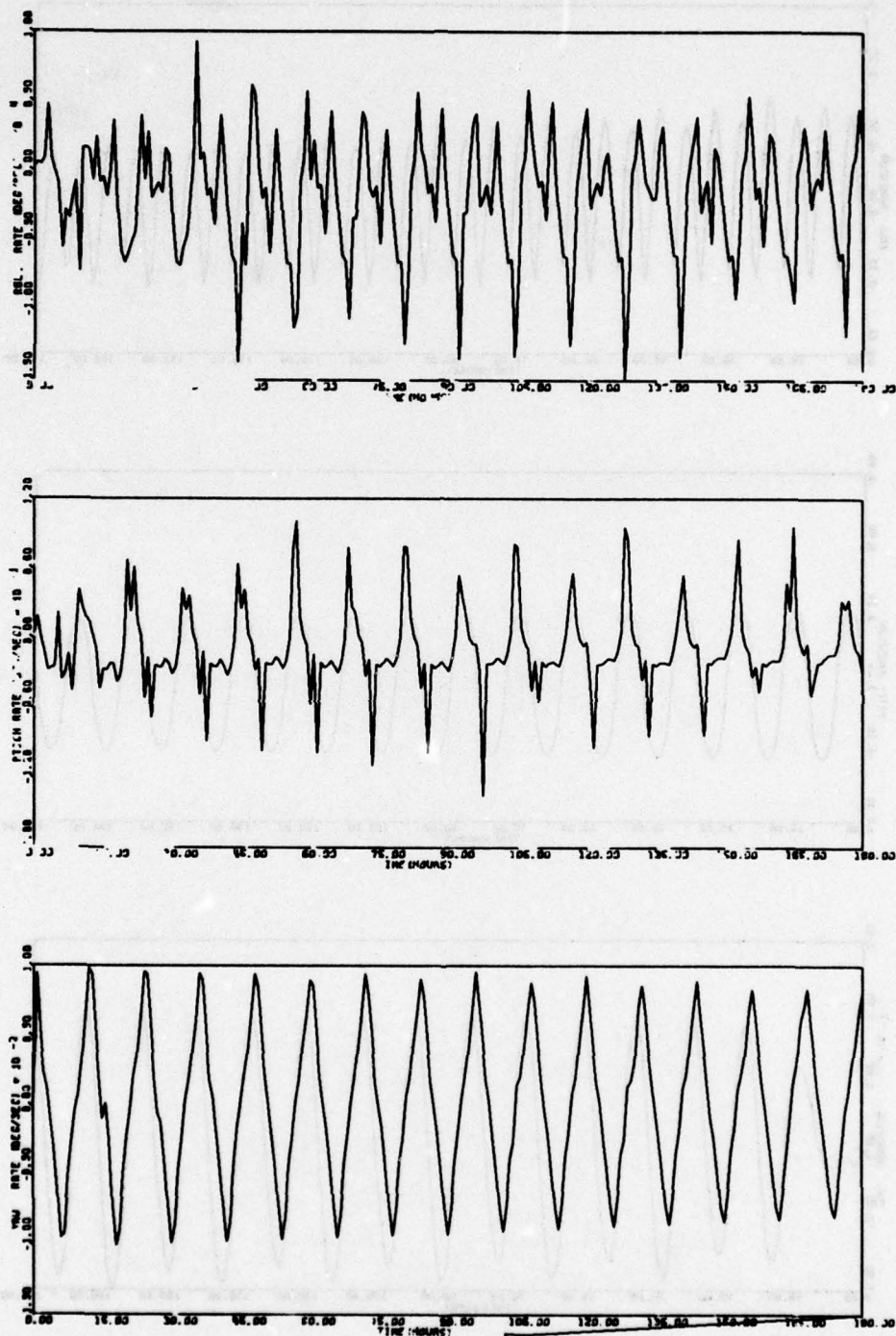


Figure 58. Run 4B - Sunline 45⁰ - 4A + Wheel
Misalignments (continued)

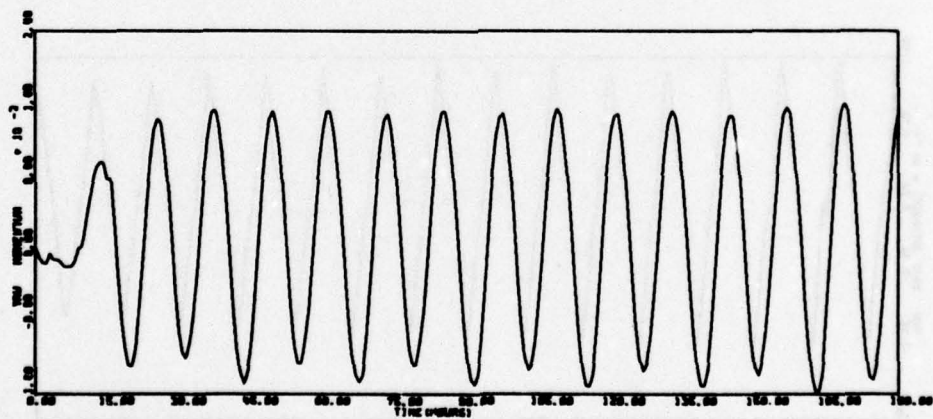
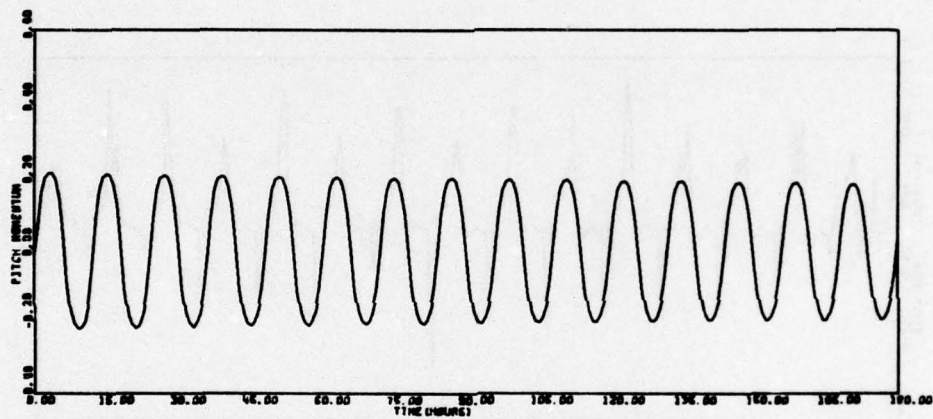
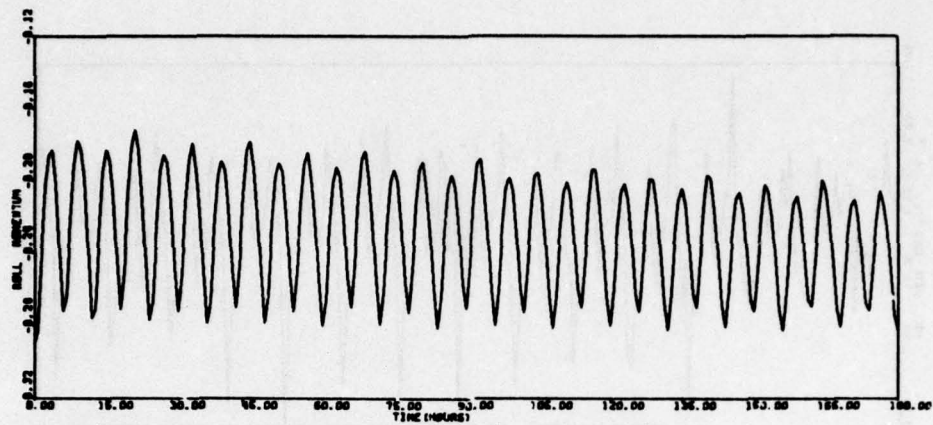


Figure 58. Run 4B - Sunline 45° - 4A + Wheel Misalignments (continued)

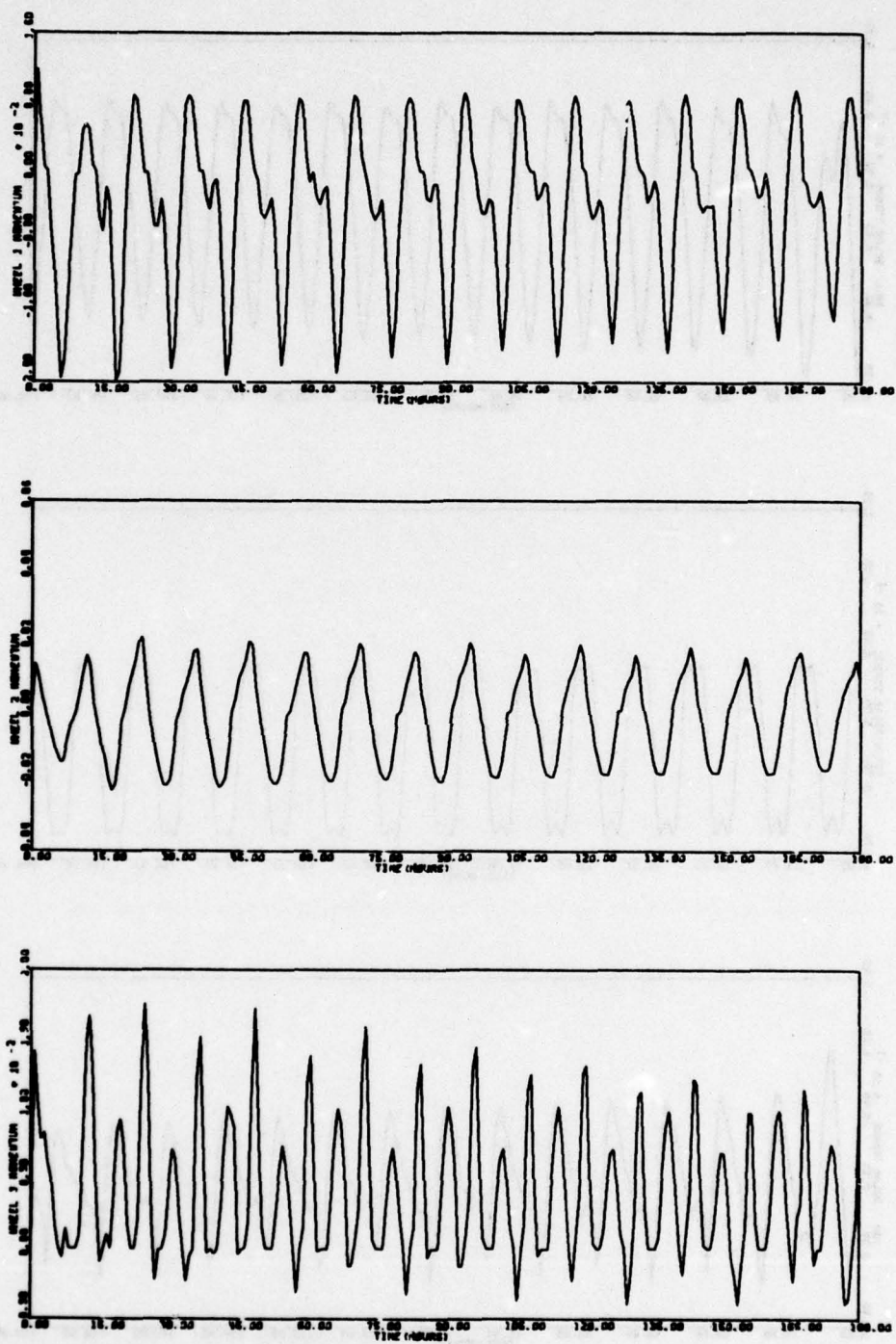


Figure 58. Run 4B - Sunline 45⁰ - 4A + Wheel Misalignments (continued)

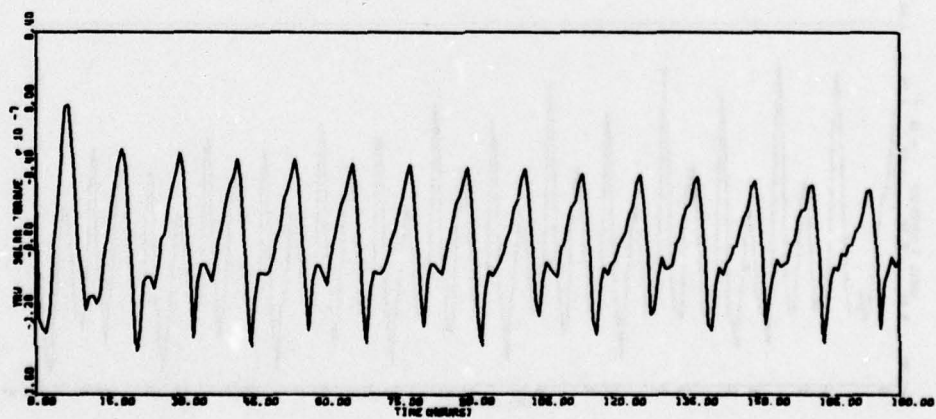
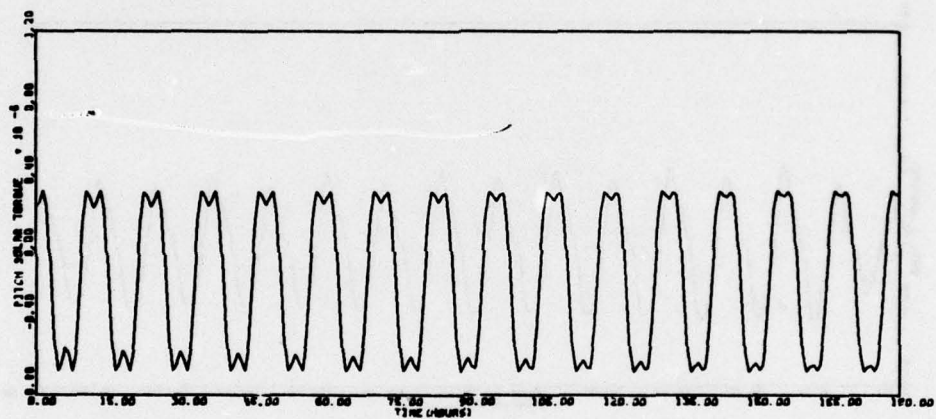
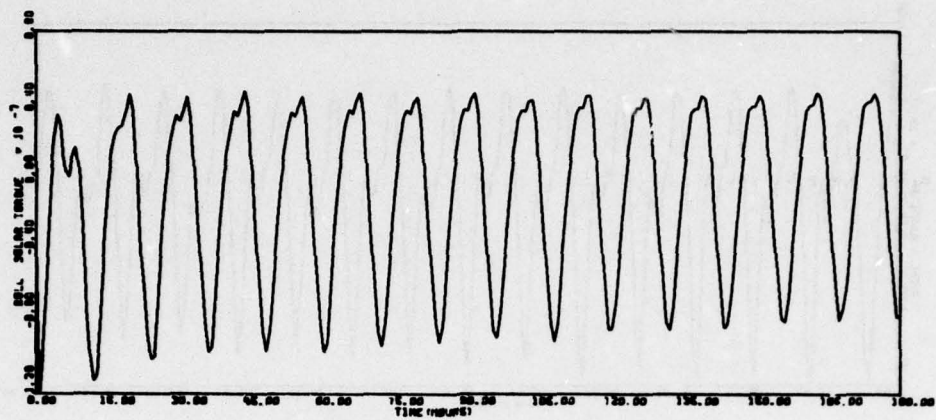


Figure 58. Run 4B - Sunline 45° - 4A + Wheel Misalignments (continued)

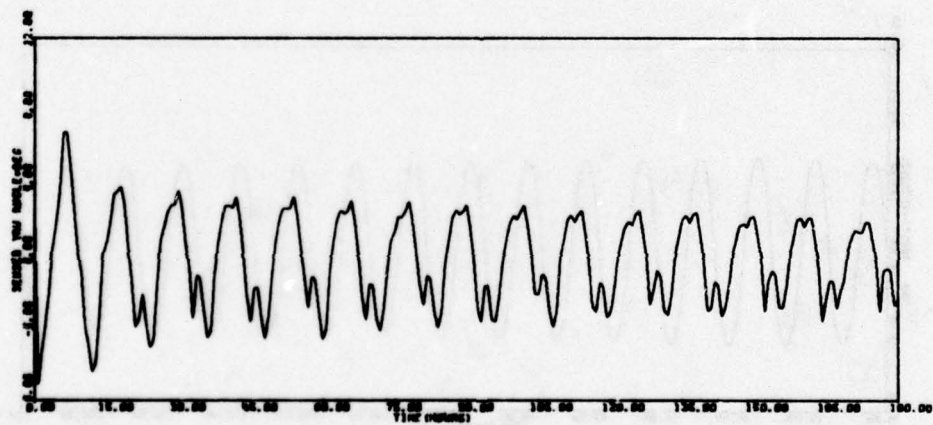
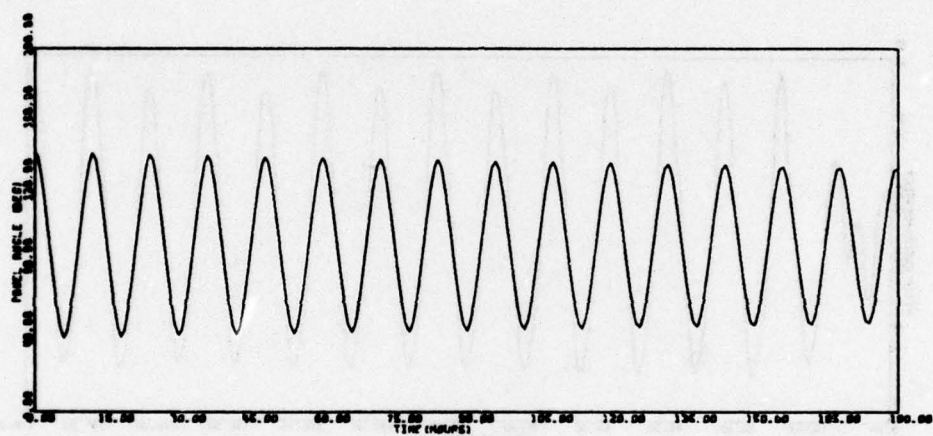
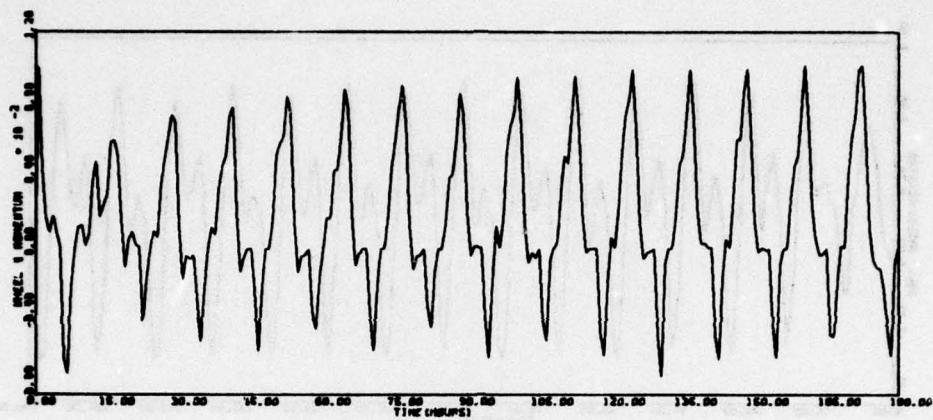


Figure 58. Run 4B - Sunline 45° - 4A + Wheel
Misalignments (concluded)

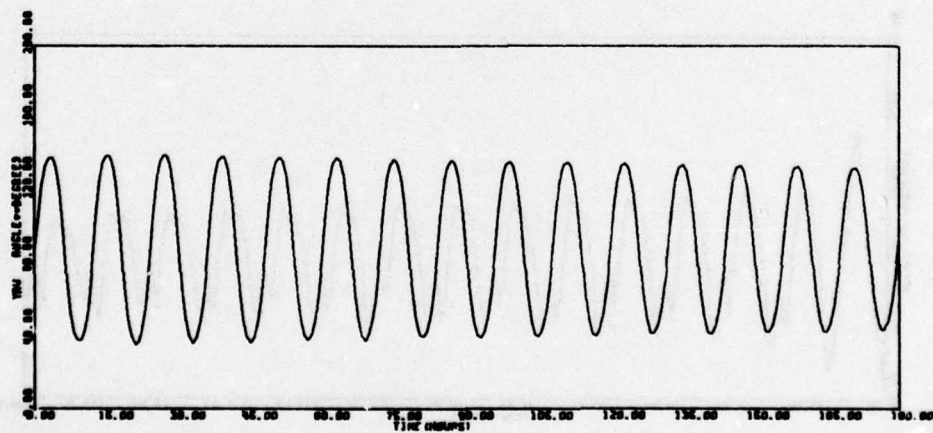
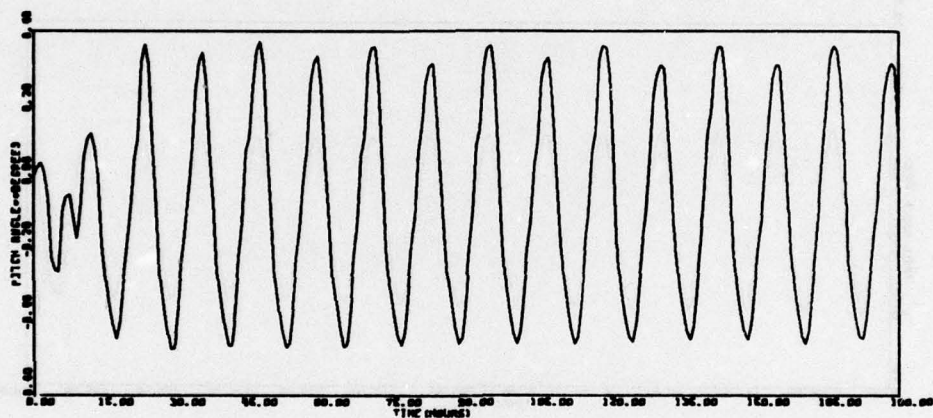
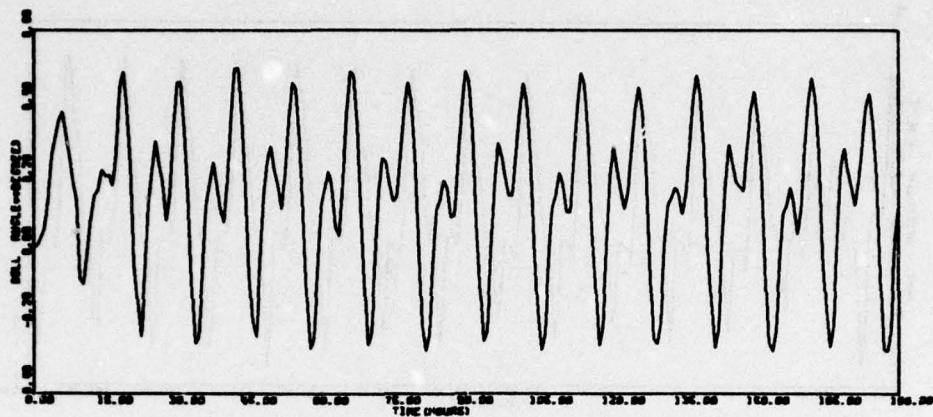


Figure 59. Run 4C - Sunline 45° - 4B + CP Shift

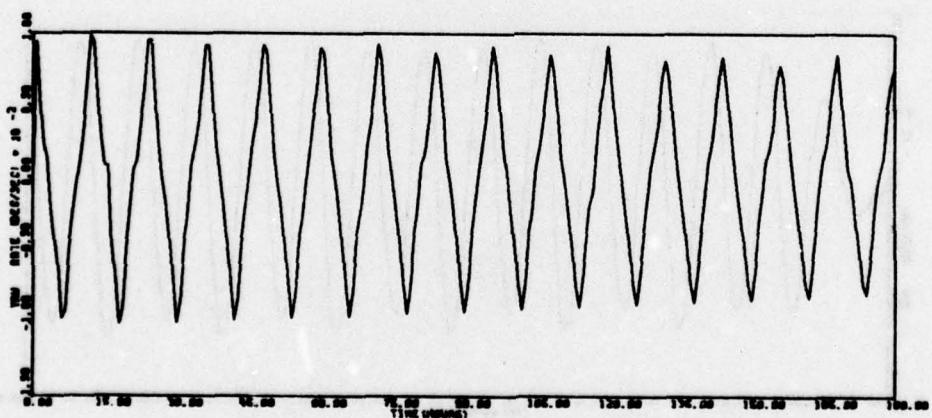
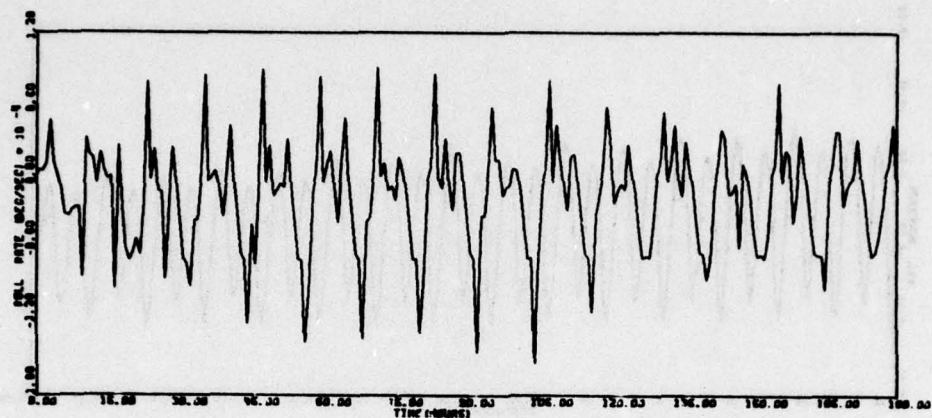


Figure 59. Run 4C - Sunline 45⁰ - 4B + CP Shift (continued)

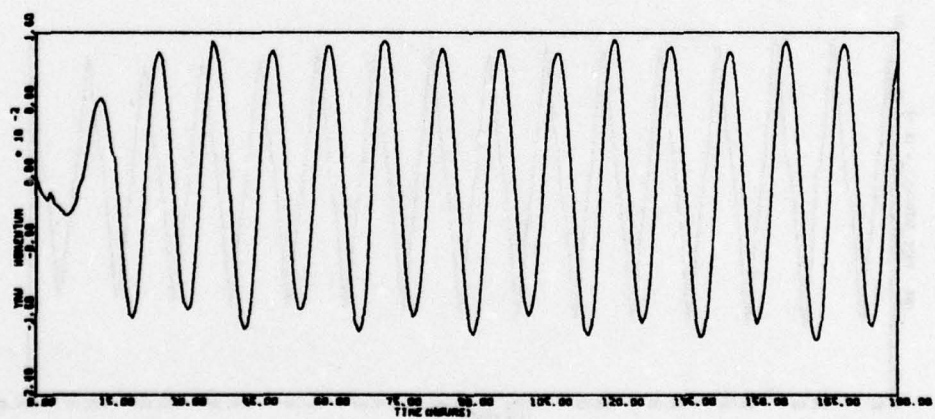
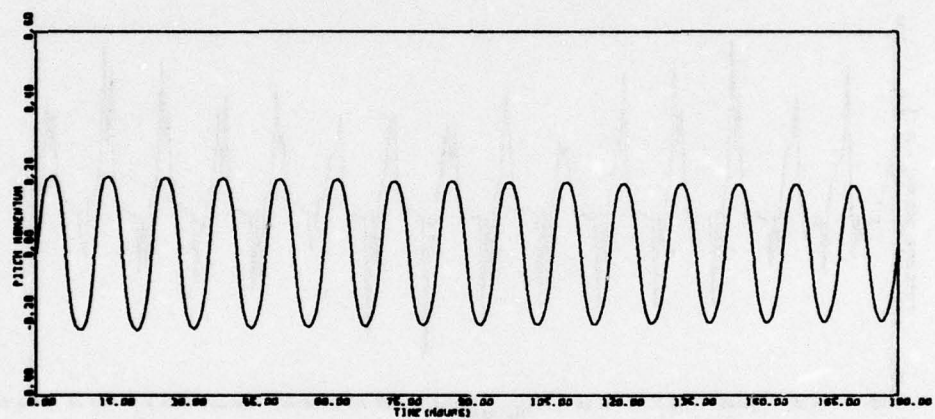
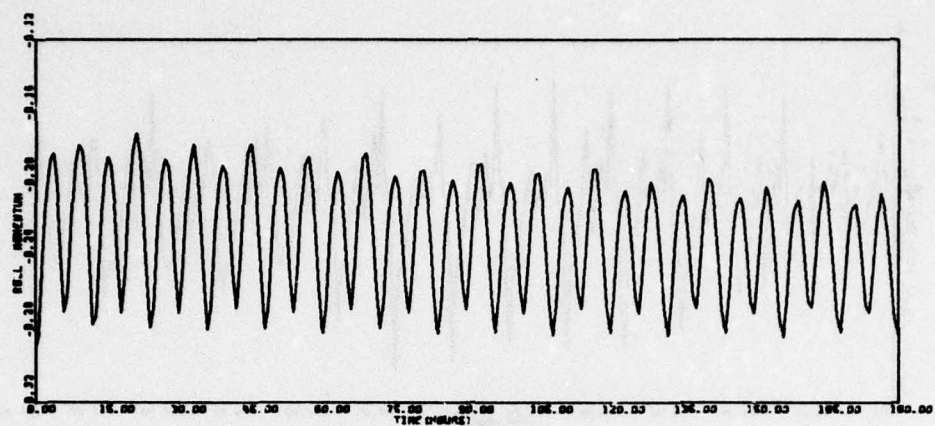


Figure 59. Run 4C - Sunline 45⁰ - 4B + CP Shift (continued)

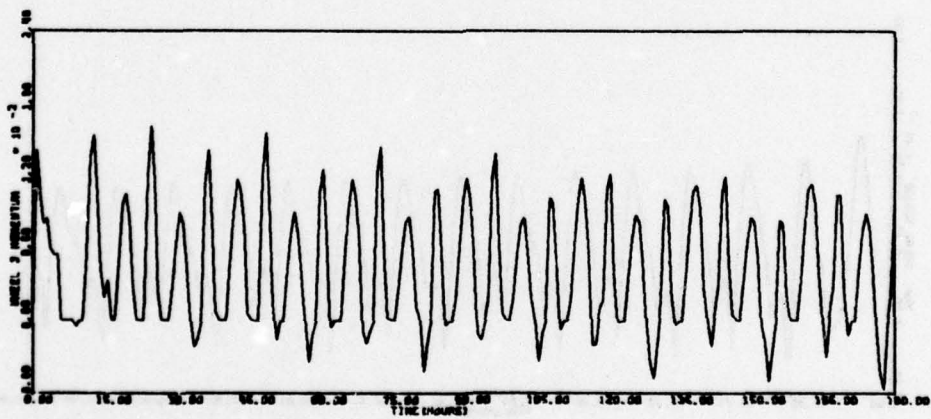
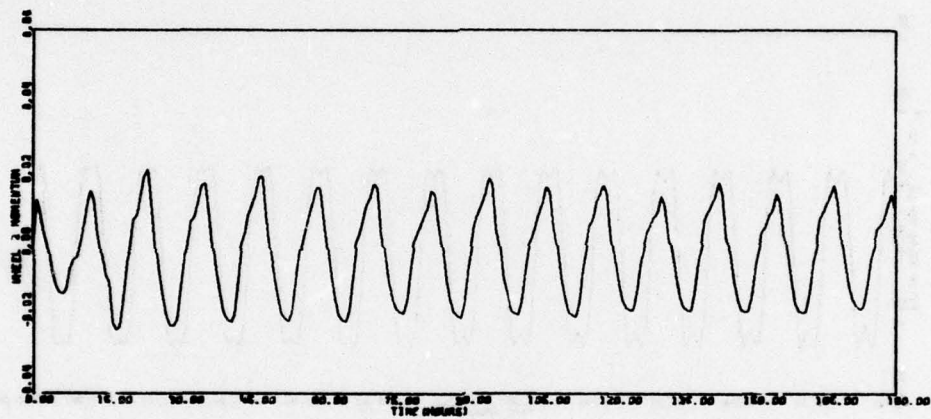
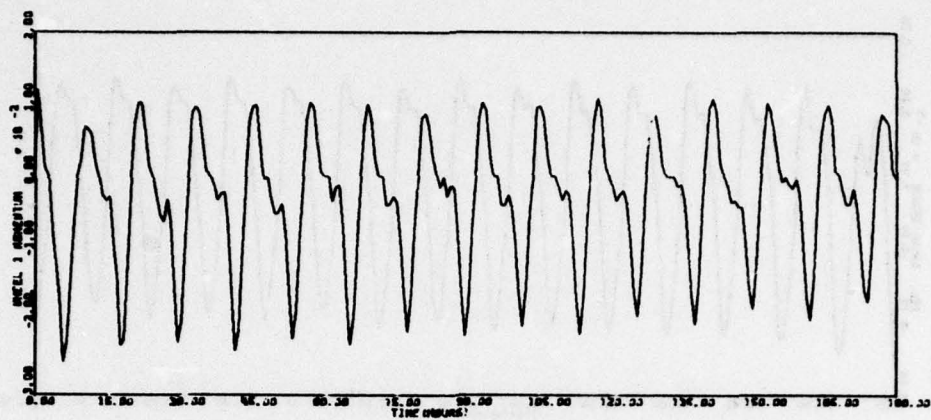


Figure 59. Run 4C - Sunline 45° - 4B + CP Shift (continued)

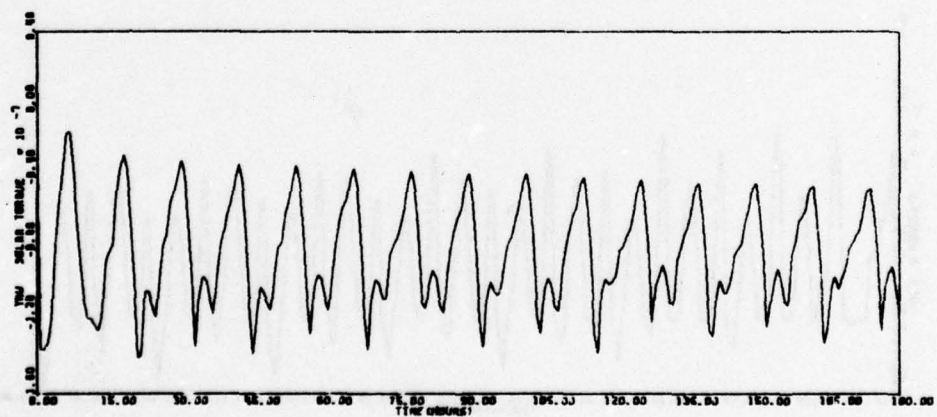
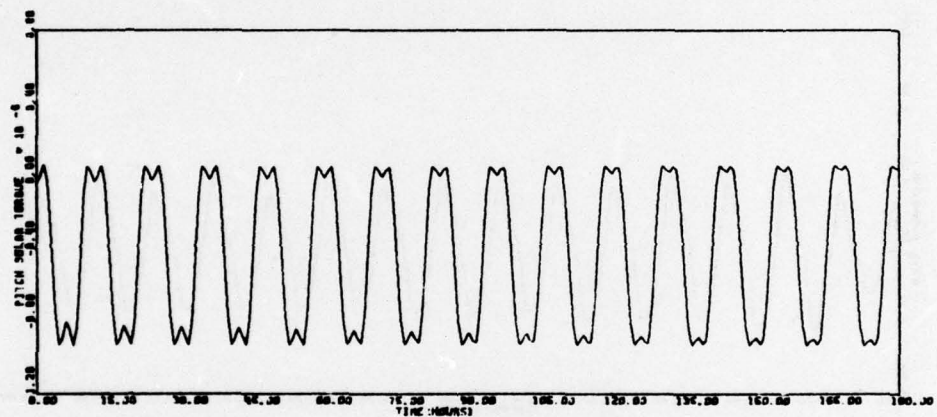
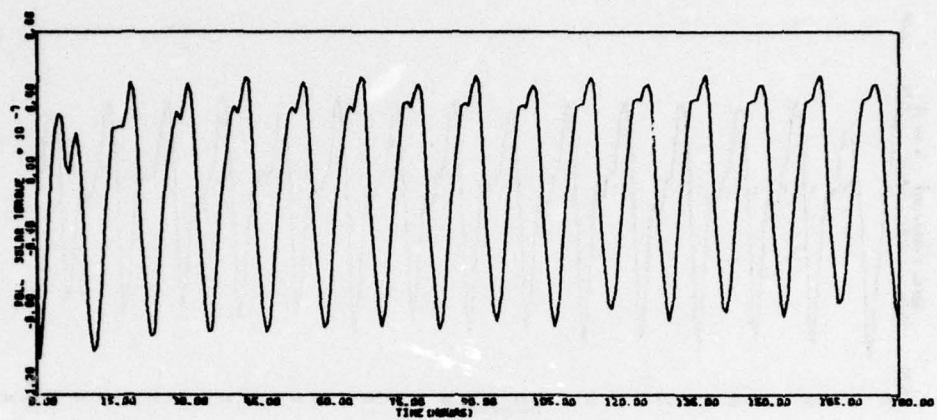


Figure 59. Run 4C - Sunline 45° - 4B + CP Shift (continued)

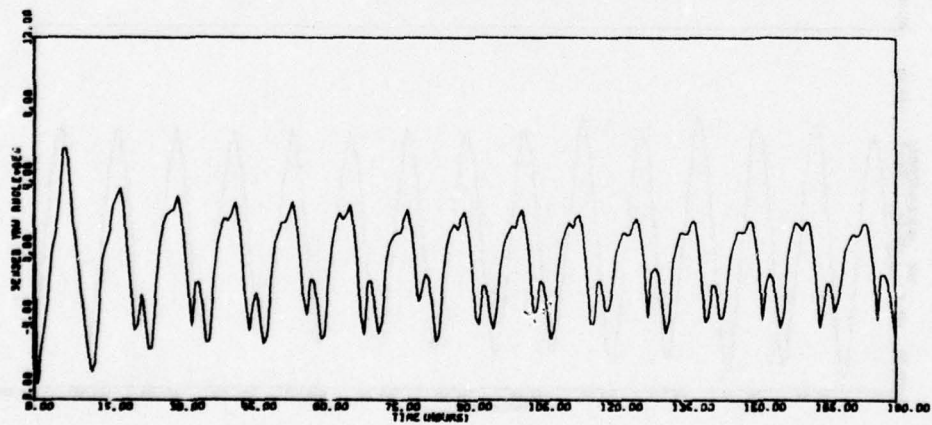
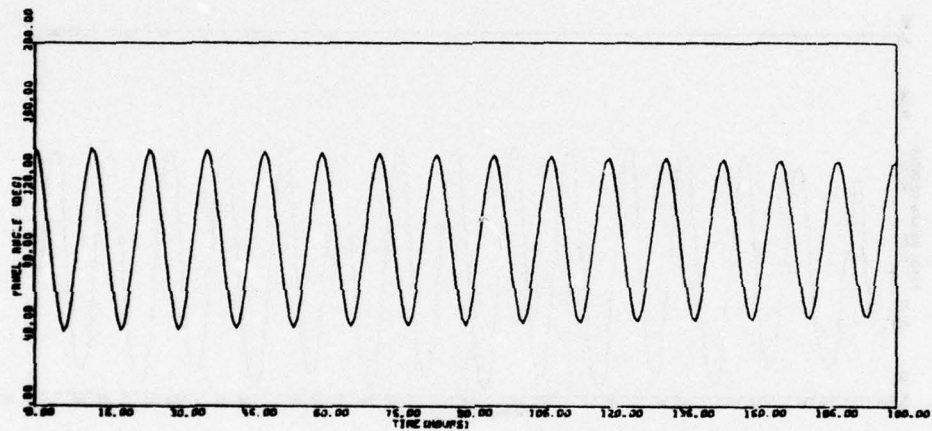
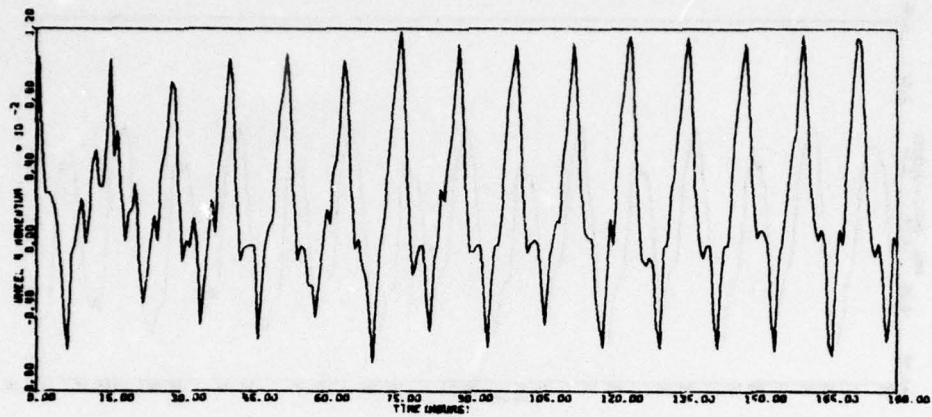


Figure 59. Run 4C - Sunline 45° - 4B + CP Shift (concluded)

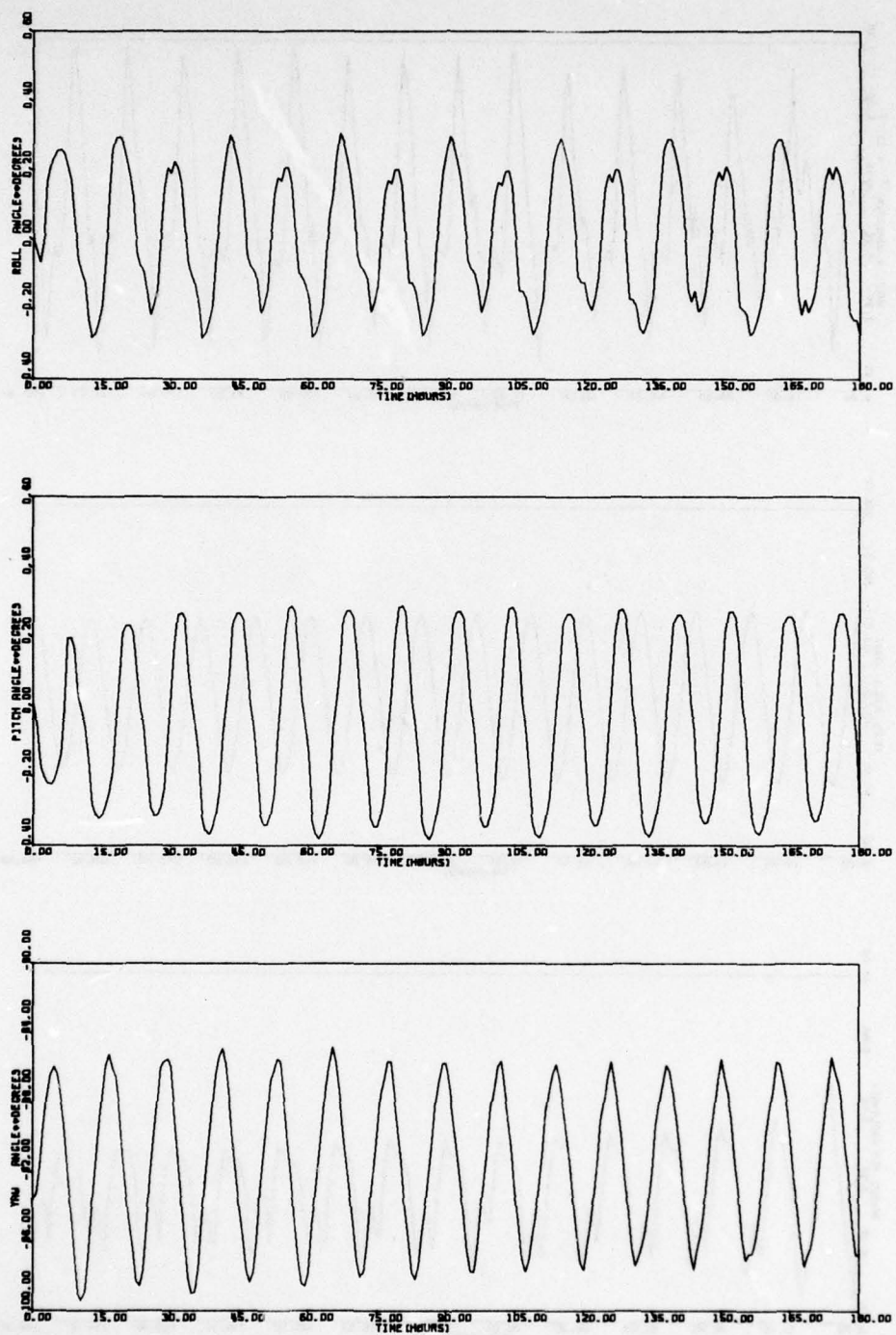


Figure 60. Run 5 - Sunline 86° - Worst Case

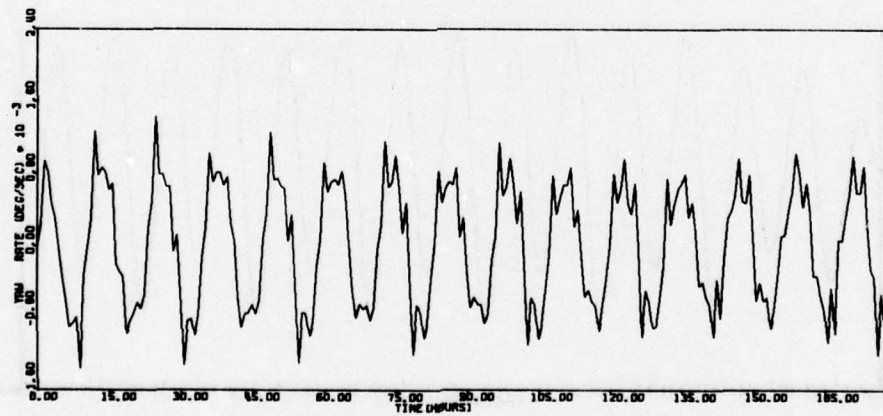
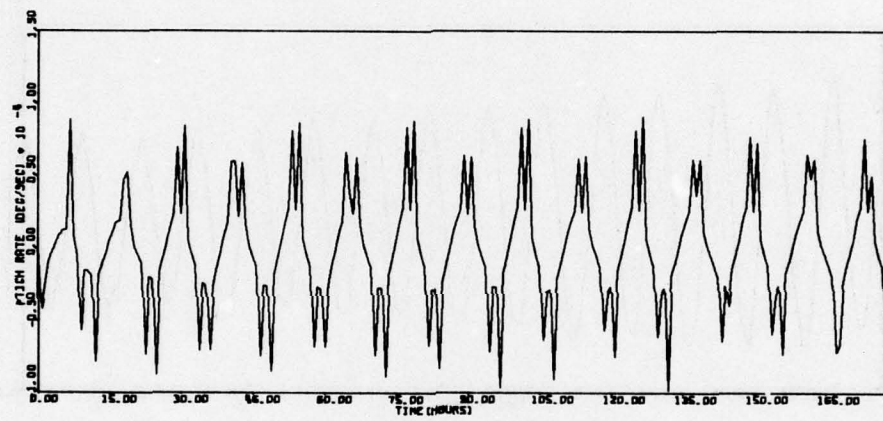
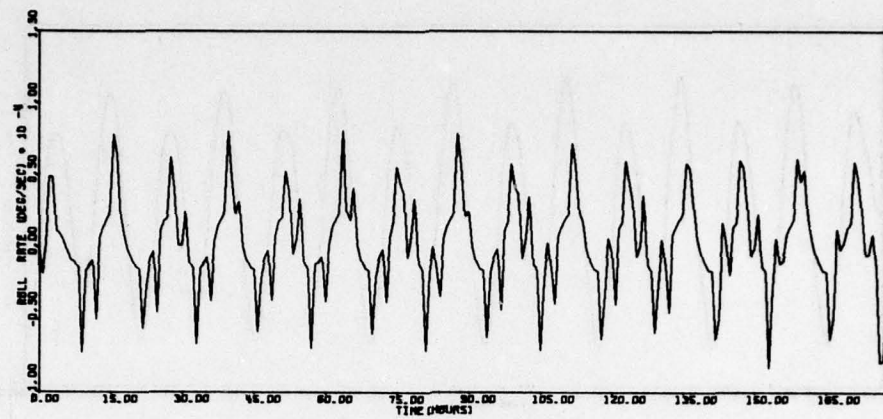


Figure 60. Run 5 - Sunline 86° - Worst Case (continued)

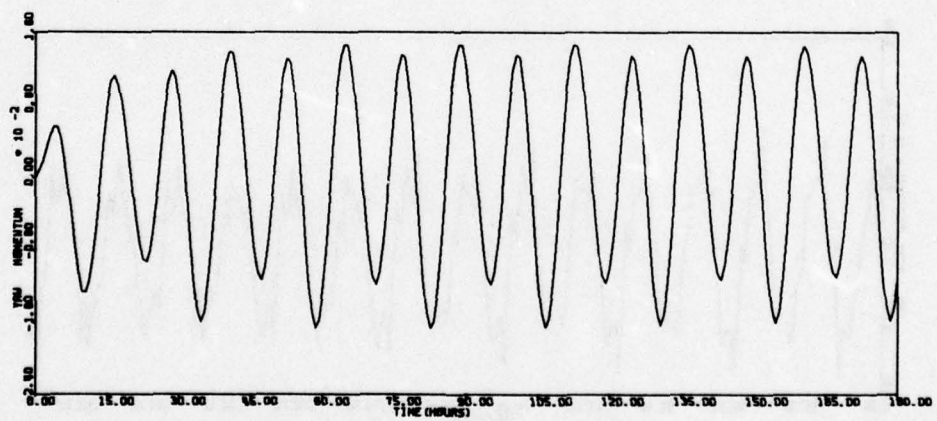
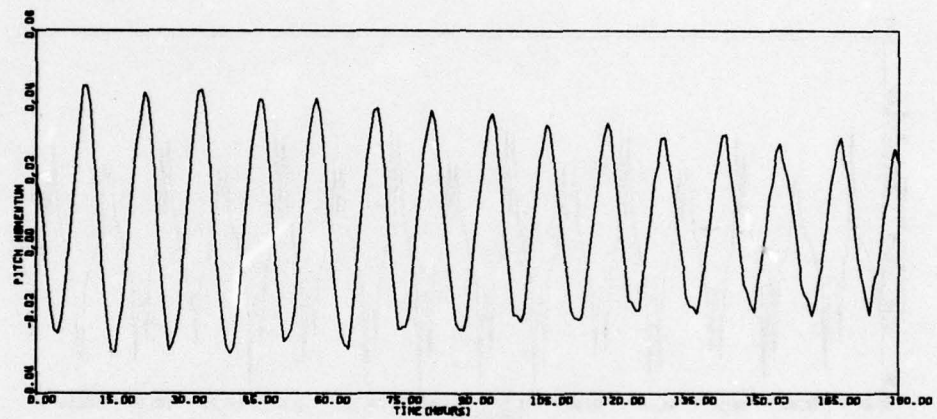
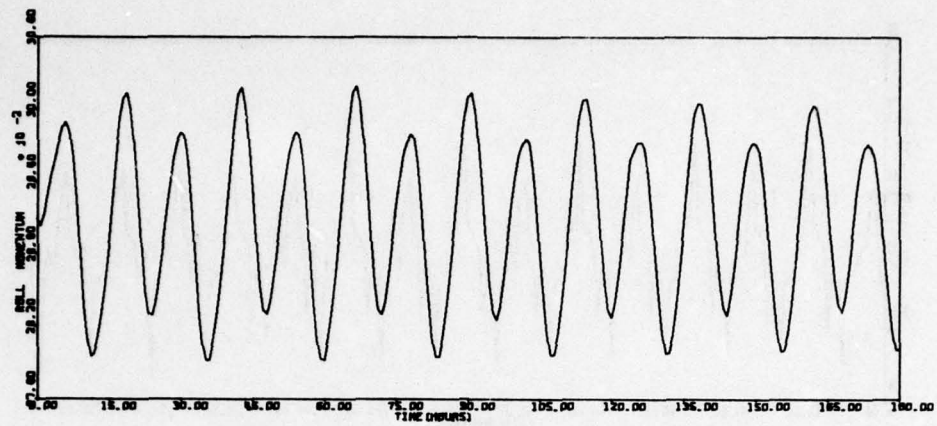


Figure 60. Run 5 - Sunline 86° - Worst Case (continued)

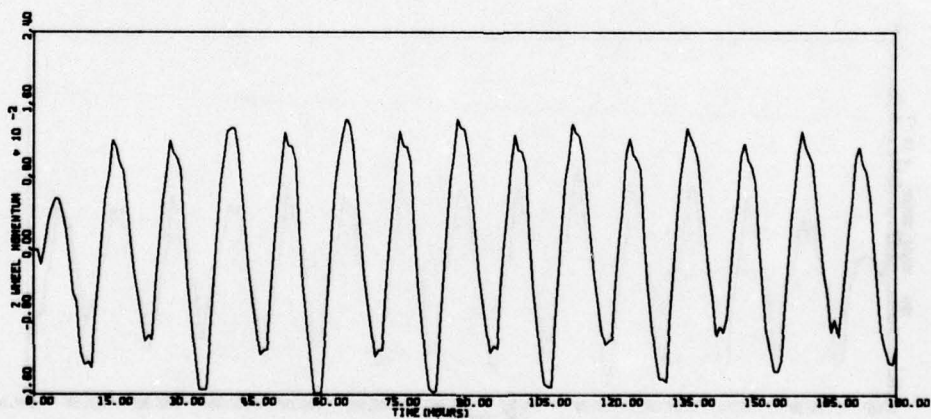
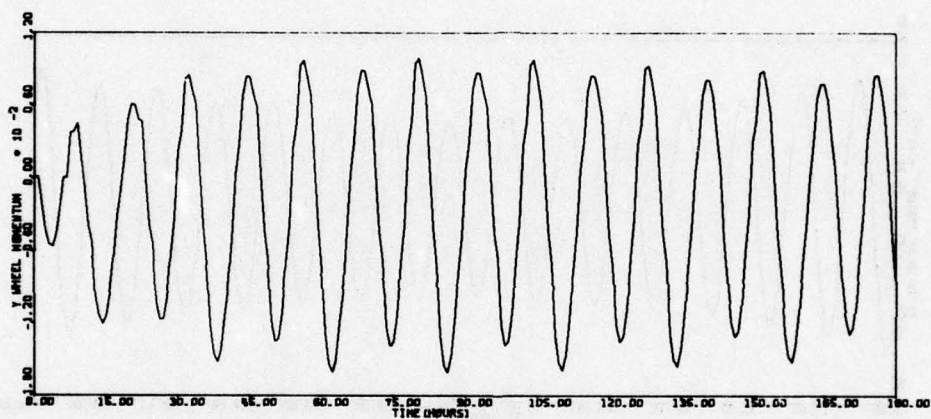
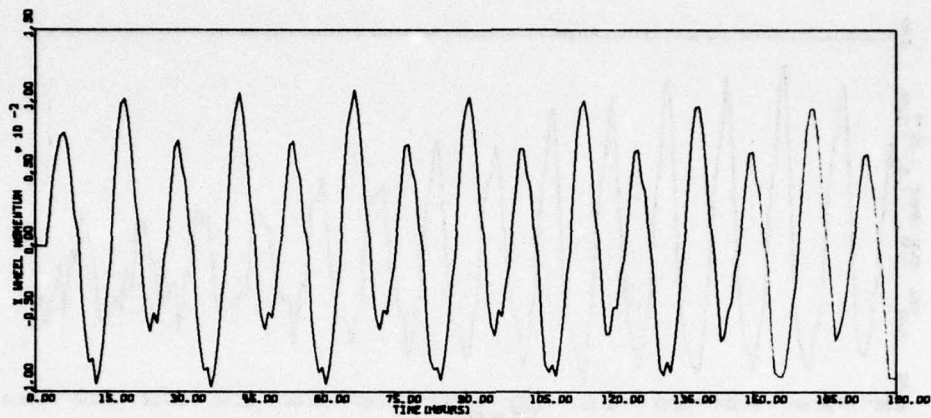


Figure 60. Run 5 - Sunline 86° - Worst Case (continued)

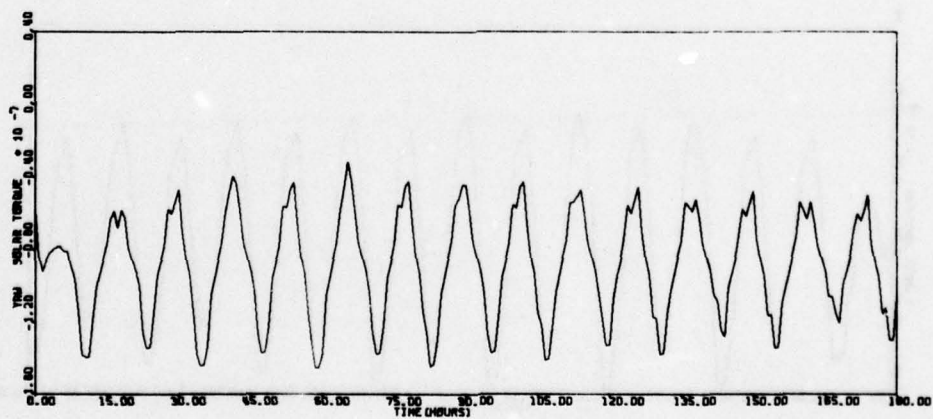
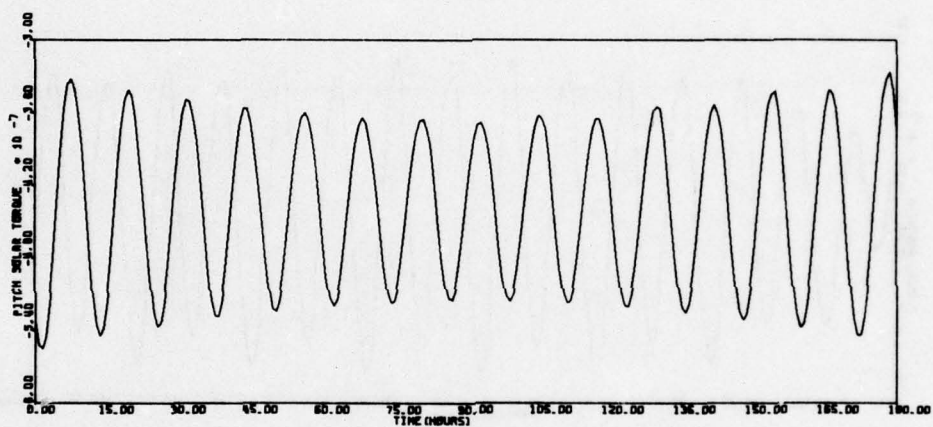
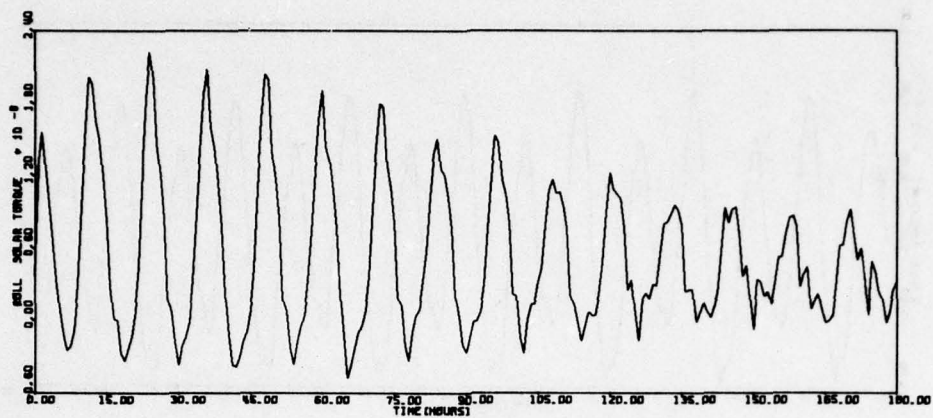


Figure 60. Run 5 - Sunline 86° - Worst Case (continued)

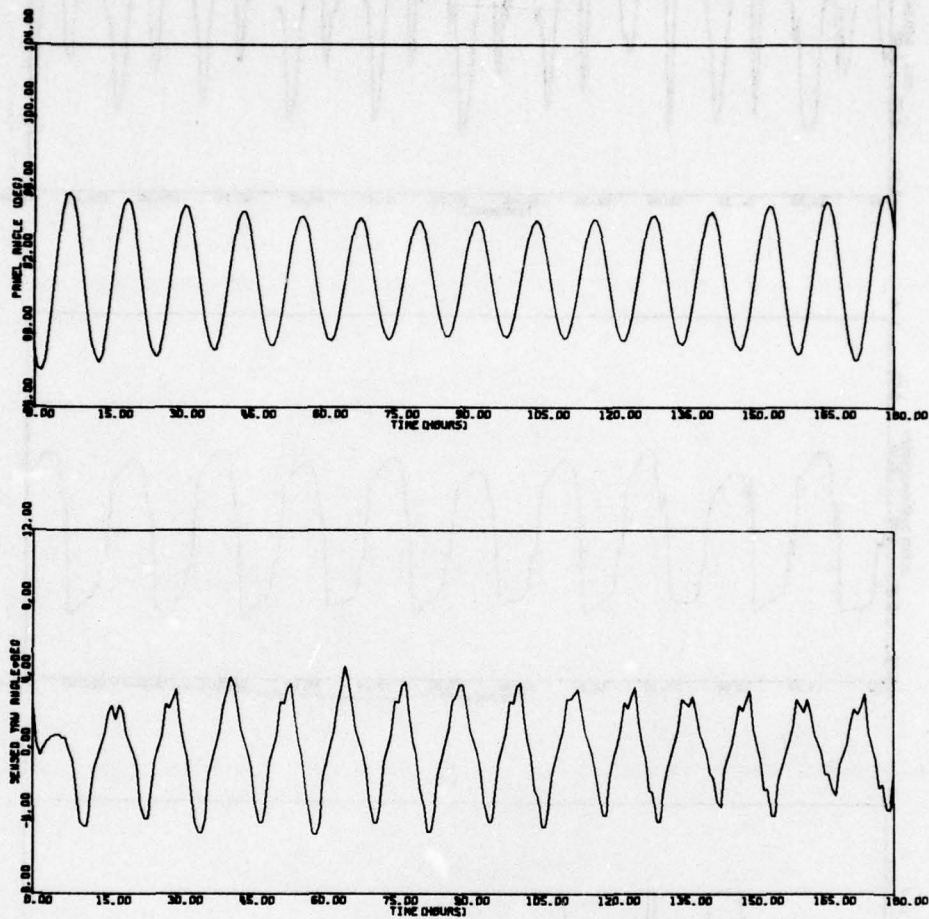


Figure 60. Run 5 - Sunline 86⁰ - Worst Case (concluded)

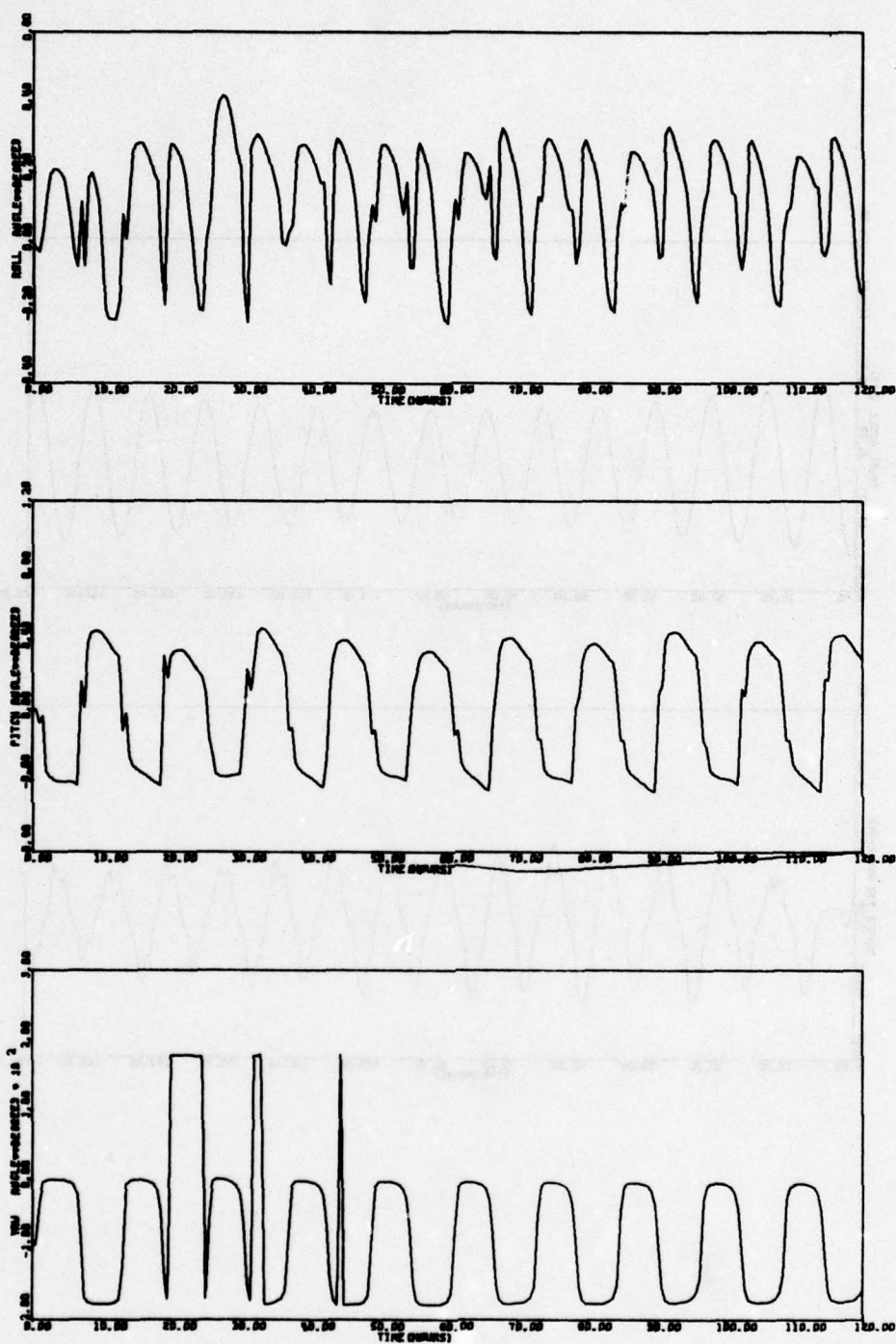


Figure 61. Run 6 - Sunline 0° - Worst Case

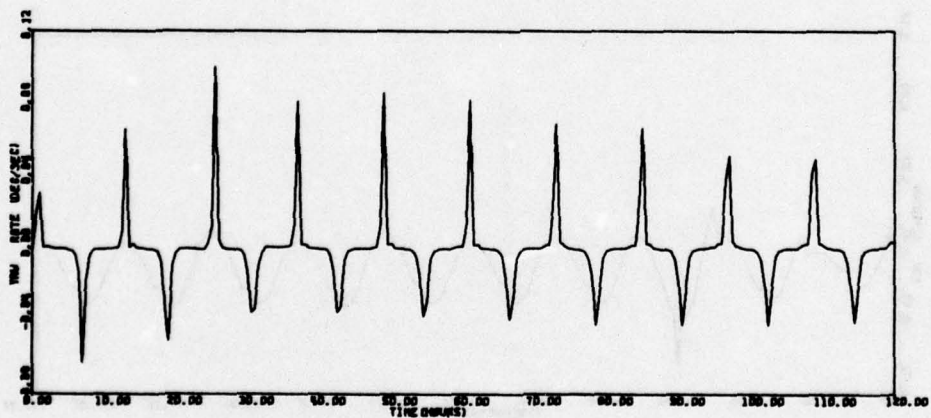
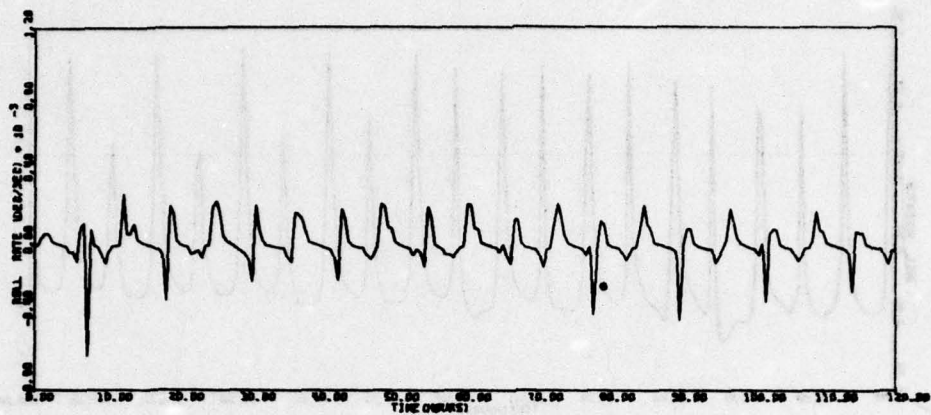


Figure 61. Run 6 - Sunline 0° - Worst Case (continued)

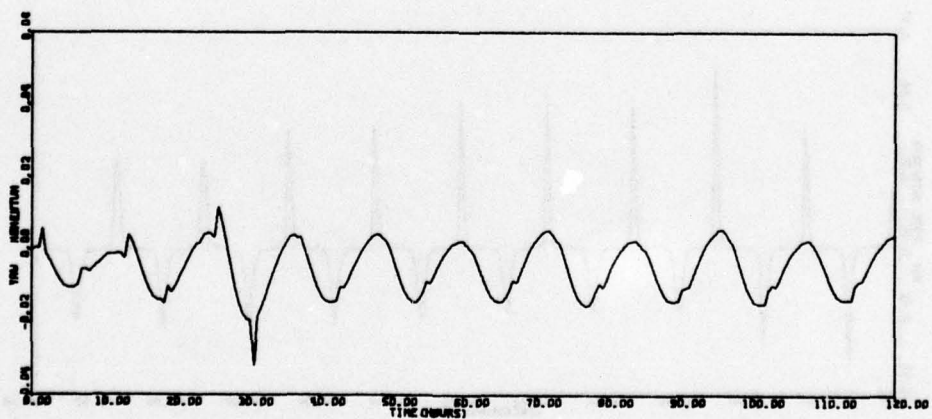
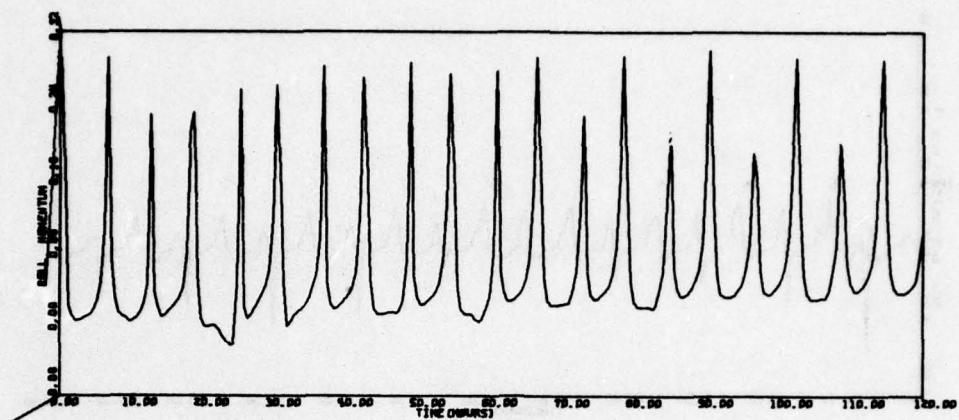


Figure 61. Run 6 - Sunline 0° - Worst Case (continued)

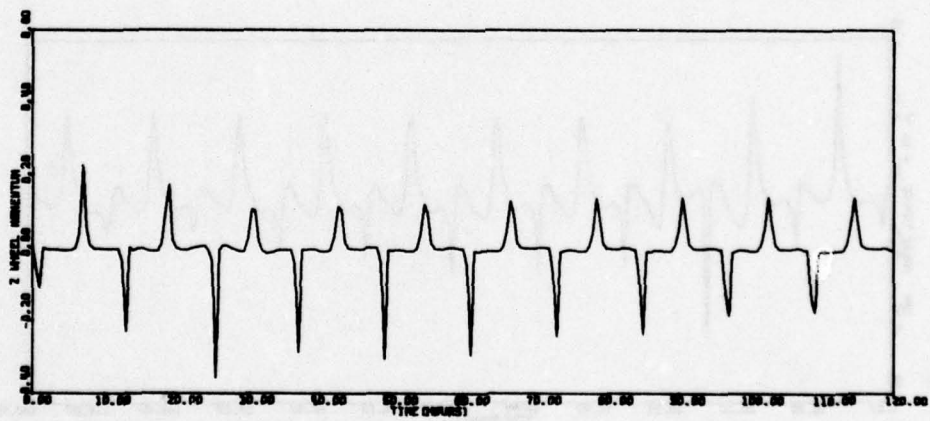
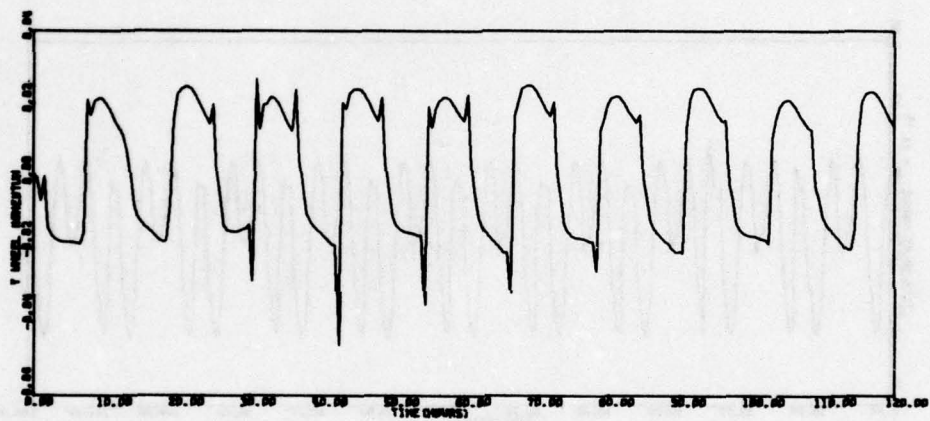
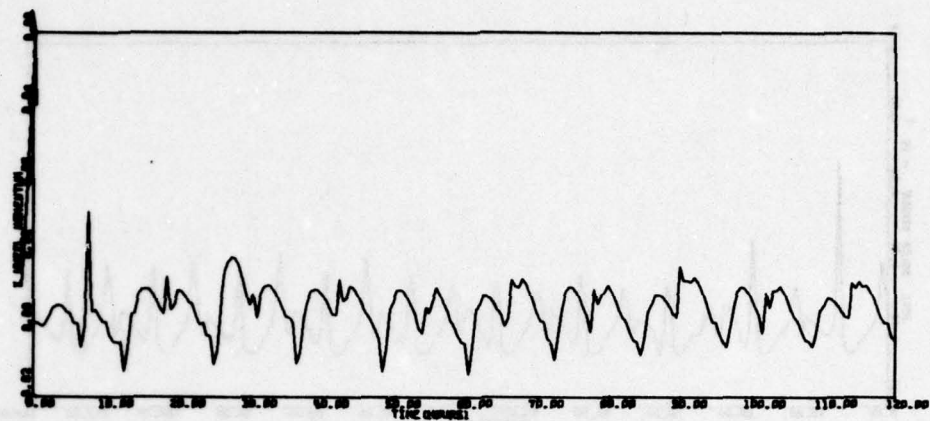


Figure 61. Run 6 - Sunline 0° - Worst Case (continued)

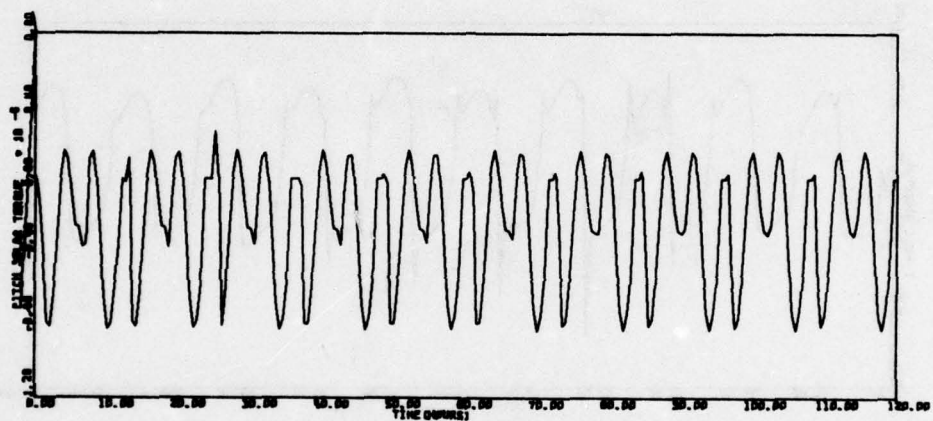
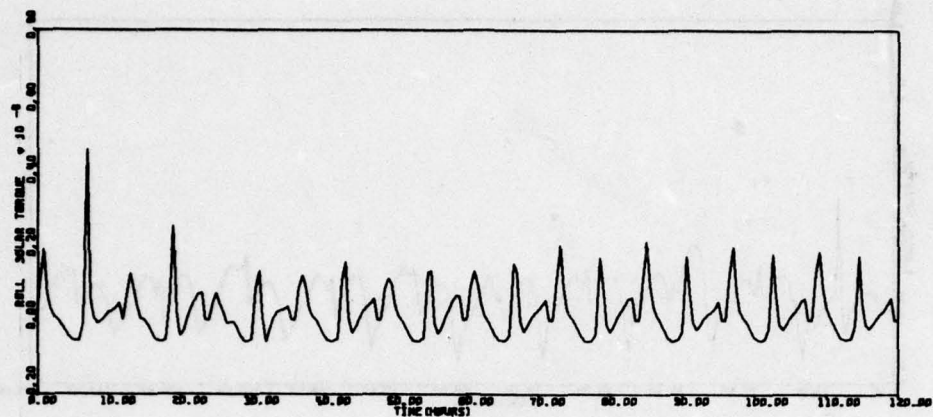


Figure 61. Run 6 - Sunline 0° - Worst Case (continued)

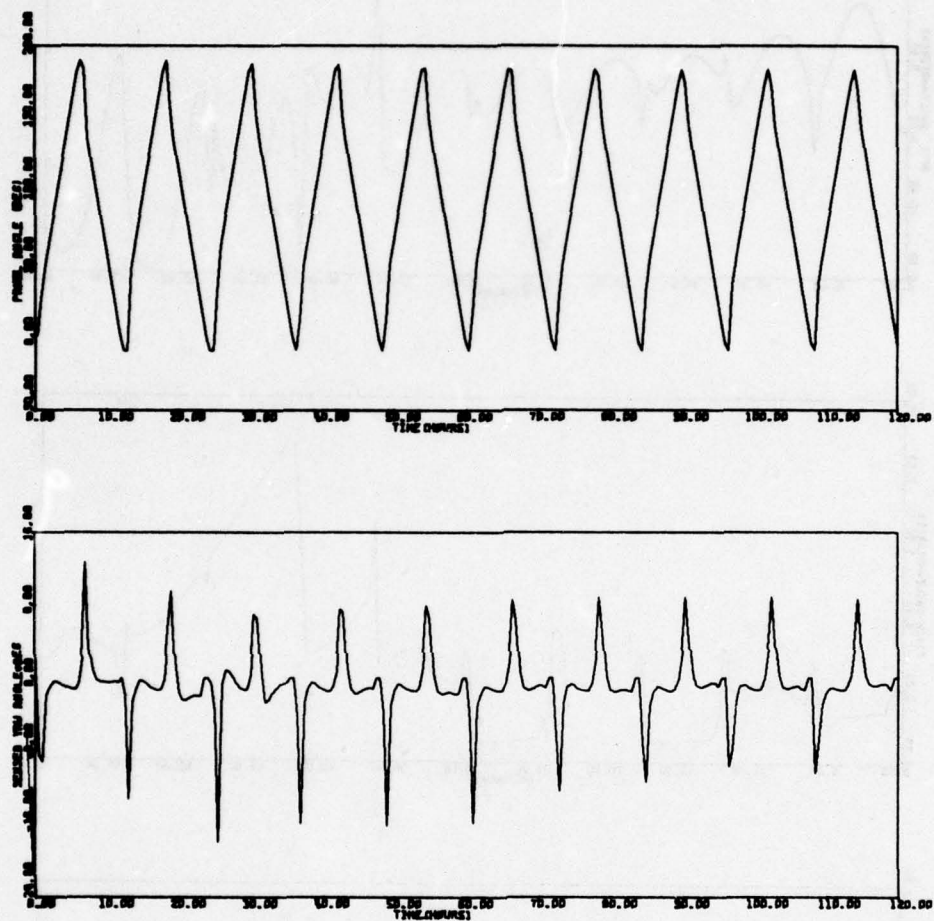


Figure 61. Run 6 - Sunline 0° - Worst Case (concluded)

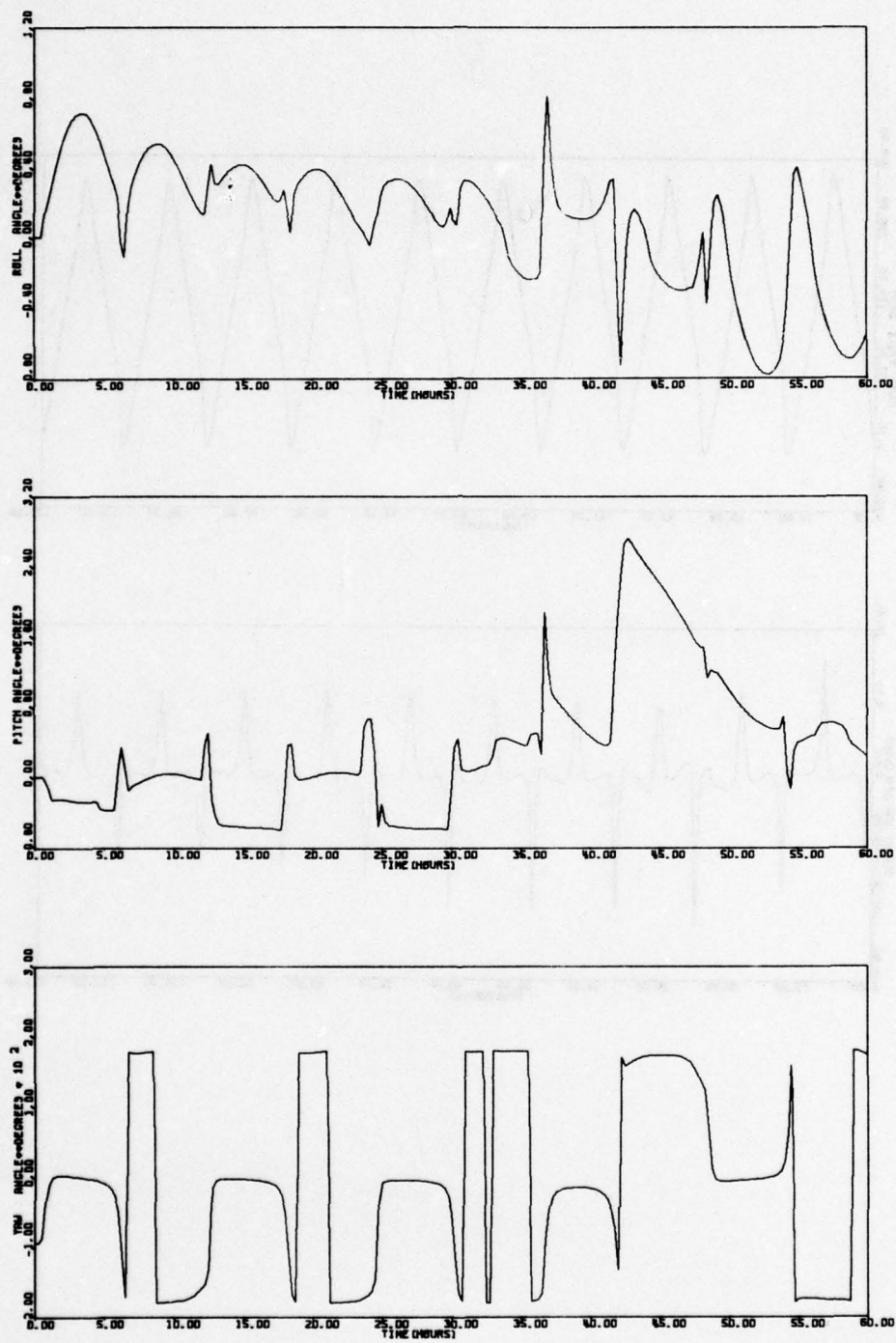


Figure 62. Run 7A - Wheel 1 Failure Compensated - Worst Case - Sunline 0°

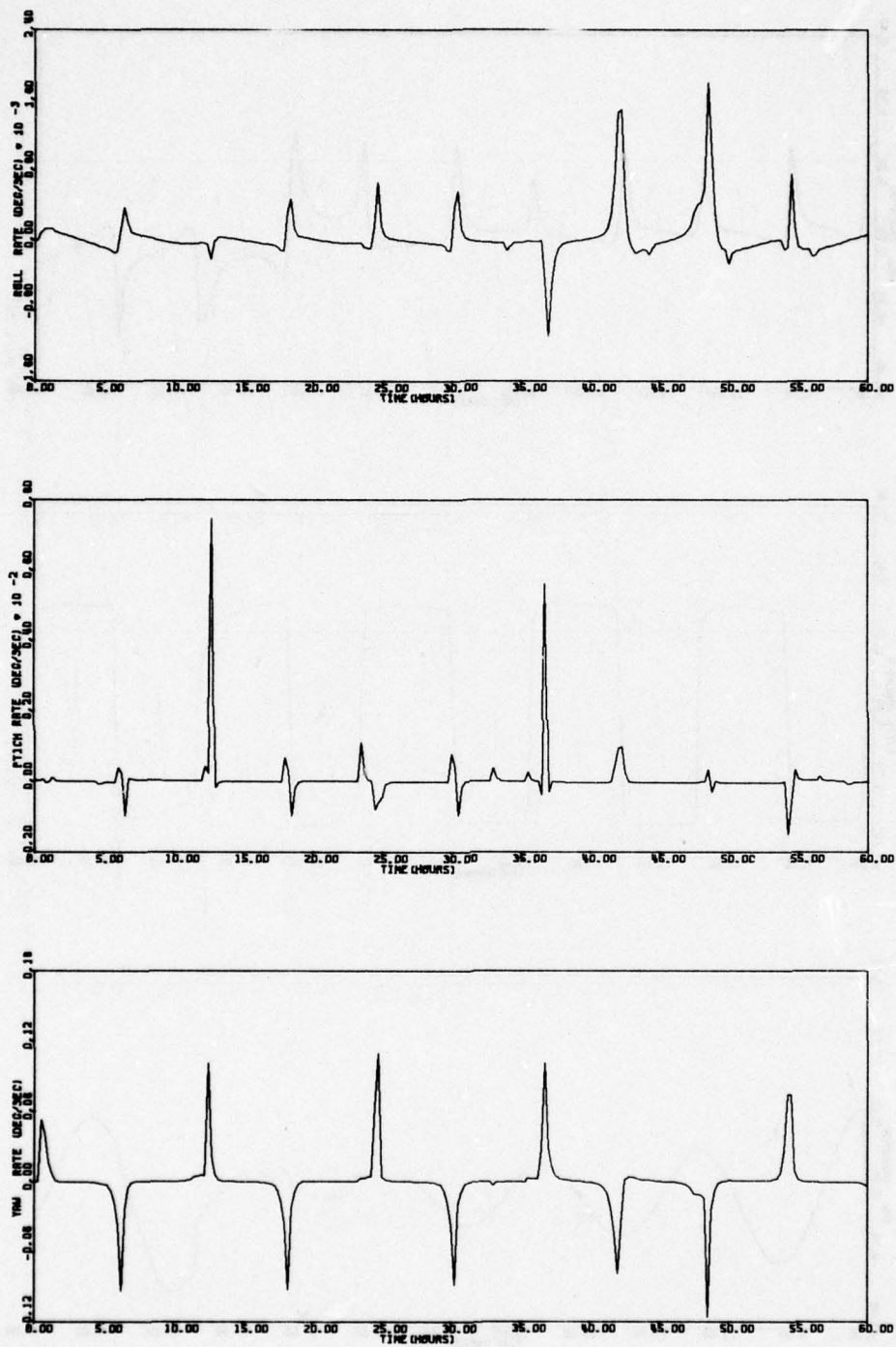


Figure 62. Run 7A - Wheel 1 Failure Compensated - Worst Case - Sunline 0° (continued)

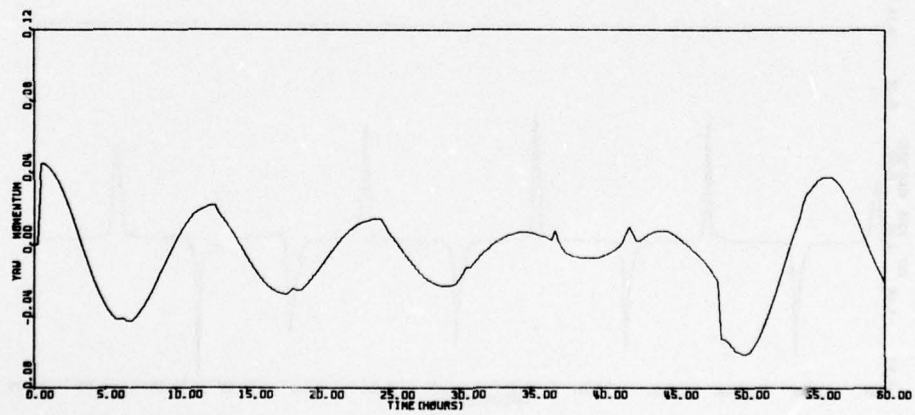
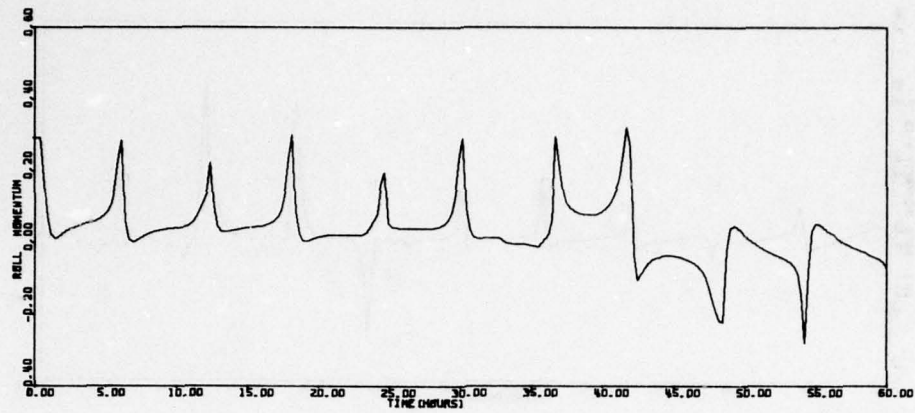


Figure 62. Run 7A - Wheel 1 Failure Compensated - Worst Case - Sunline 0° (continued)

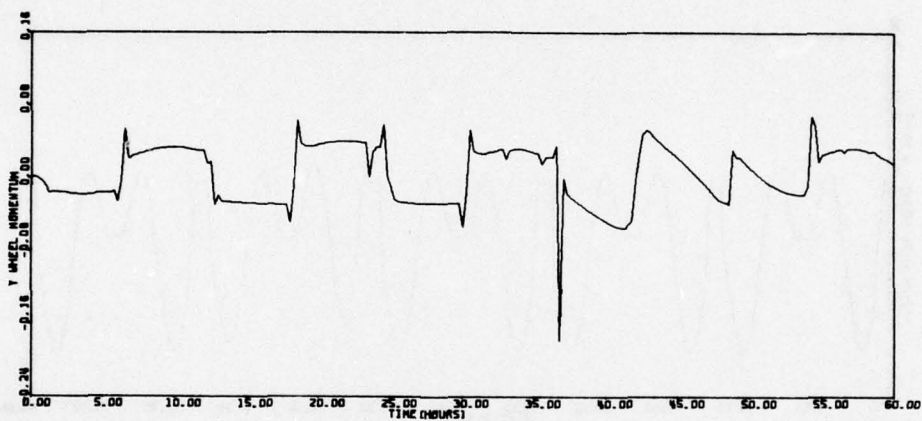
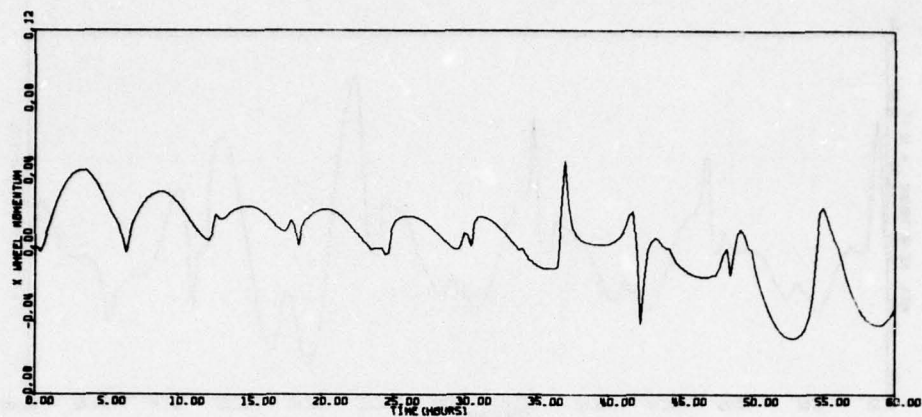


Figure 62. Run 7A - Wheel 1 Failure Compensated - Worst Case - Sunline 0° (continued)

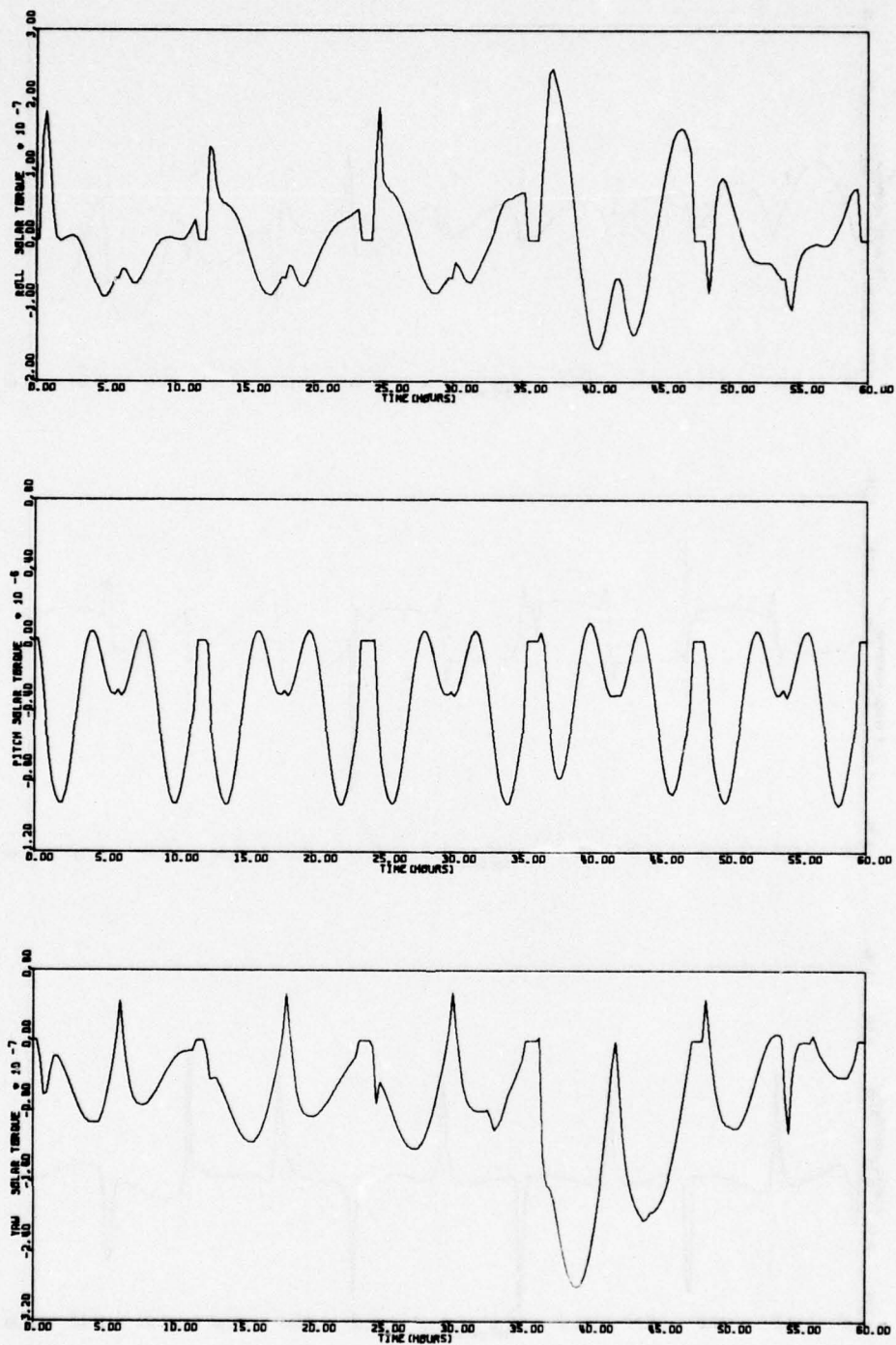


Figure 62. Run 7A - Wheel 1 Failure Compensated - Worst Case - Sunline 0° (continued)

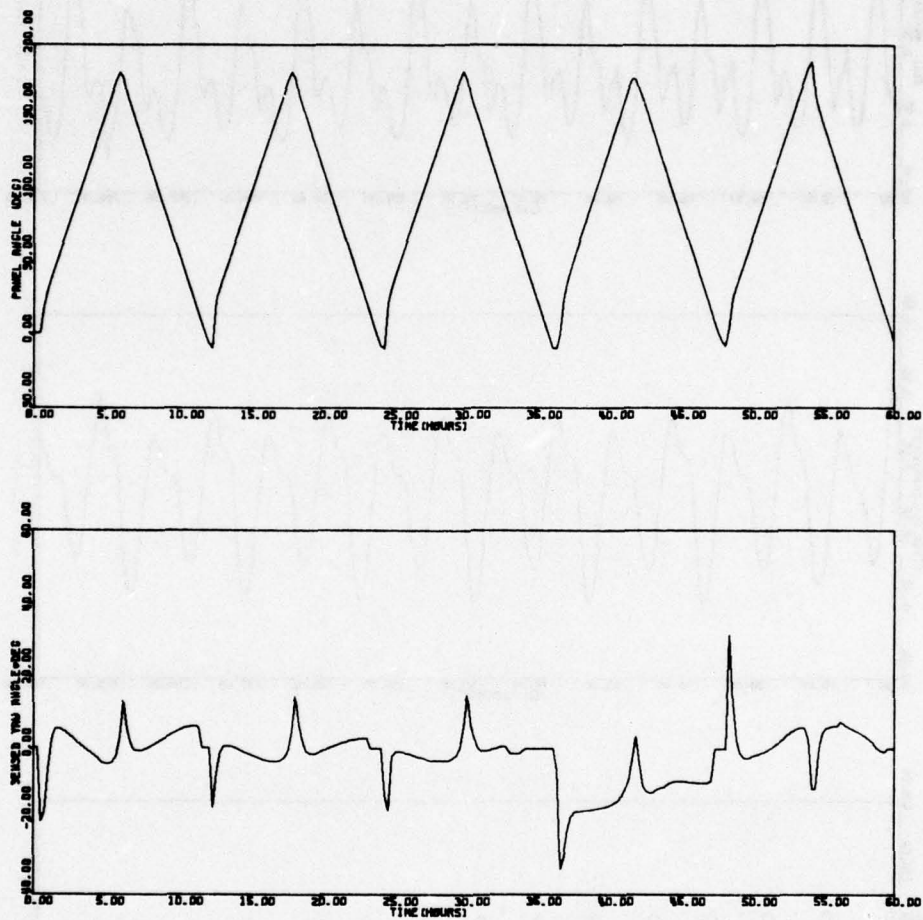


Figure 62. Run 7A - Wheel 1 Failure Compensated - Worst Case - Sunline 0° (concluded)

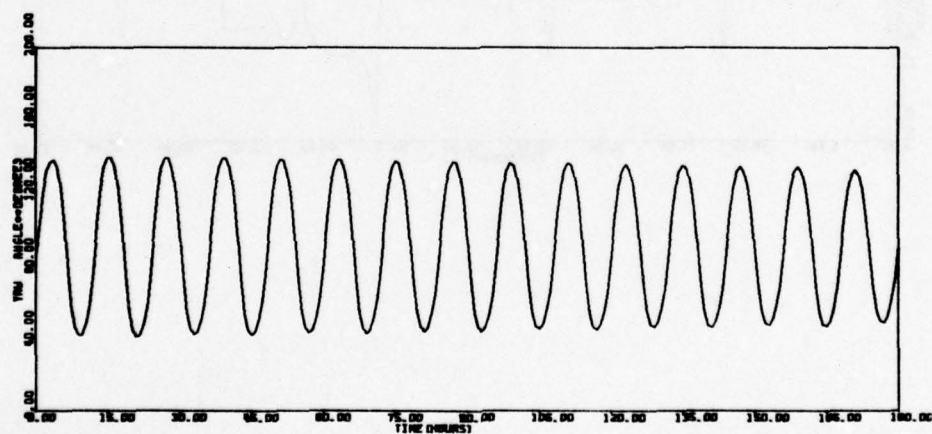
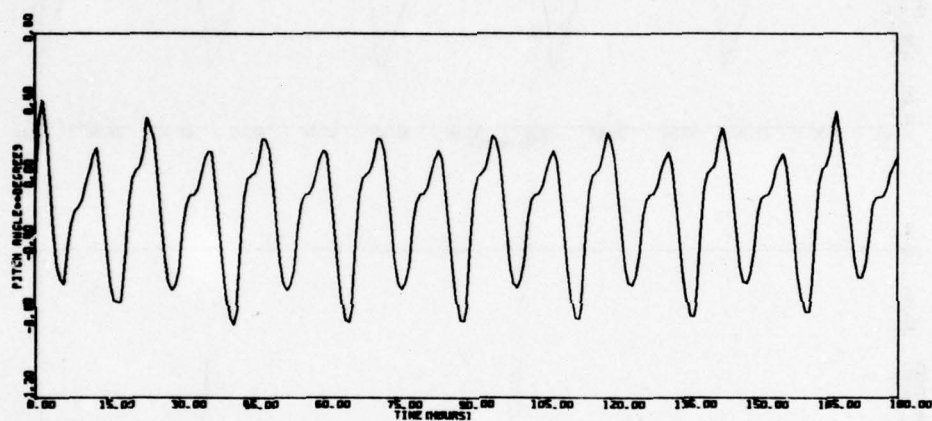
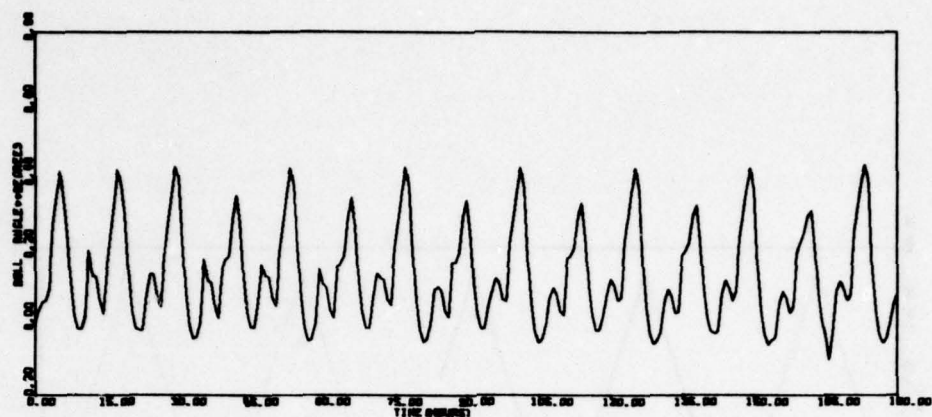


Figure 63. Run 8 - Wheel 2 Failure Uncompensated - Worst Case - Sunline 45°

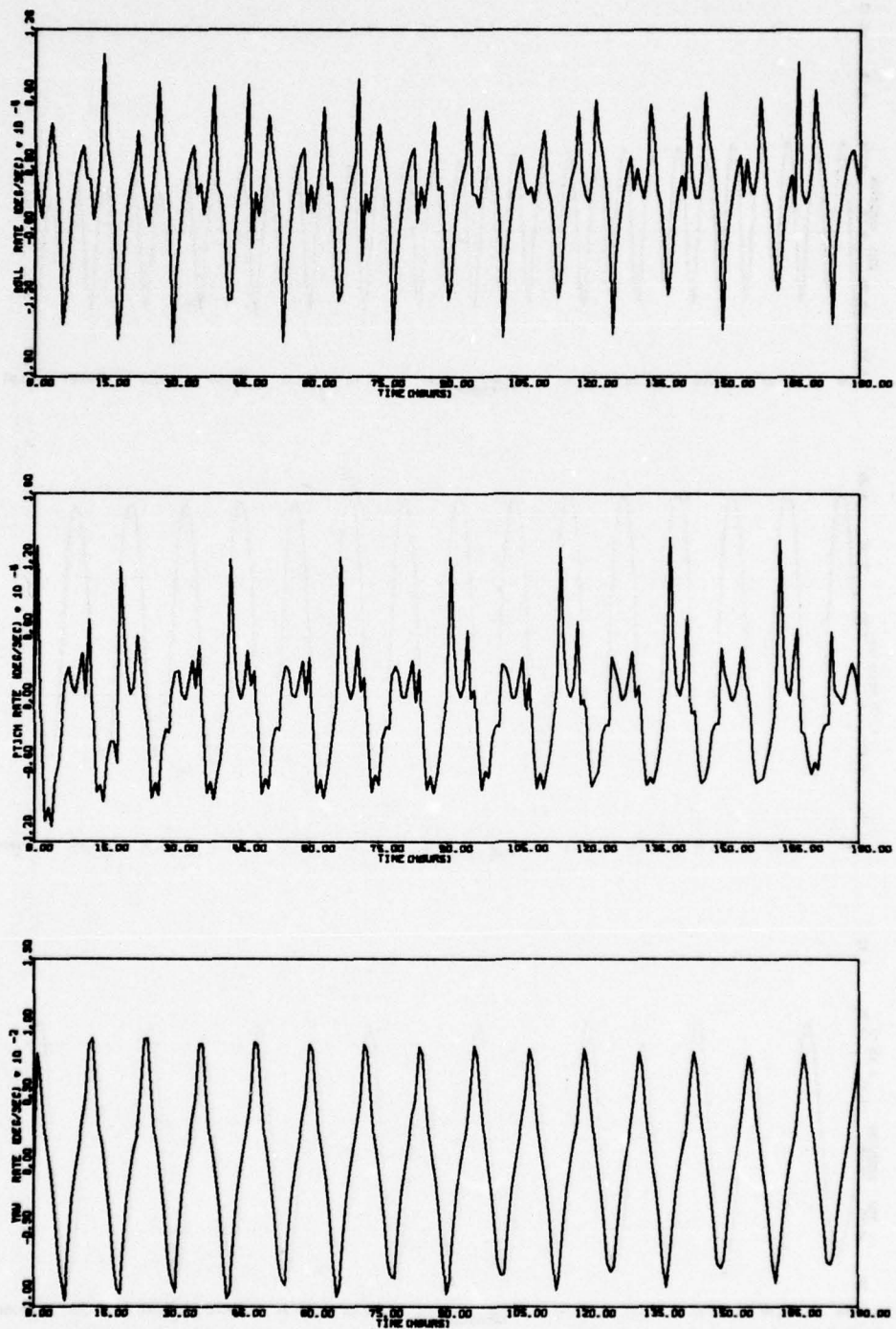


Figure 63. Run 8 - Wheel 2 Failure Uncompensated - Worst Case - Sunline 45° (continued)

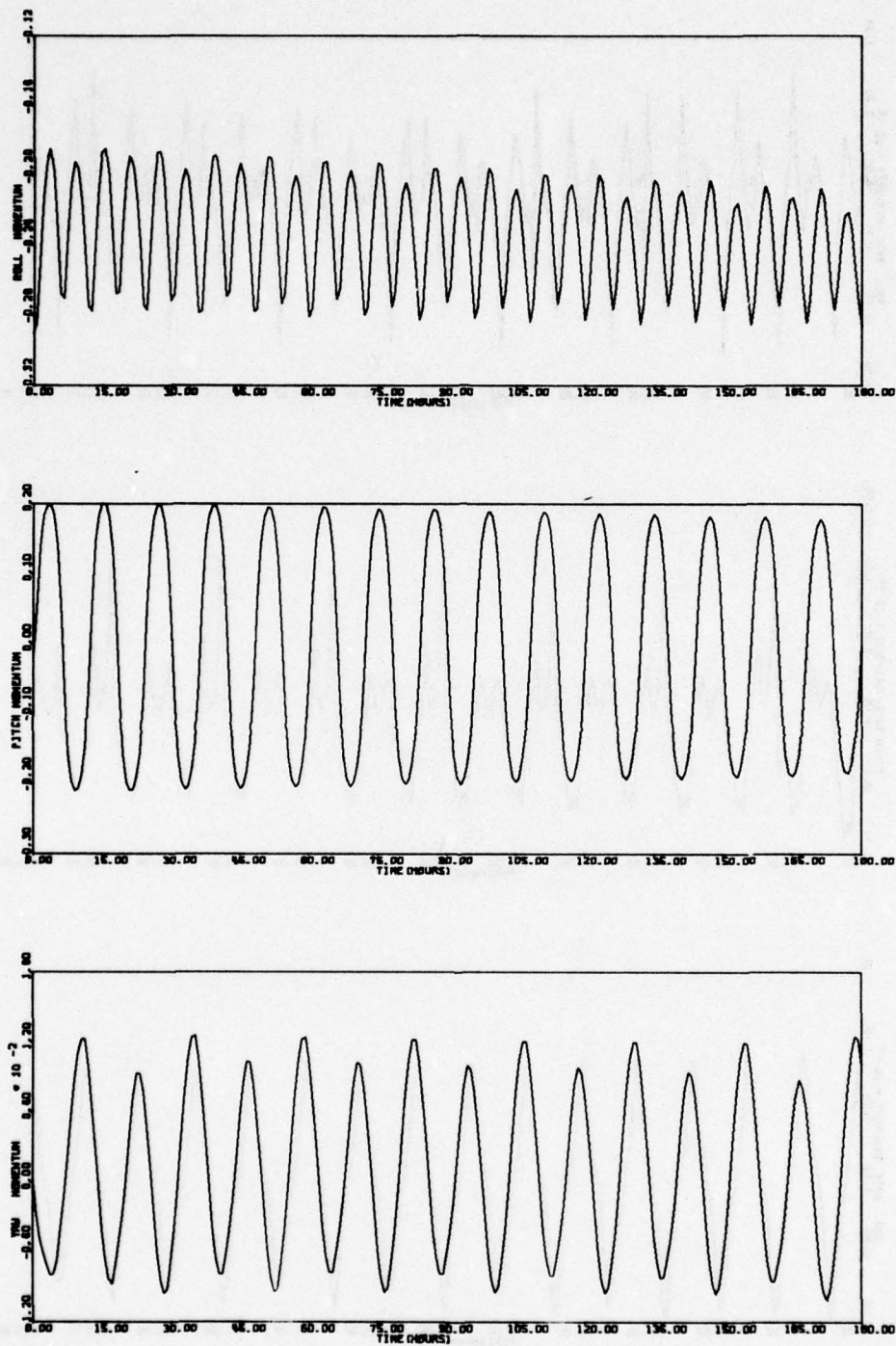


Figure 63. Run 8 - Wheel 2 Failure Uncompensated - Worst Case - Sunline 45° (continued)

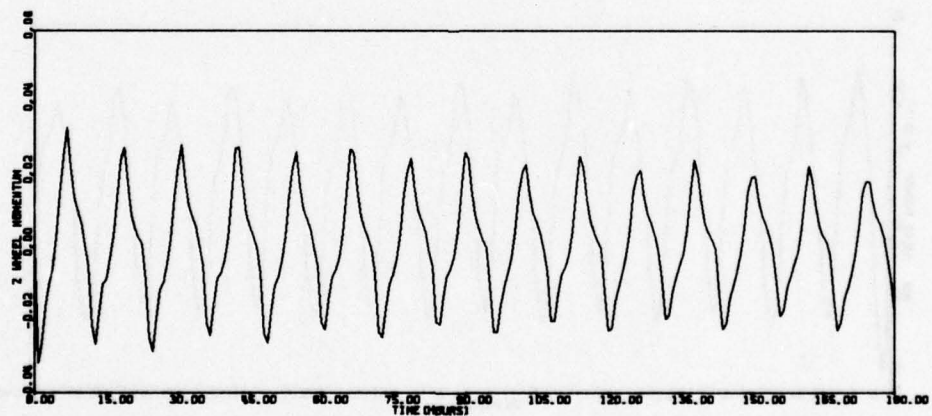
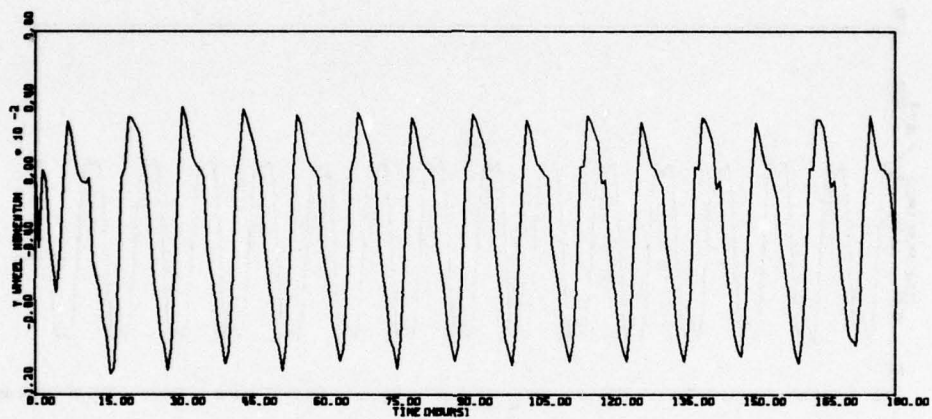
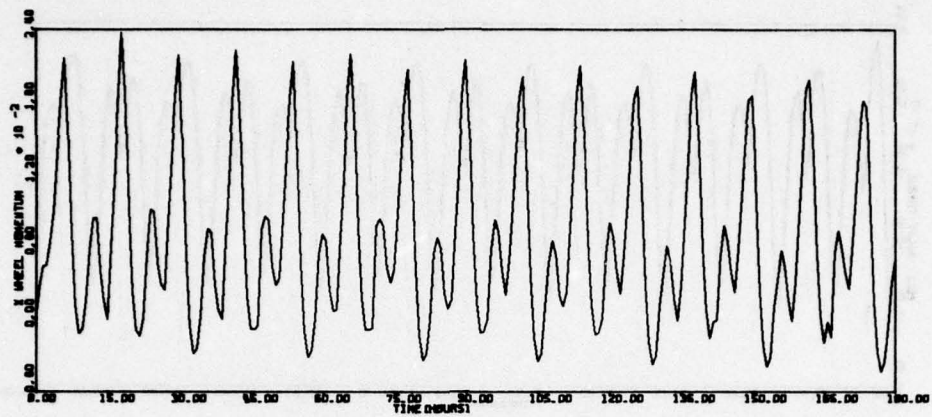


Figure 63. Run 8 - Wheel 2 Failure Uncompensated - Worst Case - Sunline 45° (continued)

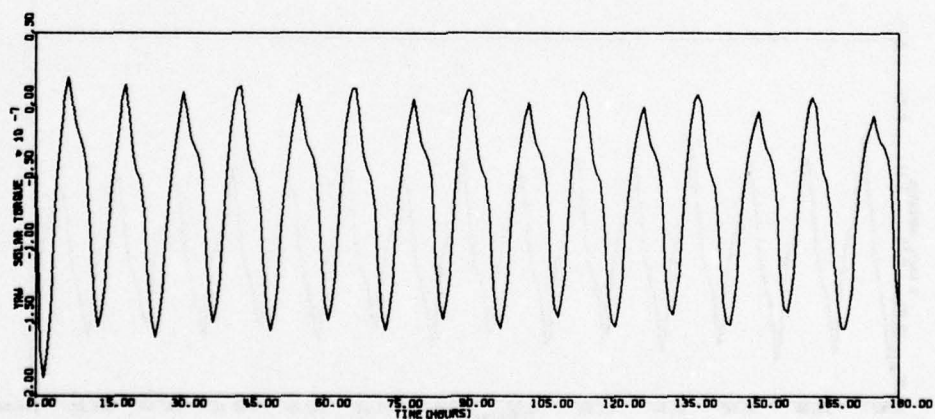
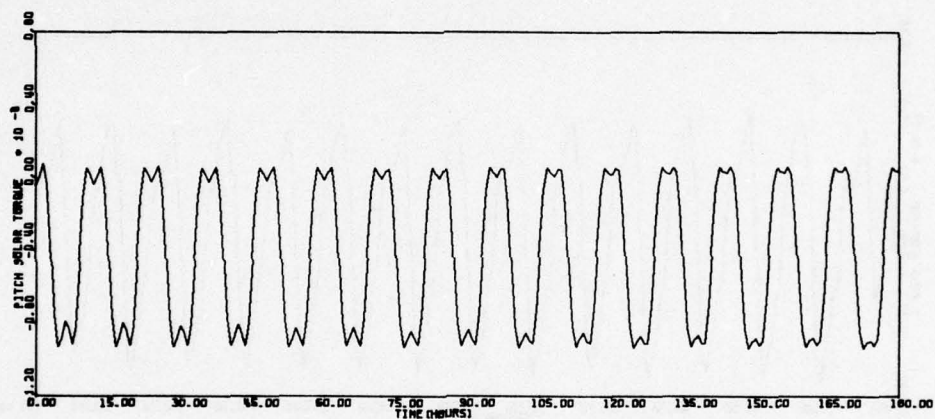
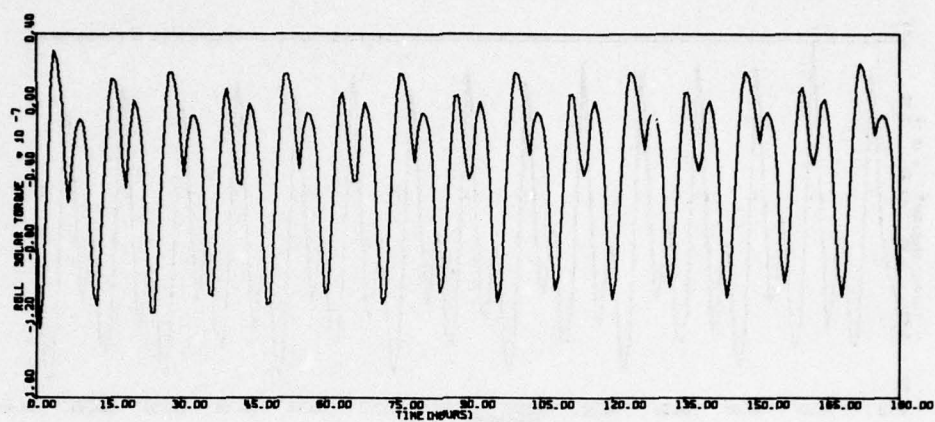


Figure 63. Run 8 - Wheel 2 Failure Uncompensated - Worst Case - Sunline 45° (continued)

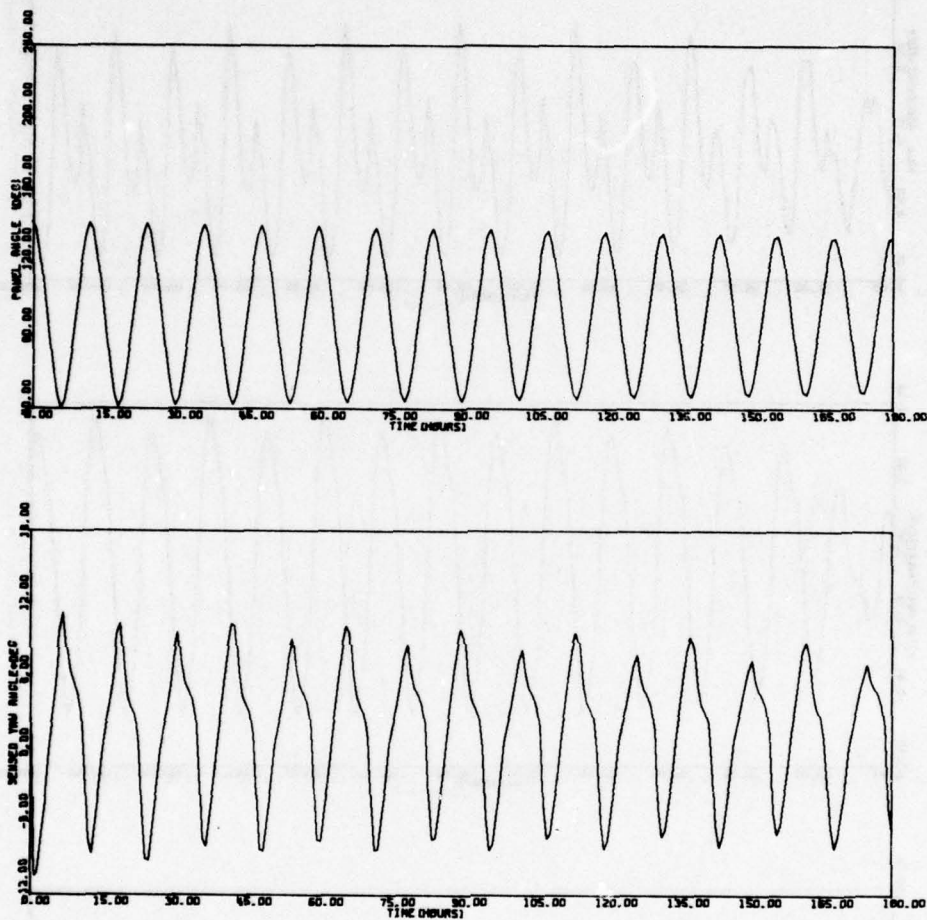


Figure 63. Run 8 - Wheel 2 Failure Uncompensated - Worst Case - Sunline 45° (concluded)

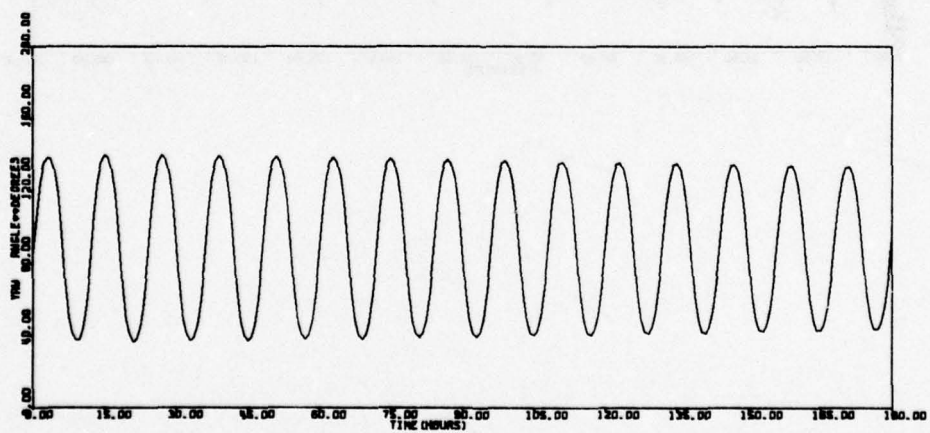
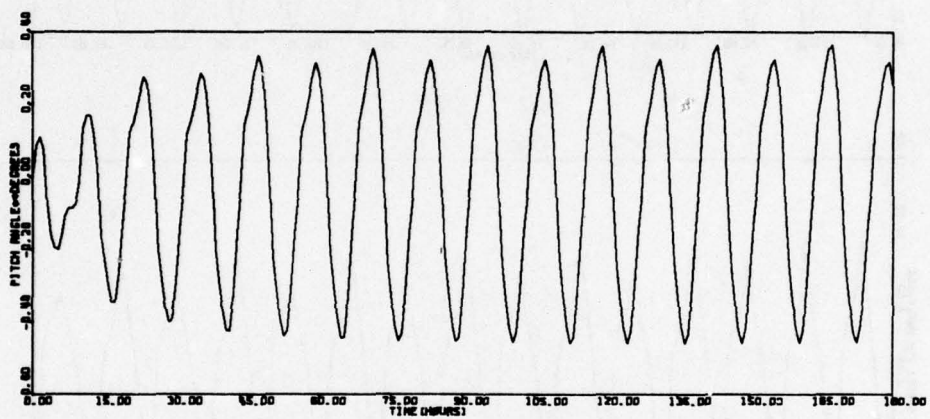
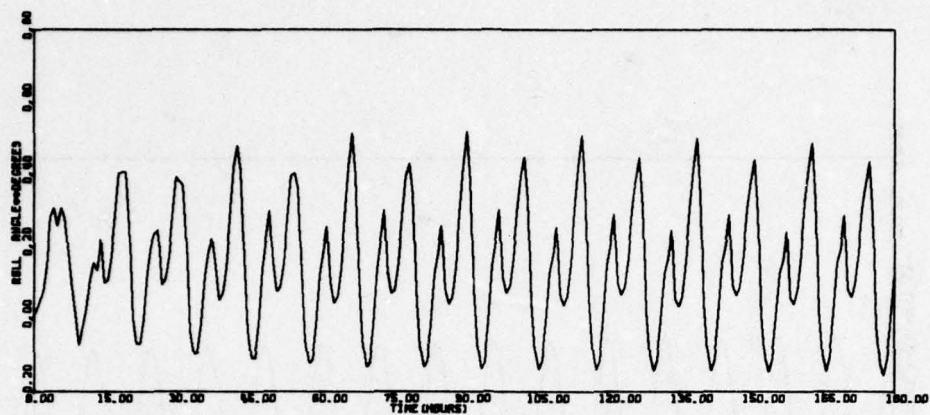


Figure 64. Run 9 - Wheel 2 Failure Compensated - Worst Case - Sunline 45°

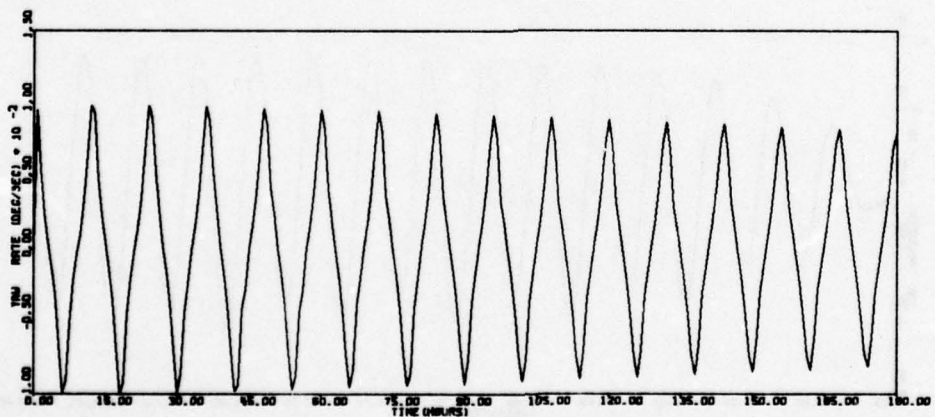
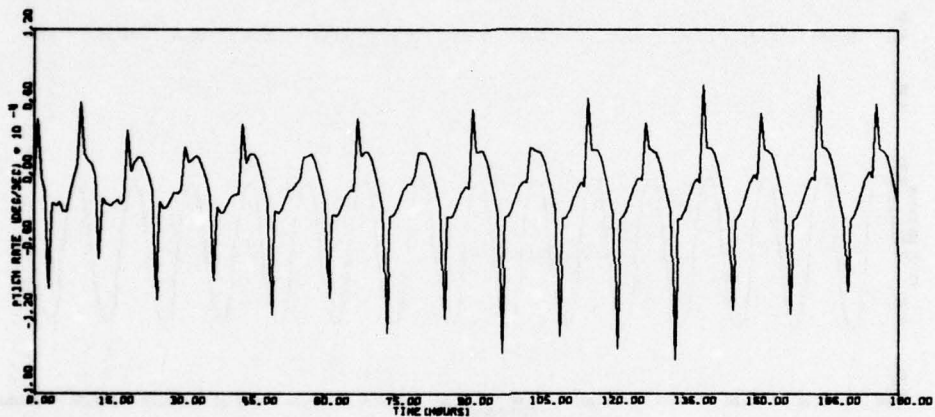
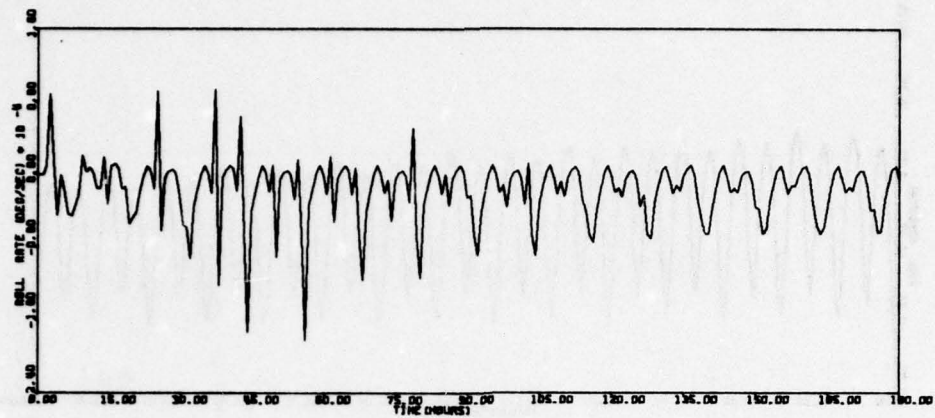


Figure 64. Run 9 - Wheel 2 Failure Compensated - Worst Case - Sunline 45° (continued)

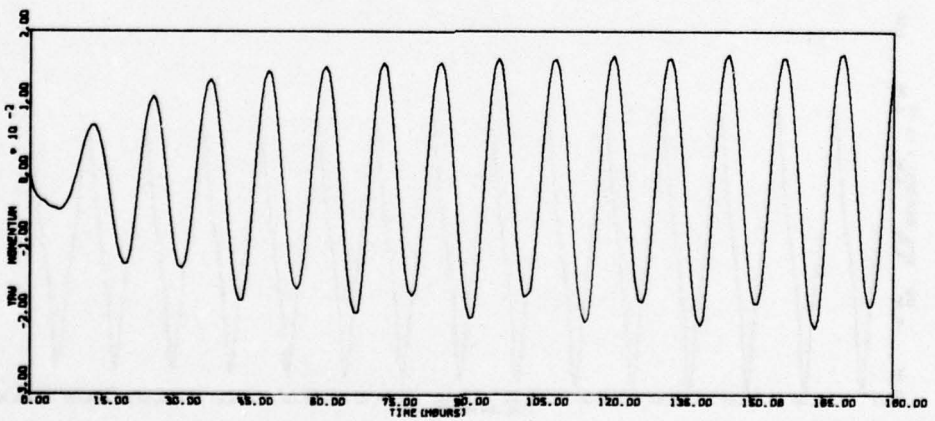
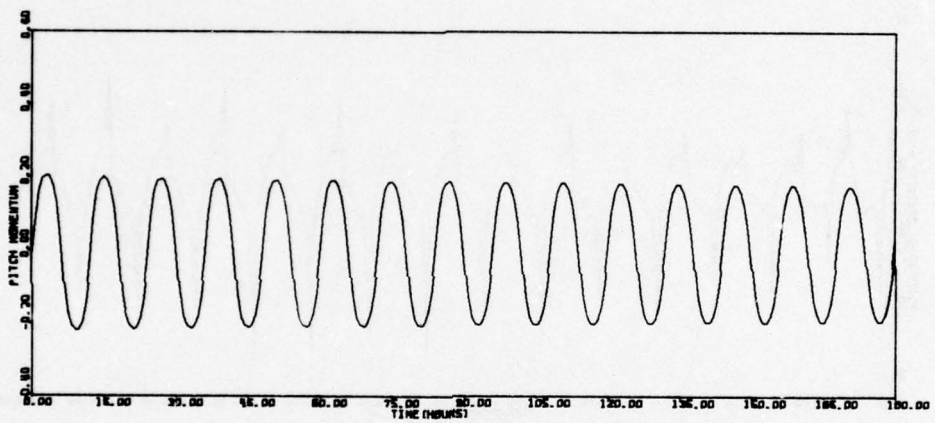
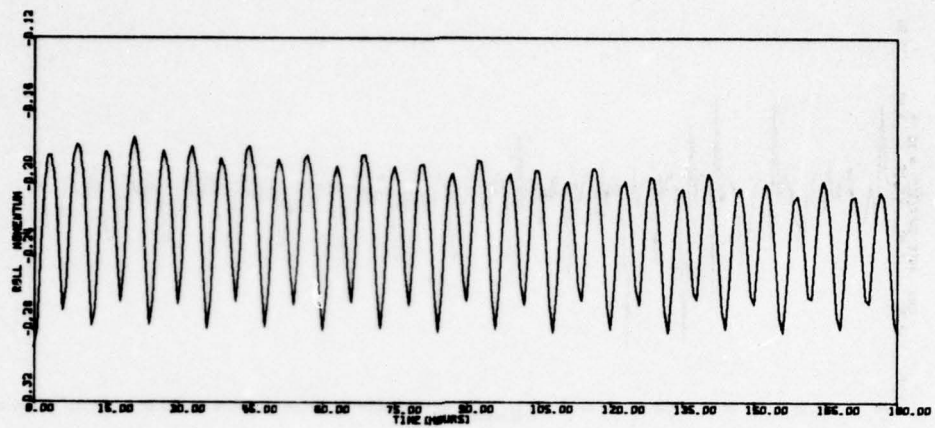


Figure 64. Run 9 - Wheel 2 Failure Compensated - Worst Case - Sunline 45° (continued)

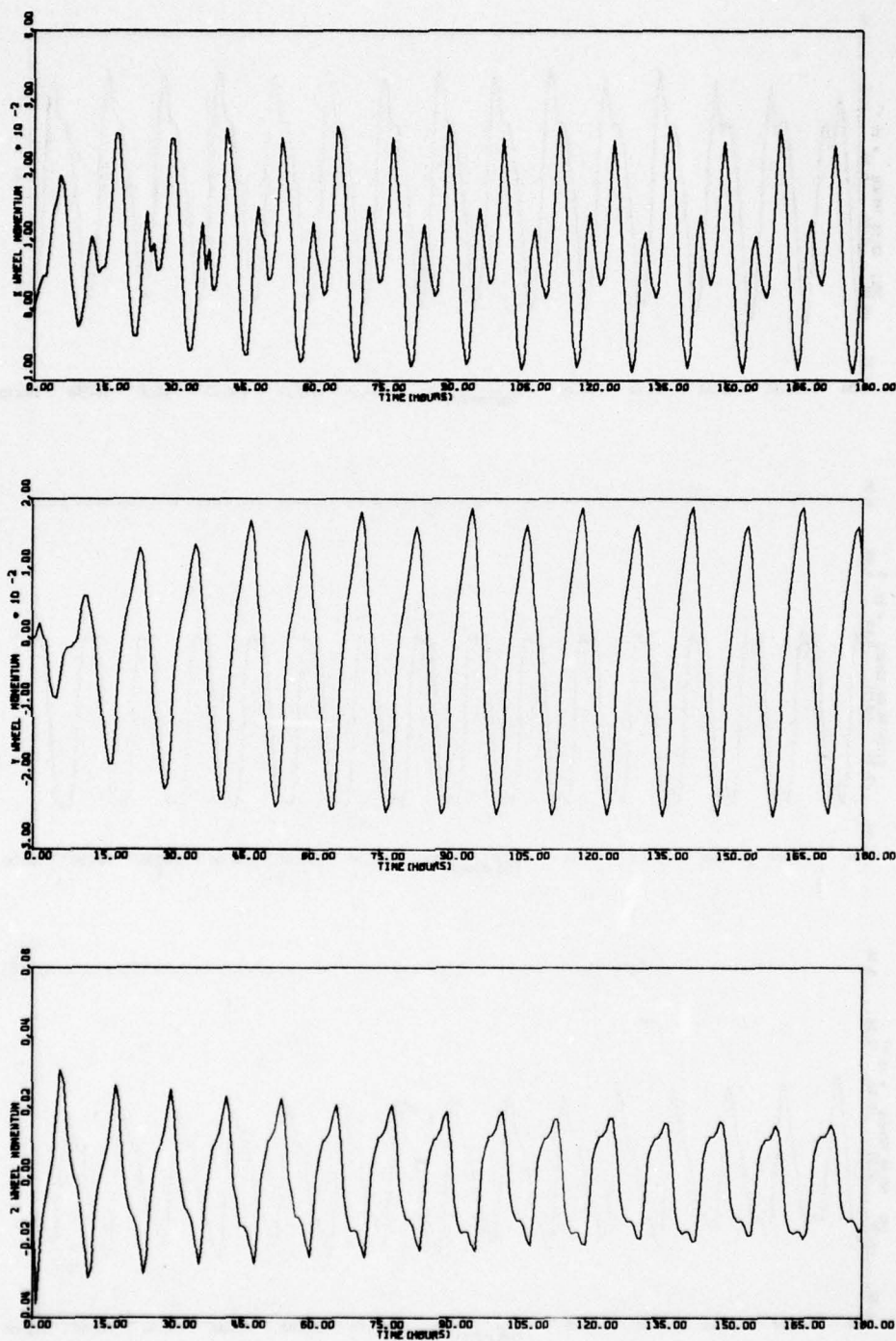


Figure 64. Run 9 - Wheel 2 Failure Compensated - Worst Case - Sunline 45° (continued)

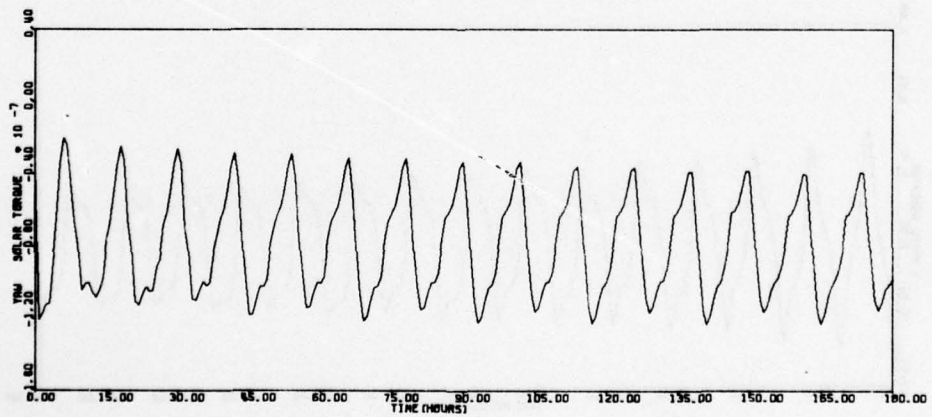
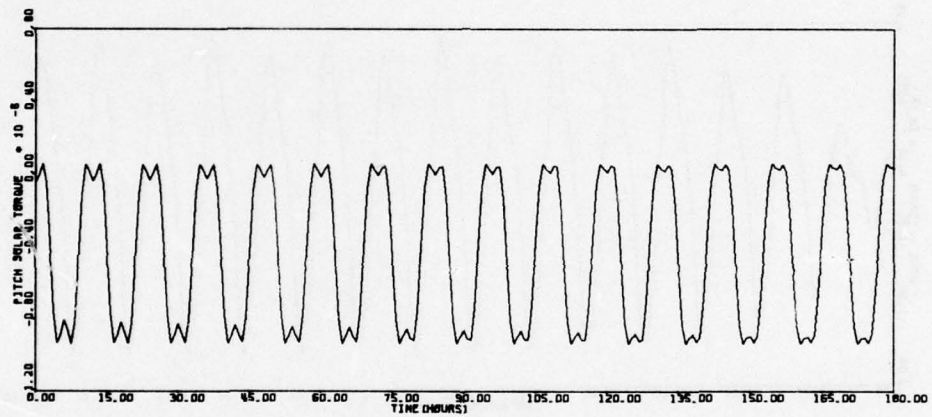
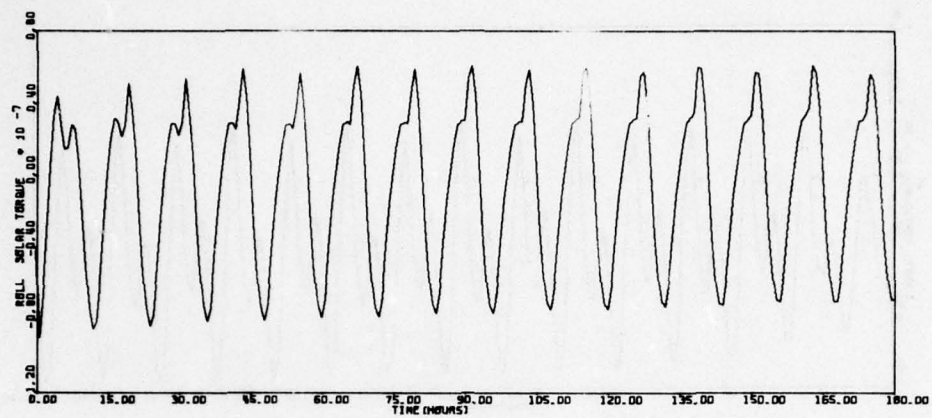


Figure 64. Run 9 - Wheel 2 Failure Compensated - Worst Case - Sunline 45° (continued)

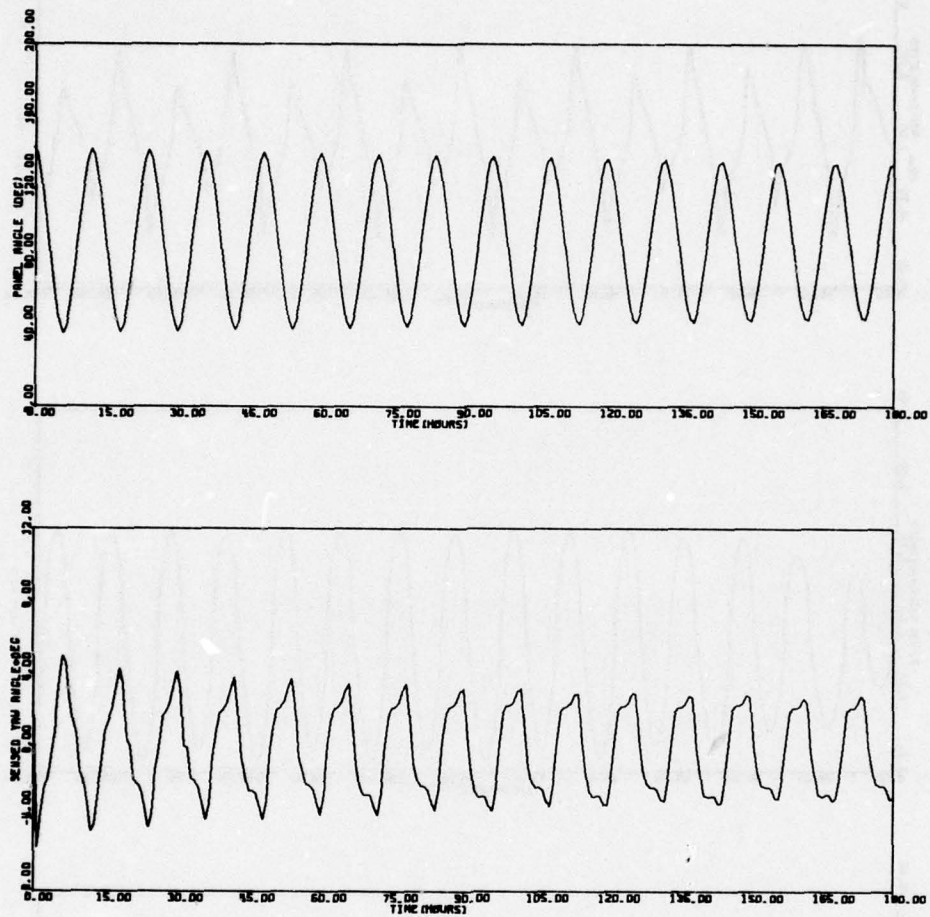


Figure 64. Run 9 - Wheel 2 Failure Compensated - Worst Case - Sunline 45° (concluded)

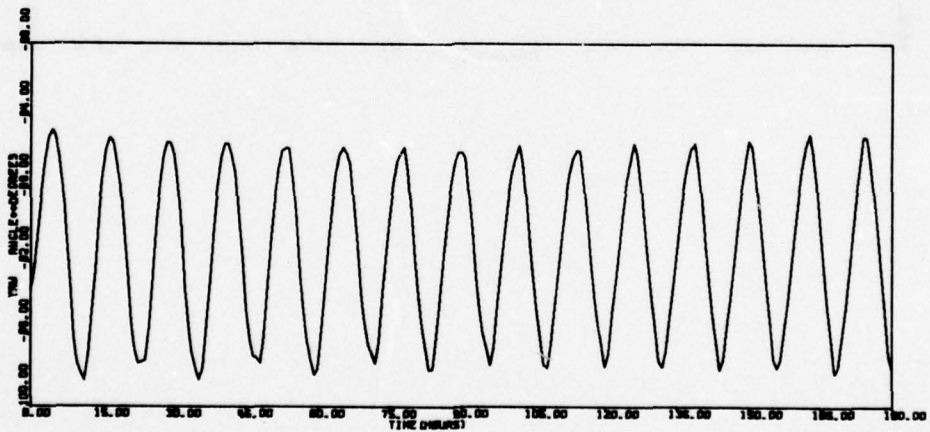
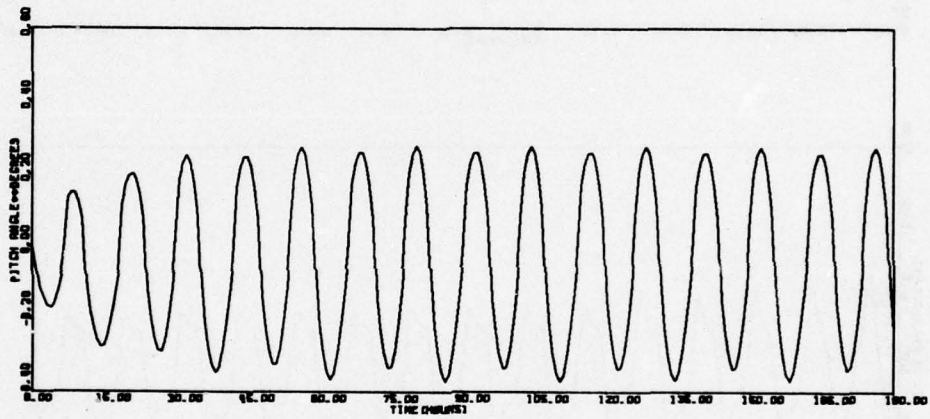
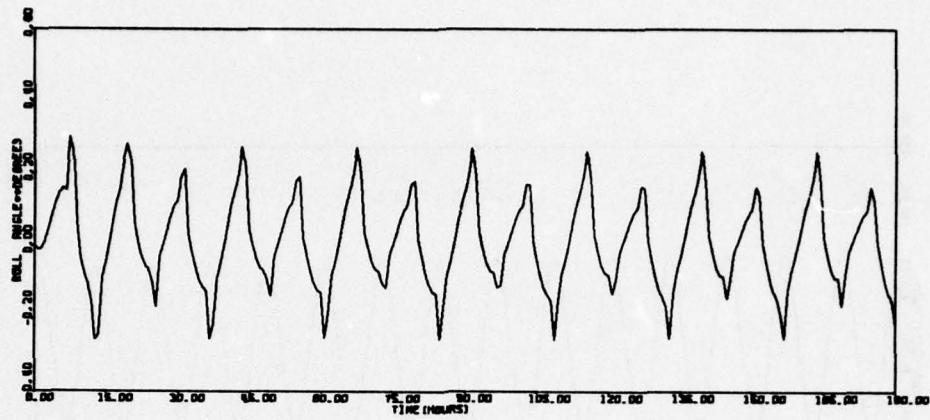


Figure 65. Run 10 - Wheel 2 Failure Compensated - Worst Case - Sunline 86°

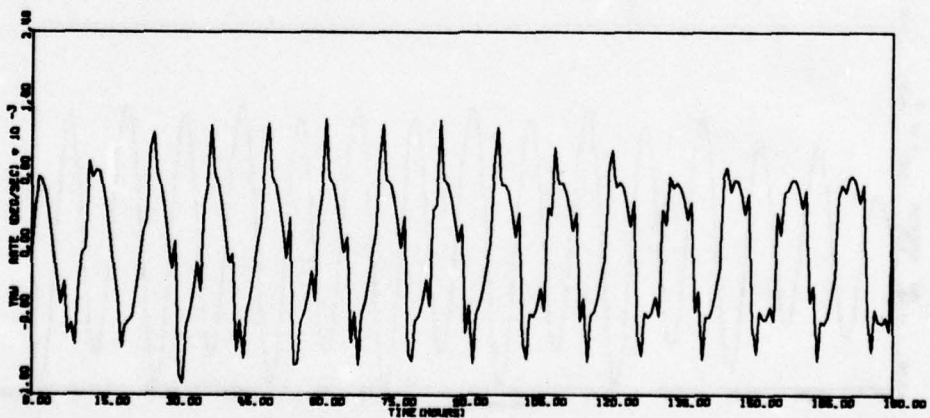
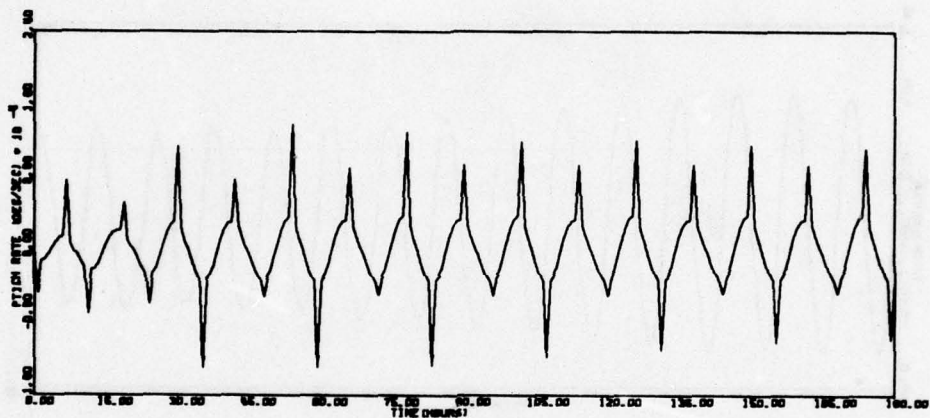
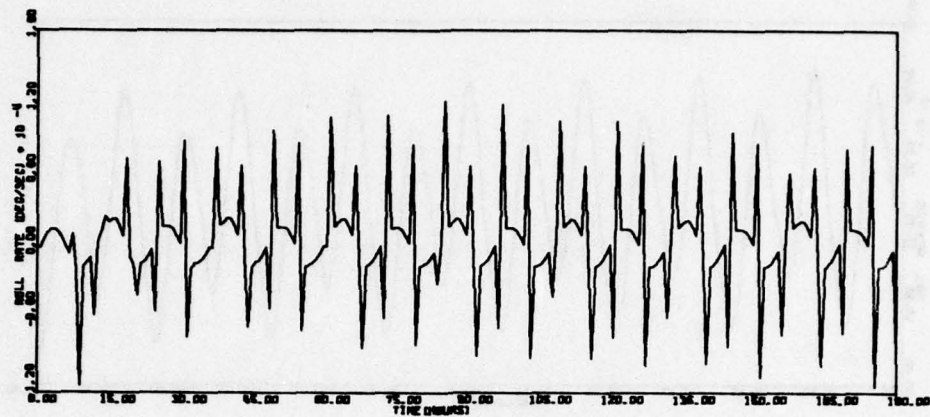


Figure 65. Run 10 - Wheel 2 Failure Compensated - Worst Case - Sunline 86° (continued)

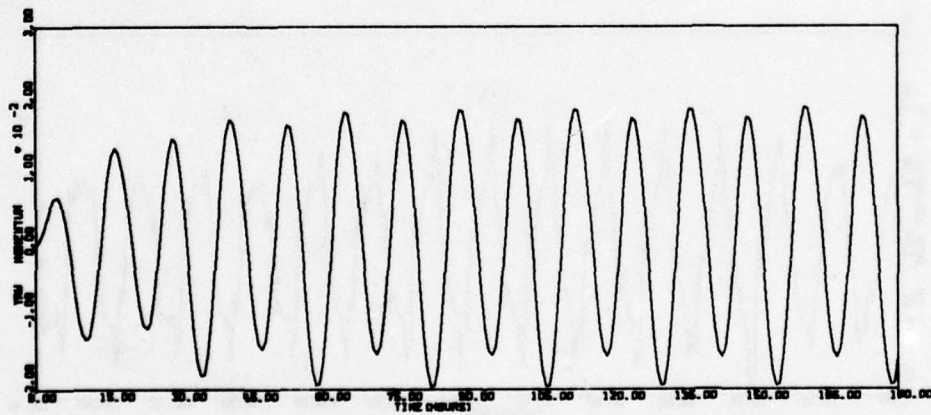
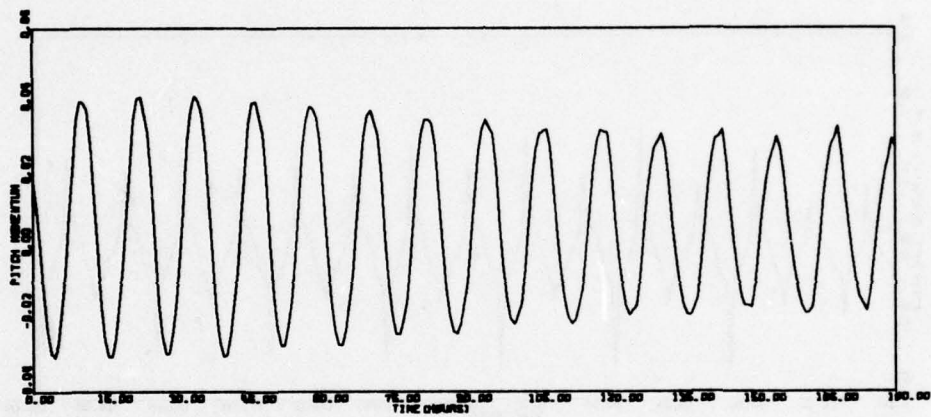
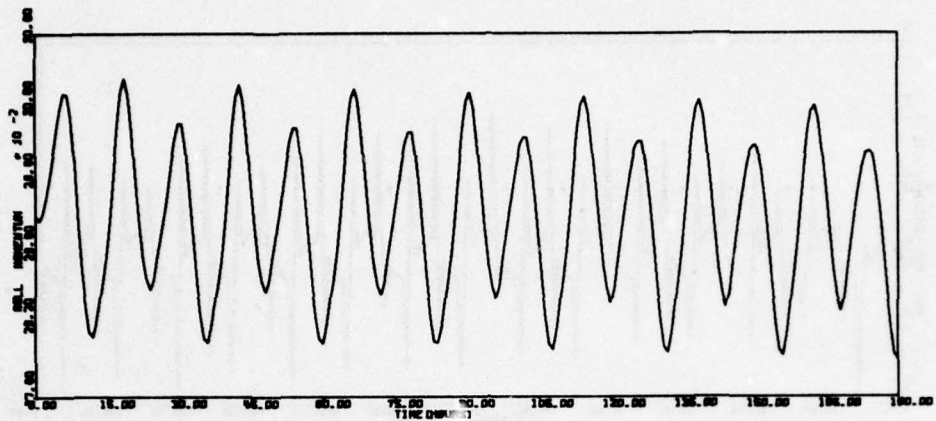


Figure 65. Run 10 - Wheel 2 Failure Compensated - Worst Case - Sunline 86° (continued)

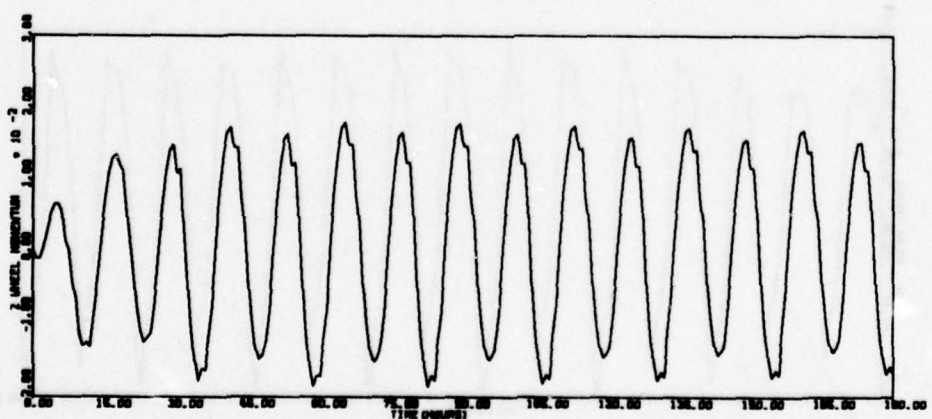
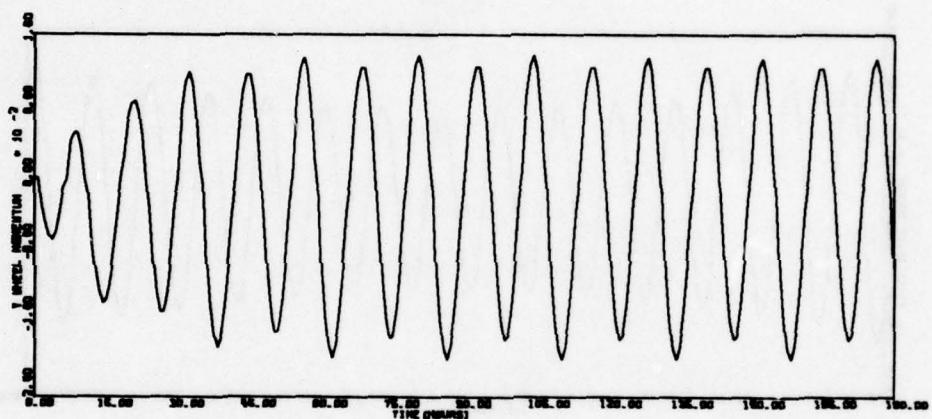
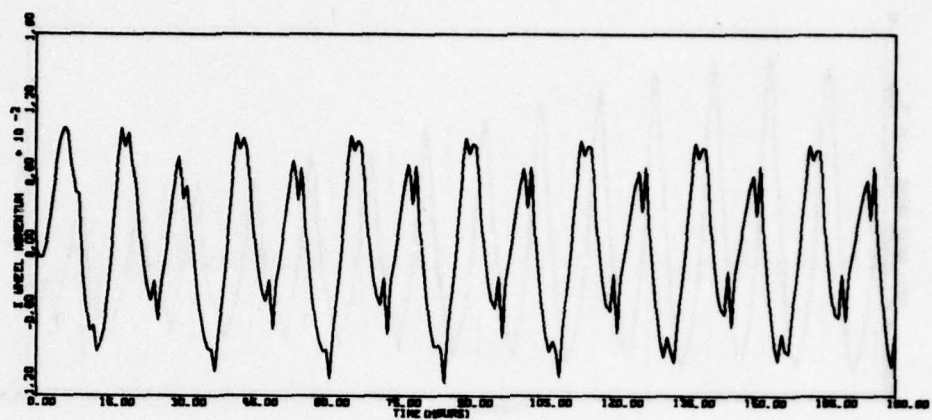


Figure 65. Run 10 - Wheel 2 Failure Compensated - Worst Case - Sunline 86^O (continued)

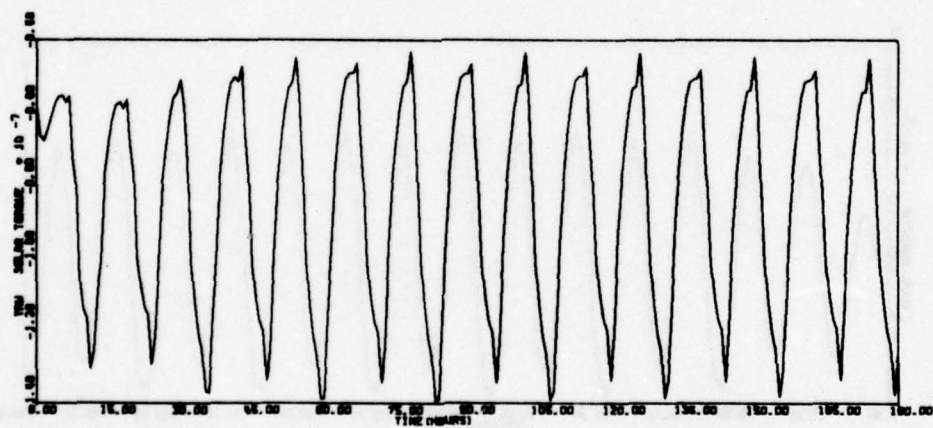
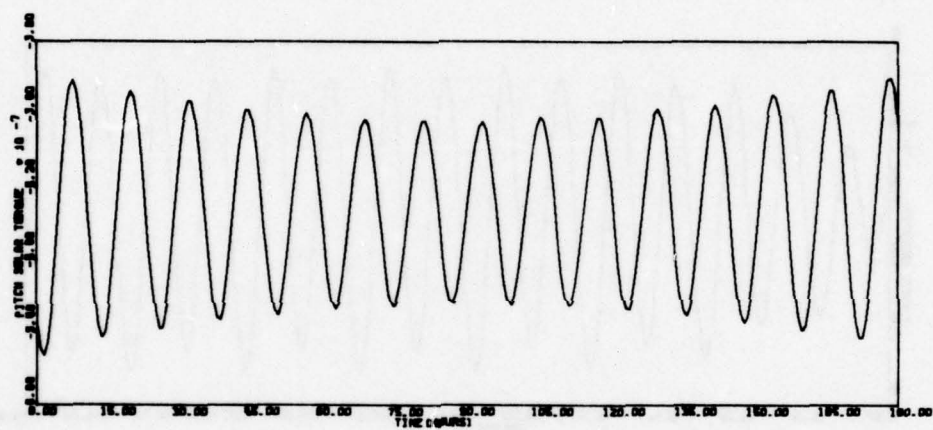
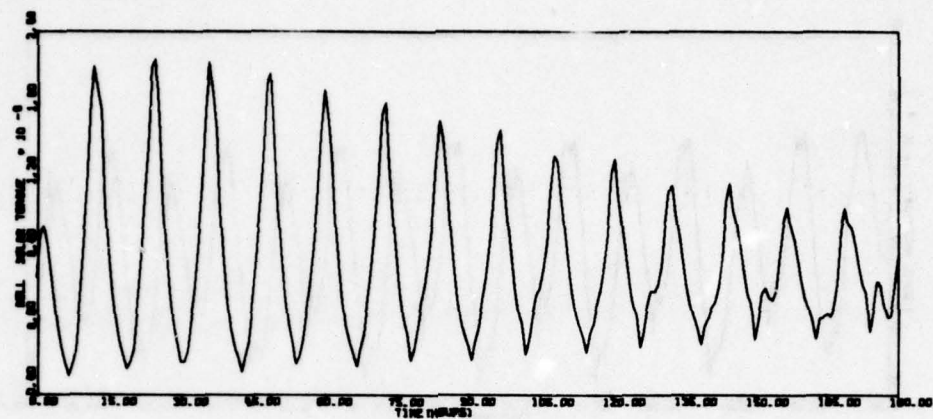


Figure 65. Run 10 - Wheel 2 Failure Compensated - Worst Case - Sunline 86⁰ (continued)

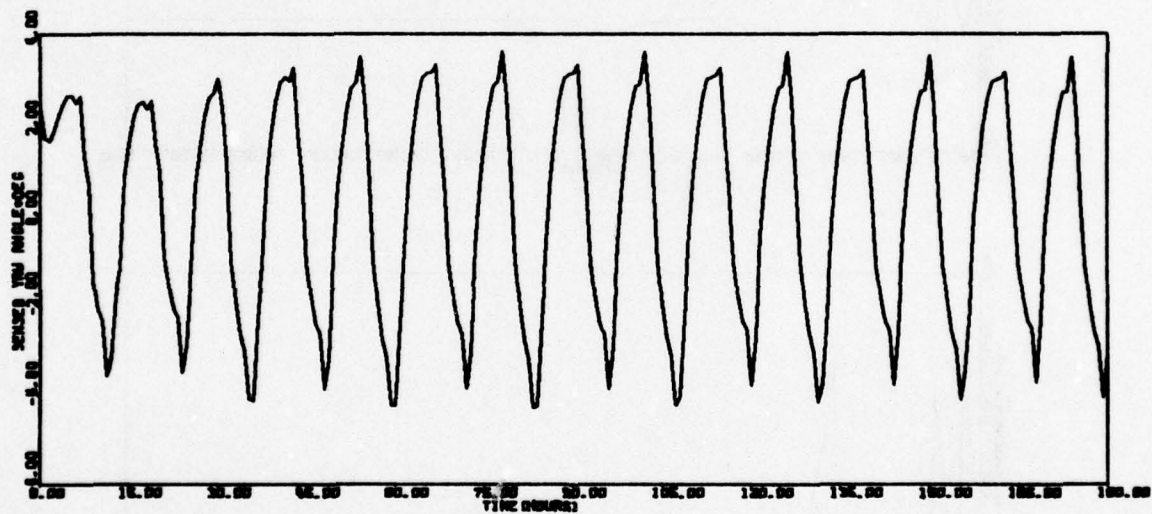
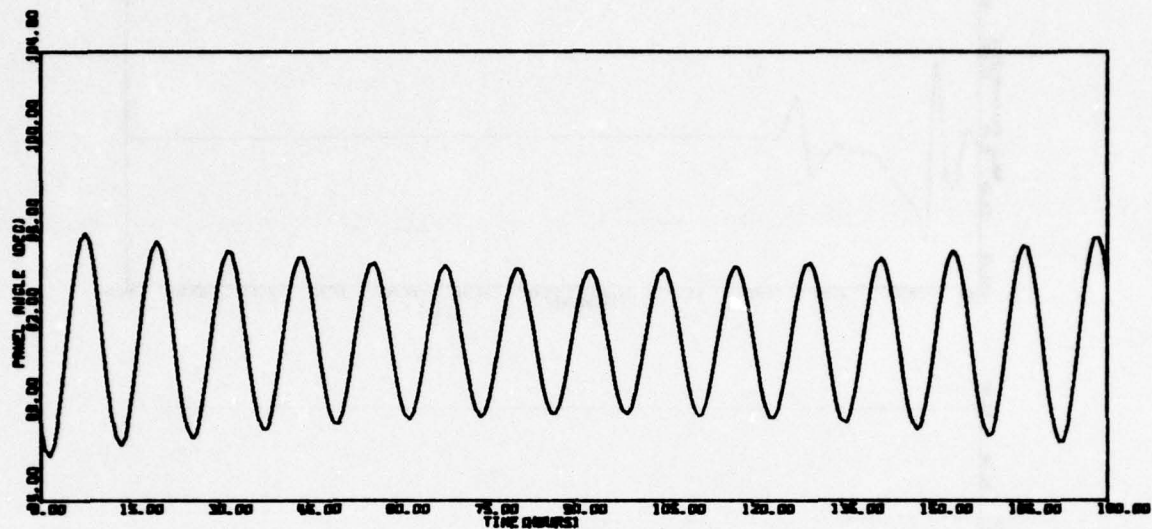


Figure 65. Run 10 - Wheel 2 Failure Compensated - Worst Case - Sunline 86⁰ (concluded)

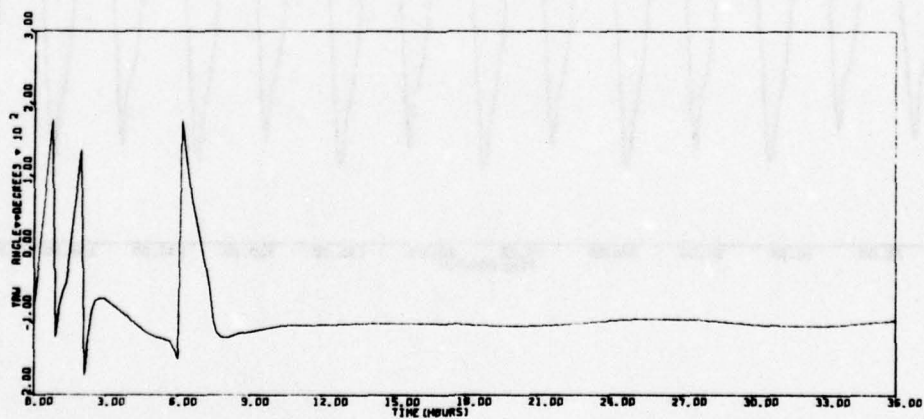
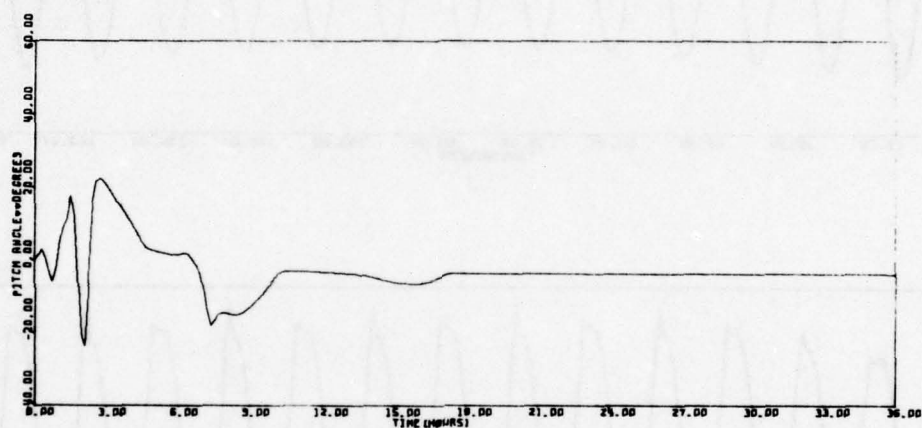
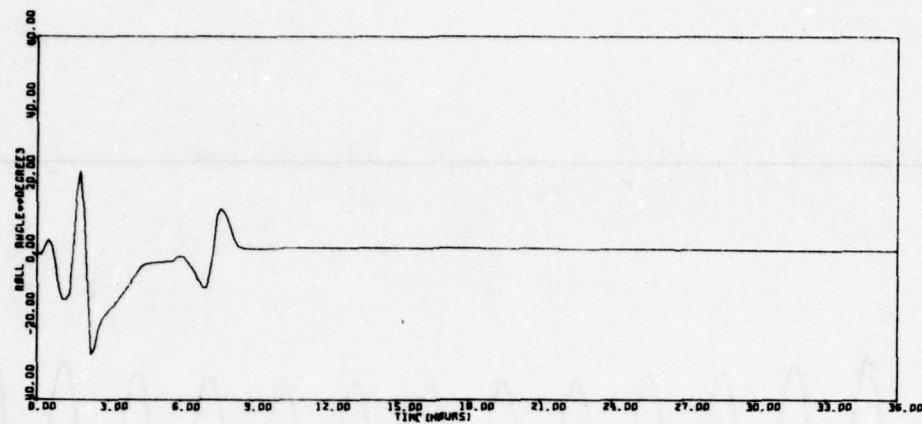


Figure 66. Run 19 - Deployment (P. Q. R.) = (.007..007..1)
(PHI. THT. PSI) = (0.0.10)

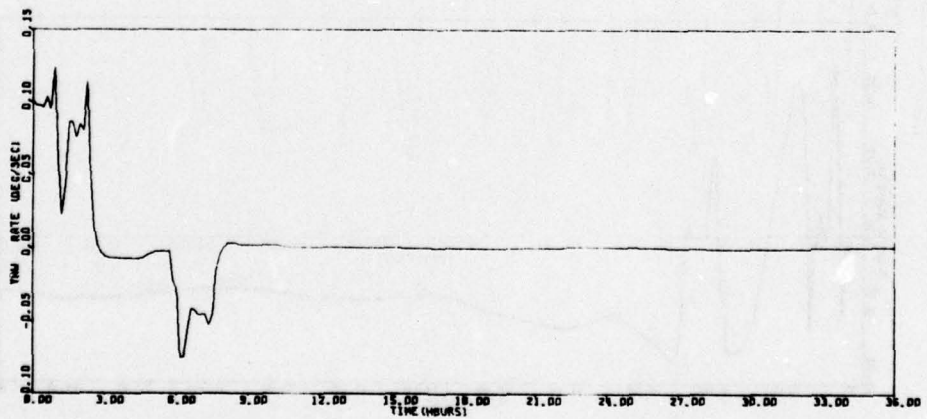
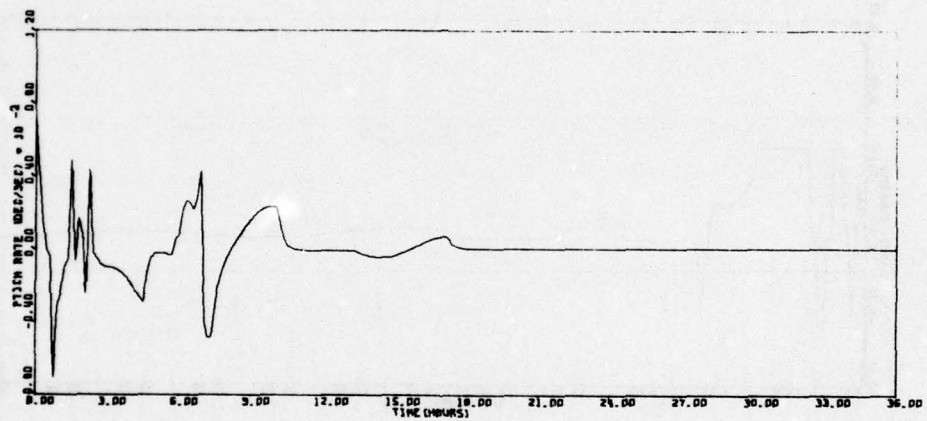
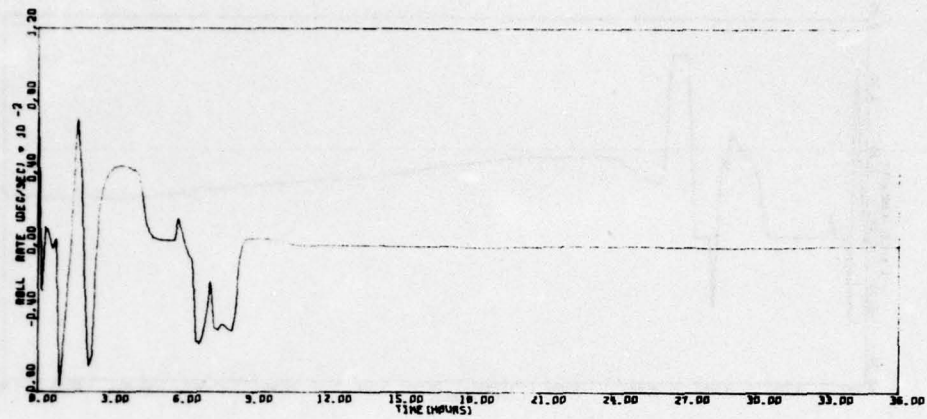


Figure 66. Run 19 - Deployment (P. Q. R.) = (.007..007..1)
(PHI. THT. PSI) = (0.0. 10) (continued)

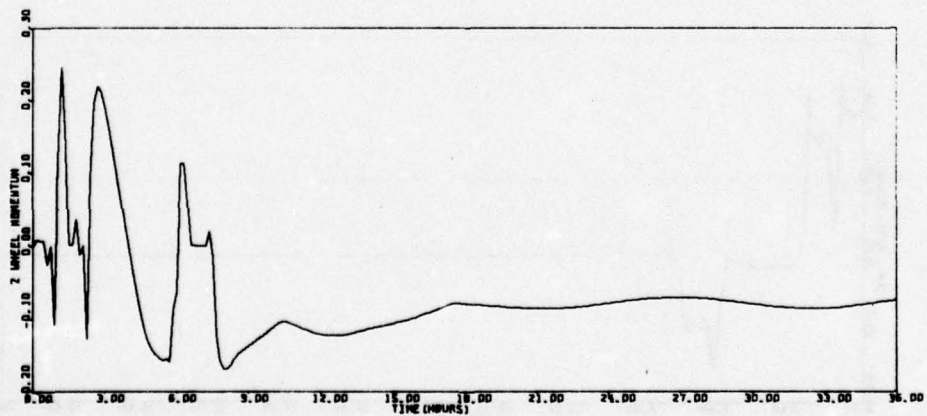
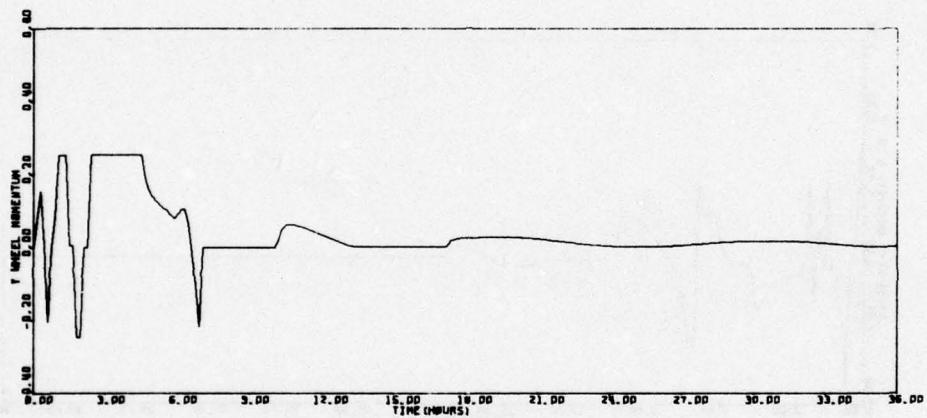
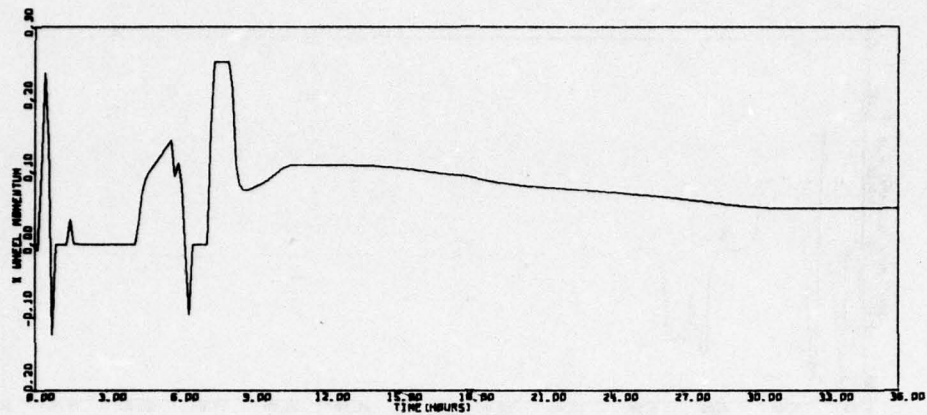


Figure 66. Run 19 - Deployment (P. Q. R.) = (.007..007..1)
(PHI. THT. PSI) = (0.0.10) (continued)

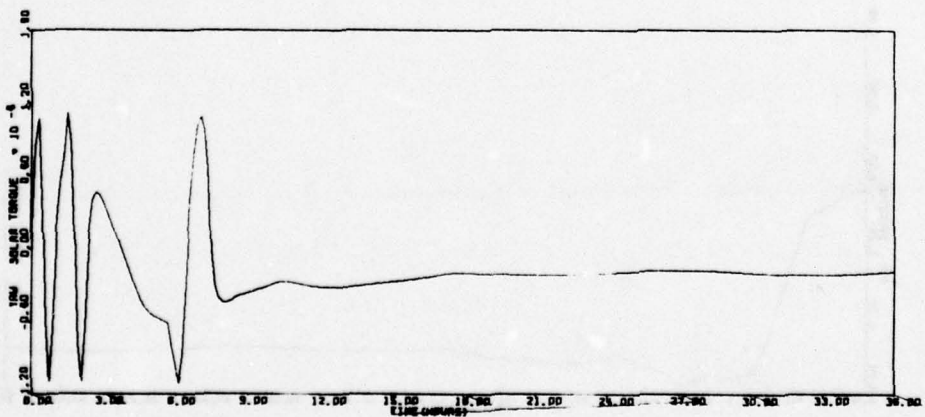
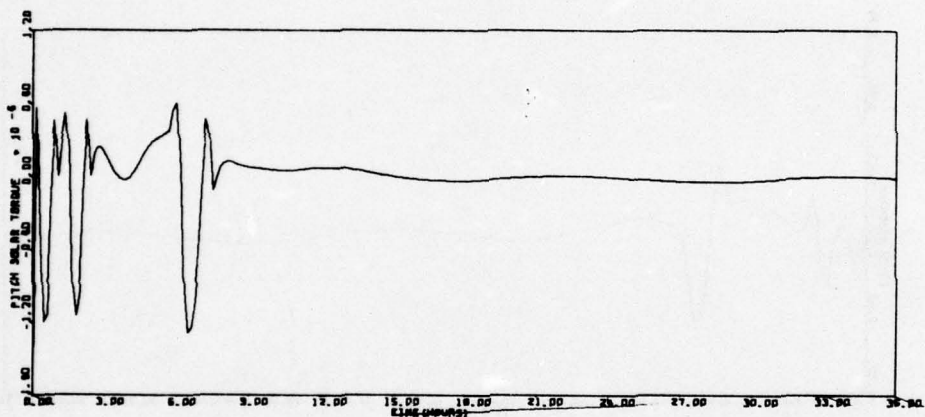
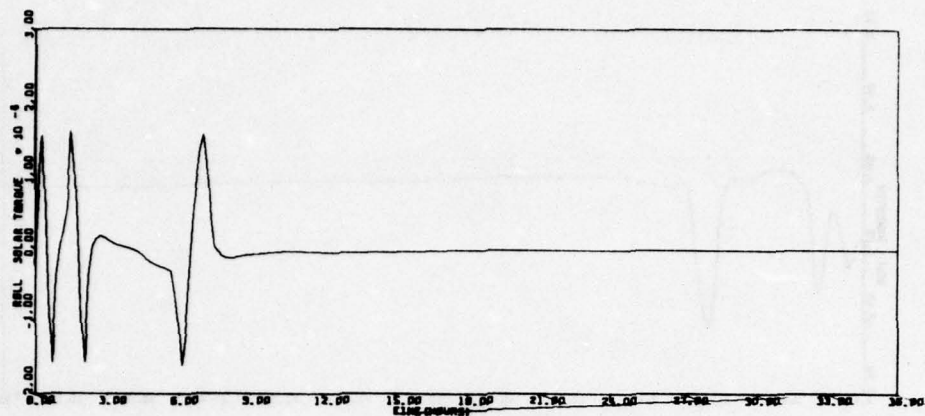


Figure 66. Run 19 - Deployment (P. Q. R.) = (.007..007..1)
(PHI, THT, PSI) = (0.0.10) (continued)

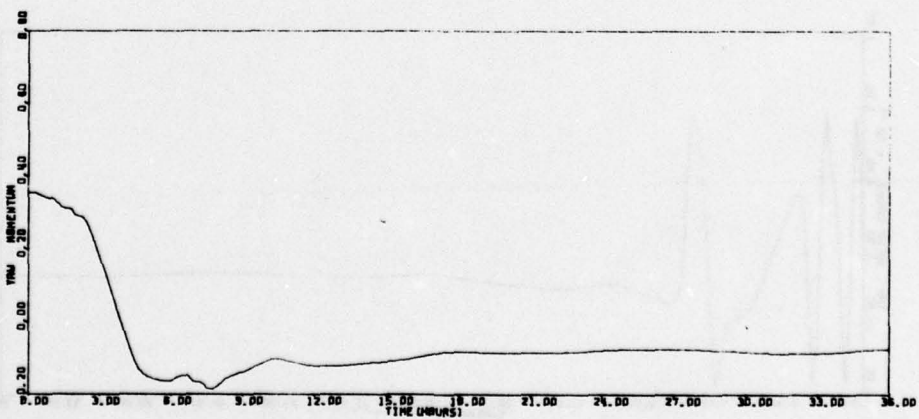
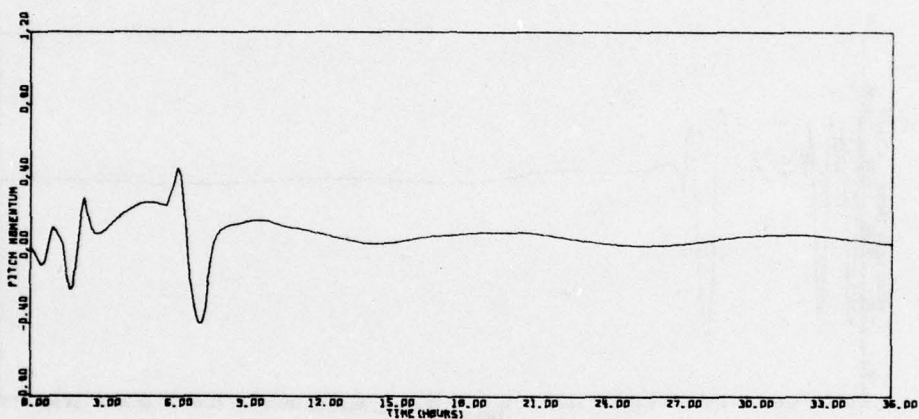
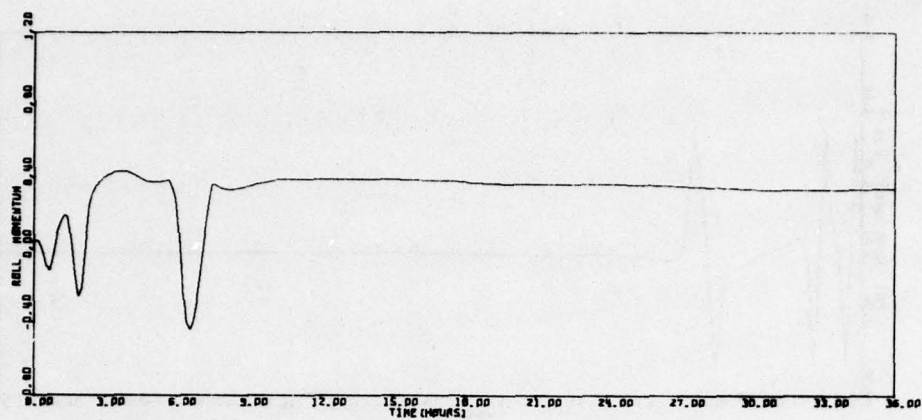


Figure 66. Run 19 - Deployment (P. Q. R.) = (.007..007..1)
(PHI. THT. PSI) = (0.0.10) (continued)

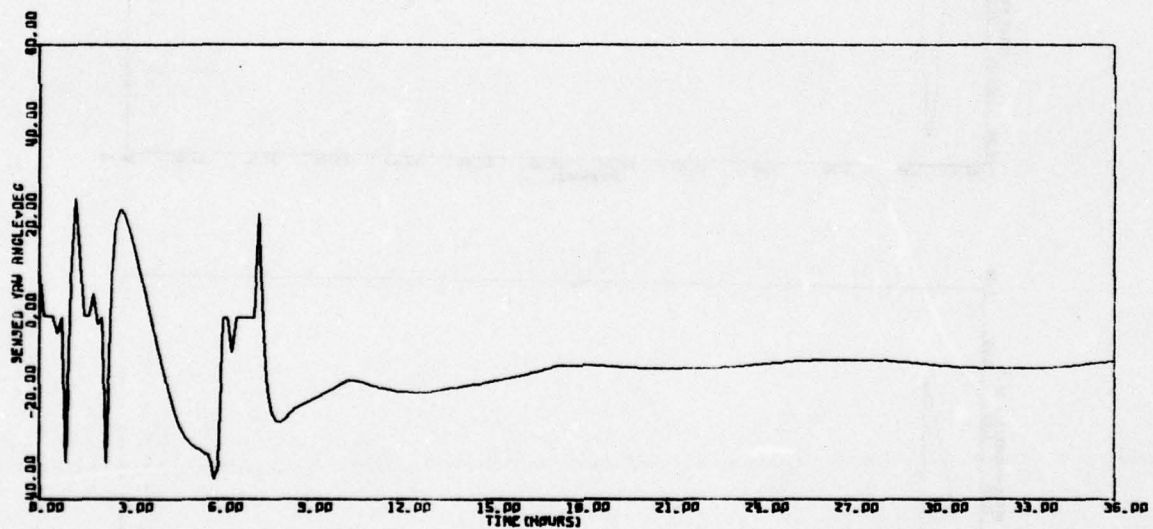
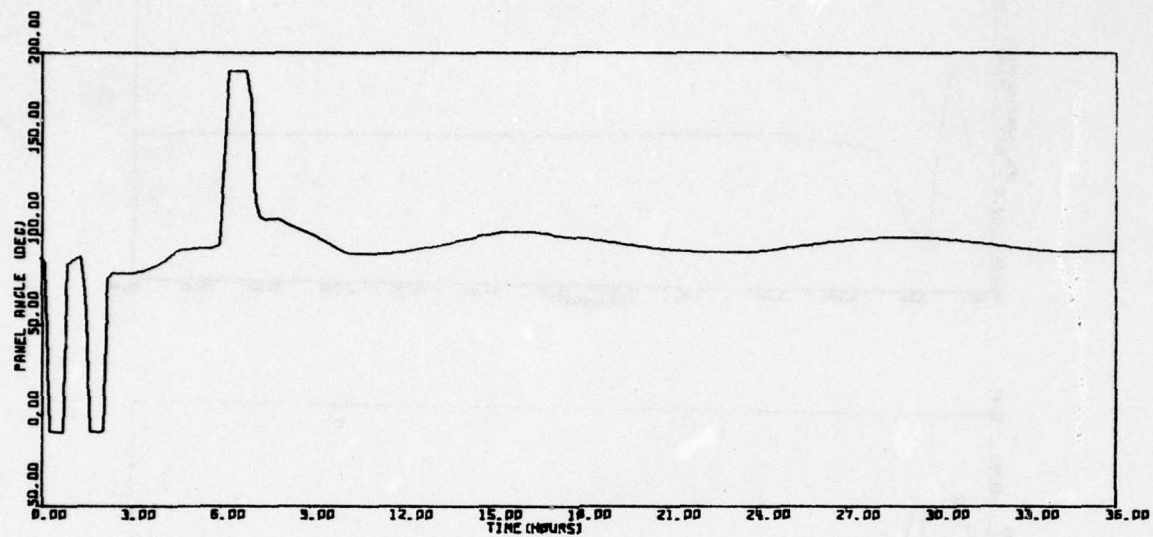


Figure 66. Run 19 - Deployment (P. Q. R.) = (.007..007..1)
(PHI, THT, PSI) = (0.0, 10) (concluded)

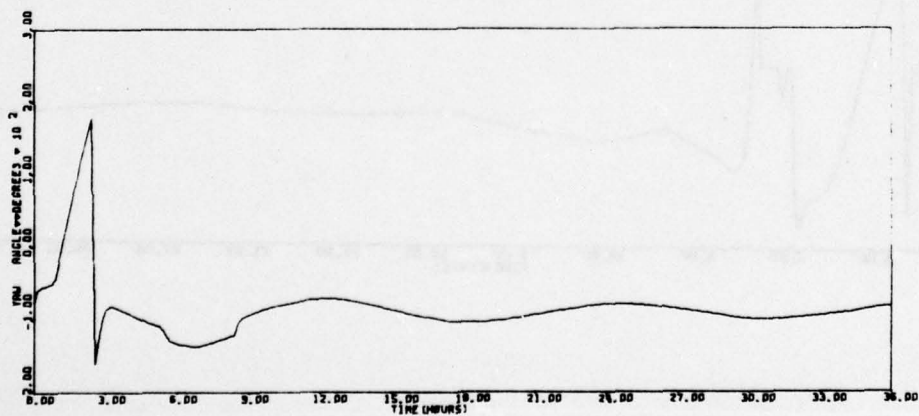
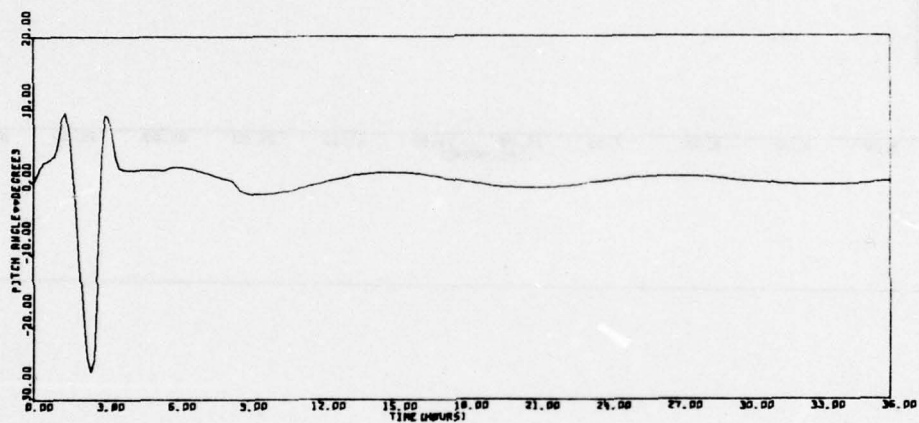
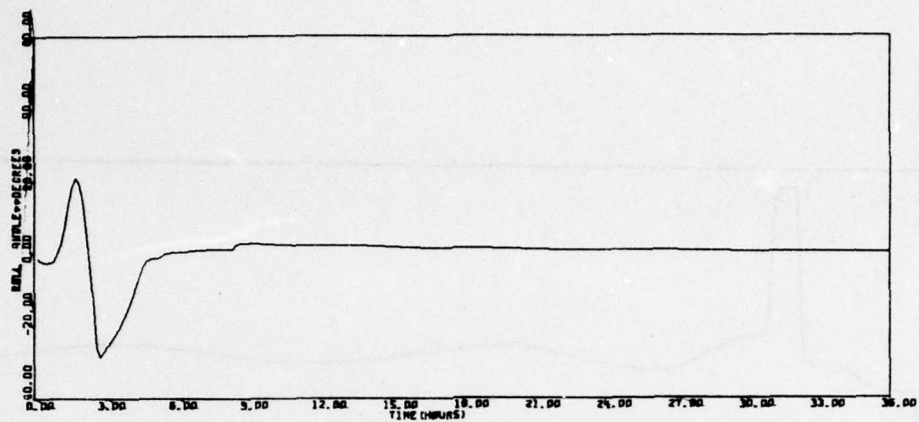


Figure 67. Run 20 - Deployment (P. Q. R.) = (.007..007..05)
(PHI. THT. PSI) = (0.0.10)

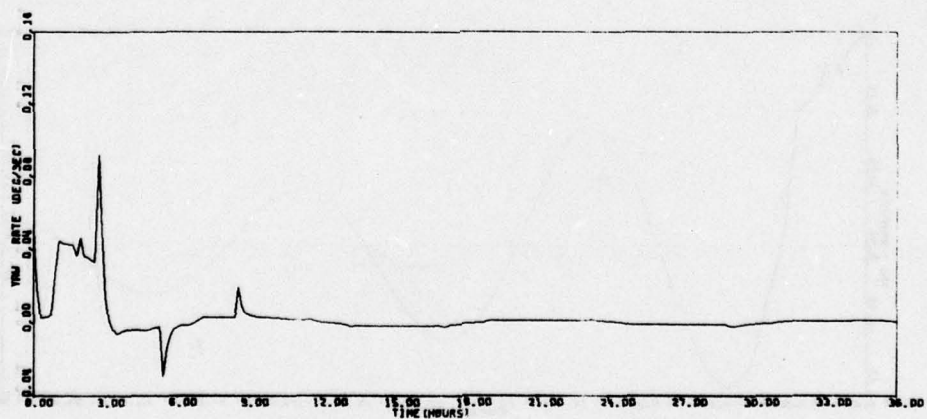
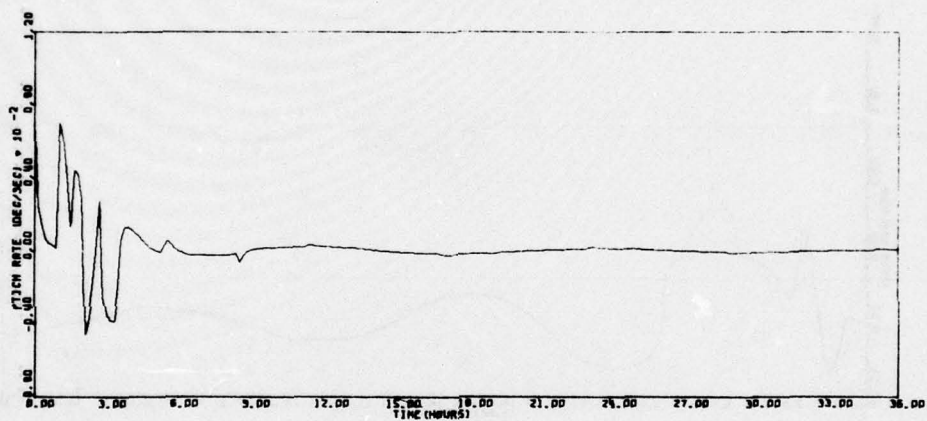
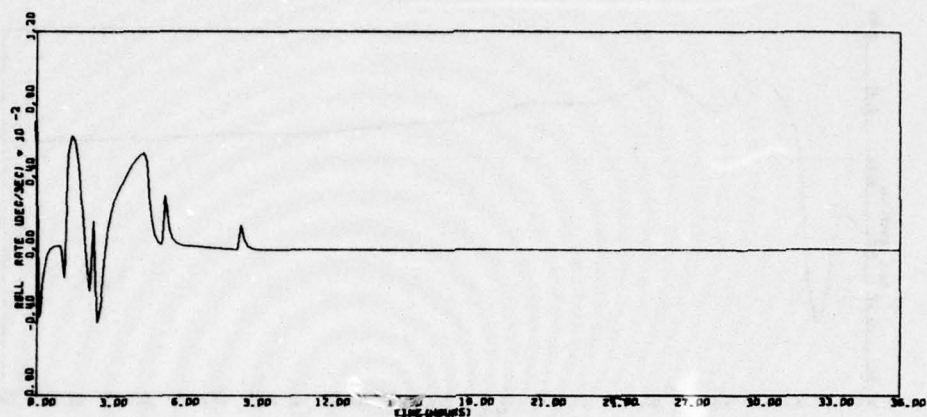


Figure 67. Run 20 - Deployment (P. Q. R.) = (.007..007..05)
(PHI, THT, PSI) = (0.0, 10) (continued)

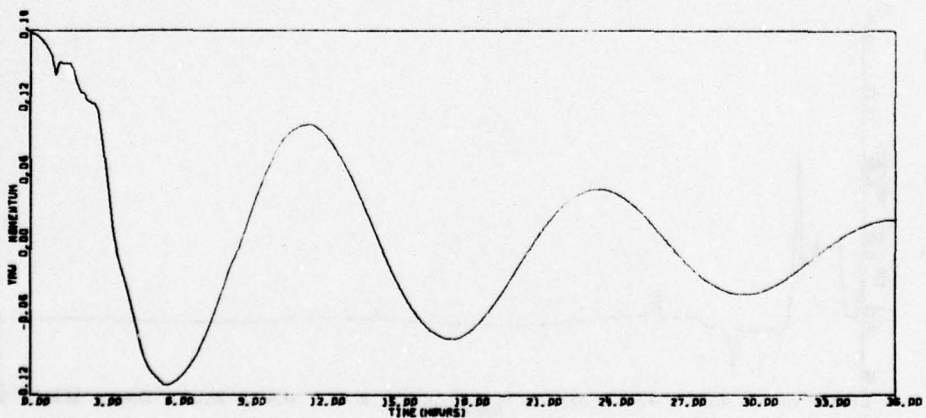
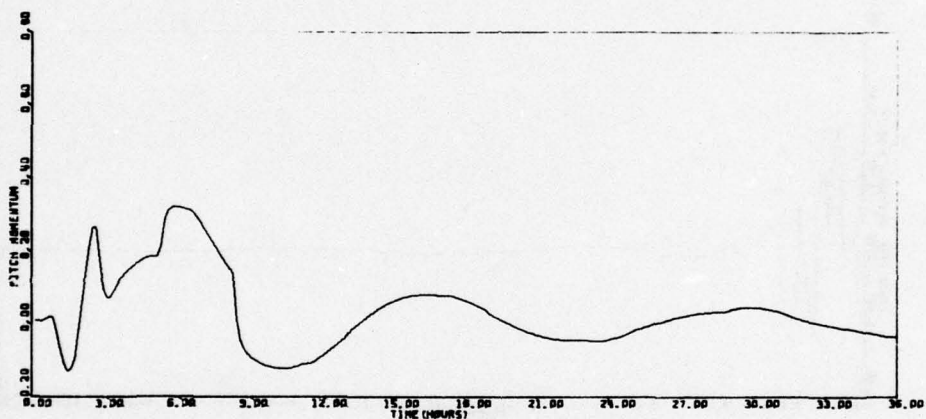
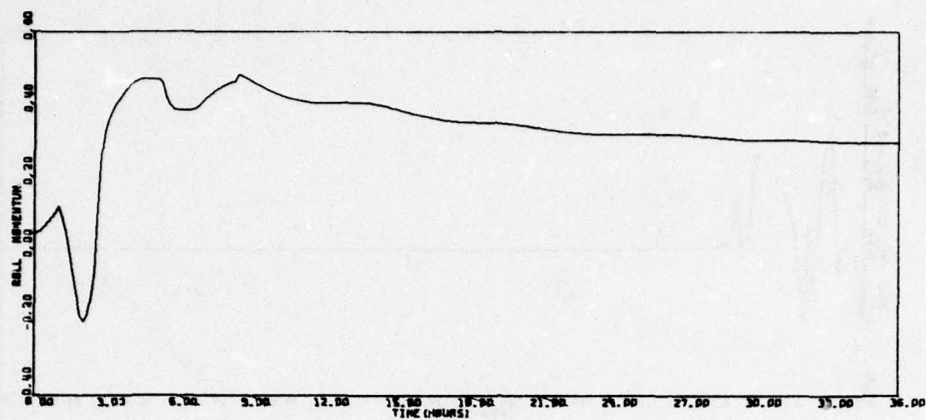


Figure 67. Run 20 - Deployment (P. Q. R.) = (.007..007..05)
(PHI, THT, PSI) = (0.0, 10) (continued)

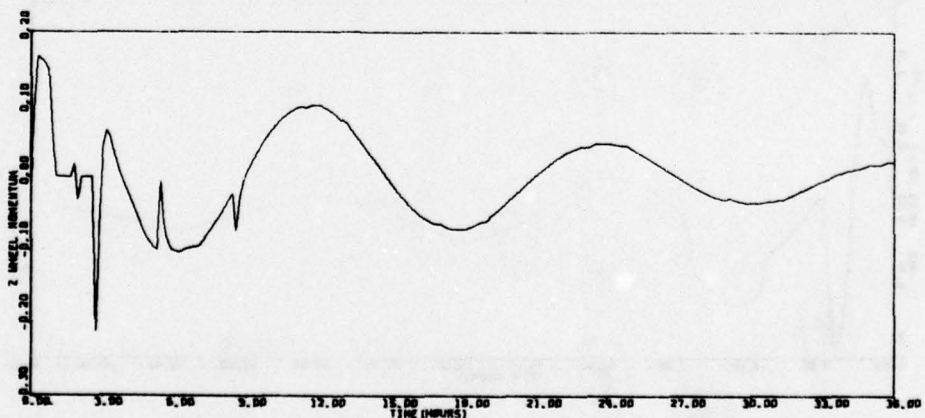
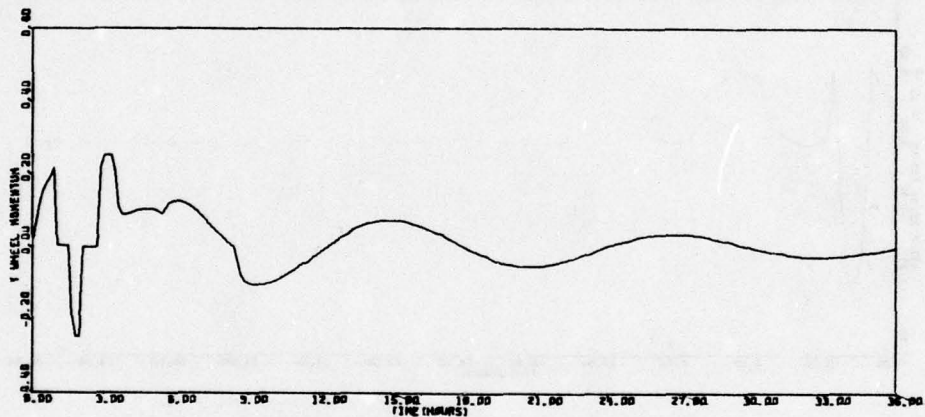
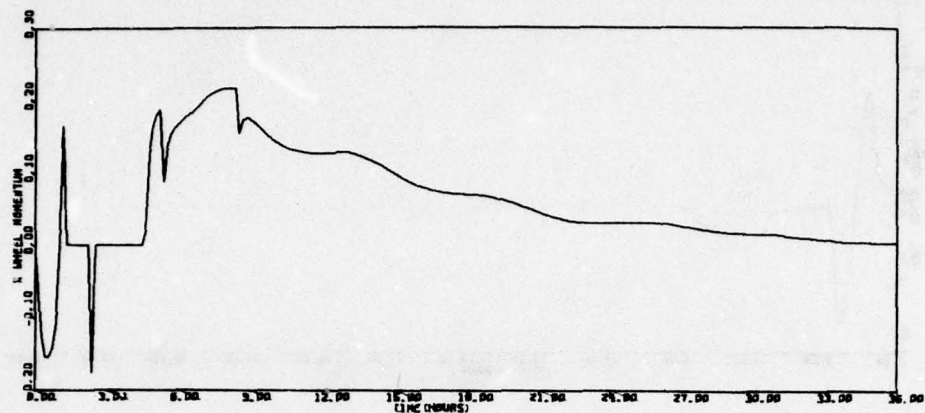


Figure 67. Run 20 - Deployment (P. Q. R.) = (.007..007..05)
(PHI, THT, PSI) = (0.0, 10) (continued)

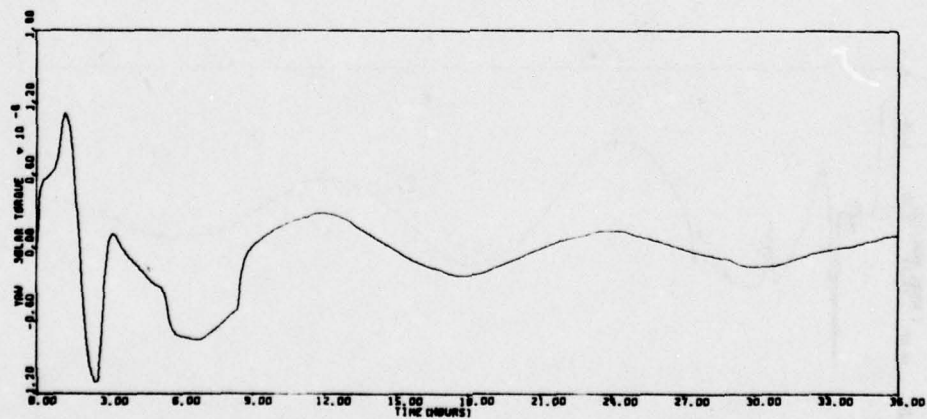
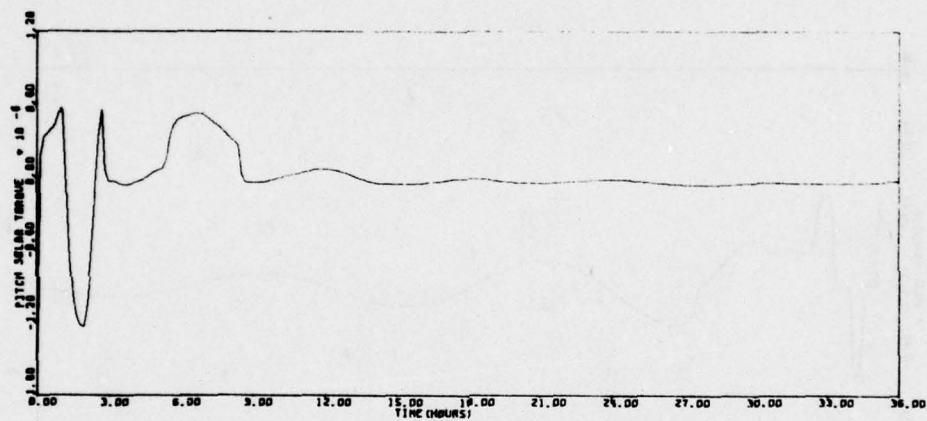
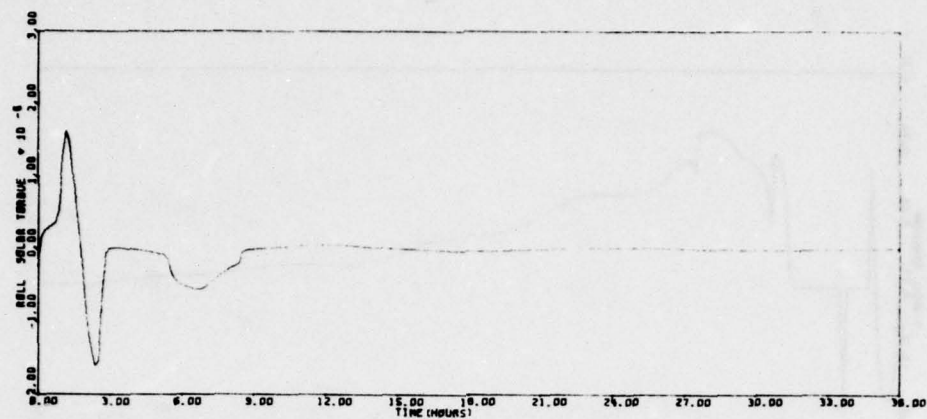


Figure 67. Run 20 - Deployment (P.Q.R.) = (.007,.007,.05)
(PHI, THT, PSI) = (0.0,10) (continued)

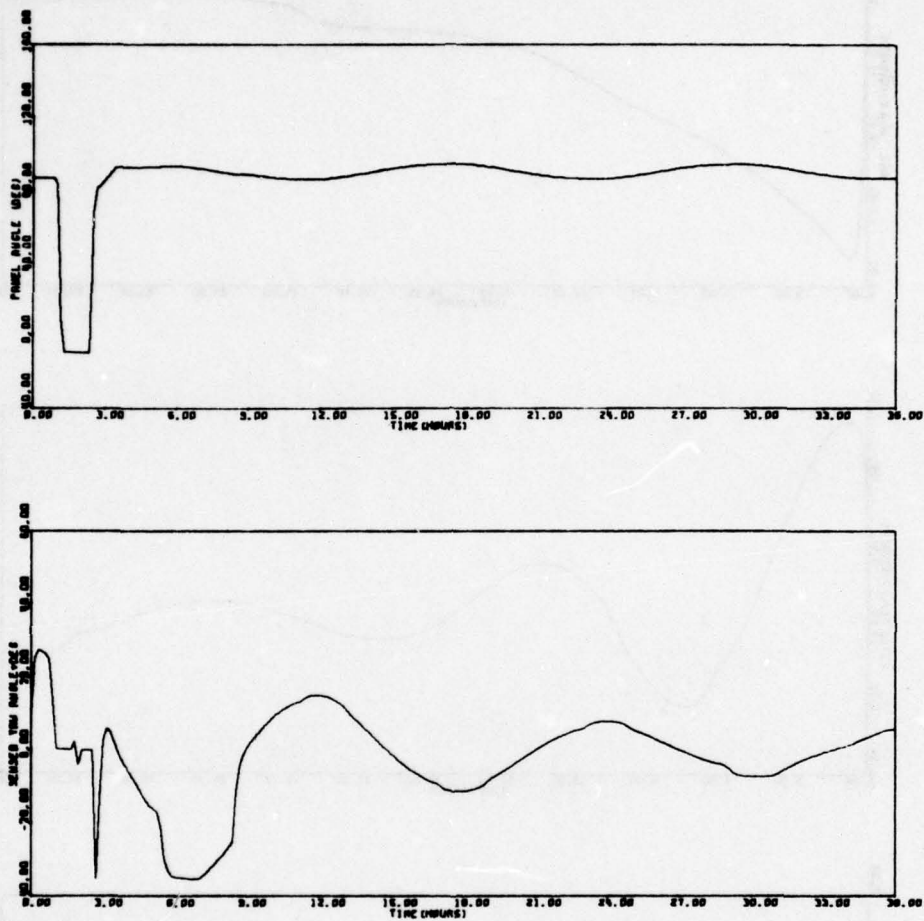


Figure 67. Run 20 - Deployment (P.Q.R.) = (.007..007..05)
(PHI, THT, PSI) = (0.0.10) (concluded)

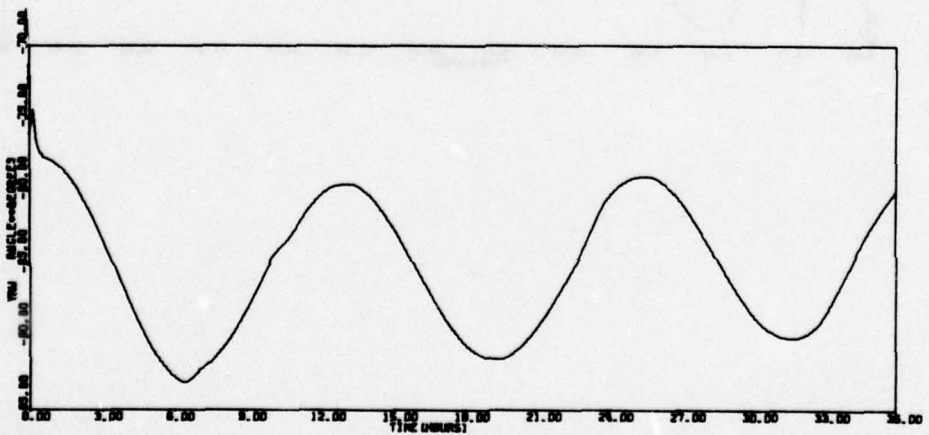
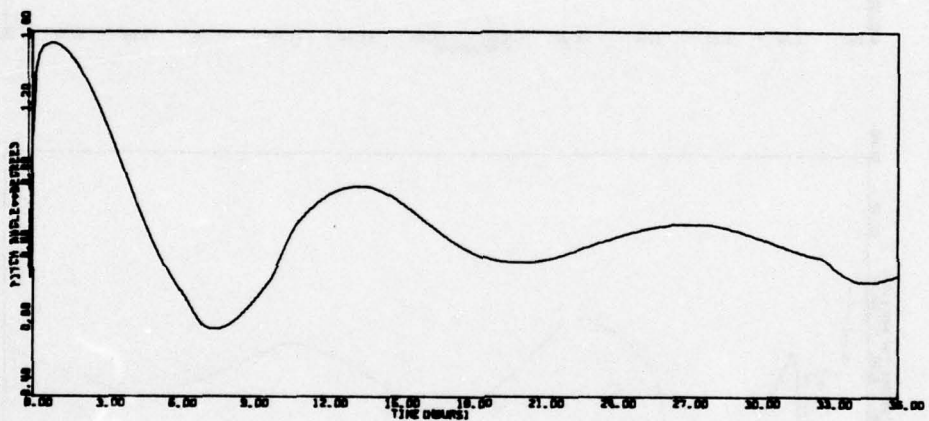
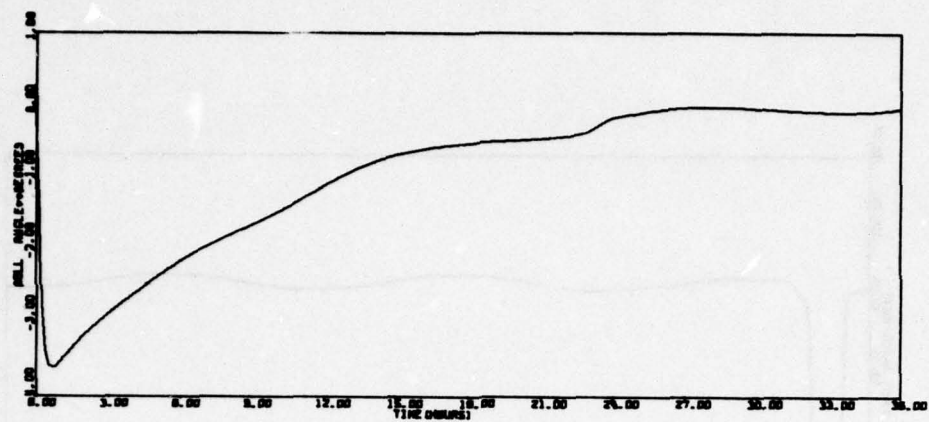


Figure 68. Run 21 - Deploy (P. Q. R.) = (.007..007.01)
 (PHI, THT, P91) = (.25..25.10.0)

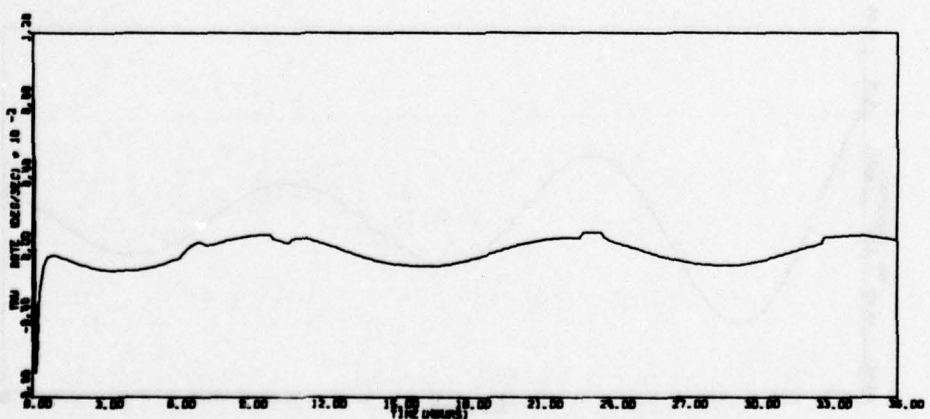
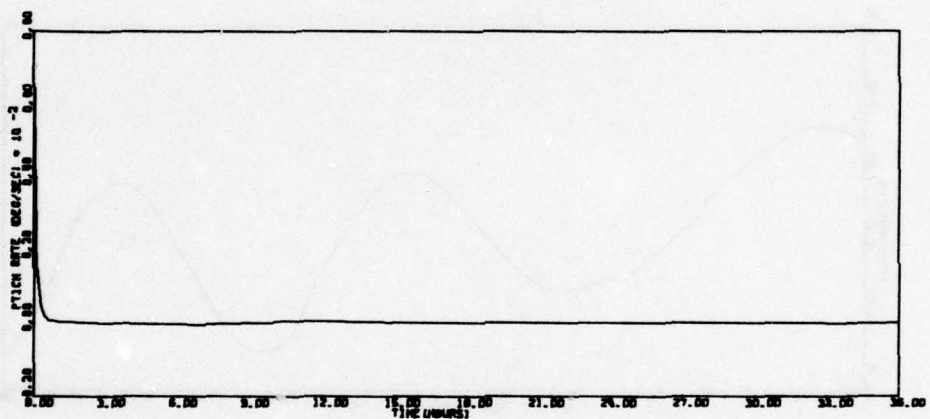
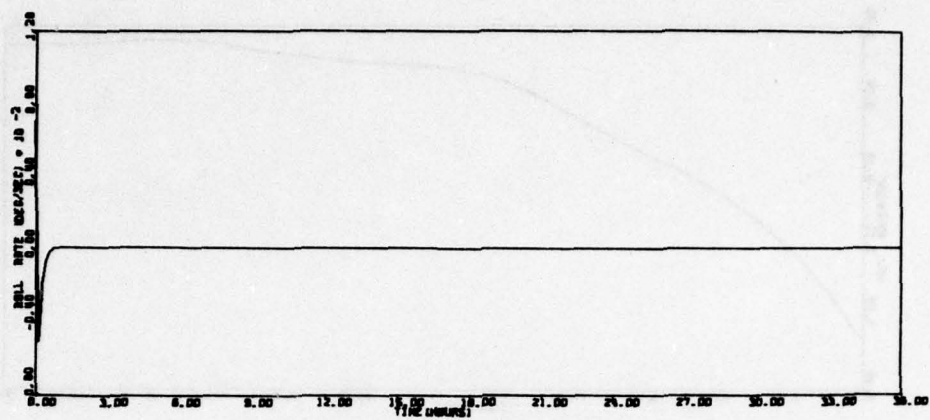


Figure 68. Run 21 - Deploy (P, Q, R) = (.007,.007,.01)
(PHI, THT, P91) = (.25,.25,10,0) (continued)

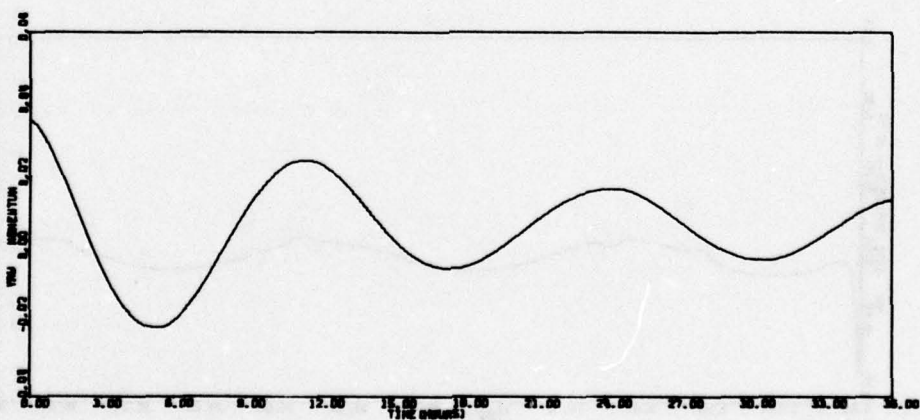
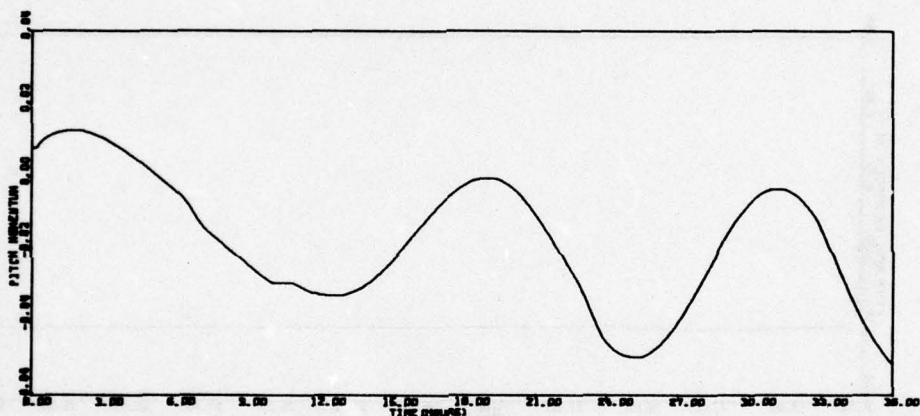
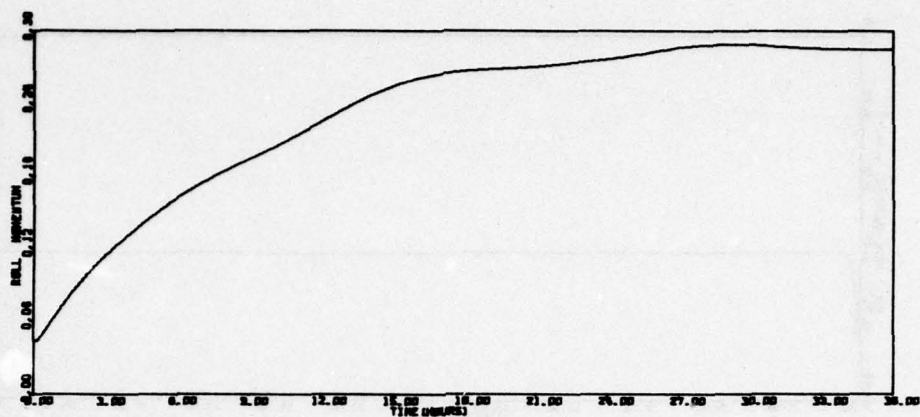


Figure 68. Run 21 - Deploy (P. Q. R.) = (.007..007..01)
 (PHI. THT. P91) = (.25..25.10.0) (continued)

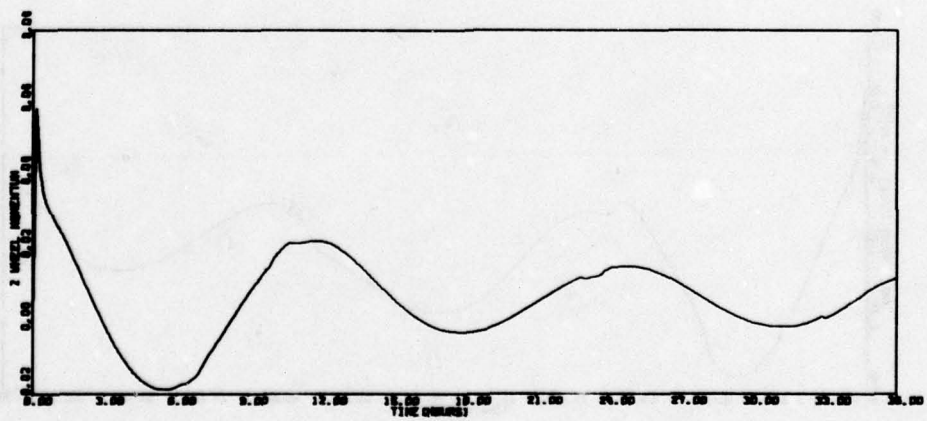
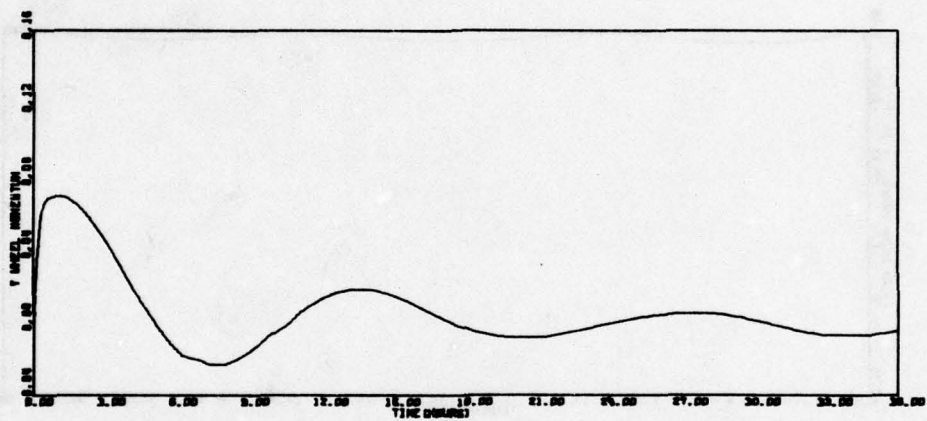
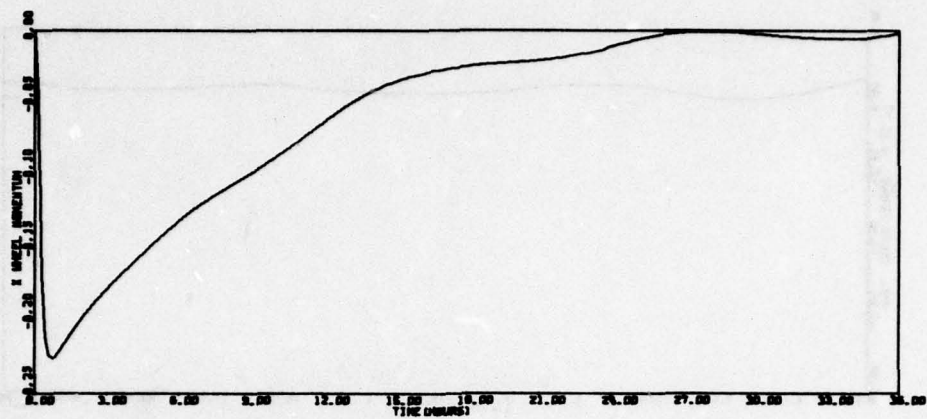


Figure 68. Run 21 - Deploy (P.Q.R.) = (.007..007..01)
(PHI.THT.P91) = (.25..25.10.0) (continued)

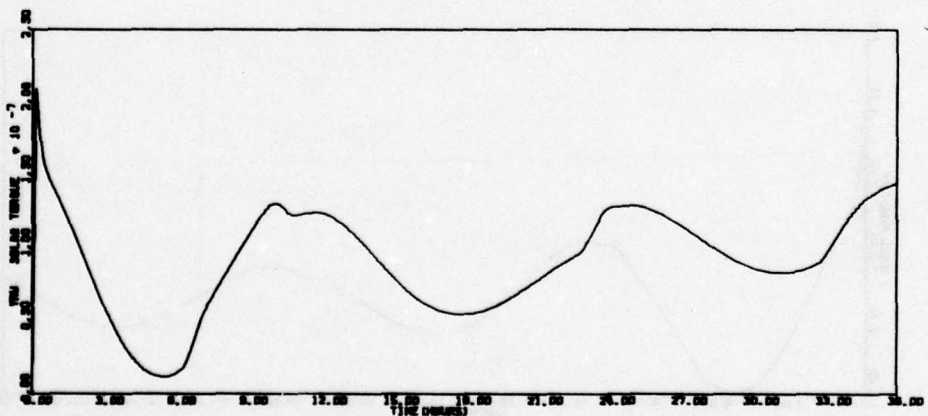
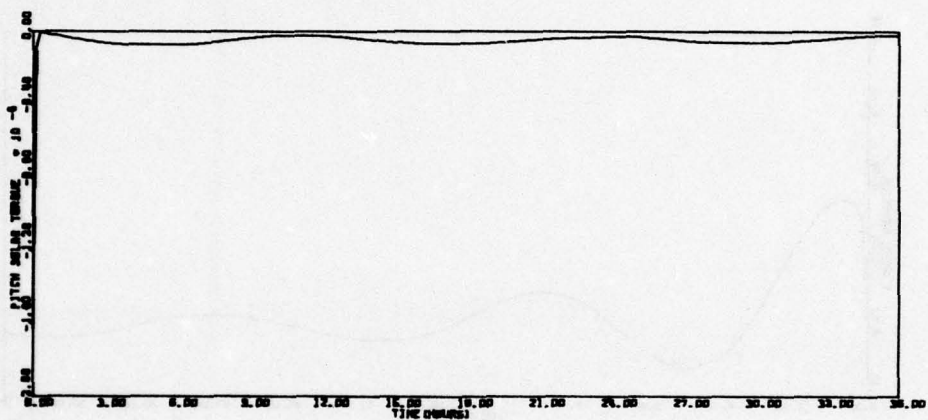
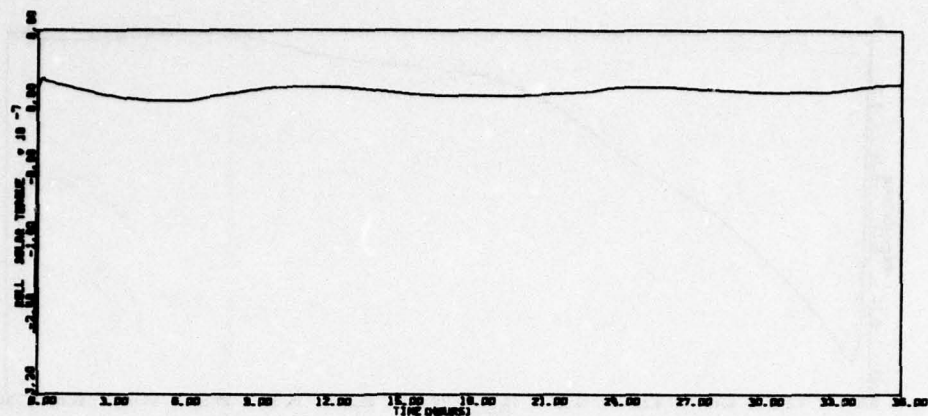


Figure 68. Run 21 - Deploy (P. Q. R.) = (.007..007..01)
(PHI. THT. P91) = (.25..25.10.0) (continued)

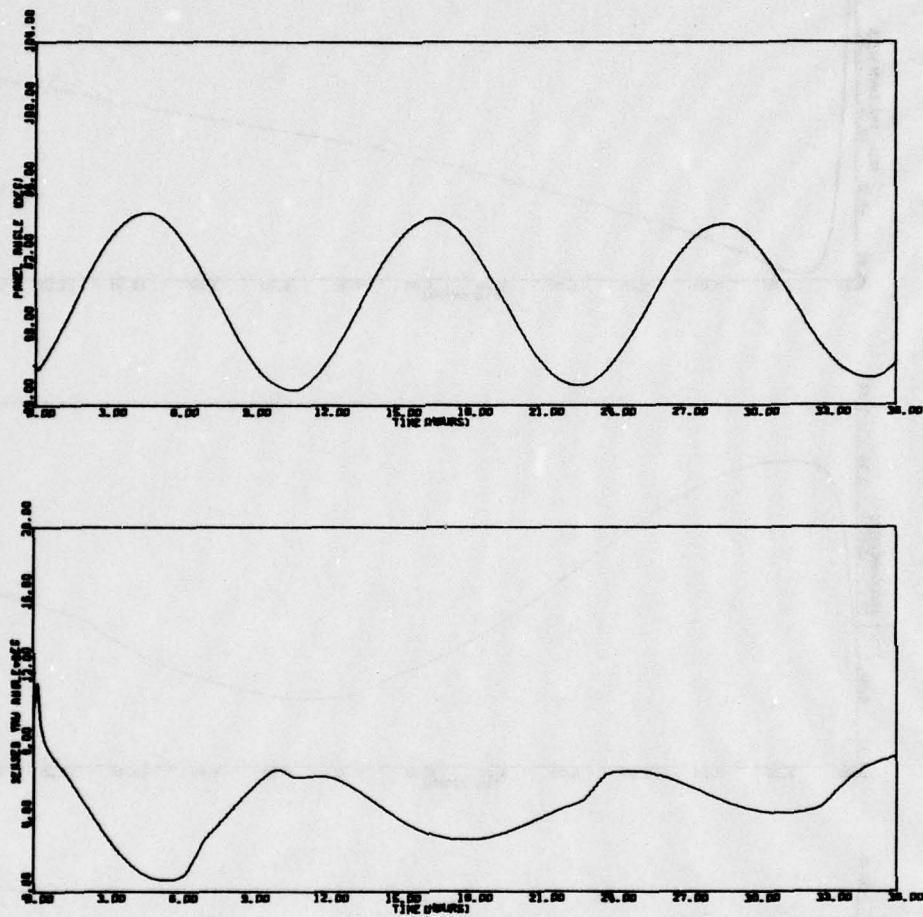


Figure 68. Run 21 - Deploy (P. Q. R.) = (.007..007..01)
 (PHI. THT. P91) = (.25..25.10.0) (concluded)

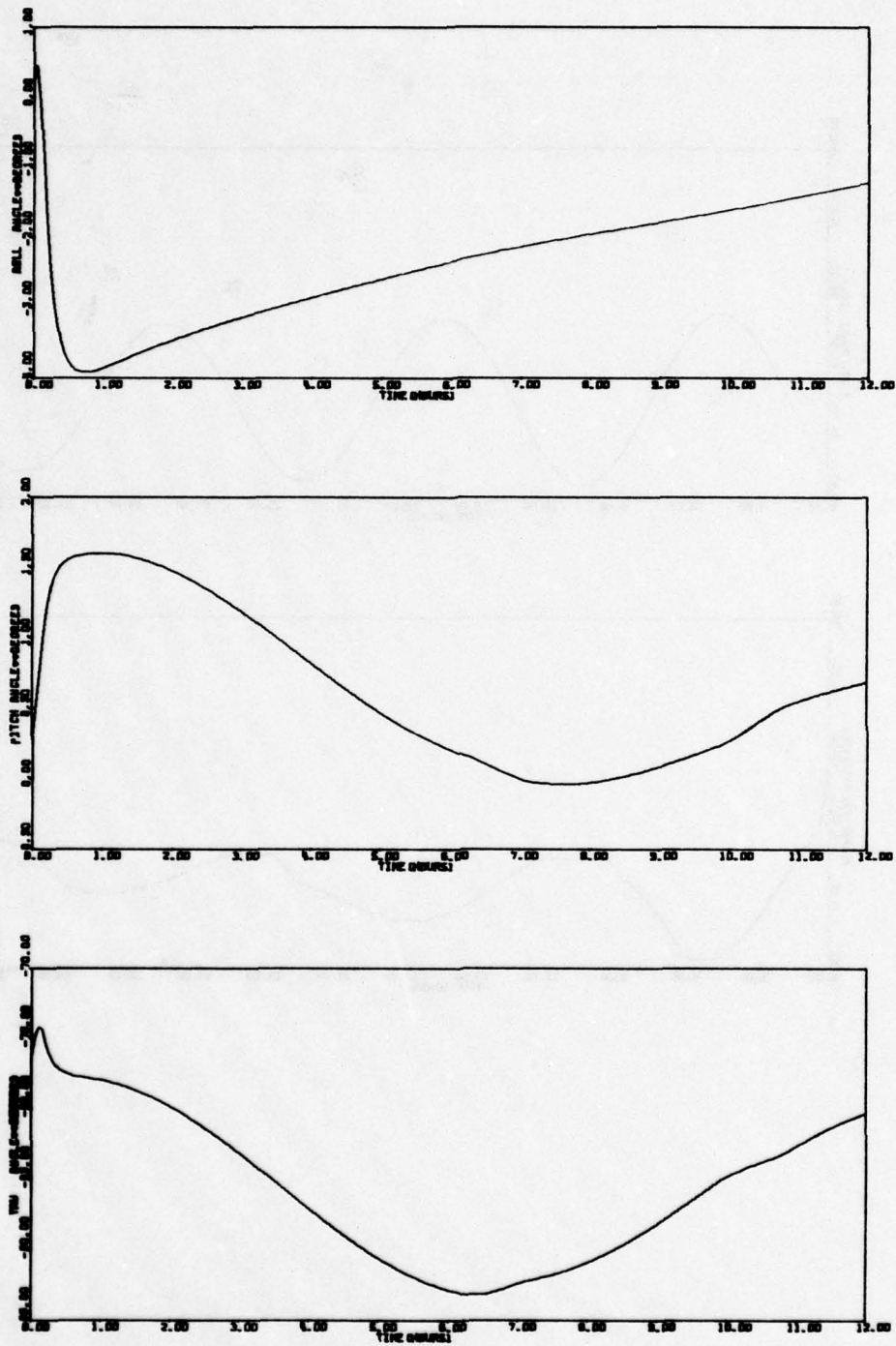


Figure 69. Run 23 - Deploy (P. Q. R.) = (.007..007..01) (PHI. THT. PSI) = (.25..25.10.0) ROD1 and ROD2 Rates Unequal

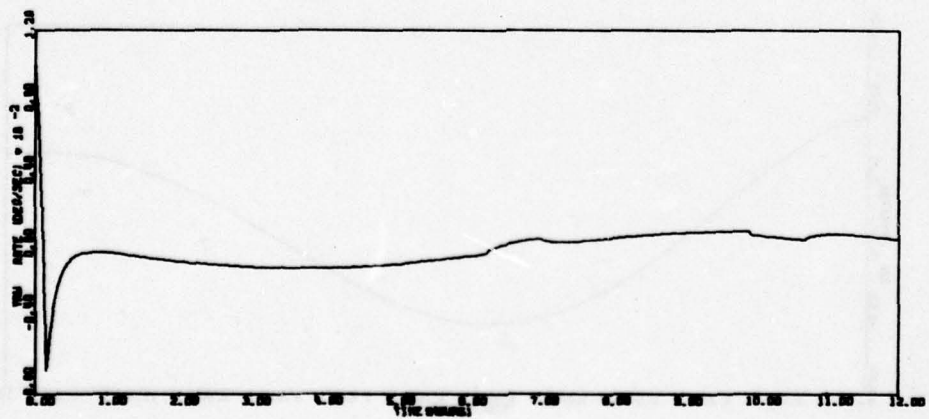
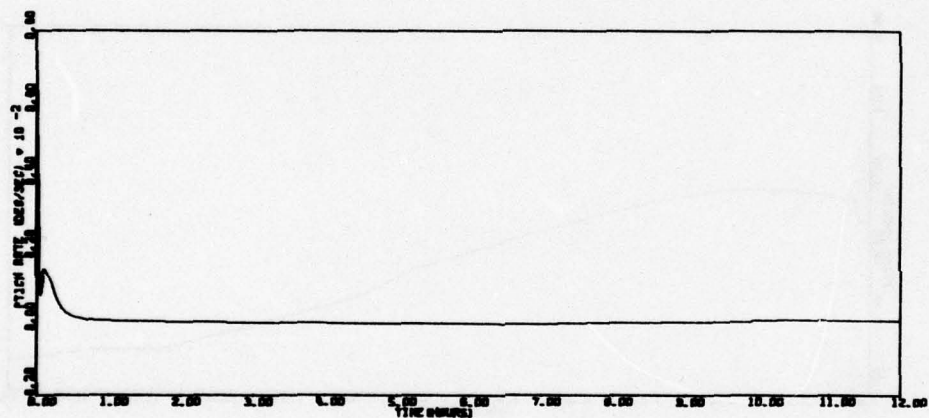
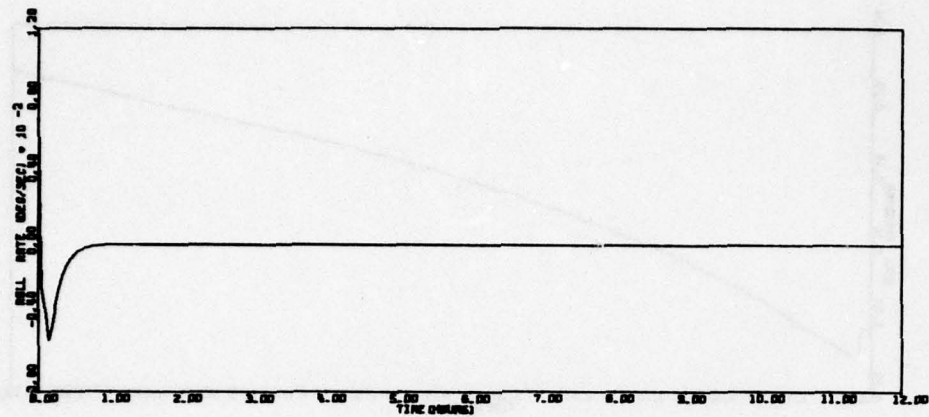


Figure 69. Run 23 - Deploy (P. Q. R.) = (.007..007..01) (PHI. THT. PSI) =
 (.25..25.10.0) ROD1 and ROD2 Rates Unequal (continued)

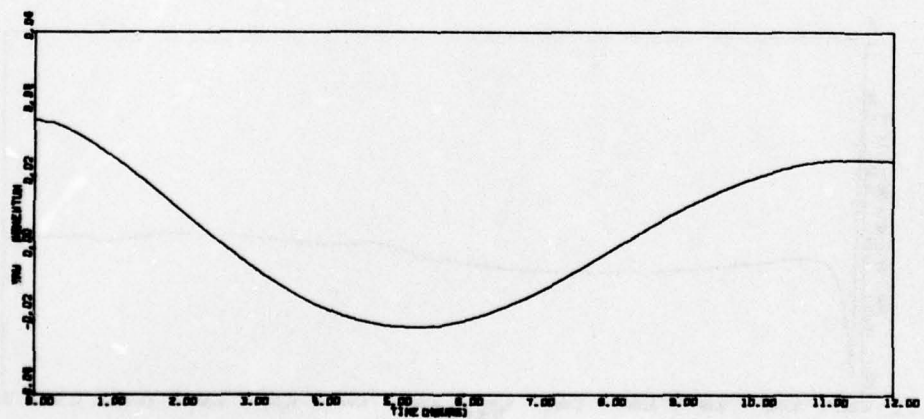
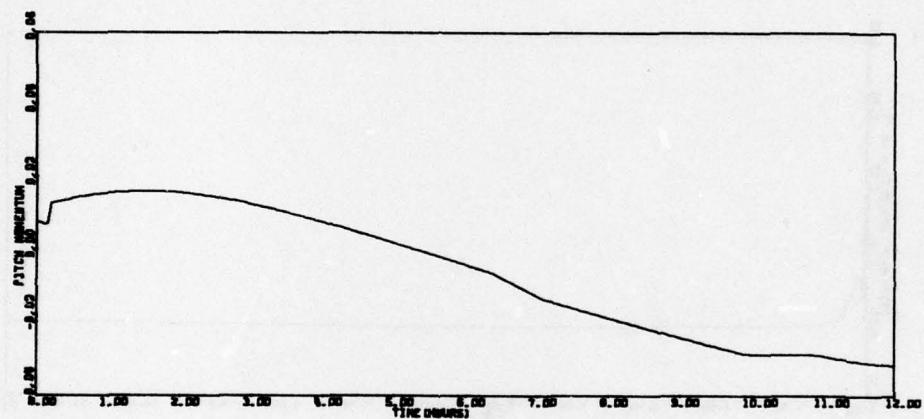
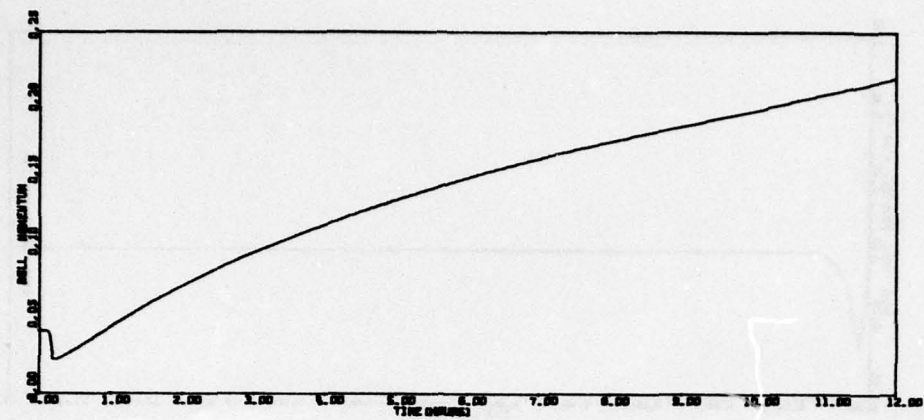


Figure 69. Run 23 - Deploy (P, Q, R,) = (.007, .007, .01) (PHI, THT, PSI) = (.25, .25, 10.0) ROD1 and ROD2 Rates Unequal (continued)

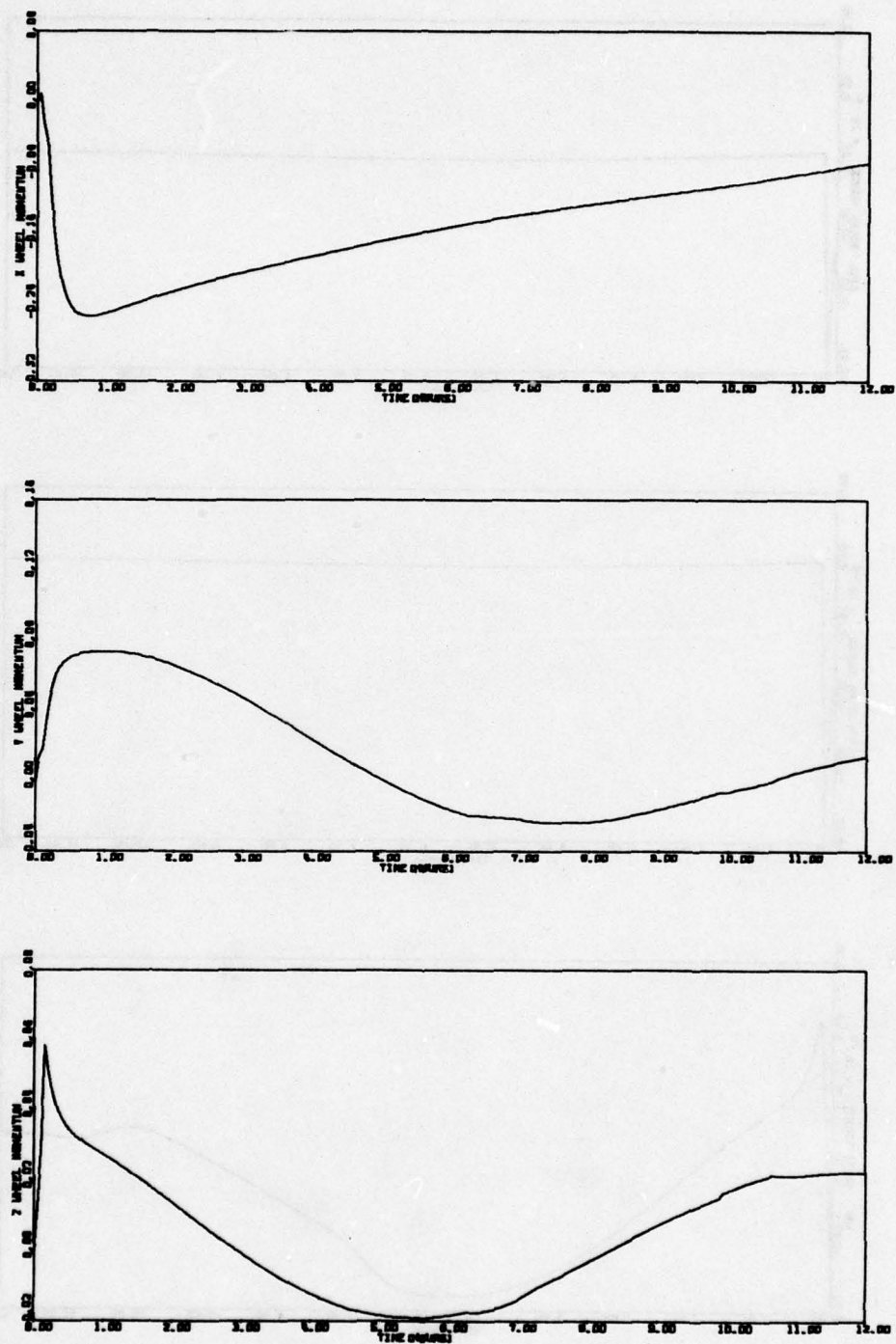


Figure 69. Run 23 - Deploy (P. Q. R.) = (.007..007..01) (PHI, THT, PSI) = (.25..25,10,0) ROD1 and ROD2 Rates Unequal (continued)

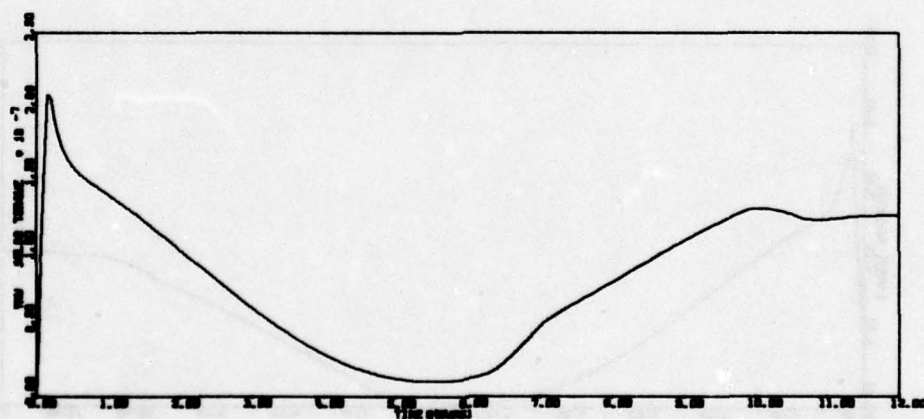
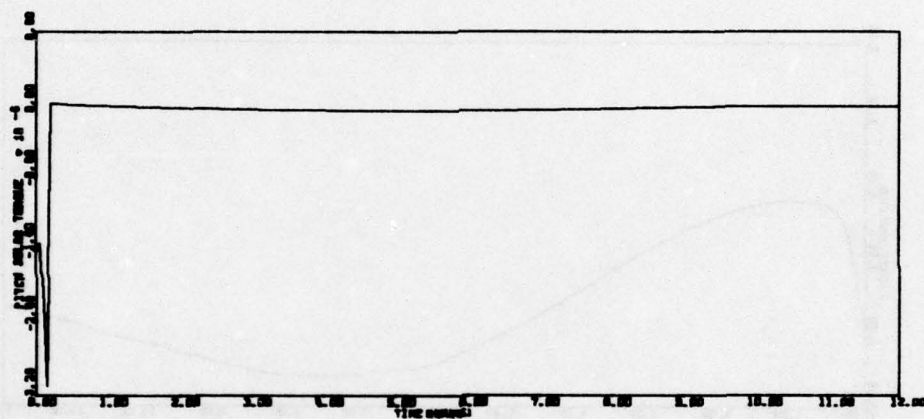
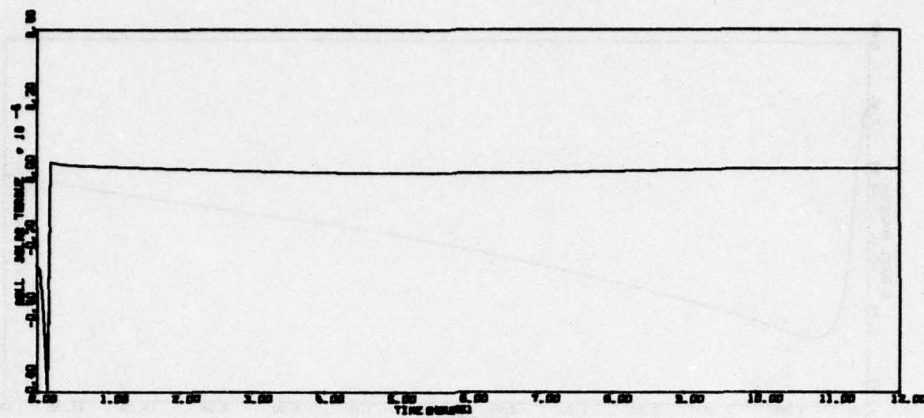


Figure 69. Run 23 - Deploy (P. Q. R.) = (.007..007..01) (PHI. THT. PSI) =
(.25..25.10.0) ROD1 and ROD2 Rates Unequal (continued)

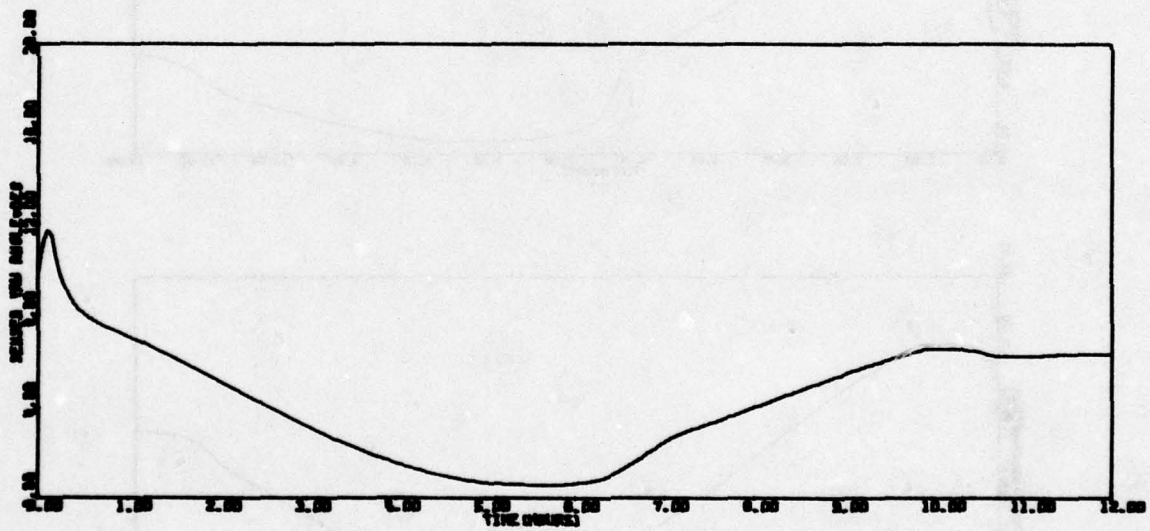
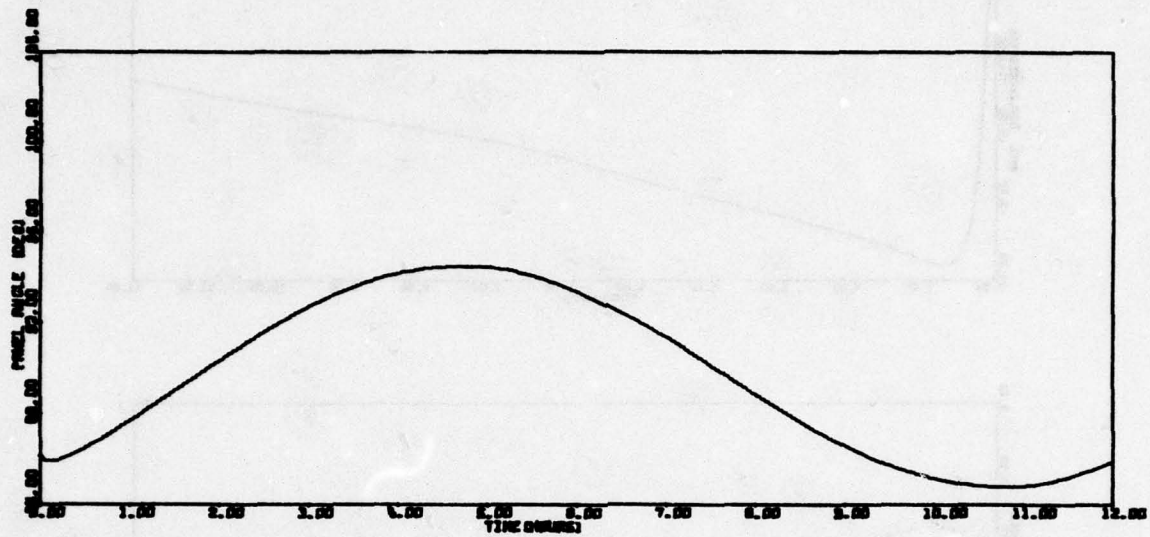


Figure 69. Run 23 - Deploy (P, Q, R.) = (.007, .007, .01) (PHI, THT, PSI) = (.25, .25, 10.0) ROD1 and ROD 2 Rates Unequal (concluded)

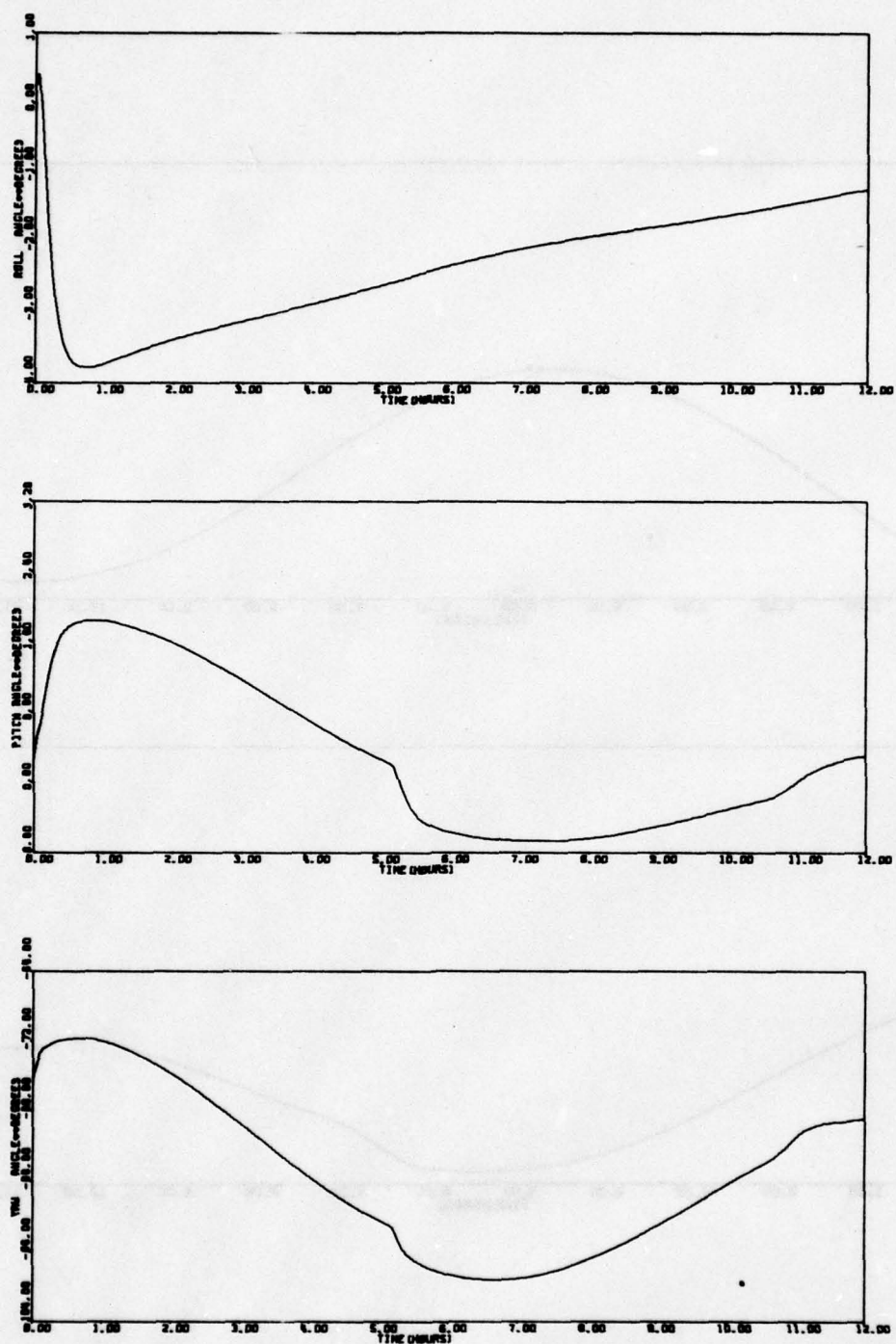


Figure 70. Run 24 - Deploy (P, Q, R.) = (.007, .007, .01) (PHI, THT, PSI) = (.25, .25, 10.0) ROD1 and ROD2 Rates Unequal KSUB(PSI) = KSUB(PSI)/2

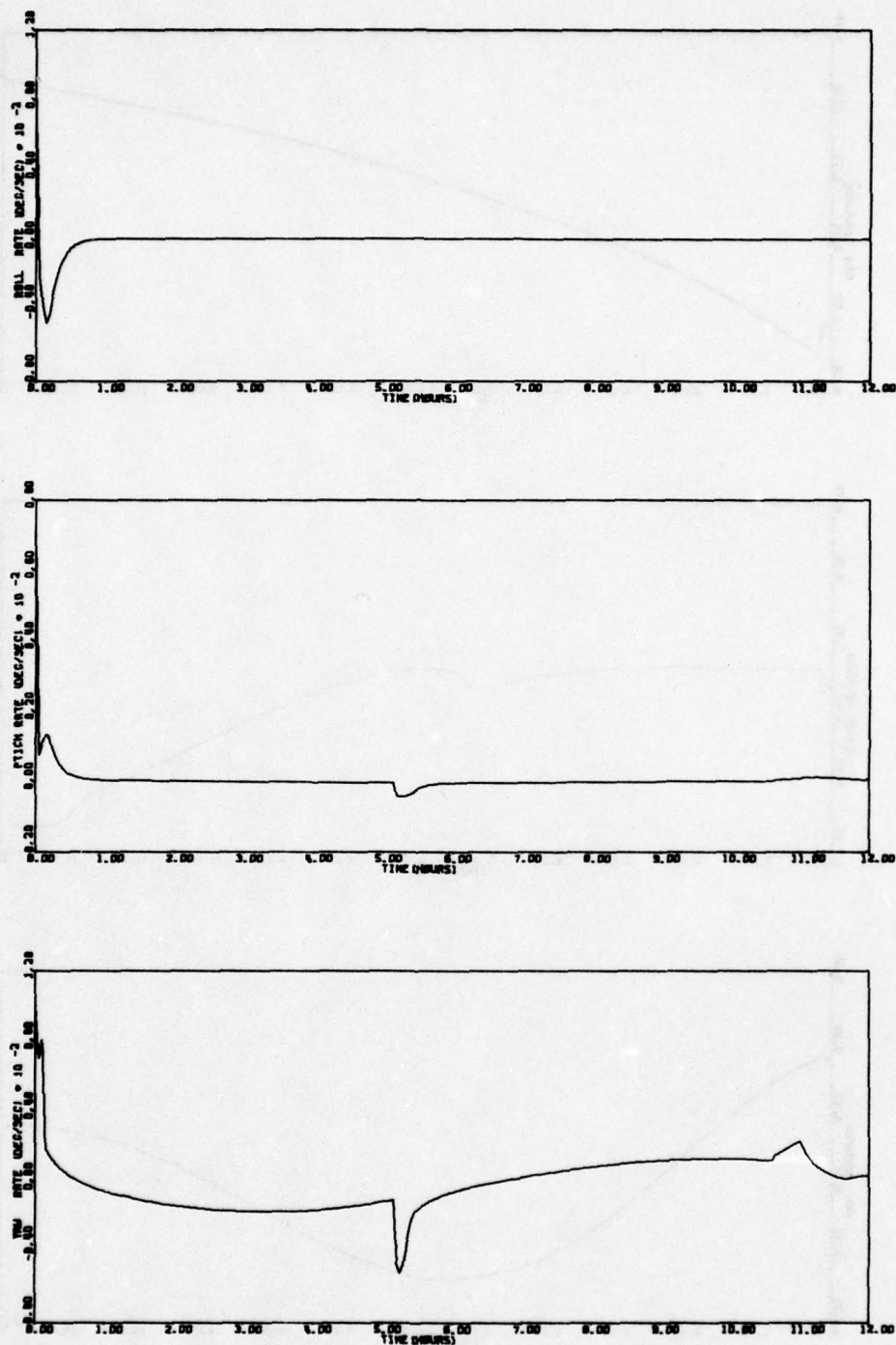


Figure 70. Run 24 - Deploy (P. Q. R.) = (.007..007..01) (PHI, THT, PSI) = (.25..25.10.0) ROD1 and ROD2 Rates Unequal KSUB(PSI) = KSUB(PSI)/2 (continued)

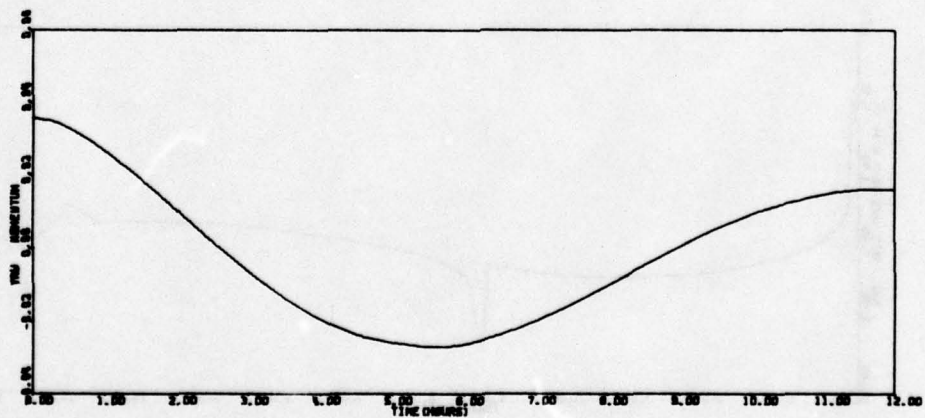
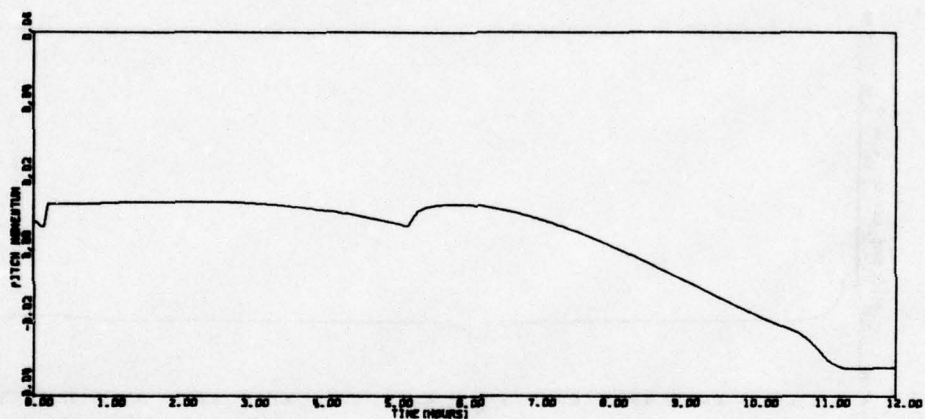
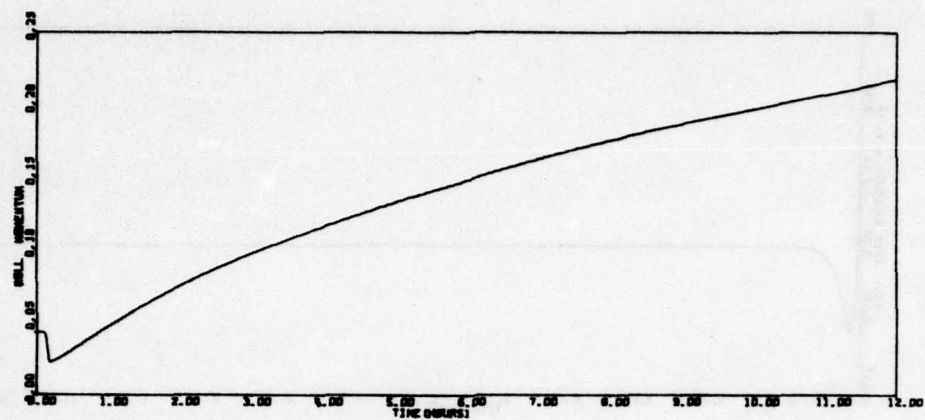


Figure 70. Run 24 - Deploy (P. Q. R.) = (.007..007..01) (PHI. THT. PSI) = (.25..25.10.0) ROD1 and ROD2 Rates Unequal KSUB(PSI) = KSUB(PSI)/2 (continued)

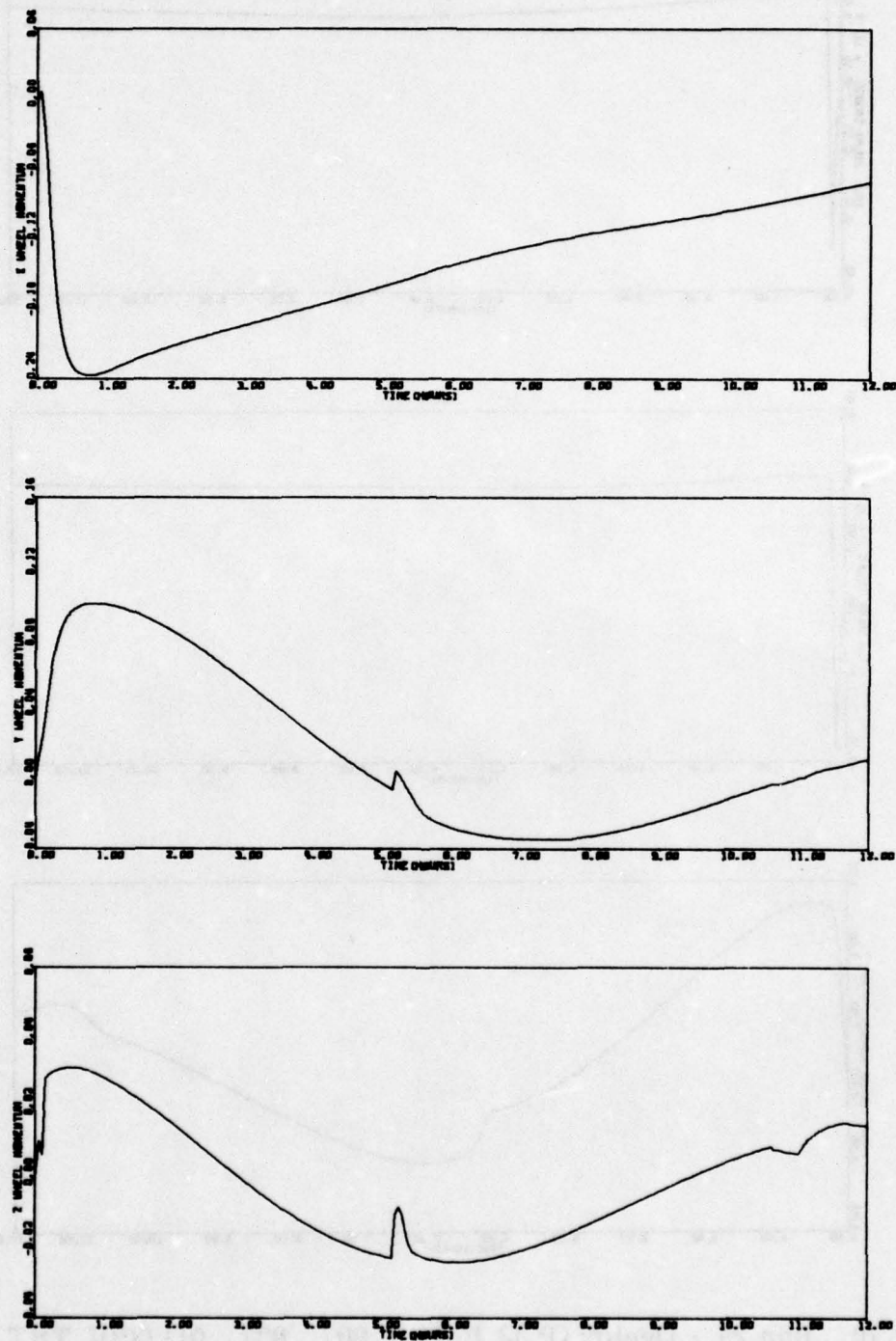


Figure 70. Run 24 - Deploy (P. Q. R.) = (.007..007..01) (PHI. THT. PSI) =
 (.25..25.10.0) ROD1 and ROD2 Rates Unequal KSUB(PSI) =
 KSUB(PSI)/2 (continued)

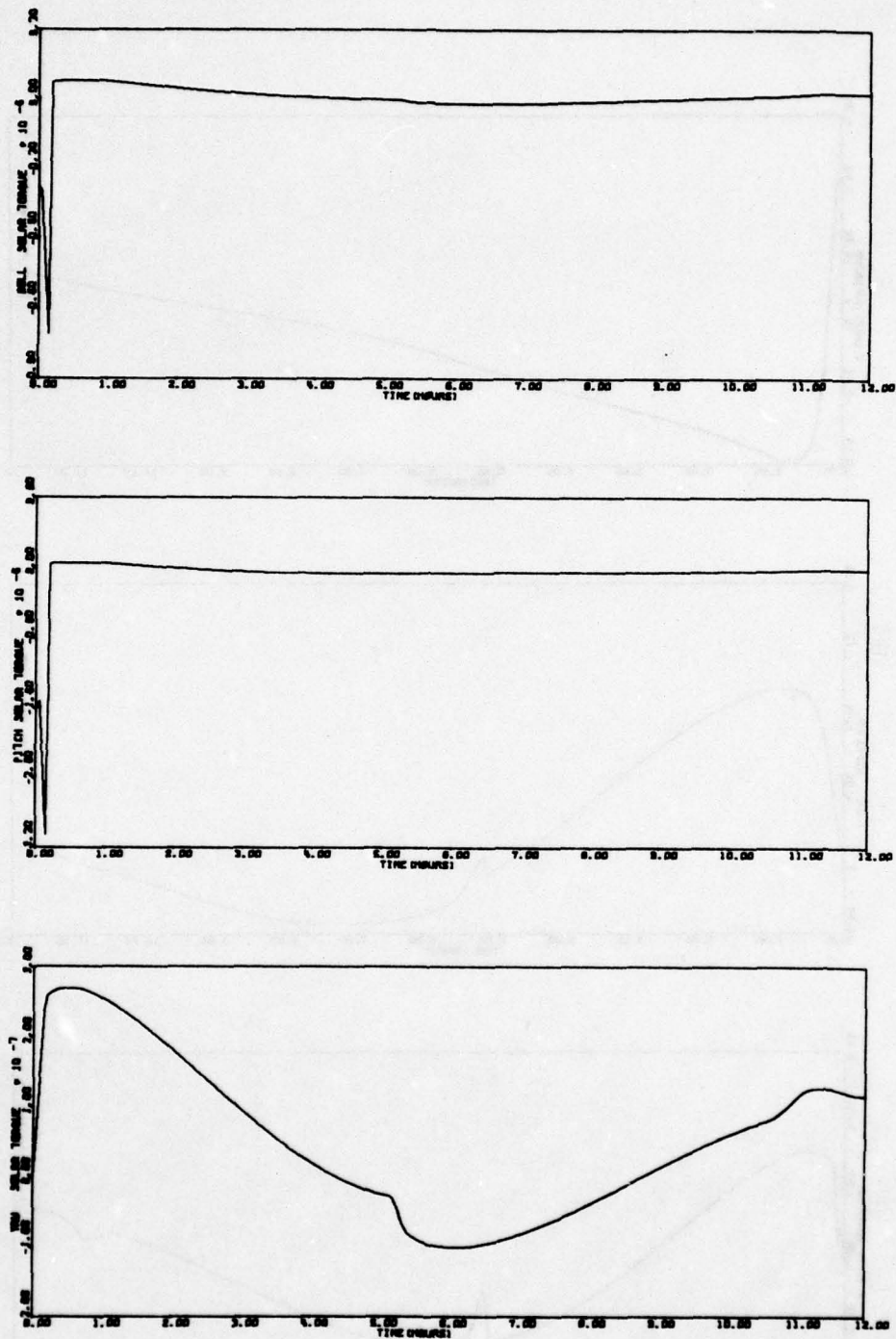


Figure 70. Run 24 - Deploy (P. Q. R.) = (.007..007..01) (PHI. THT. PSI) = (.25..25.10.0) ROD1 and ROD2 Rates Unequal KSUB(PSI) = KSUB(PSI)/2 (continued)

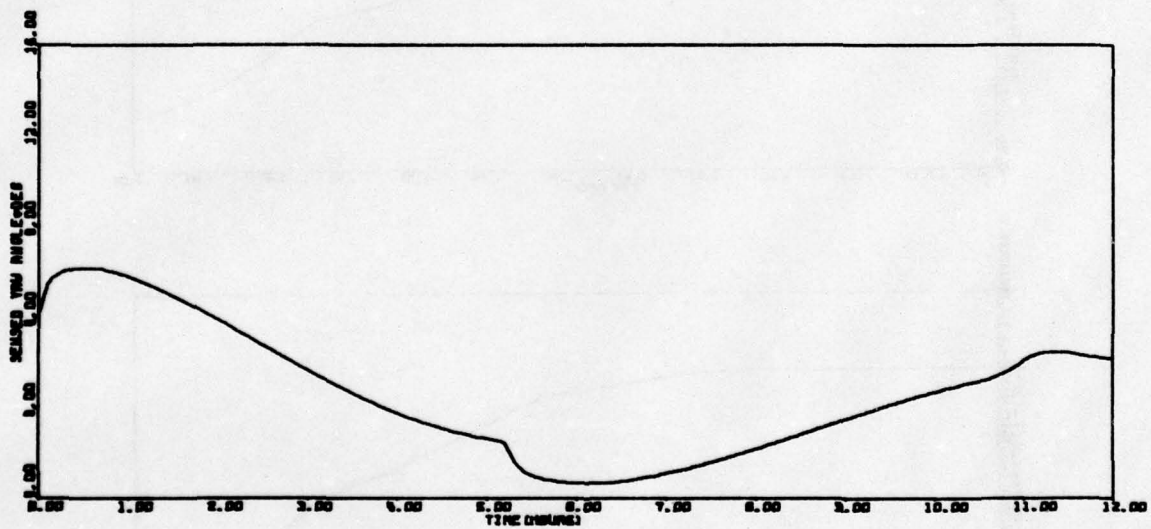
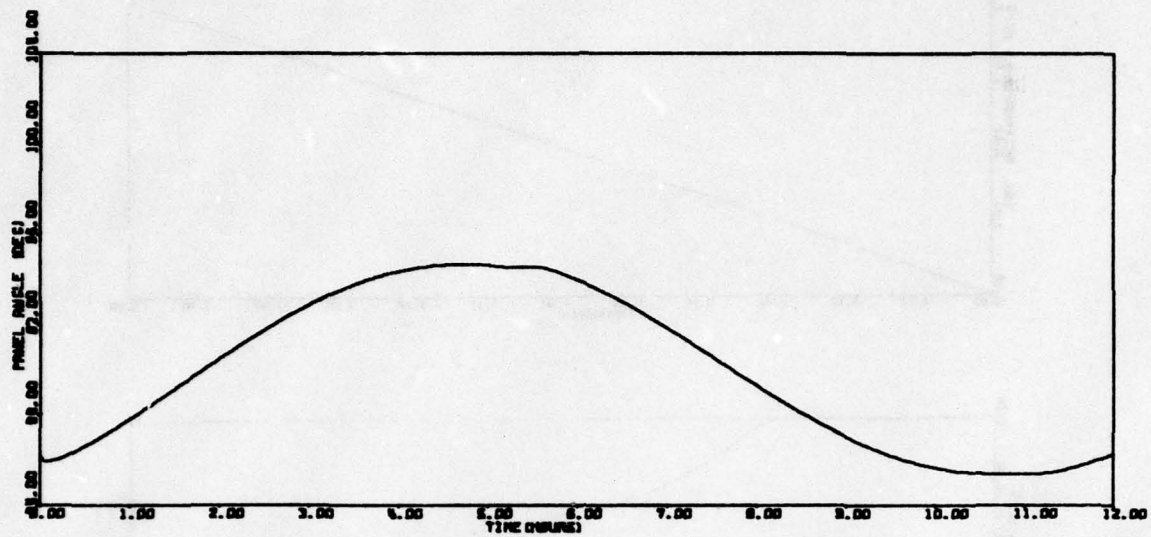


Figure 70. Run 24 - Deploy (P, Q, R.) = (.007, .007, .01) (PHI, THT, PSI) = (.25, .25, 10.0) ROD1 and ROD2 Rates Unequal KSUB(PSI) = KSUB(PSI)/2 (concluded)

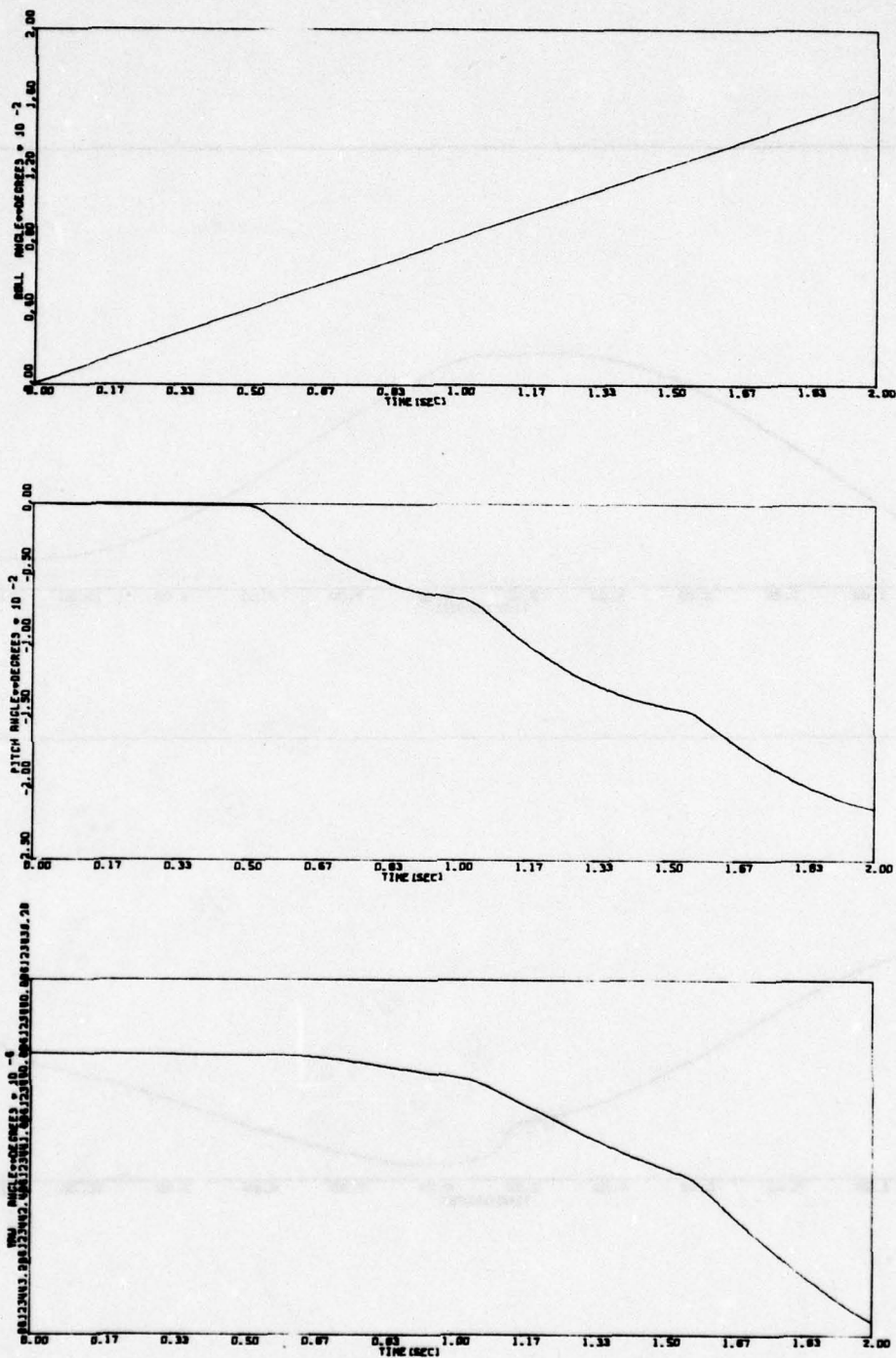


Figure 71. Run 25 - 2 Second Run 3 Body

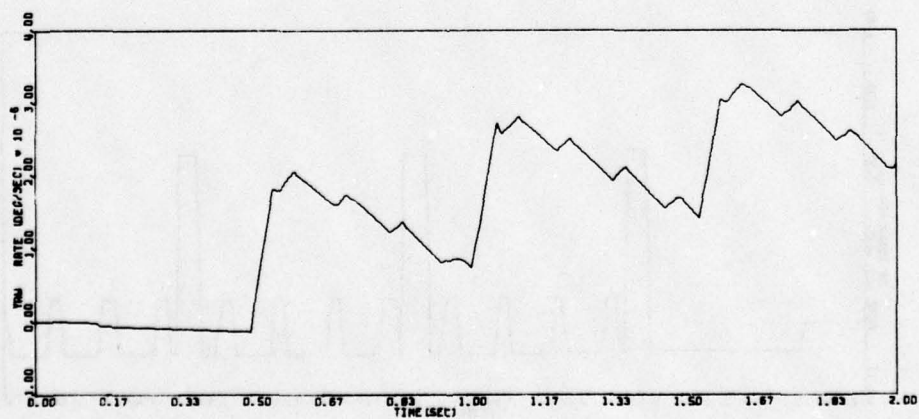
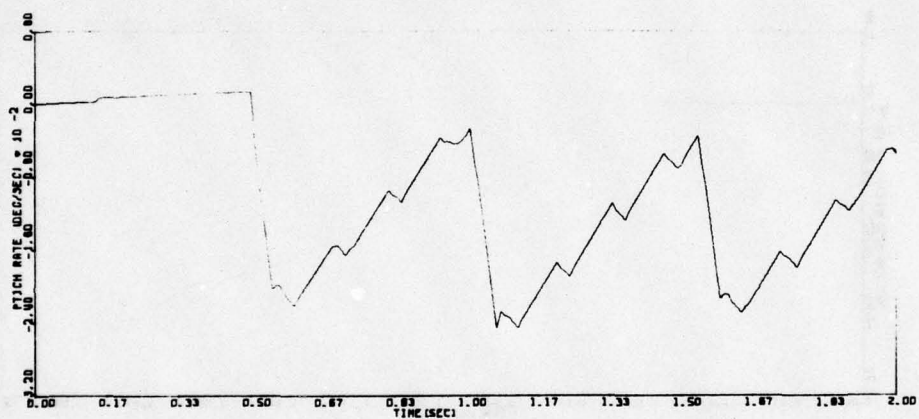
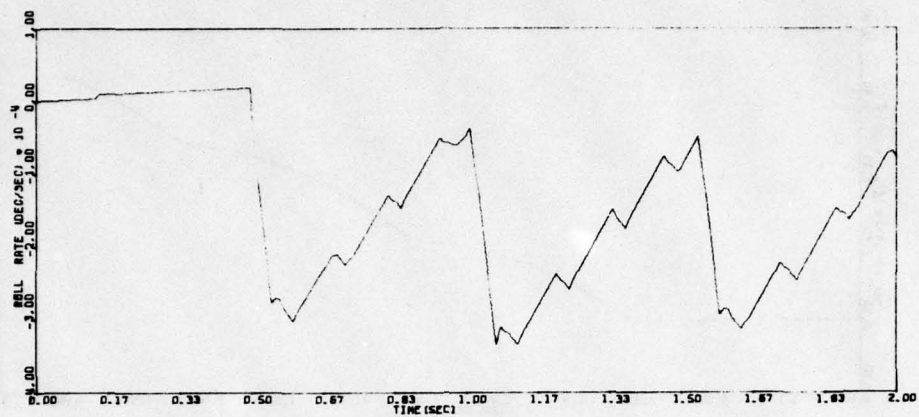


Figure 71. Run 25 - 2 Second Run 3 Body (continued)

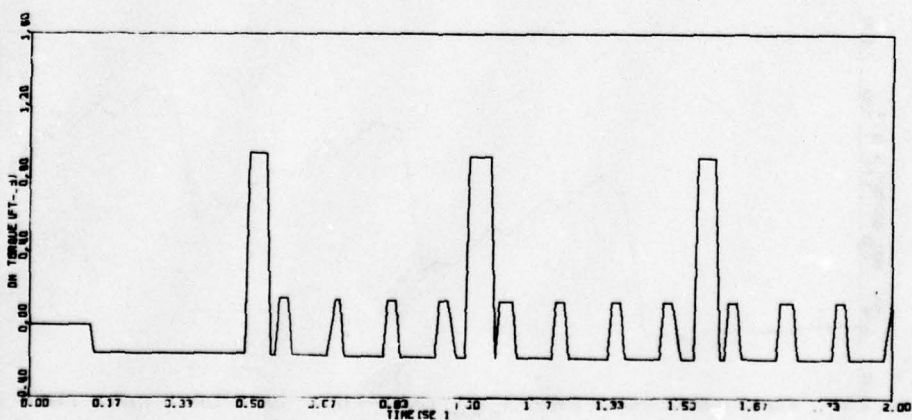
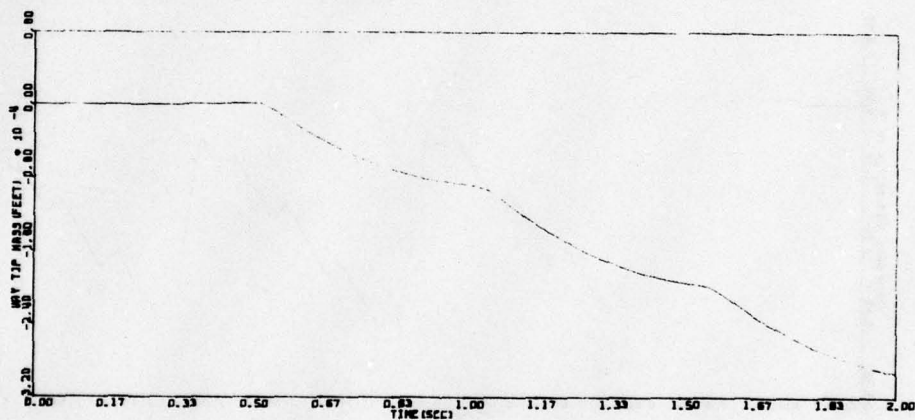
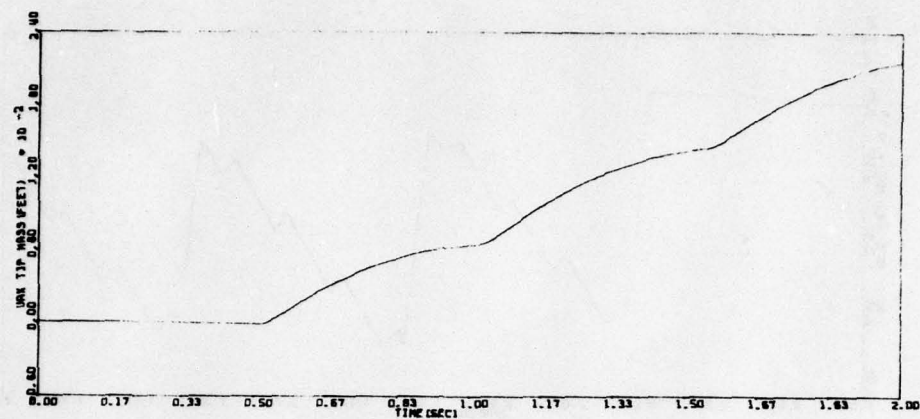


Figure 71. Run 25 - 2 Second Run 3 Body (continued)

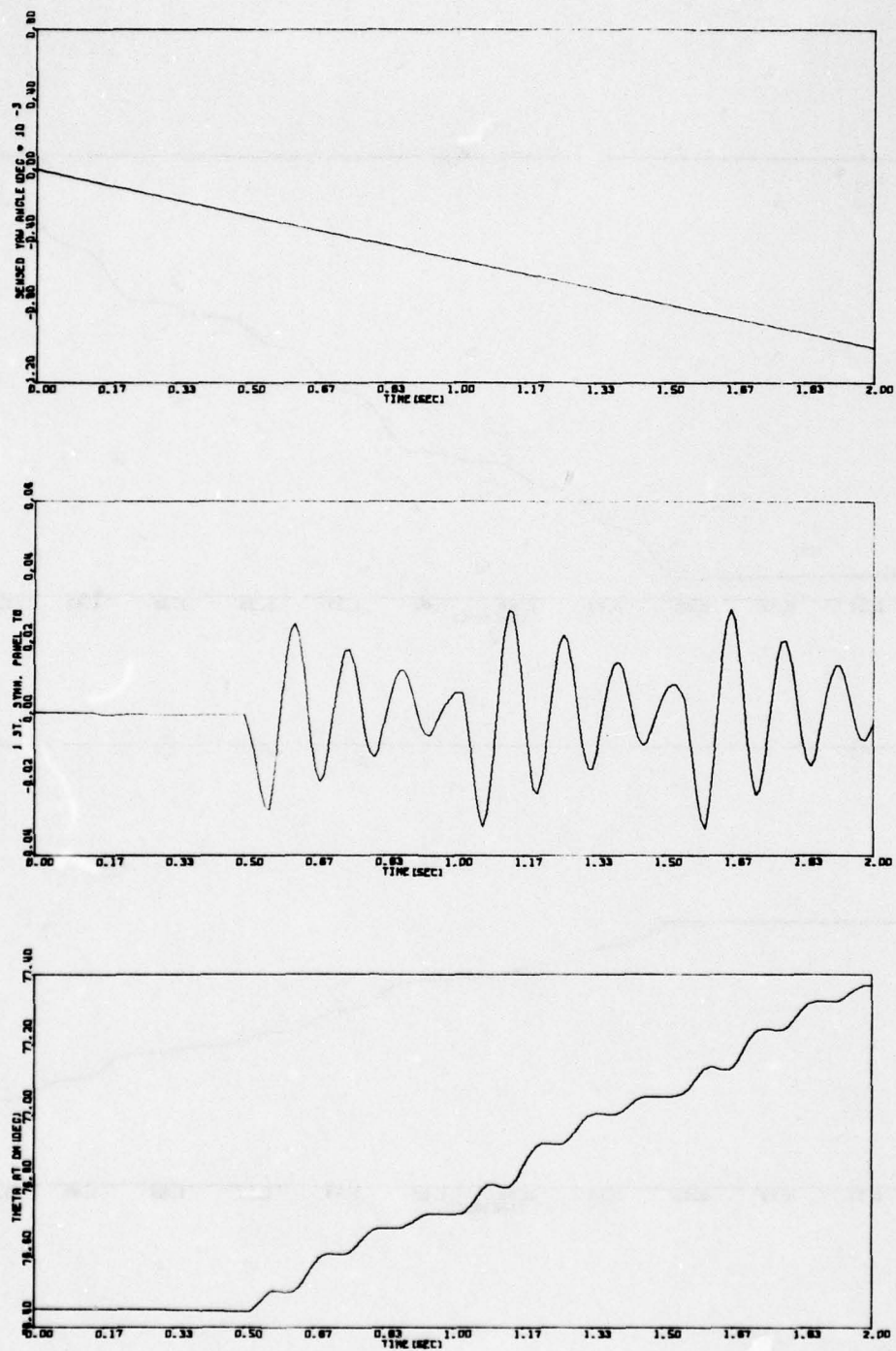


Figure 71. Run 25 - 2 Second Run 3 Body (continued)

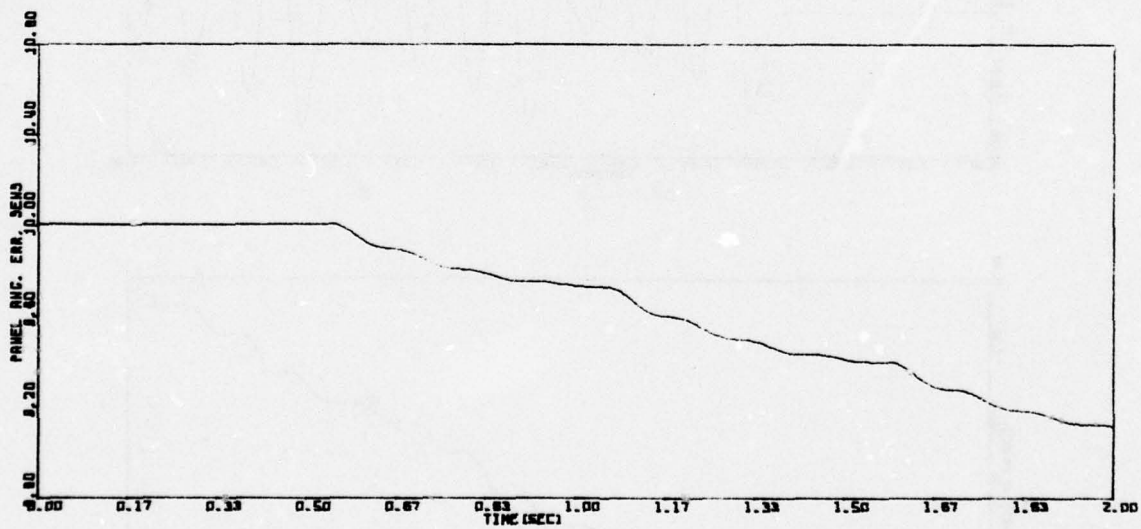
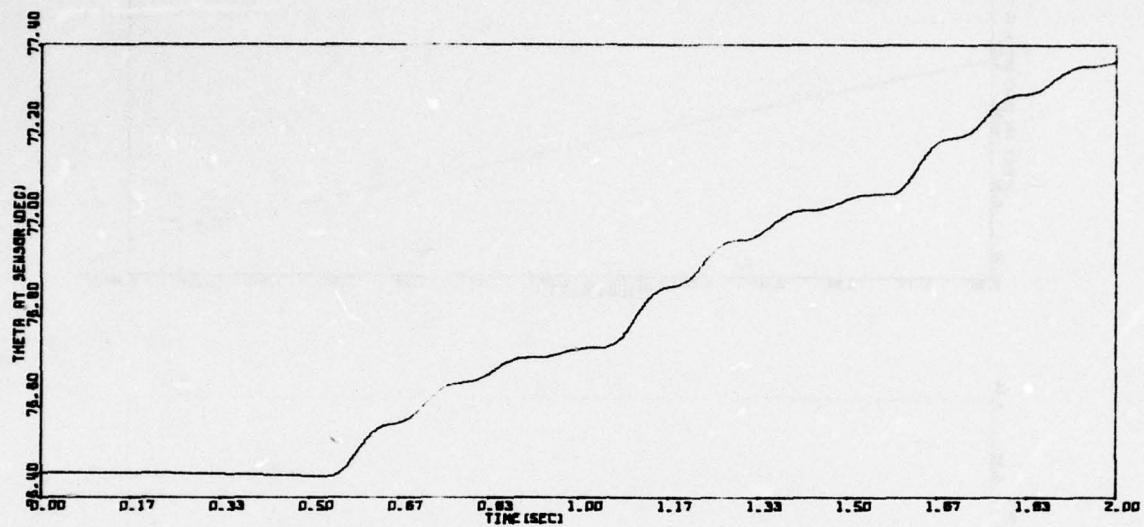


Figure 71. Run 25 - 2 Second Run 3 Body (concluded)

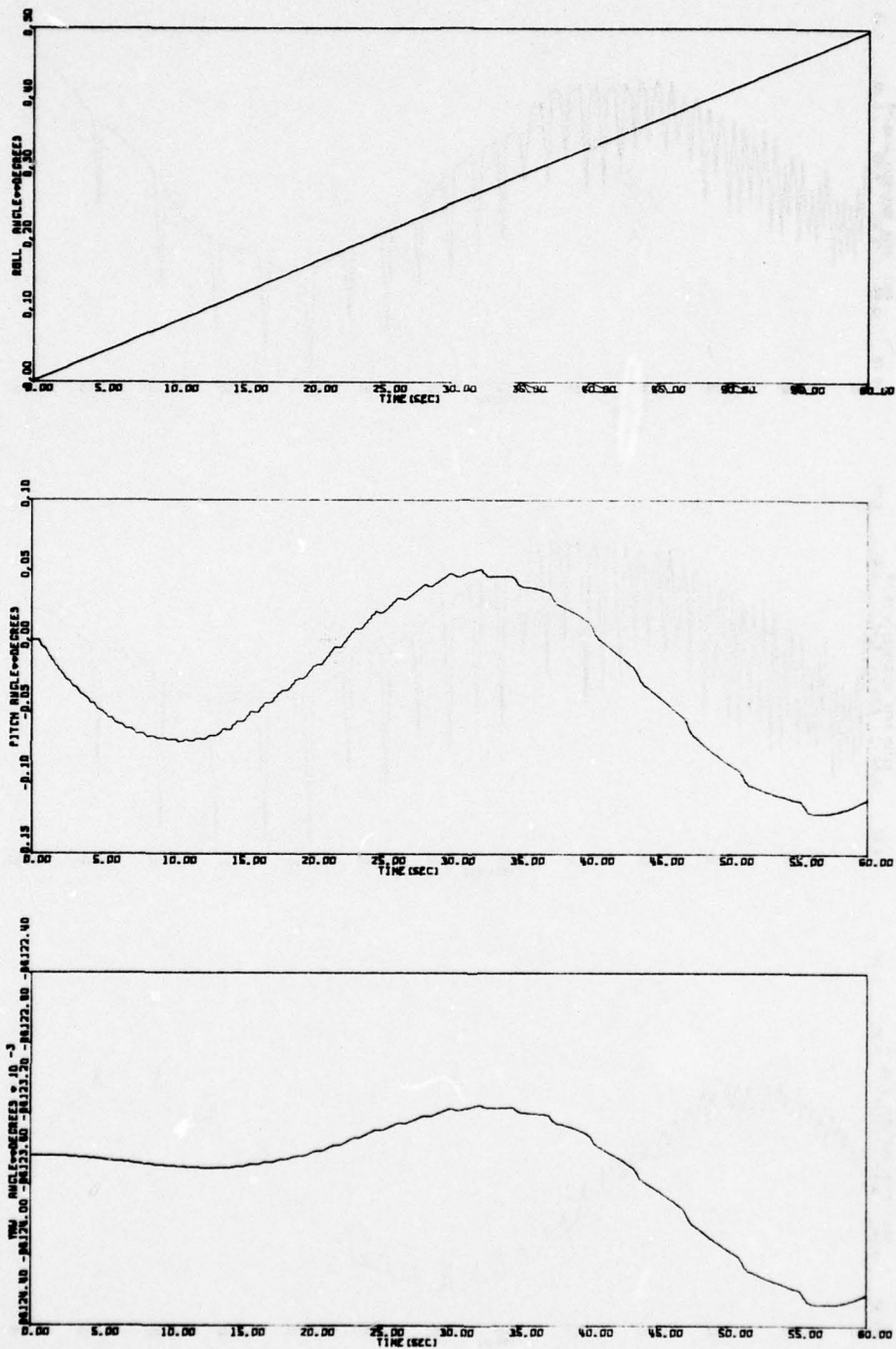


Figure 72. Run 26 - 60 Second Run 3 Body without C.E. Fix

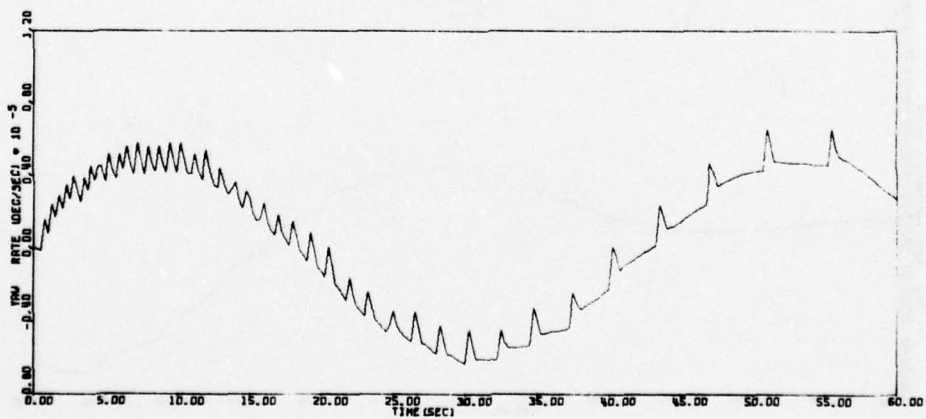
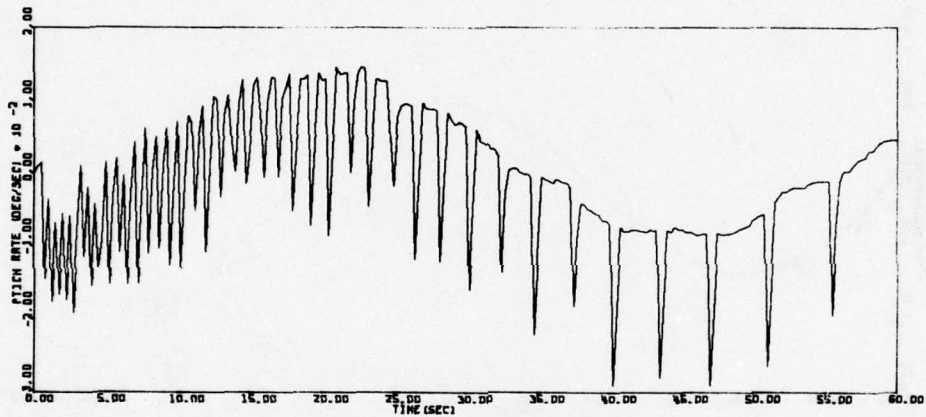
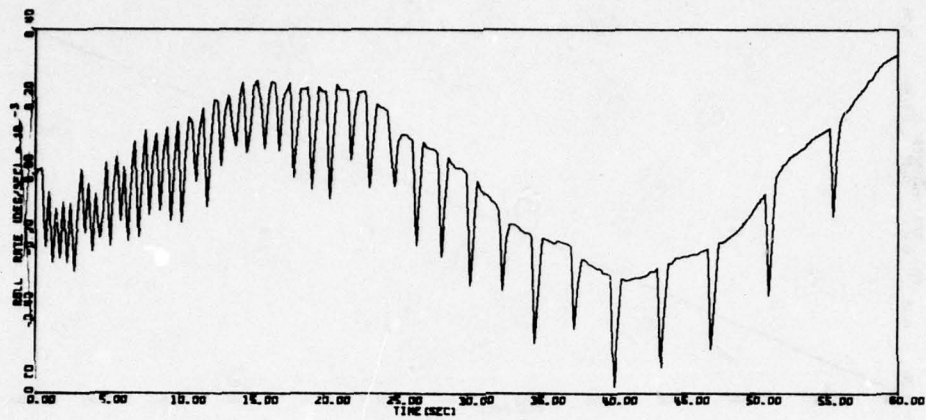


Figure 72. Run 26 - 60 Second Run 3 Body without C. E. Fix (continued)

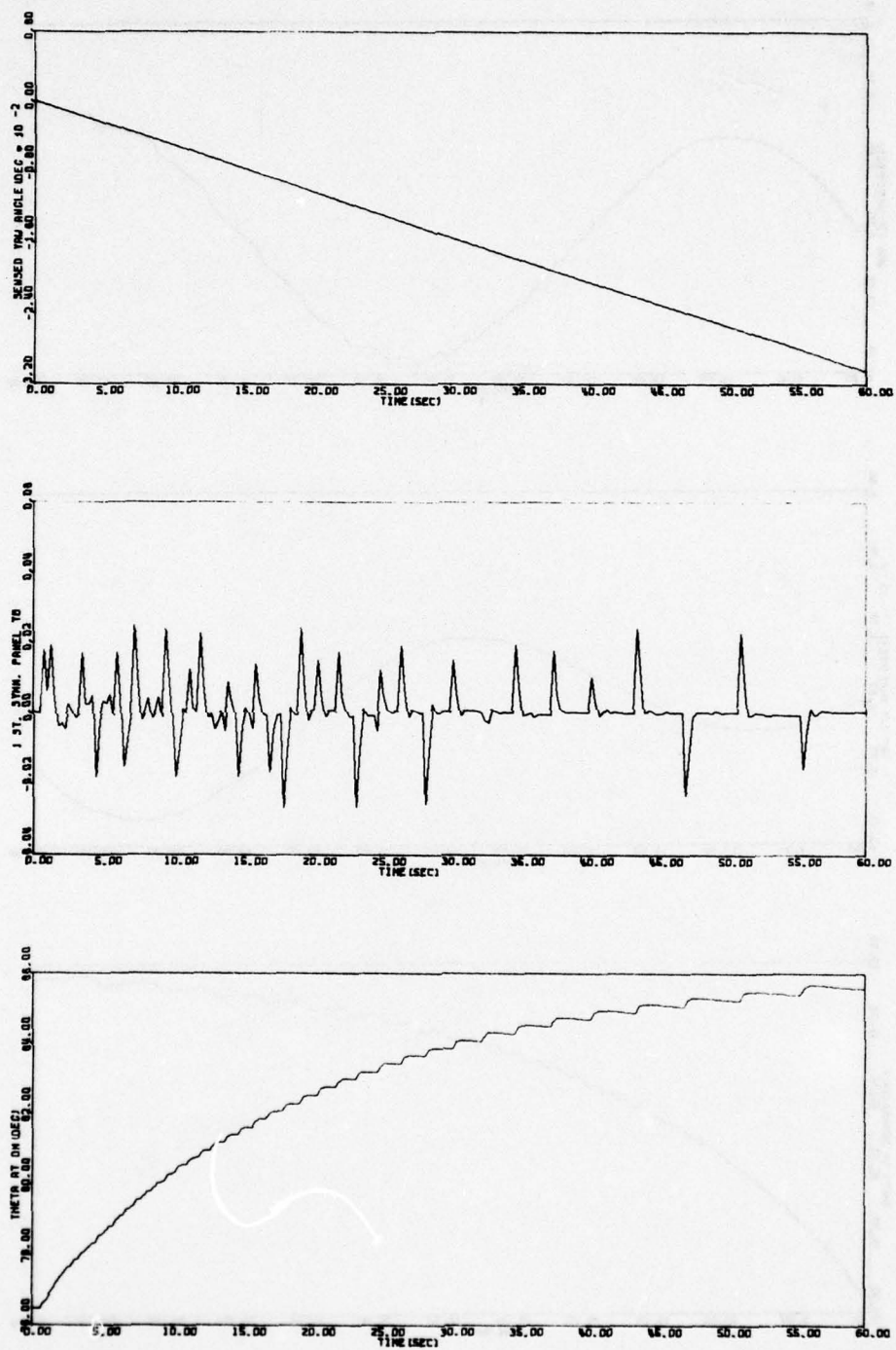


Figure 72. Run 26 - 60 Second Run 3 Body
without C. E. Fix (continued)

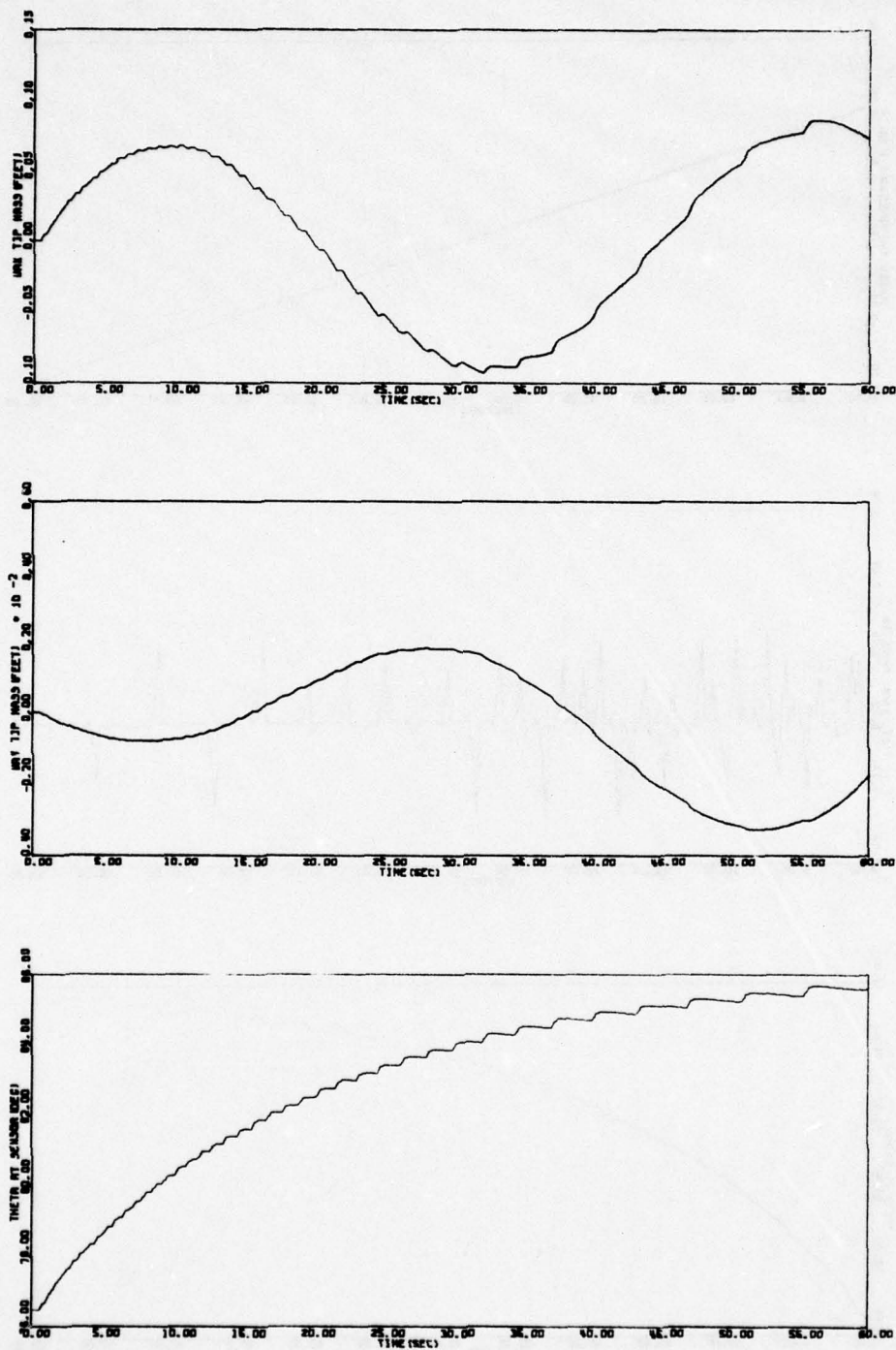


Figure 72. Run 26 - 60 Second Run 3 Body
without C. E. Fix (continued)

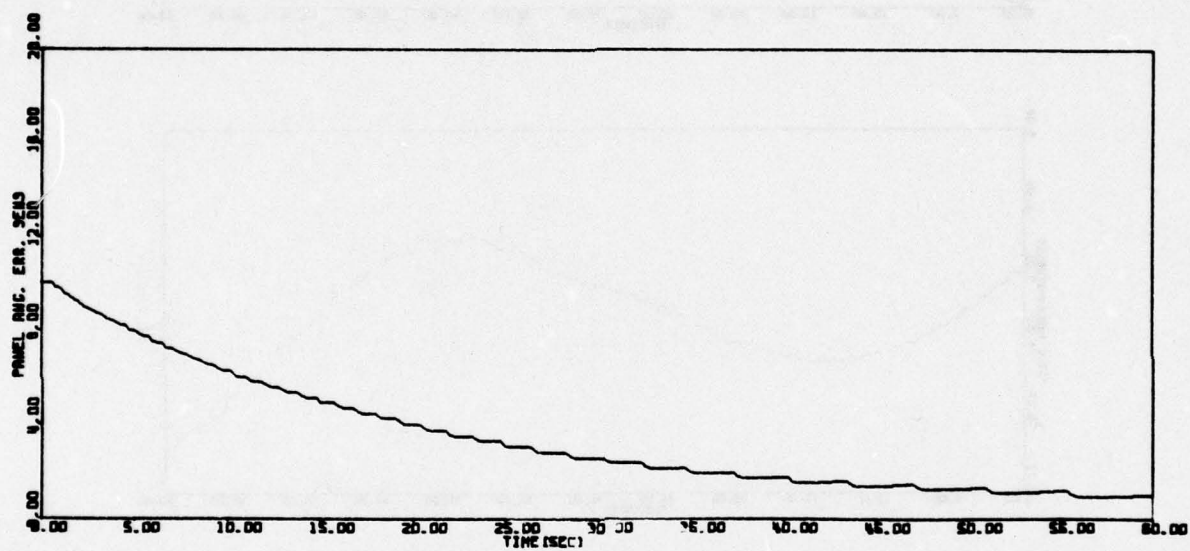


Figure 72. Run 26 - 60 Second Run 3 Body
without C. E. Fix (concluded)

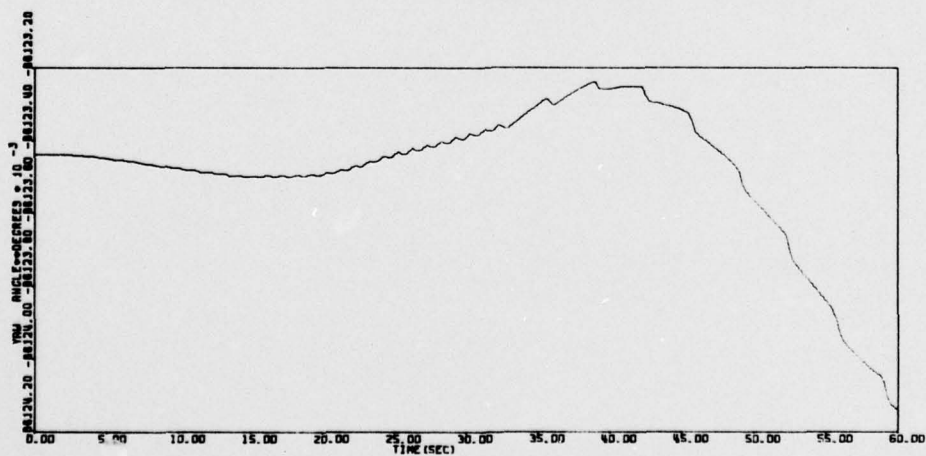
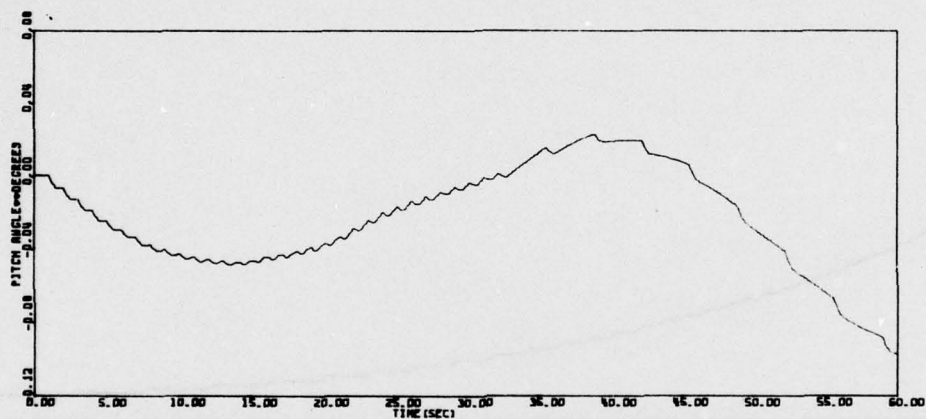
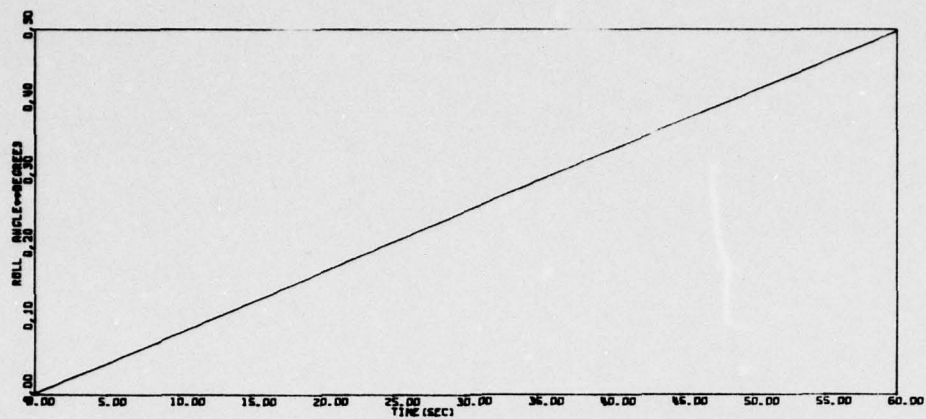


Figure 73. Run 27 - 60 Second Run 3 Body
with C. E. Fix

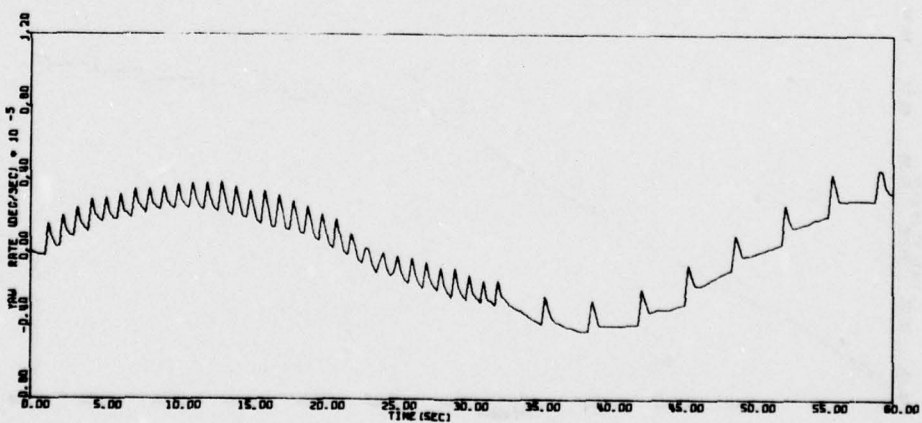
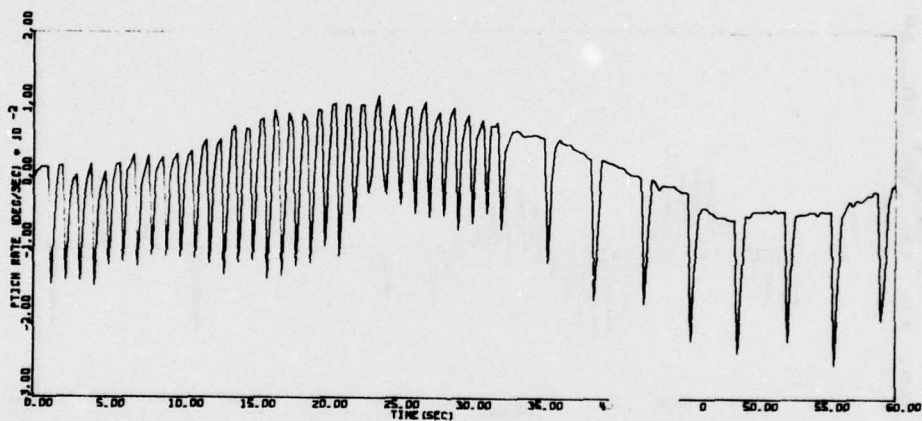
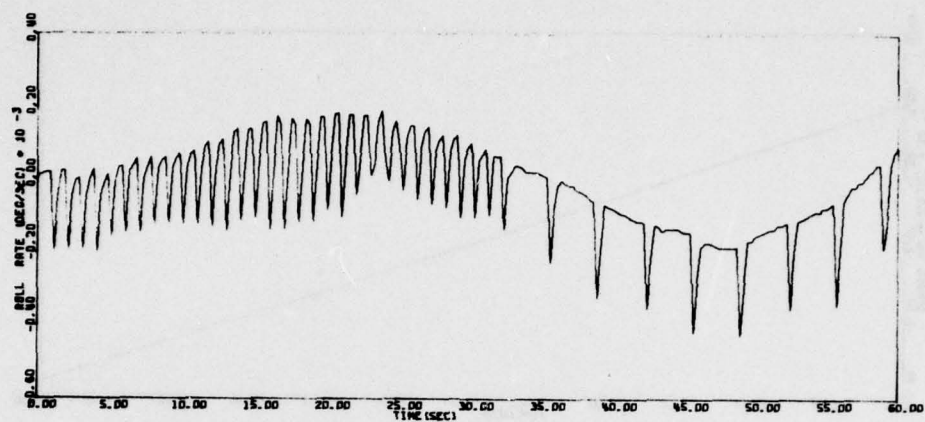


Figure 73. Run 27 - 60 Second Run 3 Body
with C. E. Fix (continued)

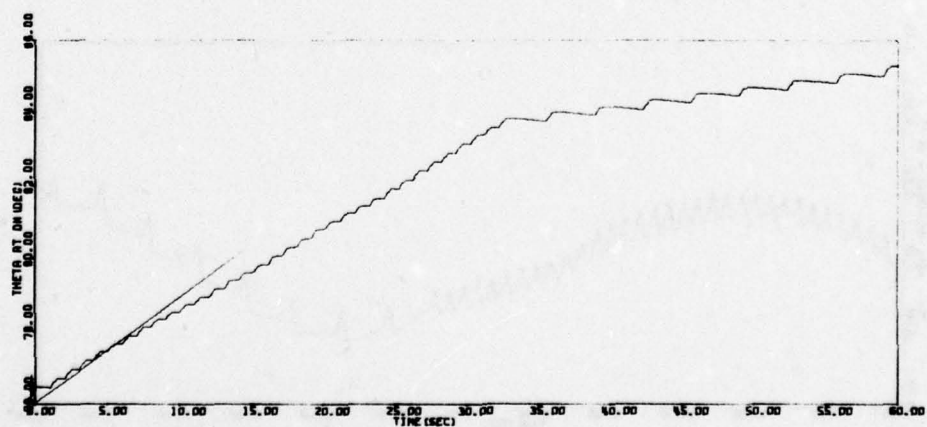
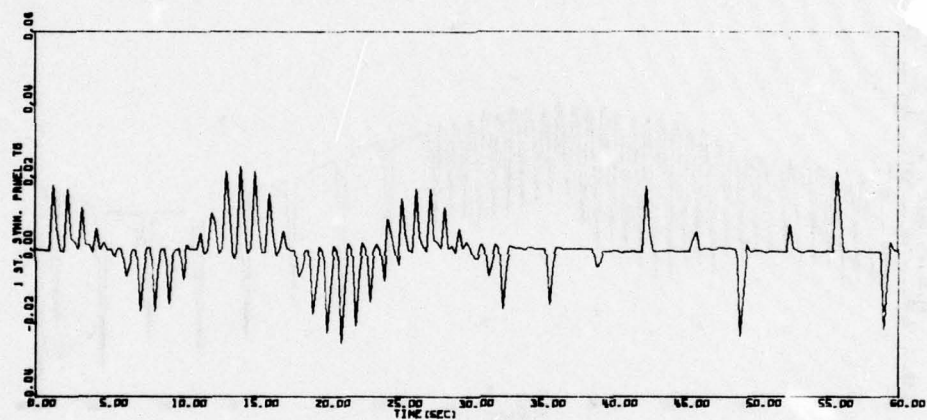
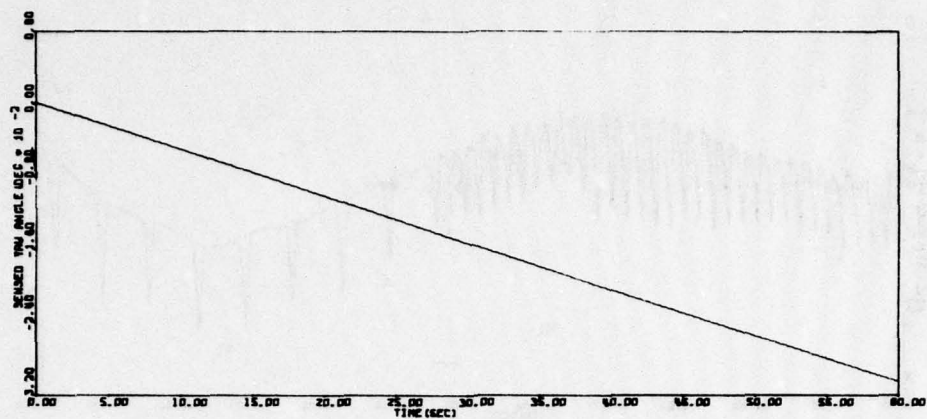


Figure 73. Run 27 - 60 Second Run 3 Body
with C. E. Fix (continued)

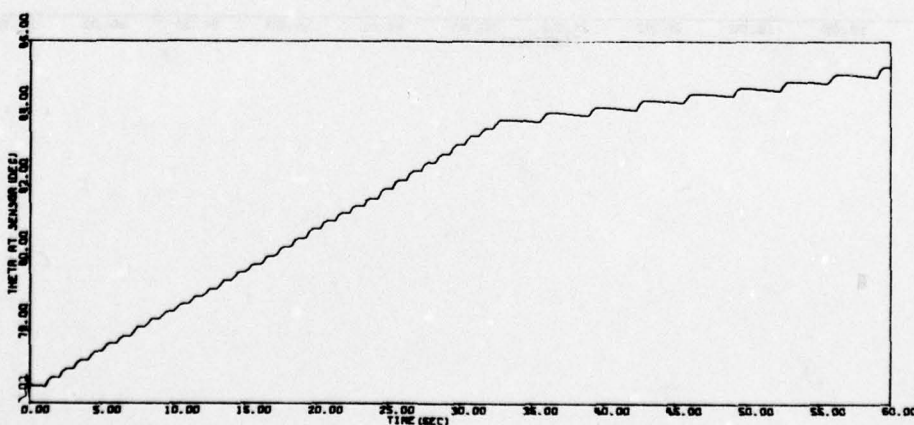
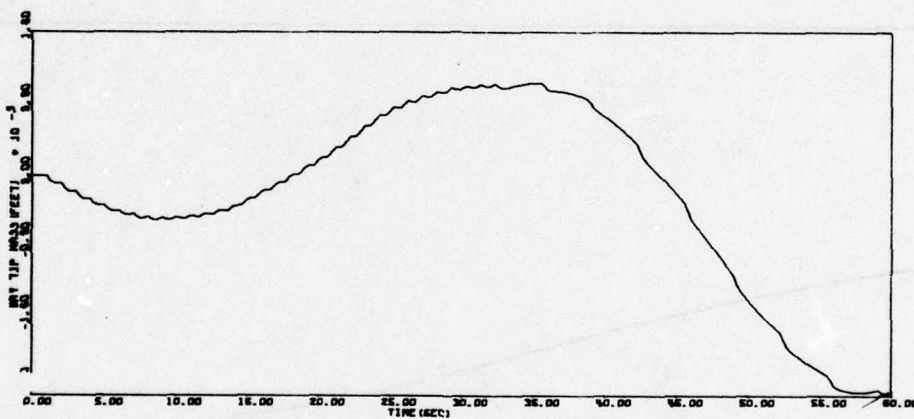
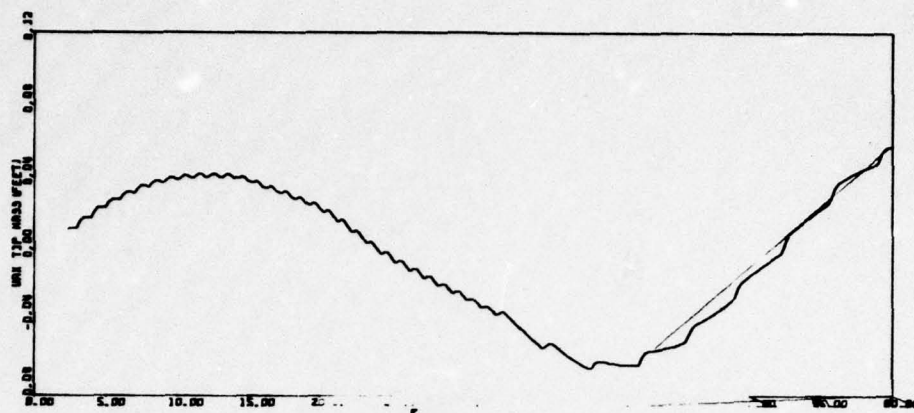


Figure 73. Run 27 - 60 Second Run 3 Body
with C. E. Fix (continued)

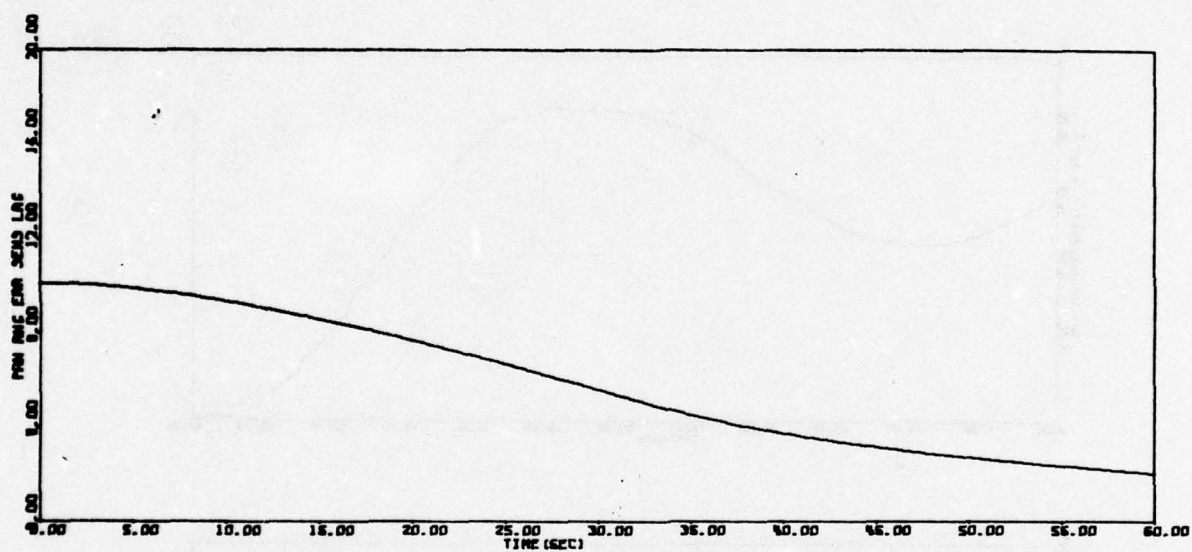


Figure 73. Run 27 - 60 Second Run 3 Pody
with C. E. Fix (concluded)

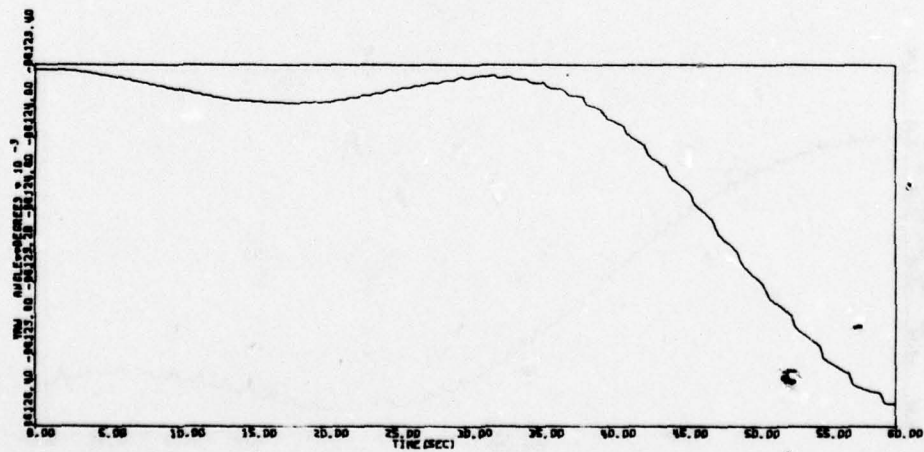
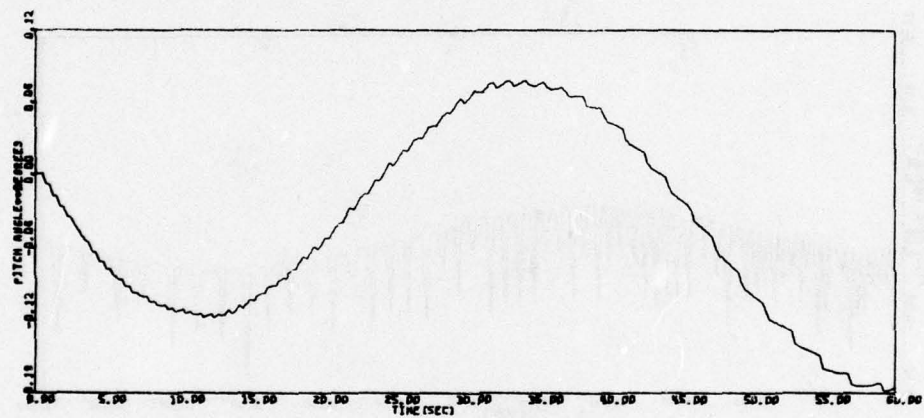
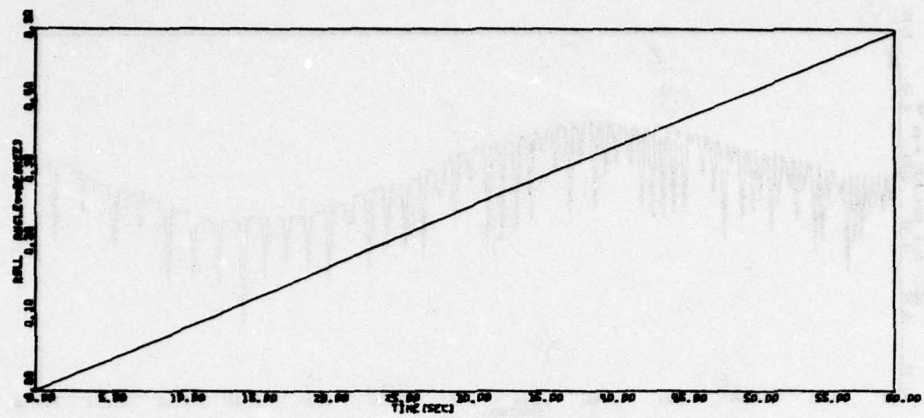


Figure 74. Run 27A - 60 Sec 3 Body Run with Locked Up Drive Motor

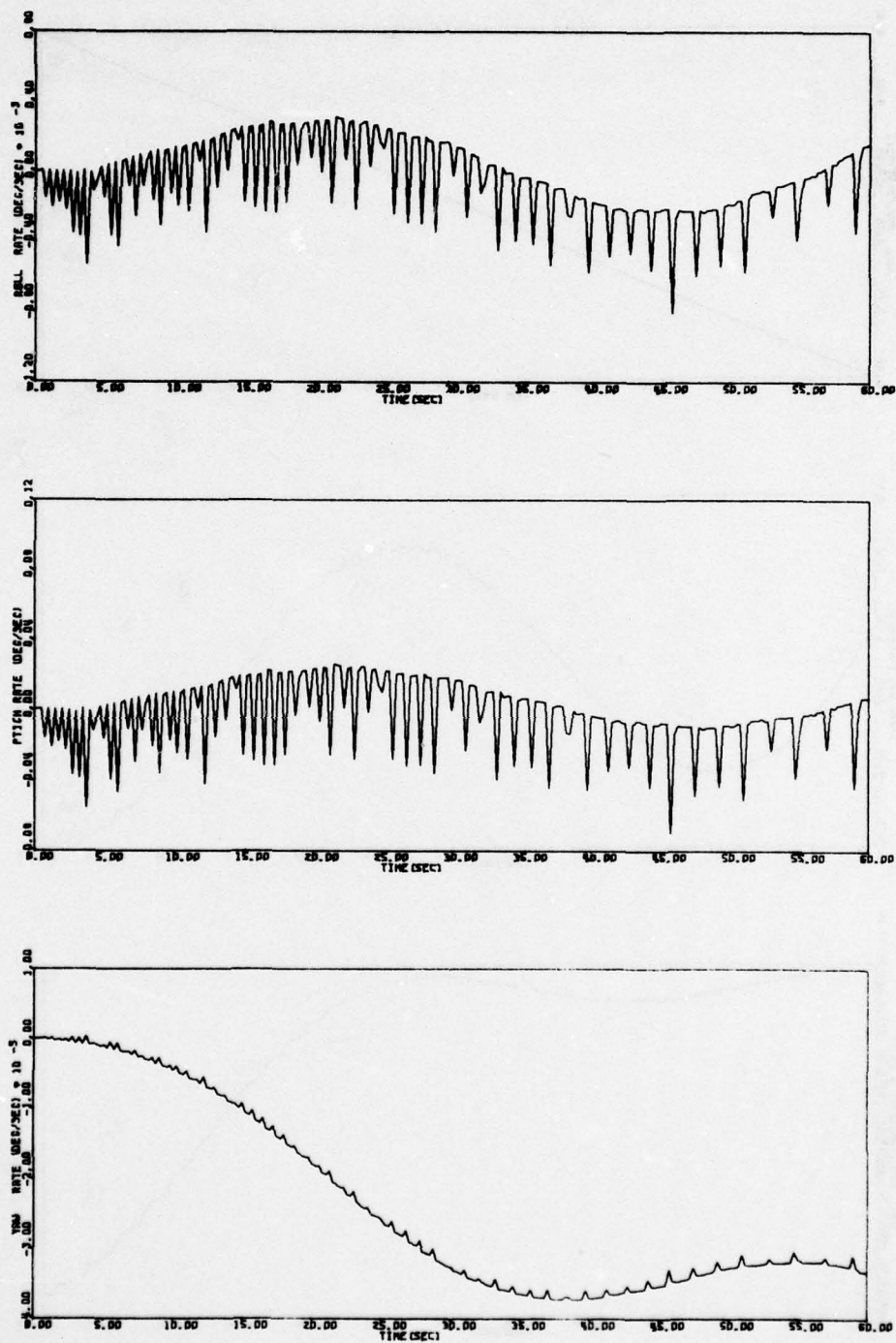


Figure 74. Run 27A - 60 Sec 3 Body Run with Locked Up Drive Motor (continued)

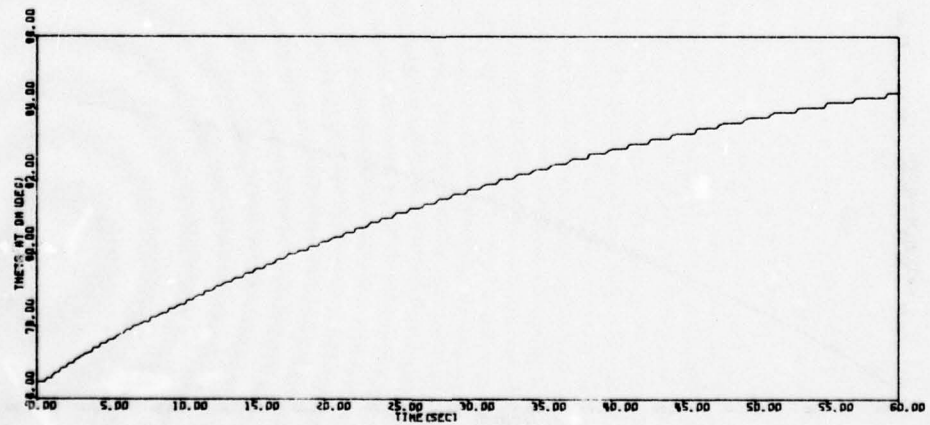
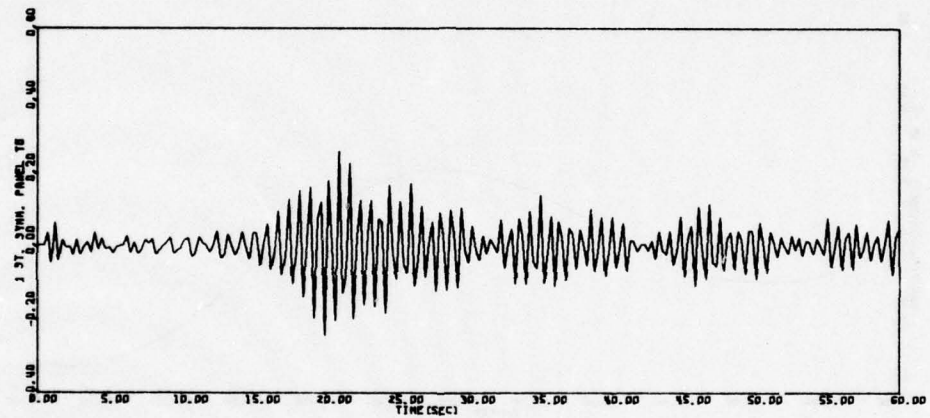
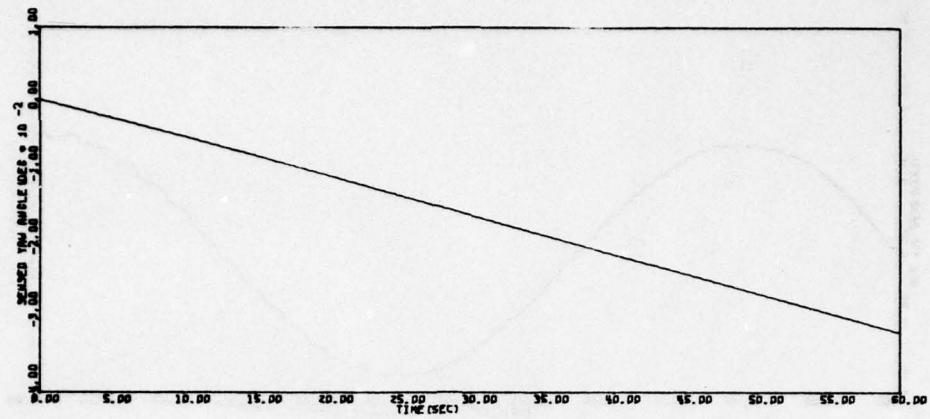


Figure 74. Run 27A - 60 Sec 3 Body Run with Locked Up Drive Motor (continued)

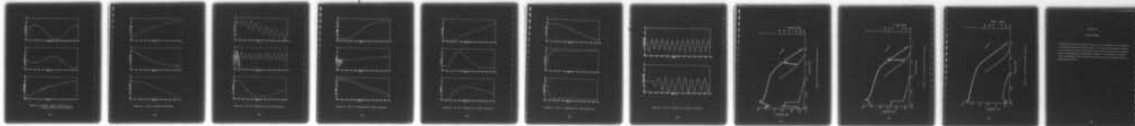
AD-A052 633

HONEYWELL INC MINNEAPOLIS MINN SYSTEMS AND RESEARCH --ETC F/G 22/2
NTS-2 INDEPENDENT STABILITY AND CONTROL ANALYSIS. VOLUME I. TEC--ETC(U)
MAR 77 R E POPE, M D WARD, S M SCHWANTES
77SRC17-VOL-1

UNCLASSIFIED

NL

4 OF 4
AD
A052633



END
DATE
FILMED
5-78
DDC

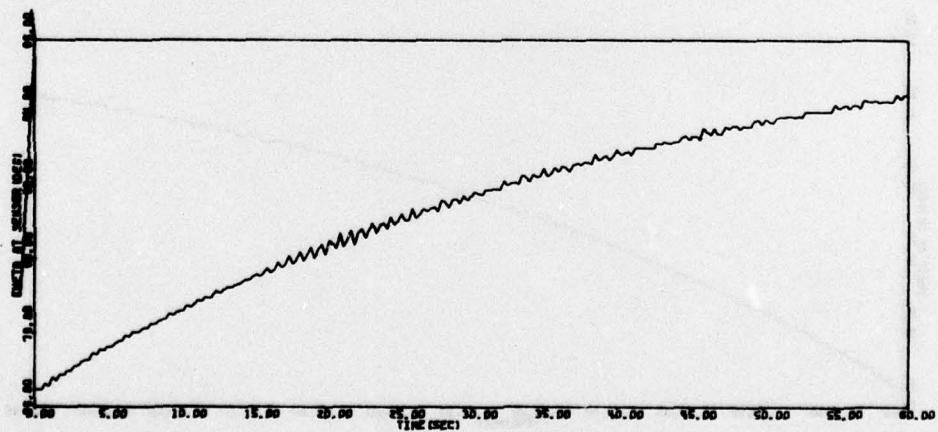
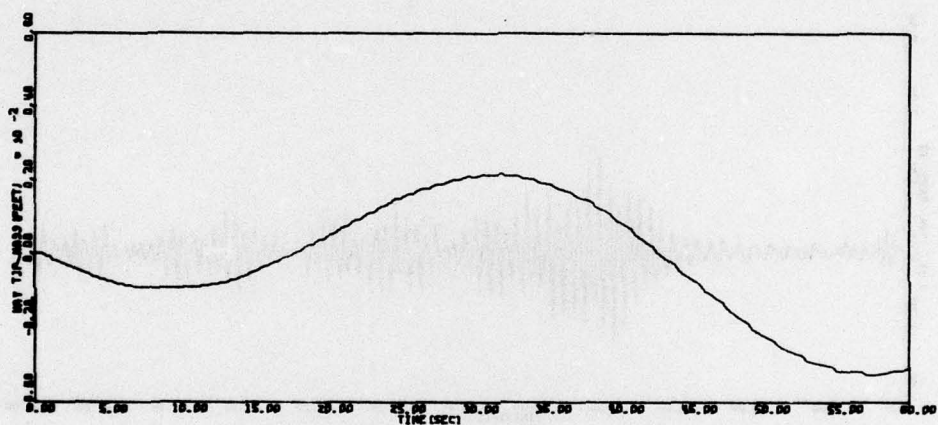
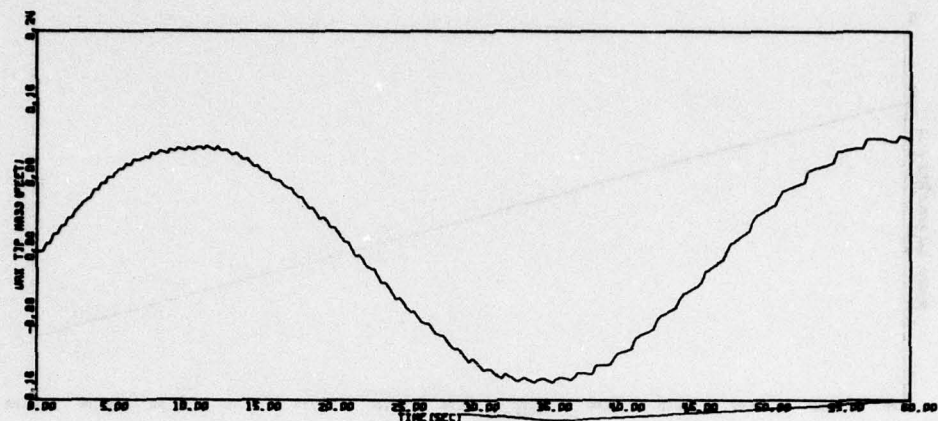


Figure 74. Run 27A - 60 Sec 3 Body Run with Locked Up Drive Motor (concluded)

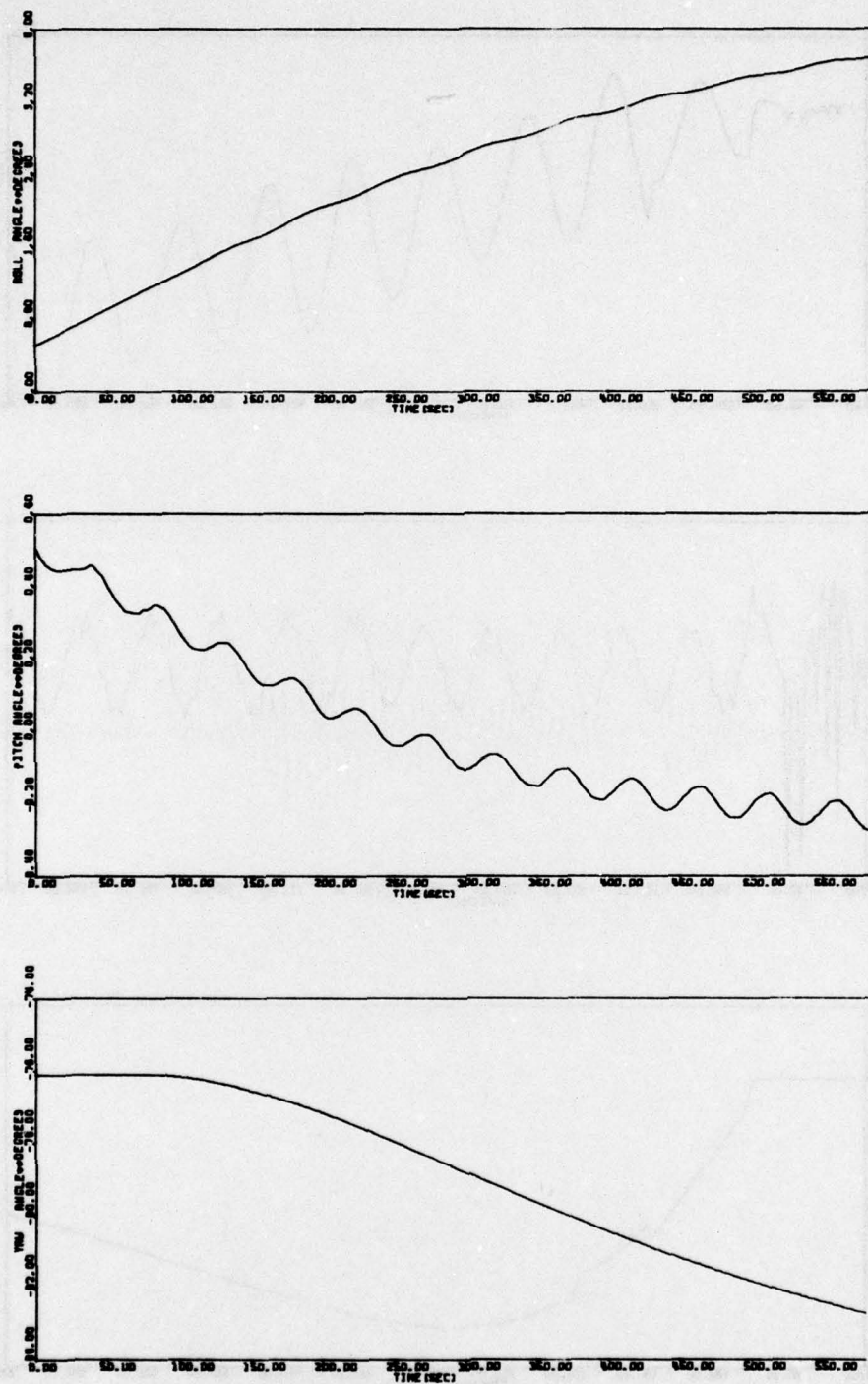


Figure 75. Run 28 - 10 Minute Run 3 Body

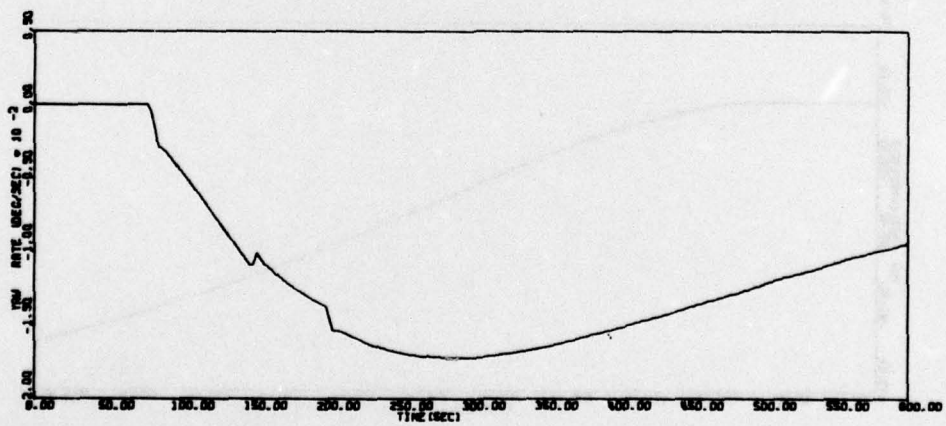
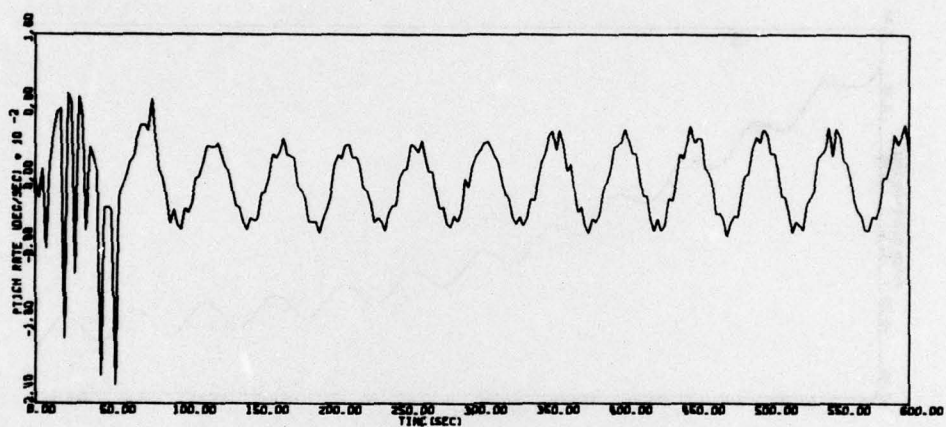
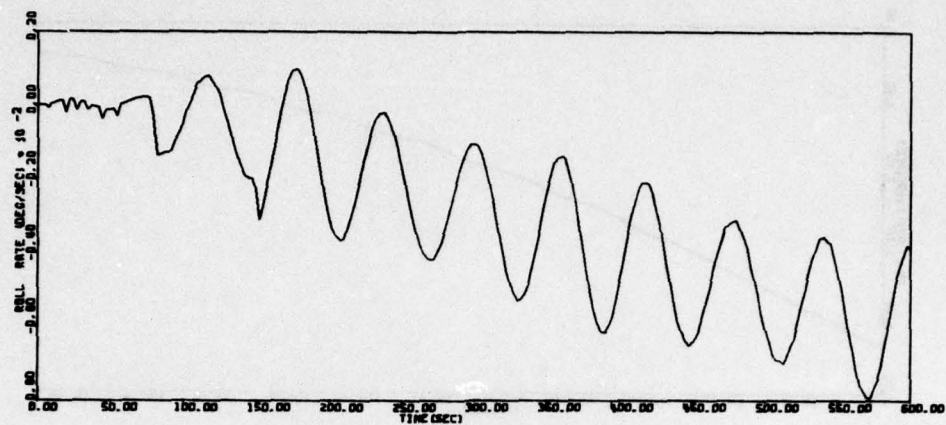


Figure 75. Run 28 - 10 Minute Run 3 Body (continued)

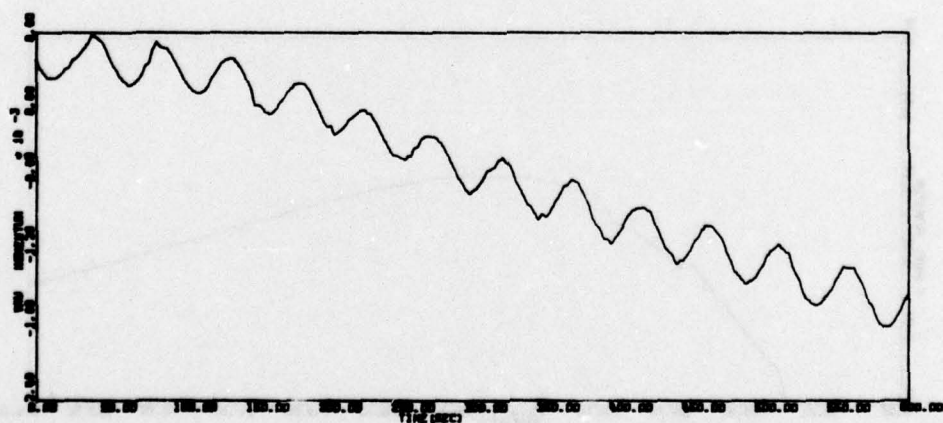
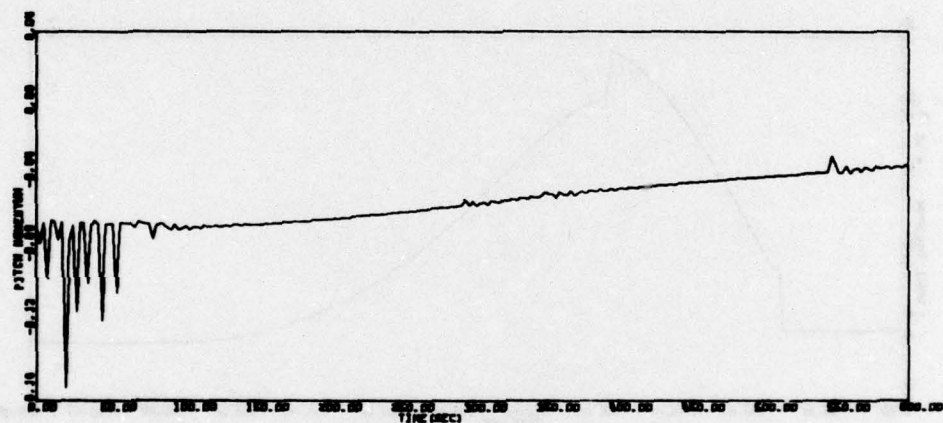
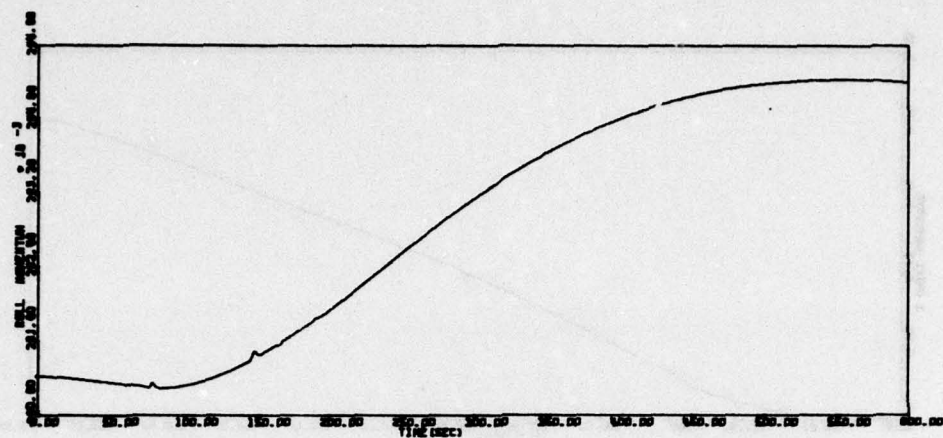


Figure 75. Run 28 - 10 Minute Run 3 Body (continued)

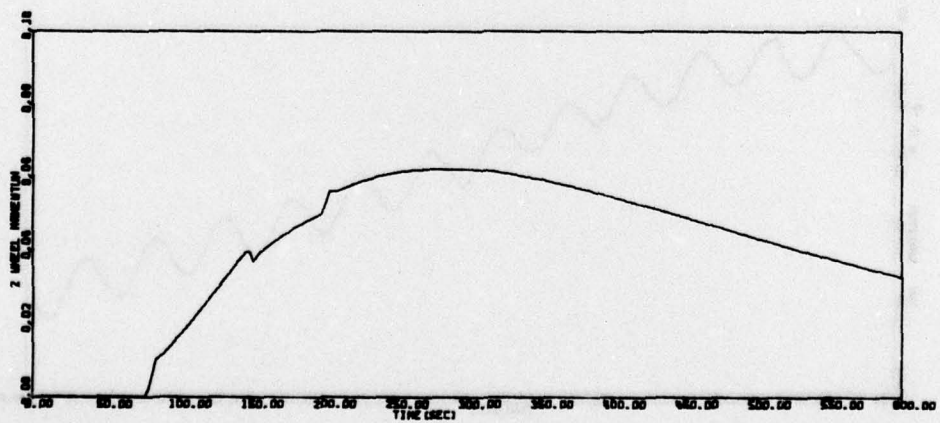
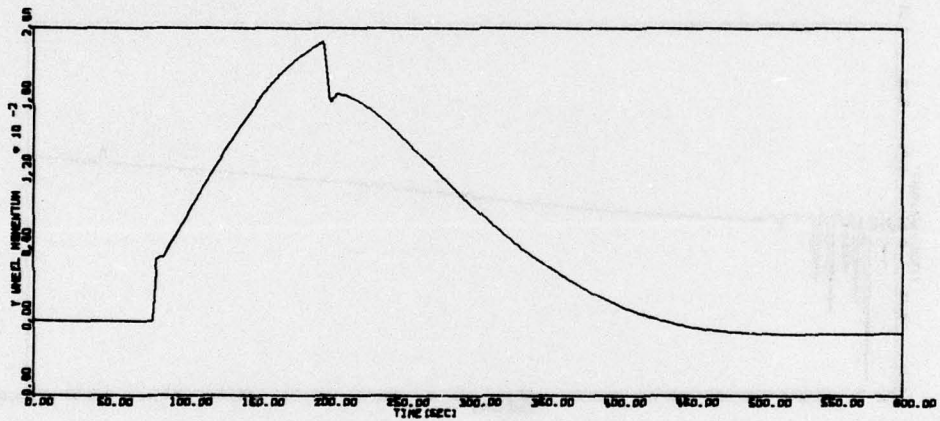
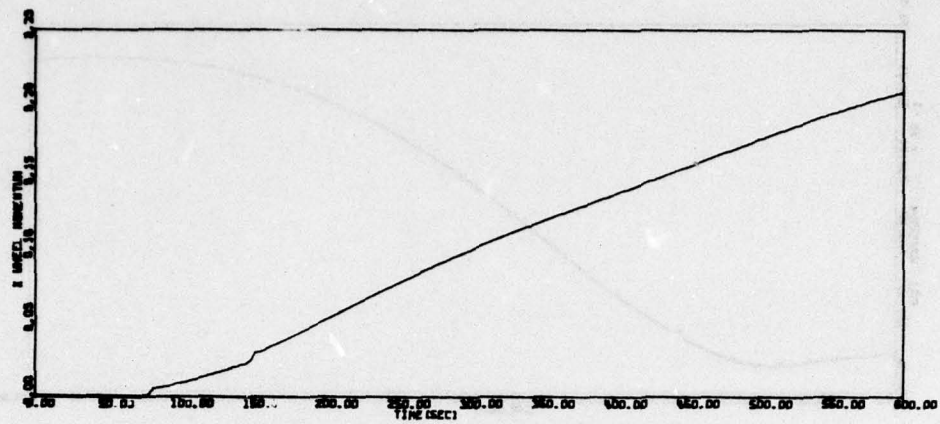


Figure 75. Run 28 - 10 Minute Run 3 Body (continued)

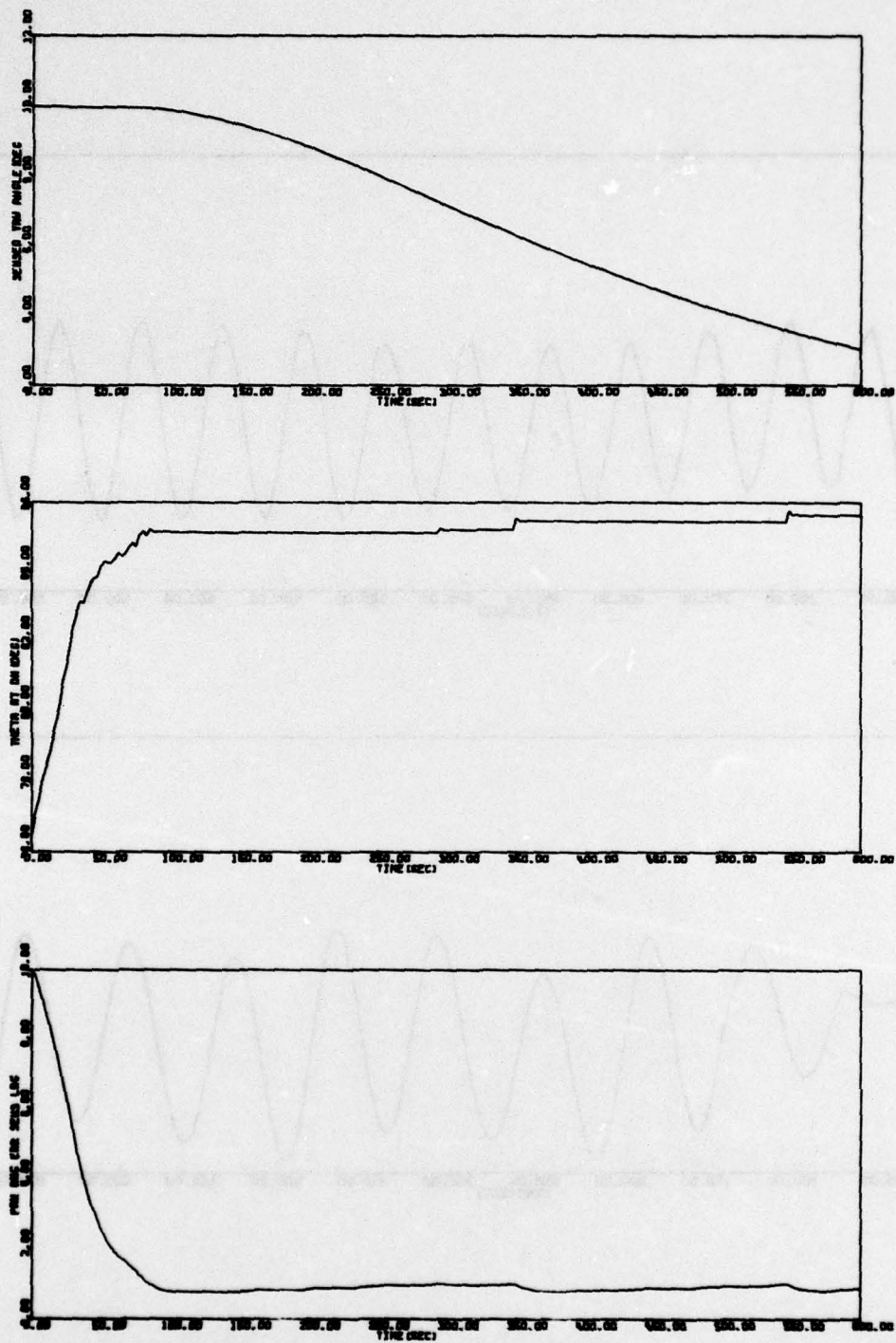


Figure 75. Run 28 - 10 Minute Run 3 Body (continued)

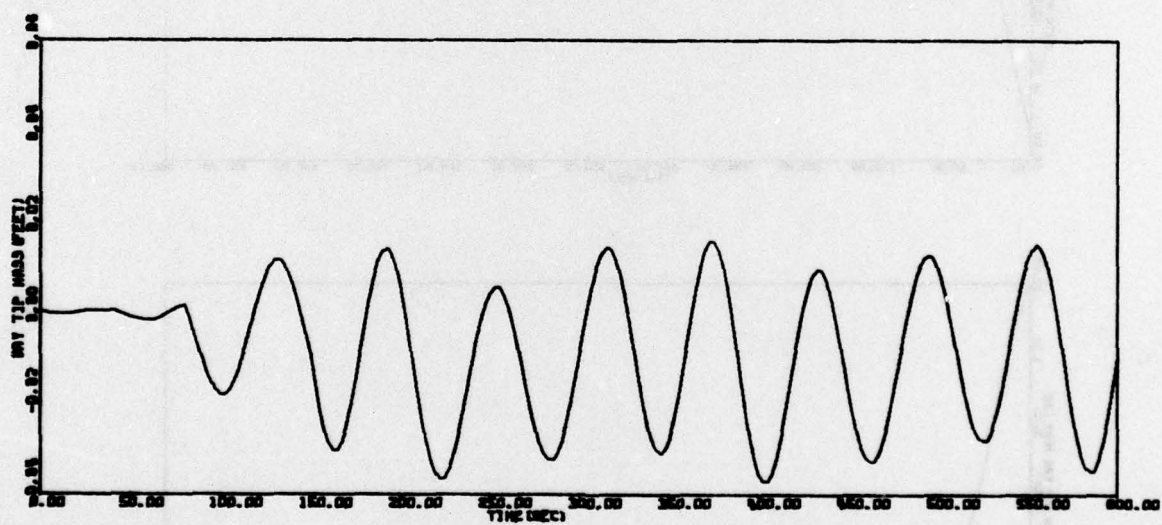
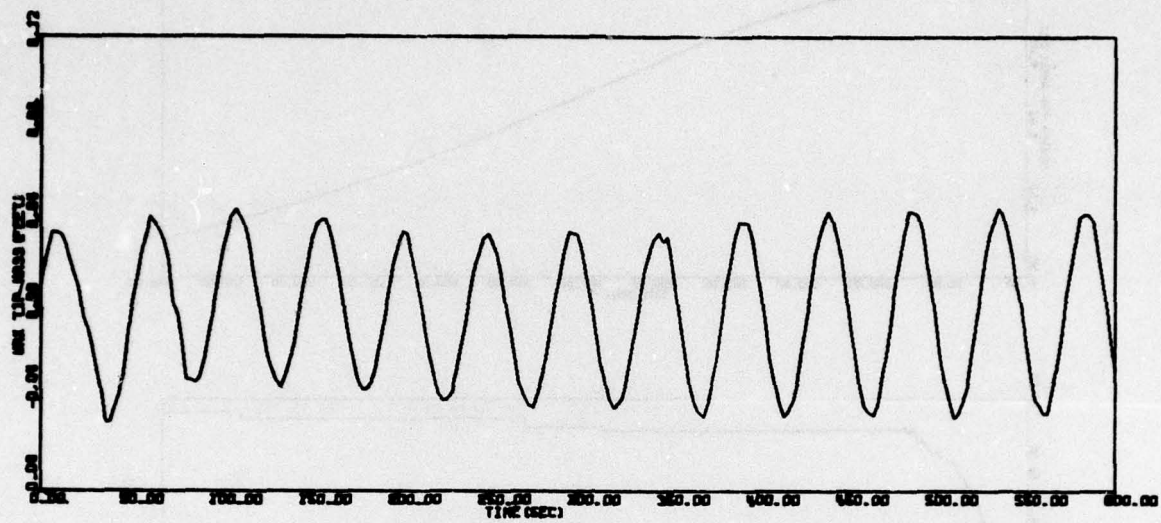


Figure 75. Run 28 - 10 Minute Run 3 Body (concluded)

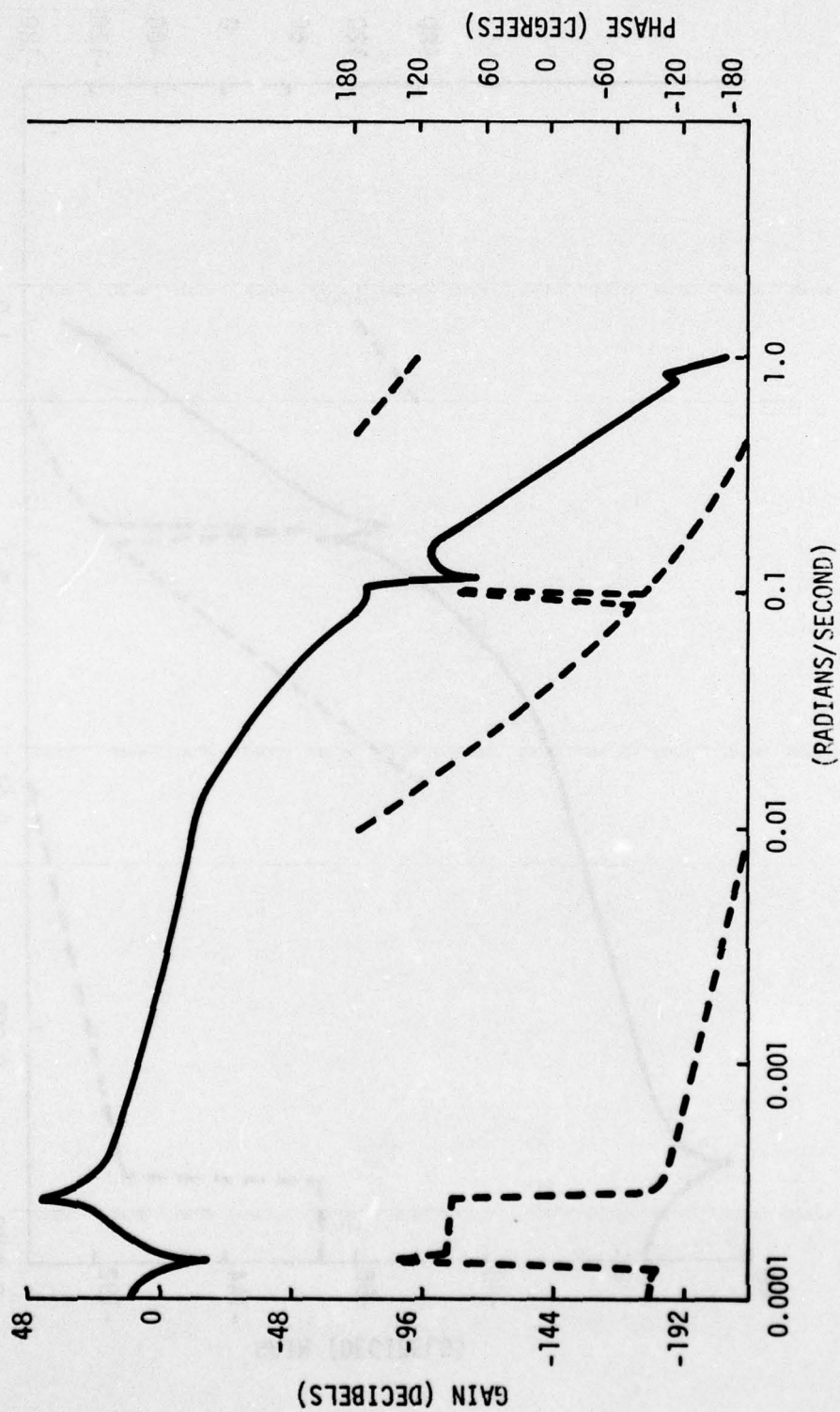


Figure 76. Roll Wheel Frequency Response

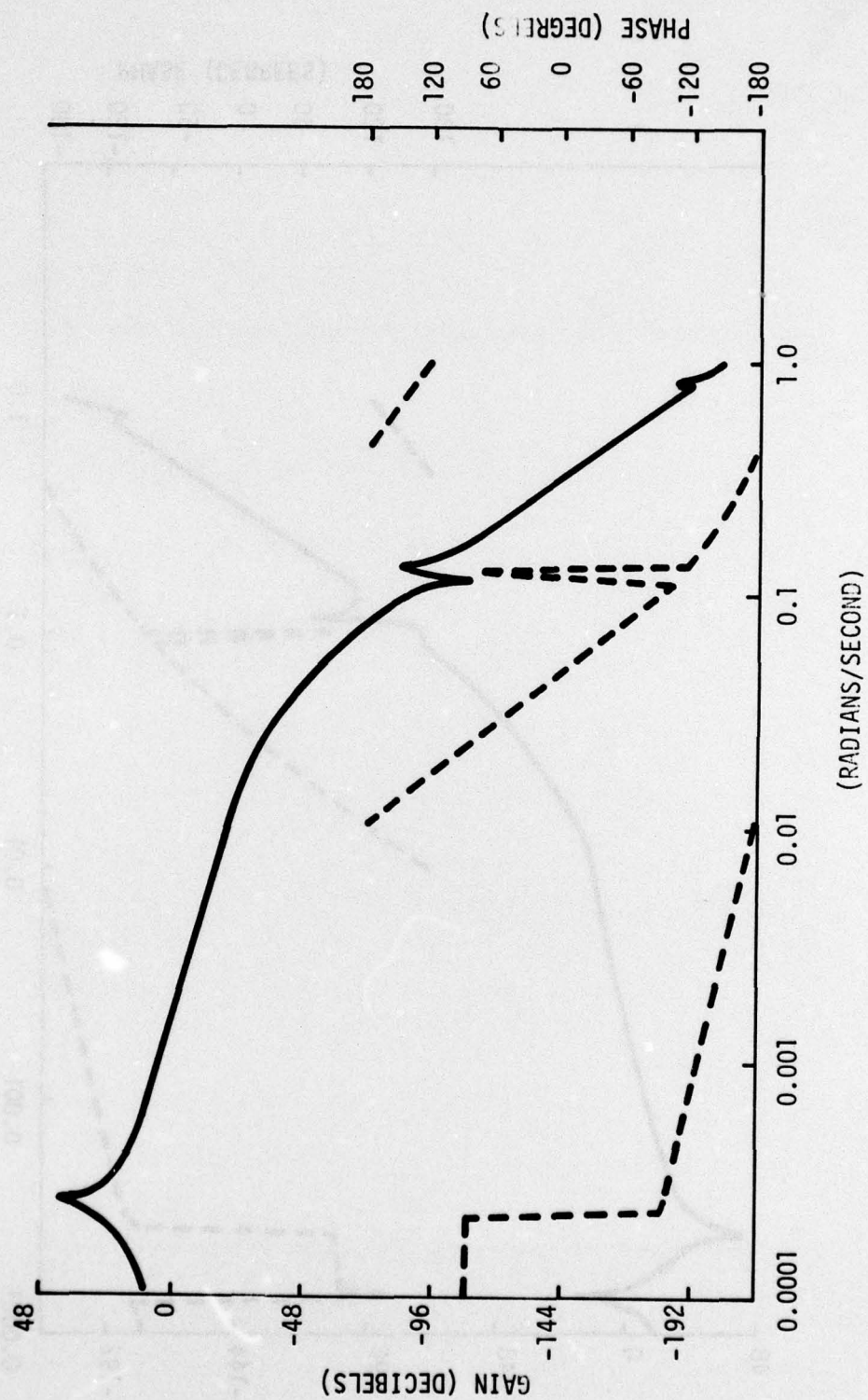


Figure 77. Pitch Wheel Frequency Response

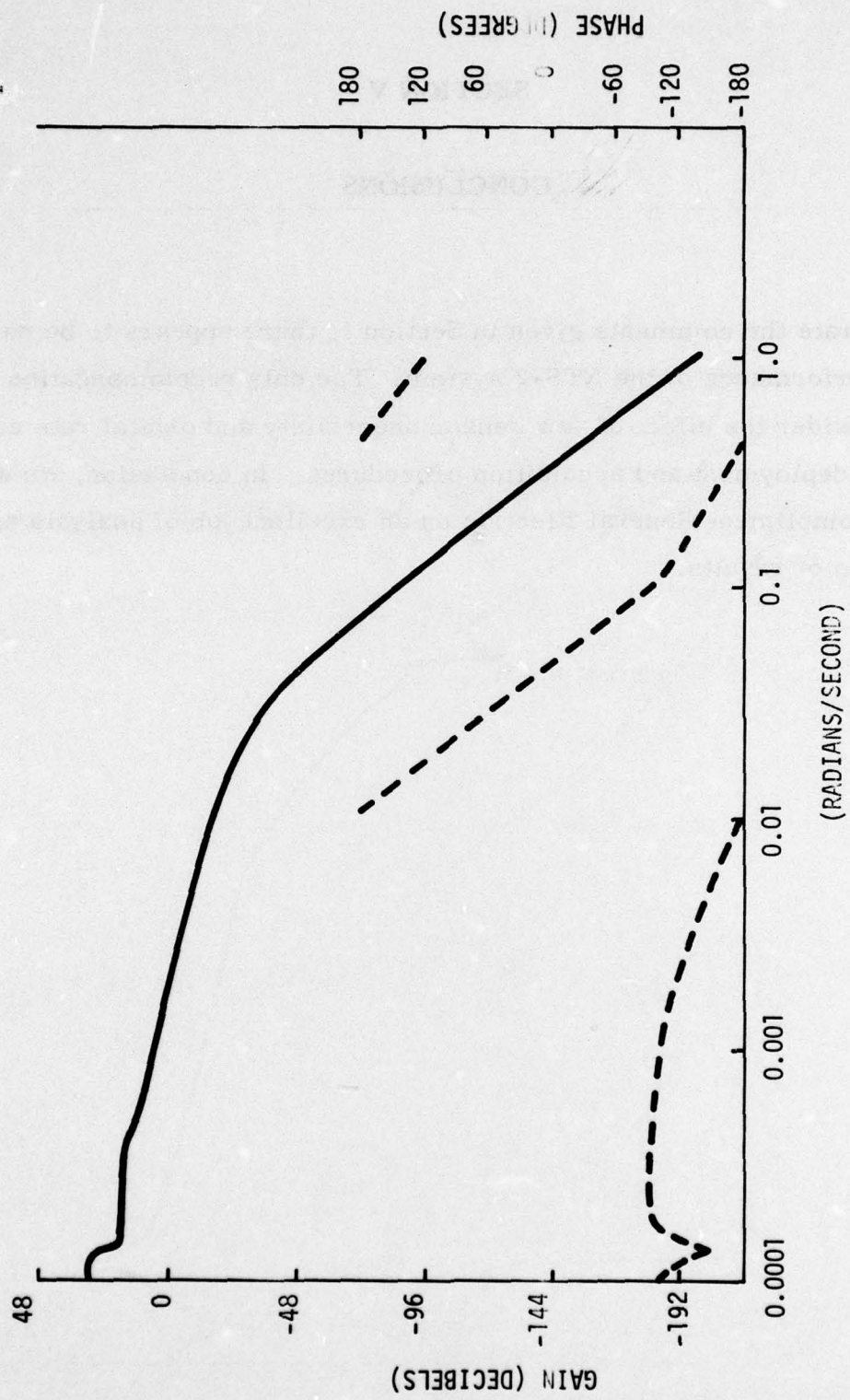


Figure 78. Yaw Wheel Frequency Response

SECTION V

CONCLUSIONS

To reiterate the comments given in Section I, there appears to be no problem in the performance of the NTS-2 system. The only recommendation we have is to consider the effect of yaw sensor uncertainty and orbital rate considerations on deployment and acquisition procedures. In conclusion, we would like to compliment General Electric on an excellent job of analysis and documentation of results.